# DETAILED CONTENTS

# P R E F A C E

The first "Isotopic and Molecular Processes" conference was held in Cluj - Napoca, Romania on September 23 - 25, 1999 under this aegis of the National Agency for Science, Technology and Innovation.

The conference was organised by the National Institute for Isotopic and Molecular Technologies in cooperation with Physics Department of the "Babes - Bolyai" University.

The scientific programme covered the full range of isotopic and molecular processes and their applications in physics, chemistry, chemical physics and biophysics.

Except lectures by invited speakers, there were oral communications and poster sessions. There were 86 scientific participants from Romania and 4 from abroad. The plenary lectures were held in the morning, followed by oral communications presented in two parallel sessions. The papers scheduled as posters were presented in the afternoon at the poster session arranged in the Hall of the "Raluca Ripan" Chemistry Institute, Cluj - Napoca. These plenary lecture, oral contributions and posters are collected in this book, which constitutes the proceeding of the 1st Conference on Isotopic and Molecular Processes.

At the opening ceremony the Vice Major of Cluj - Napoca, Dr.Ing. Nicolae Ruja, welcomed the participants. The conference was then opened by the Director of the National Institute for Isotopic and Molecular Technologies, Dr. Cornel Cuna, after which Acad. Marius Peculea addressed the conference.

During the conference, an Opening Mixer was held in the Glass Hall of the Institute and a Conference Dinner in the "Stadion" Hotel restaurant. A day - time social programme, primarily intended for foreign scientists, included an excursion to Belis - Fântânele and other local sights.

# PREFACE

The financial support given by the National Agency for Science, Technology an Innovation was greatly appreciated. The help received from the Town Hall Cluj - Napoca is gratefully acknowledged. Special thanks are due to the following sponsors: S.C. Tehnofrig S.A., S.C. Ursus S.A., Prodvinalco S.A., Napolact S.A., Panegrano S.A., S.C. Napopan S.A., Jasco Able S.R.L., Redox Trading 2000 S.R.L., Coop. "Arta Juc¾riilor", RATUC, Sonic S.R.L., Natex S.R.L., S.C. Elador S.A., S.C. Inplast Prod. Mixt. Comp. S.R.L.

On behalf of the Organising Committee we wish to express to many persons who helped in the successful organisation of the conference, our most cordial thanks for their hard work, enthusiasm and friendly cooperation. Also we wish to thank the chairmen, the lectures and all the participants who made the conference a stimulating scientific event.

Finally, one express our desire to organise this type of conference in future each two year, to fulfil thus the promise we made at the closing ceremony of the conference.

C. Cuna and V. Cosma — Chairman - Organising Committee

A. Pamula — Secretary

STUDIA UNIVERSITATIS BABEŞ-BOLYAI, PHYSICA, SPECIAL ISSUE, 2000

# PROCEDEU PENTRU DETERMINAREA CAPACITĂŢII DE PRODUCŢIE GARANTATE PENTRU O UZINĂ DE APĂ GREA

## (APA GREA - TEHNOLOGIE ROMÂNEASCĂ -)

## *PROCEDURES TO DETERMINE THE GUARANTEED PRODUCTION CAPACITY OF A HEAVY WATER PLANT*

**MARIUS PECULEA,**

*Academia Română, Bucureşti*

Programul Nuclear Naţional, care a devenit operant începând cu anul 1970, a avut printre principalele obiective şi industrializarea producerii de apă grea. Fiind o tehnologie de vârf şi cu intenţia ca industria românească să aibe o participare maximă, s-a dezvoltat cu prioritate o bază de cercetare, localizată la Râmnicu Vâlcea, care a primit numele generic de Uzina G, de la apa Grea.

Un fenomen fizic sau chimic poate fi transpus într-o tehnologie printr-o infinitate de soluţii, care depind de capabilitatea intelectuală a persoanelor, de dezvoltarea de moment a nivelului industrial şi de starea economică, respectiv de posibilităţile de finanţare. In baza fenomenelor fizico-chimice de separare izotopică, Uzinei G i-a revenit rolul de interfaţă între ştiinţă şi tehnologie, ea elaborând, în timp, nu numai procesele tehnologice de separare a apei grele, ci şi echipamentele, aparatura de măsură şi control şi analizoarele de concentraţie izotopică. In acest fel construcţia fabricii de apă grea, localizată la Drobeta Turnu Severin numită ROMAG, reprezintă o realizare a ştiinţei şi industriei româneşti, care practic a permis României să fie considerată o ţară care a fost capabilă să-şi creeze propria industrie.

Separarea apei grele se realizează prin succesiunea a două procese tehnologice, primul fiind un schimb izotopic la două temperaturi între apă şi hidrogenul sulfurat, proces numit în continuare biterm, cu rolul de extragere al deuteriului din apa de alimentare, al doilea proces fiind distilarea sub vid a apei, numită în continuare distilare, cu rolul de finisare a apei grele, respectiv de concentrare finală până la nivelul cerut de reactoarele nucleare, ceea ce reprezintă o concentrare a ei în deuteriu mai mare de 99,8% molare. Cele două procese tehnologice au fost alese ţinând cont că bitermul este alimentat cu apă, ceea ce îl face complet independent de orice alt proces tehnologic şi la începutul anului 1970 dispunea de cea mai mare experienţă industrială la nivel mondial şi distilarea se baza pe experienţa de laborator de la Institutul de Fizică Atomică din Cluj.

Suportul ştiinţific pentru industrializarea tehnologiei de separare a apei grele a fost Uzina G. Ea a fost prima unitate de cercetare de dezvoltare tehnologică înfiinţată odată cu Comitetul de Stat pentru Energia nucleară (1 martie 1970). Scopul principal al Uzinei G a fost verificarea tehnologiei de separare a apei grele şi a avut ca obiective dezvoltarea de metode şi aparatură pentru analiza izotopică şi elaborarea de metode pentru simularea şi proiectarea proceselor de separare. Prima etapă a început cu construcţia şi punerea în funcţiune a unei instalaţii pilot semiindustrială, după care s-a trecut la verificarea proceselor de separare. A doua etapă, rezultată din experimentarea instalaţiei pilot, a fost crearea condiţiilor de transfer a cunoştinţelor ştiinţifice şi tehnice către industrie, având ca intermediar Institutul de Inginerie Tehnologică pentru Industria Chimică. Din colaborarea cu institutul de proiectare a rezultat ce trebuie să dezvolte cercetarea ştiinţifică pentru a realiza un transfer tehnologic în industrie. Practic cercetarea trebuia să asigure şi să garanteze:

- schema tehnilogică, cu bilanţurile de substanţe, energie şi profilul izotopic
- calitatea produsului şi controlul lui
- consumurile specifice la nivel concurenţial
- preţul de cost al produsului la nivel de competiţie
- know-how-ul pentru construcţia echipamentelor, a elaborării de materiale speciale, a tratamentelor termice şi termochimice care să asigure calitatea echipamentelor şi prin aceasta să reducă la minim riscul industrial.

Această interfaţă între ştiinţă şi tehnologie poate fi rezumată, prin raportul dintre capacitatea reală a instalaţiei şi capacitatea de proiect, relaţie care trebuie să garanteze buna funcţionare a fabricii de apă grea. Relaţia descrie legătura

$$Q_R = C_D \bullet C_F \bullet C_R \bullet Q_P \bullet T_P$$

unde $Q_R$ este capacitatea reală; $Q_P$ capacitatea de proiect; $T_P$ timpul de proiect afectat funcţionării instalaţiei; şi trei coeficienţi, fiecare cu o valoare mai mică decât unu şi care reprezintă $C_D$ coeficientul de disponibilitate; $C_F$ coeficientul de fiabilitate; $C_R$ coeficientul de relaxare. Cei trei coeficienţi reprezintă abaterea procesului real faţă de condiţiile de proiectare, care descriu un proces cu funcţionare în regim staţionar şi fără defecţiuni. Cei trei coeficienţi sunt obiectivele care trebuie avute în vedere pe timpul existenţei instalaţiilor, care necesită îmbunătăţiri continue, pentru a rămâne competitive.

Coeficientul de disponibilitate reprezintă raportul dintre producţia momentană integrată pentru perioada de timp proiectată şi producţia proiectată. Coeficientul de disponibilitate este în primul rând afectat de funcţionarea în regim nestaţionar a instalaţiilor de separare izotopică, procese foarte sensibile la orice variaţie, cât de mică, a parametrilor de operare, cum sunt temperaturile, presiunile, debitele şi peste tot alimentarea cu energie. Pentru determinarea producţiei momentane s-a elaborat un model matematic de calcul care descrie procesul nestaţionar influenţat

de variaţia parametrilor de operare. Modelul a permis determinarea variaţiei în timp a producţiei, starea momentană a instalaţiei (profilul izotopic) cu indicarea conducerii procesului tehnologic într-un domeniu cât mai apropiat de cel static şi determinarea zestrei de apă grea în lungul instalaţiei, obiectiv urmărit de legislaţia de "safe-guard".

Verificarea programului de calcul s-a făcut prin experimentarea instalaţiei pilot, unde s-a urmărit variaţia profilului izotopic în funcţia de parametrii de operare. Profilul izotopic în lungul instalaţiilor, cel calculat faţă de cel măsurat, indiferent de parametrii de operare, se diferenţia prin una şi aceeaşi constantă, care s-a dovedit a fi eficienţa elementelor de contact. Un model matematic nu depinde de mărimea saltului de scară, cât timp eficienţa elementului de contact este o funcţie atât de scară cât şi de încărcare (debite). Pentru reuşita transpunerii la scară industrială a rezultatelor stabilite la nivel de instalaţie pilot şi indirect de garantare a capacităţii de producţie, determinarea comportării elementelor de contact, talere şi umpluturi, s-a realizat la scara 1:1 în cadrul unui laborator specializat al Uzinei G pentru testarea lor.

Laboratorul de testare a talerelor a fost dotat cu trei standuri experimentale având ca echipament central câte o coloană cu diametrele de 1,5; 2,7 şi 5,3 m, care reprezentau, prima dimensiunea instalaţiei pilot şi celelalte două dimensiunile reale ale coloanelor instalaţiei industriale. Comportarea elementelor de contact s-a determinat în sistemul apă-aer, funcţie de enegia cinetică a gazului, mod de testare universal valabil.

Raportat la modul de testare a elementelor de contact, sistemul procesului de separare este format de apă-hidrogen sulfurat, care are o comportare diferită faţă de sistemul apă-aer, ceea ce a impus introducerea unor relaţii de similitudine care să ţină cont de proprietăţile sistemului de separare. In totalitate testele realizate în sistemul apă-aer au fost recalculate în sistemul apă-hidrogen sulfurat şi raportarea rezultatelor s-a făcut în funcţie de cifra Weber, car pe lângă energia cinetică a gazului ţine cont şi de tensiunea superficială a lichidului (apă saturată cu hidrogen sulfurat). Acest nou mod de interpretare a putut explica şi soluţiona toate perturbaţiile apărute la punerea în funcţiune a instalaţiilor industriale, consecinţă directă fiind atingerea capacităţii de proiect.

O problemă aparte a format-o elementul de contact pentru distilare. S-a optat pentru o umplutură ordonată, cu o geometrie bine definită, pe care apa urma să curgă într-un strat cât mai subţire, practic la nivelul stratului limită, reducând astfel la minim rezistenţa la difuzia izotopului în lichid. Performanţa acestei umpluturi, de cca 3 ÷ 4 ori mai bună ca a unei umpluturi similare din industria chimică, se datorează combinării unor procese, toate contribuind la mărirea gradului de udabilitate a suprafeţei pe care se scurge lichidul. Au fost luate în considerare capilaritatea, mărirea tensiunii superficiale prin curbare mecanică şi aplicarea unui tratament termochimic.

Condiția de optimizare a prețului de cost impune cascadarea instalațiilor de separare izotopică, dar la care trebuie ținut cont de marea sensibilitate a procesului. Practic, orice abatere a parametrilor de funcționare a unui etaj oarecare, influențează negativ atât în aval cât şi în amonte funcționarea cascadei, deranjând profilul izotopic al acesteia, care în final se traduce prin eliminarea de izotop prin linia de deseu, respectiv prin scăderea producției. Pentru reducerea la minim a influenței negative a perturbației unui etaj din ansamblul cascadei, instalația de fabricare a apei grele a fost prevăzută doar cu câte două etaje pentru fiecare proces în parte, respectiv pentru biterm şi pentru distilare. Prin această soluție s-a obținut o creştere a stabilității în funcționarea instalației şi deci a disponibilității ei.

Modelul matematic care descrie regimul nestaționar de funcționare a instalațiilor şi determinarea comportării reale a elementelor de contact au permis stabilirea cu precizie a coeficientului de disponibilitate.

Coeficientul de fiabilitate a fost determinat printr-un studiu statistic susținut de experimentarea instalației pilot pe o perioadă de 5 ani. El a scos în evidență comportarea echipamentelor dinamice, a materialelor de construcție a echipamentelor statice şi a aparaturii de măsură şi control.

Echipamentul dinamic principal a fost compresorul pentru recircuirea hidrogenului sulfurat, practic elementul vital al procesului, de mare complexitate constructivă şi ca atare şi foarte scump, aşa ca instalația a fost dotată doar cu un echipament activ (fără rezervă). Fiind unicat, garantarea funcționării lui fără defecțiuni, trebuia asigurată în intervalul dintre revizii, interval echivalent cu 16000 ore. Testarea compresorului experimental s-a realizat în instalația pilot, care după o funcționare continuă de cca. 7000 ore, tehnologia lui a fost transferată de IMG-Bucureşti, unde s-a executat seria de compresoare pentru ROMAG, compresoare cu o capacitate echivalentă de 2,5 MW. Datorită acțiunii corosive a hidrogenului sulfurat umed, compresorul a fost executat dintr-un aliaj special de oțel inoxidabil, constructiv având un singur rotor montat în consolă şi un stator rotoric. Etansarea arborelui motor s-a realizat cu o presetupă hidrodinamică, garda hidraulică fiind asigurată de un circuit de ulei; neavând nici o piesă în contact direct, s-a putut asigura o funcționare sigură practic infinită în timp.

O atenție deosebită a fost acordată materialelor din care a fost construită instalația de separare bitermă (coloane şi conducte). Hidrogenul sulfurat umed şi apa cu hidrogen sulfurat solvit (pH ~ 3) sunt agenți foarte corosivi. Cu toate acestea, pentru competitivitate, s-a apelat la un oțel carbon, elaborat la Galați, caracterizat de o structură fină, omogen, controlat după elaborare pe întreaga suprafață a tolelor şi supus unui tratament de detensionare. Oțelul a purtat indicativul de G 52/28 şi rețeta lui a fost elaborată de ICEM - Bucureşti. Rezistența lui la coroziune a fost asigurată printr-un tratamet termo-chimic special, brevet al Uzinei G, şi a căpătat numele generic de "piritizare". In esență pasivarea oțelului carbon se realiza prin transformarea sulfurilor de fier, formate la contactul cu hidrogenul sulfurat, din sulfuri sărace în sulf în sulfuri bogate în sulf, respectiv în

pirită, care mărea rezistența la coroziune cu cca $10^5$ ori față de oțelul netratat. Prin "piritizare" viața echipamentelor a fost dublată, cu un efect benefic asupra prețului de cost al apei grele.

Soluția de hidrogen sulfurat în apă formează un cristalo-hidrat care se solidifică la temperaturi mai mici de 30 $^{o}$ C. Aparatura de măsură şi control şi liniile lor de impuls au fost concepute special pentru această situație şi au fost prevăzute cu linii însoțitoare termostatate. Insoțitorii, formați din țevi subțiri, alimentați cu abur de joasă presiune, au fost aglomerați prin intermediul unui ciment termoconductor, elaborat la Uzina G, cu aparatura de măsură şi a liniilor de impuls, realizându-se o termostatare, cu o temperatură practic uniform repartizată.

Odată cu creşterea fiabilității instalațiilor, pe lângă garantarea capacității de producție, s-a obținut o importantă scădere a riscului instalației de producere a apei grele.

Cel de-al treilea coeficient, cel de relaxare, mai puțin luat în considerare pentru instalațiile din industria chimică, în schimb pentru instalațiile de separare izotopică a apei grele, el devine hotărâtor în alegerea soluțiilor tehnologice. Cu titlu informativ, care este sugestiv pentru instalațiile de separare a apei grele, perioada de intrare în regim de extracție (producție), poate atinge 2-3 luni, în funcție de modul de operare. O perturbație oarecare în proces, necesită deasemenea timpi îndelungați pentru refacerea profilului izotopic, timp în care producția este mult redusă, sau prezintă fluctuații importante. In lungul instalației zestrea de izotop, ca urmare a profilului izotopic, reprezintă o cantitate de apă grea echivalentă cu producția a 3~5 luni, funcție de soluția tehnologică adoptată. Toate acestea au contribuit la alegerea unui sistem de legare între etajele instalațiilor ca ele să poată funcționa independent. La apariția unui deranjament major, etajele intră în funcționare în circuite închise, păstrându-şi zestrea şi profilul izotopic, astfel încât la repornire, timpul de relaxare, de reintrare în producție, să nu depăşească 24 ore. In acelaşi scop s-a urmărit ca zestrea de izotop în lungul instalației să fie menținută la un nivel minim, lucru realizat prin talere operate la un nivel minim de lichid, evitarea de rezervoare intermediare, nivele minime de lichid în baza coloanelor, ş.a. Realizarea şi menținerea unei zestre minime şi a unui profil izotopic constant s-a datorat şi sistemului de extracție continuu, aplicat la ultimul etaj de separare, respectiv la extracția continuă şi controlată a producției de apă grea, cu o concentrație mai mare în deuteriu de 99,8% molare.

Garantarea calității produsului a determinat dezvoltarea analizelor izotopice, a urmelor de elemente chimice şi a purificării gazelor. S-au realizat spectrometre de masă performante pentru măsurarea maselor moleculare 2 şi 3 (a hidrogenului şi a hidrogenului deuterat), densimetru cu vibrator (pentru întregul domeniu de concentrație a apei grele), spectrometru în infraroşu (pentru analiza produsului, respectiv concentrații mari de apă grea), conductivimetre, metode gazcromotografice. Aparatura a fost construită în două variante, pentru analize discrete în laboratoare şi pentru analize în flux (în linie) ataşate direct la instalațiile de separare.

Procesul de separare biterm este un mare consumator de energie termică, practic 90% din energia introdusă în proces. Pentru garantarea consumurilor specifice o atenţie deosebită s-a acordat studiilor de recuperare a energiei, efectuate prin compararea diagramelor de flux energetic cu cele de flux exergetic. Cu ajutorul lor s-a determinat gradul maxim de recuperare a energiei termice şi s-a dat soluţia constructivă pentru buclele termice care asigurau umiditatea (principalul consumator de energie termică) şi dezumificarea (prin recuperare) hidrogenului sulfurat.

Confirmarea tehnologiei de separare a apei grele s-a făcut prin compararea în final a preţului de cost al produsului cu tehnologii similare. Pentru aceasta s-a dezvoltat o teorie, numită funcţia tehnologică, care a permis determinarea unor coeficienţi de comparaţie aplicate la 4 instalaţii, coeficienţi unde valorile mai mici decât unu reprezintă tehnologii rentabile, avantajul lor crescând odată cu scăderea valorii coeficientului.

| MR | MC | SRP | UZG |
|---|---|---|---|
| 0,9 | 0,894 | 0,825 | 0,761 |

Tabelul are urmatoarea semnificaţie:

MR - modul industrial românesc
MC - modul industrial canadian
SRP - Savannah River Plant (SUA)
UZG - instalaţia pilot a Uzinei G

Datele comparative între fabricile de apă grea, analizate prin metoda funcţiei tehnologice sunt redate în tabelul din continuare, unde se pot observa diferenţele între tehnologii şi în special cele patru poziţii care deosebesc instalaţia americană SRP şi instalaţia Uzinei G, notate în tabel prin "X", şi care evidenţiază îmbunătăţirile aduse de Uzina G, ulterior transferate la ROMAG.

| **OBIECT** | **SRP** | **UZG** | **MC** | **MR** |
|---|---|---|---|---|
| Capacitate pe modul, t, $D_2O$/an | 20 | 2 | 400 | 90 |
| Numărul de etaje ale schimbului izotopic | 2 | 2 | 3 | 2 |
| Concentraţia, % (D/H+D) a produsului schimbului izotopic | 15 | 15 | 45 | 20 |
| Separarea etajului unu al schimbului izotopic | 4 | 4 | 4 | 10 |
| Diametrul coloanei etajului unu, în m | 3,4 | 1,5 | 8,5 | 5,3 |
| Inălţimea coloanelor etajului unu, în m | 35 | 50 | 85* | 60 |
| Numărul de coloane în paralel în etajul unu | 1 | 1 | 3 | 3 |
| Tipul de taler din coloanele de schimb izotopic | cu clopoţei | perforate | | |
| Soluţia constructivă pentru coloanele cald-rece | separate | separate | suprapuse | separate |
| Linia de legătură între etajele instalaţiei biterm | gaz+lichid | lichid | gaz | lichid |

| OBIECT | SRP | UZG | MC | MR |
|---|---|---|---|---|
| Umidificarea şi dezumificarea hidrogenului sulfurat | în schim-bătoare de căldură | prin contact direct pe talerele din coloanele de schimb izotopic | | |
| Tipul coloanelor de distilare | cu talere | cu umplutură | | |
| Obținerea hidrogenului sulfurat | propriu | propriu | din țiței | propriu |

* se referă la înălțimea totală a coloanelor cald-rece suprapuse

Cercetările asupra tehnologiei de separare a apei grele au continuat şi dupa transferul tehnologic către industrie şi chiar după începerea construcției instalației industriale, ele urmărind îmbunătățirea valorii celor trei coeficienți, de disponibilitate, de fiabilitate şi de relaxare. Rezultatul acestor cercetări s-a concretizat prin introducerea unei coloane de echilibrare izotopică în amonte de instalația biterm. Noua instalație de separare a apei grele prevăzută cu coloană de echilibrare izotopică este o premieră mondială şi experimentarea ei pe mai mulți ani la Uzina G a dat o satisfacție totală. Coloana de echilibrare permite alimentarea instalației de separare a apei grele pe linie de gaz, având ca primă consecință că în instalație nu mai intră impuritățile aduse cu apa de alimentare. Circulația de fluide în instalația de separare se realizează în circuite închise, cu substanțe curate, singurul component care se transmite în lungul fluxului tehnologic fiind izotopul greu al apei, respectiv deuteriul. Prin vehicularea de substanțe curate depunerile de inerte din instalație s-au redus de peste 25 de ori, ceea ce a permis mărirea timpului între reviziile planificate şi odată cu aceasta mărirea producției.

Coloana de echilibrare fiind plasată în amonte de instalație are rolul şi unui rezervor tampon izotopic, ceea ce măreşte stabilitatea în operare şi odată cu aceasta creşte coeficientul de disponibilitate.

Programul de apă grea din cadrul Programului Nuclear Național a fost o demonstrație a capabilității cercetării şi industriei româneşti de a crea o tehnologie avansată printr-un efort propriu.

# REAL TIME STUDIES IN INFRARED MULTIPHOTON DISSOCIATION

**M. SANTOS, B. SAMOUDI, L. RUBIO, L. DÍAZ and J.A. TORRESANO**

*Instituto de Estructura de la Materia, C.S.I.C., Serrano, 121, 28006-Madrid. Spain*

Infrared Multiphoton Dissociation (IRMPD) in polyatomic molecules is one of the more general techniques for inducing unimolecular reactions from the ground electronic state and for obtaining free radicals with a high degree of vibrational and rotational energy [1]. Analysis of the Spontaneous Luminescence (SL), emitted in the dissociation process, and Laser Induced Fluorescence technique (LIF) allows to follow in real time the production of the radicals providing valuable data about both, the kinetics of the dissociation reactions and the nascent energy distribution among the produced fragments [2].

In this work we review the results that we have recently obtained from the SL and LIF studies of some fragments formed in the IRMPD of 2-chloroethenylsilane (CES) and vinylbromide (VBr) [3-5]. We give two examples of the analysis of the SL signal produced in the dissociation process as result of two different mechanisms: the inverse electronic relaxation of a primary radical and the direct electronic relaxation of collisionally produced excited fragments. Results from the application of LIF technique to the products of both parent molecules reveal that these are always produced vibrationally hot.

Laser induced photodecomposition of silicon compounds is a problem of current interest due to its potential role in chemical vapour deposition of silicon-based films [6,7]. Thermal and photolytic decompositions of haloalkenyl silanes have received only very limited attention. We have carried out several studies on the IR laser driven reactions of silanes for chemical vapour deposition of Si/C/H materials [8] and, in particular, on the $CO_2$ laser-powered decomposition of CES as well as on the properties of the solid materials produced by this decomposition [9]. The knowledge of the dissociation mechanisms and the resulting intermediary species is essential to understand and control the properties of the films. These properties usually depend on the wavelength and the fluence of the laser radiation, and also on the precursor pressure. We have studied the SL produced in the IRMPD of CES both in the collisionless and collisional regimes. This emission is attributed to the intermediate excited $SiH_2$ formed in the dissociation process, giving support to the IR laser-induced decomposition channels of CES postulated in our previous paper [3]. Besides, the nearly instantaneous formation of $SiH_2$ suggests that the chloroethene elimination channel is dominant. On the other hand, the LIF excitation spectrum of the $SiH_2$ radicals produced in the dissociation process indicates that the nascent fragments are vibrationally excited, at least in the bending mode.

Elementary reactions involving small carbon species like $C_2$ and $C_3$ play an important role in the high temperature chemistry of hydrocarbons, as, for example, in the formation and decay of the recently discovered $C_{60}$ fullerene [10,11]. $C_2$ is formed following IRMPD of a variety of polyatomic molecules [12-14], and among them, vinylhalides are systems that posses simple laser induced chemistry [15-16]. We have studied for the first time the IRMPD of VBr applying SL and LIF techniques. The obtained SL emission spectrum have been assigned to the Swan bands of the excited $C_2$ molecule ($d^3\Pi_g \rightarrow a^3\Pi_u$ transition) and to the CH fragment ($A^2\Delta \rightarrow X^2\Pi$ transition). We have observed that the formation of these species is due to the simultaneous interaction of collisions and infrared radiation on the initially formed excited precursor, probably acetylene. We have carried out LIF detection of the produced fragments obtaining that the population of $C_2$ formed in the ground state is vibrationally hot.

## EXPERIMENTAL

A Lumonics K-103 TEA $CO_2$ laser is employed for the IRMPD of the samples. It is equipped with a frontal Ge multimode optics (35 % reflection) and a rear diffraction grating with 135 lines/mm blazed at 10.6 μm. In all the cases the wavelength is checked with a 16-A spectrum analyser (Optical Eng. Co.). The laser operates with a mixture of $CO_2$, $N_2$ and He in the proportion 8:8:84, the pulse temporal profile being monitored with a photon drag detector (Rofin Sinar 7415). This temporal profile consists of a spike of 60 ns (FWHM) followed by a tail of approximately 3 μs long. In some experiments we have suppressed $N_2$ in the mixture to obtain a tail-free pulse of 60 ns (FWHM).

The photolysis experiments are performed in static conditions in CES experiments and under gas flow in the case of VBr. Cells of 4.5 cm diameter and 12 or 25 cm length are used, both fitted with a pair of NaCl windows orthogonal to another pair of quartz windows. The $CO_2$ laser beam is focused at the centre of the reaction cells by NaCl lenses of 10 or 24 cm focal lengths. In some experiments tight focused irradiation was used employing a 5 cm focal length lens and a 10 cm long cell. Analysis of the final stable products is carried out by FTIR spectroscopy.

Fluorescence is induced in the formed fragments by means of a $N_2$-pumped dye laser (PRA LN107) with a bandwidth of 1.6 $cm^{-1}$ at 500 nm. The beam, counter-propagating to the $CO_2$ laser beam, is focused by a 50 cm quartz lens at the focus of the infrared beam. The relative energy of the dye laser was controlled with a Thorlabs high speed silicon detector.

Spontaneous luminescence and induced fluorescence are detected through a quartz window at right angle to the laser axis after focusing onto a P28 RCA photomultiplier tube through interference filters centred at 610, 560, 488 and 431 nm (10 nm FWHM in all the cases) for $SiH_2(0,1)$, $C_2(0,1)$, CH(0,1) and CH(0,0) transitions respectively. To obtain the SL spectra, the signal was dispersed with a Jarrell Ash 25 cm monocromator (7 nm resolution) or with a Bausch and Lomb 10 cm monocromator with 2 mm slits that was used as filter (15 nm resolution).

The $CO_2$ laser pulse, picked up with the photon drag detector, triggers a Tektronix TDS 540 digital oscilloscope that is used to collect the signals and send them to a personal computer where they are averaged and analysed. The delay between the $CO_2$ laser and the probe laser is controlled by a Berkeley Nucleonic BNC 7036A to within ~ 50 ns. The $CO_2$ laser fluence is calculated as the ratio of the pulse energy, as measured with a Lumonics 20D pyroelectric detector, and the FWHM cross-sectional beam area, measured at the cell position with a pyroelectric array Delta Development Mark IV. The obtained fluences using the 10 or 24 cm focal length lenses are in the range 13-170 J/cm$^2$ . The sample pressure in the gas flow cell is measured with a 0-10 hPa MKS Baratron gauge being the rate of the $CO_2$ pulse so that a new fresh sample is irradiated in each shot. 2-chloroethenylsilane is prepared following the chemical procedure given elsewhere [17]. The VBr samples have been purchased from Merck (99.0 %) and degassed prior to use.

## RESULTS AND DISCUSSION

### Spontaneous Luminescence

In Figure 1 (a) and (b) we give the SL spectra obtained by irradiating 0.5 mb of CES and 4 mb of VBr with infrared pulses of 75 and 170 J/cm$^2$, respectively. The spectrum obtained for CES is broad and structureless, indicating that many rovibronic levels are excited. These spectral features are typically found in luminescent emissions from infrared multiphoton absorption and dissociation of molecules and have been explained in terms of intermode coupling in the molecular quasicontinuum and inhomogeneous broadening of the luminescence spectrum [18]. The spectrum obtained in dissociation of VBr consists in several vibronic bands without rotational resolution, superimposed to a broad background. It is much better resolved than in the case of CES, what may be due to the nature of the emitting species, diatomic fragment with high quantum yield, and to the origin of the mechanism giving rise to the fluorescent emission.

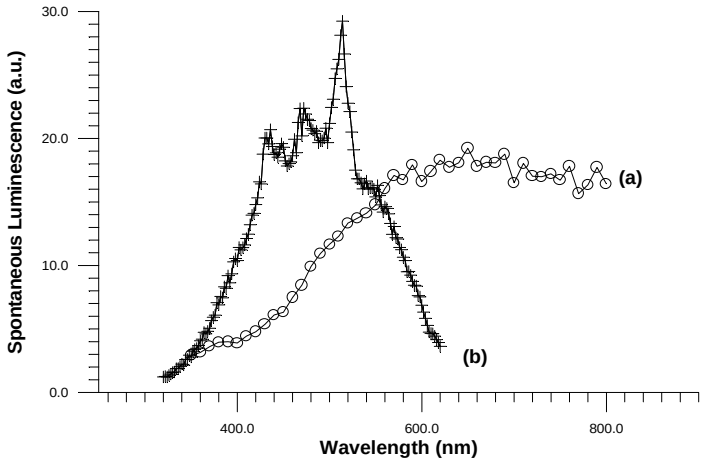


Figure 1. Emission spectra of the SL resulting from the IRMPD of CES (a) and from VBr (b)

Figure 2 shows the temporal profiles of the luminescence signals filtered at 516 nm for several initial pressures of VBr (profiles a-d). Luminescence signals consist in an initial maximum followed by another broad one. The first maximum, that appears at pressures higher than 1.3 hPa, always peaks 80 ns after the $CO_2$ maximum (160 ns after the onset of the laser pulse), conditions at which no collisions between VBr molecules take place; its rise always follows the $CO_2$ pulse, indicating that radical production is driven by the temporal profile of the $CO_2$ laser pulse. The second maximum consists in a broad signal that reaches the maximum at a time at which more than two collisions between VBr molecules have taken place. The time between the two maxima decreases linearly with the pressure. Such temporal profiles of SL are characteristic of all the luminescence signals detected along the whole spectrum of Figure 1. In addition, we have compared the luminescence spectra gating the signal at each of the two obtained maxima, and no difference have been found. This result rules out the possibility of two different emission processes at two different times. Irradiation of CES produces a luminescence signal which consists in an unique maximum that peaks also around 80 ns and also follows the rise of the $CO_2$ pulse for all the studied pressure interval ( profile e).

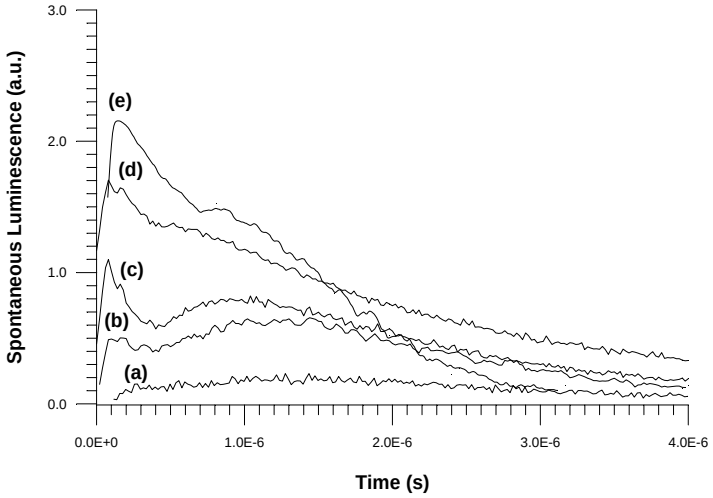


Figure 2. Temporal profiles of the SL from different initial pressures of VBr (a-d) and from CES (e).

The maximum intensity of the spontaneous luminescence at 650 nm as a function of the initial pressure of CES in the cell is given in Figure 3(a). The linear dependence in the pressure range between 0.1- 0.6 mbar indicates that, within this interval, the luminescence stems from a collisionless process. For pressures higher than 0.6 mbar the slope of that linear dependence decreases, suggesting a pressure quenching of the luminescence and/or a decrease in the rate of production of the emitting species in the multiphoton process. To elucidate between these two

possibilities we have plotted the luminescence intensity versus pressure at different times after that corresponding to the maximum of the signal. A shift to lower values of the pressure transition between both regimes is clearly observed, indicating that a cumulative luminescence quenching process induced by collisions is the responsible effect. The dependence of the luminescence signal on the VBr pressure is shown in the Figure 3(b). The variation of the luminescence is linear with pressure but shows a threshold behaviour as is typical of a collisional origin of the emitting precursors.

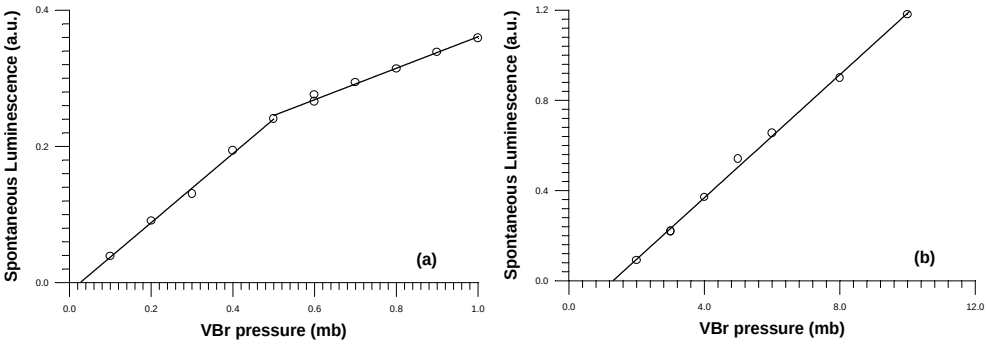


Figure 3. VBr (a) and CES (b) pressure dependence of the SL intensity

Due to the fact that the emission band originated from the bending vibrational transitions $(0,\nu_2',\ 0) \rightarrow (0,\nu_2'',0)$ in $SiH_2$ extends in the range 500-800 nm [19], we have assigned the observed luminescence to the decay from the $^1B_1$ electronic state to the $^1A_1$ ground state of silylene. Besides, the detected maximum about 650 nm coincides with the (0, 1, 0) $\rightarrow$(0, 1, 0) transition as could be expected if one consider that its Franck-Condon factor is the largest among those for the first seven $(0,\ \nu_2'.\ 0) \rightarrow (0,\ \nu_2'',0)$ transitions [20]. From the independence of the substrate pressure on the delay between the laser pulse and the onset of the luminescence, and the threshold character of the fluence dependence of the luminescence that we have observed for CES, we suggest that the most probable reason for the production of visible emission in the MPD of CES is the inverse electronic relaxation (IER) of a primary fragment formed in the laser pulse time.

The detection of silylene gives support to the previously postulated reaction paths for the infrared multiphoton dissociation of 2-chloroethenylsilane, and suggests that, at high fluence conditions, the chloroethene elimination channel dominates the dissociation reaction.

In the spectrum obtained from VBr, we assign the obtained bands at 436, 472, 514 and 560 nm to the emissions from the $C_2$ ($d^3\Pi_g$–$a^3\Pi_u$) $\Delta\nu$=2, 1, 0 and -1 Swan bands and those at 430, 486 nm to the emissions from the CH($A^2\Delta$–$X^2\Pi$) $\Delta\nu$=0 and –1 transitions. The obtained dependence of the luminescence on pressure as well as the temporal profiles of the signals indicate that the production of the

excited $C_2$ and CH species arises from a collisional assisted process taking place in the time of the $CO_2$ laser pulse. As the initial maximum for $C_2$ or CH appears always 160 ns after the onset of $CO_2$ pulse, smaller than the time for one collision between VBr molecules at the threshold pressure for this maximum (185 ns), it is suggested that the initial dissociation of VBr takes place through a non collisional process.

**Laser induced fluorescence**

When the probe dye laser wavelength is scanned, after 600 ns of the MPD of CES, the LIF excitation spectrum of Figure 4 is obtained. The temporal profile of the signals can be fitted to single exponential functions with decay times between 200 and 300 ns. There are four bands in the excitation spectrum which we have assigned to the sequence of vibrational bands of the $\nu_2$ mode of $SiH_2$ with $\nu'$-$\nu''$ = 2 [20,21]. According to the calculated Franck-Condon factors for these transitions [21], it appears that the larger part of the population of the nascent $SiH_2$ fragments are produced vibrationally hot. In these experimental conditions it was not possible to resolve the rotational structure of the vibronic transitions.

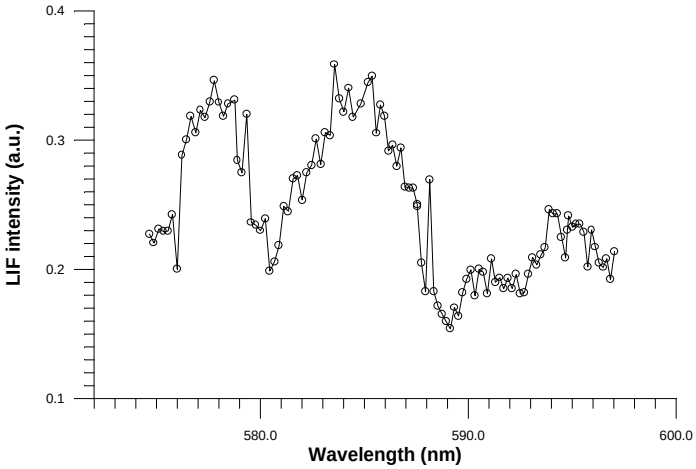


Figure 4. LIF excitation spectrum following the IRMPD of CES

LIF signal recorded at 578.4 nm and at 588.15 nm when the time delay between the $CO_2$ laser and the probe laser is increased is given in Figure 5. For the band at (020)-(000) of the $SiH_2$ fragment, the fluorescence intensity at 578.4 nm reaches a maximum 1 μs after the $CO_2$ laser while for the band at 588.15 nm the LIF signal reaches its maximum 3 μs after the photolysis pulse. Similar effects to those of the line at 588.15 nm have been described in LIF studies following MPD of some organosilanes [22,23], and have been explained by the accumulation of the nascent rotational population in a selected set of states by rotational cooling induced by collisions with the buffer gas. This signal retains its maximum intensity during longer time, probably reflecting the time scale for the rotational cooling.

The decay tail detected in both cases may contain contributions from both, the diffusion of the radical out of the viewing region, and the reaction of the :$SiH_2$ with the parent or other decomposition products.

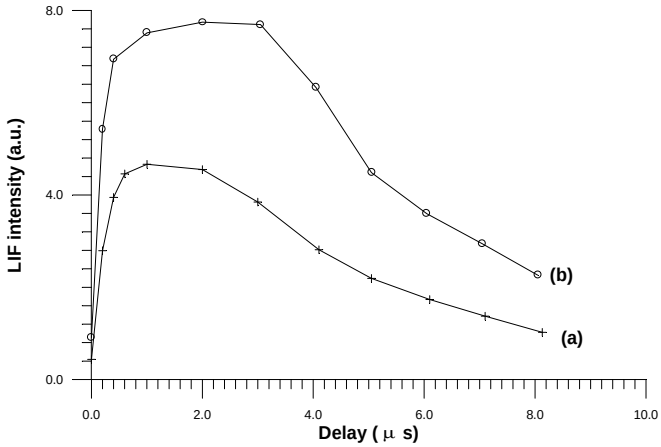


Figure 5. LIF signal intensity vs. the time delay between the photolysis of CES and the probe pulse at (a) $\lambda$ = 578.4 nm and (b) $\lambda$ = 588.2 nm.

We have scanned the dye laser wavelength 800 ns after the infrared irradiation of 0.5 mb of pure VBr obtaining the LIF excitation spectra of $C_2$ shown in Figure 6 a and b. It can be observed that, besides the bandheads corresponding to the (0,0) and (1,0) transitions, those corresponding to the (1,1) and (2,1) transitions are also observed. In addition, some spiky rotational structure corresponding to the R branch of the $\nu''$= 0 level can be identified. The appearance of the (1,1) and (2,1) bandheads denotes that a rather high proportion of $C_2$ fragments are formed in the $\nu''$= 1 vibrational levels and, therefore, vibrationally hot. The collisional character of the $C_2$ production from the IRMPD of VBr, may be the responsible for the hotter vibrational temperature, as was proven in the IRMPD of $C_2H_4$ [24]. From the values of the integrated areas of the bands in Figure 6 and the Franck-Condon factors [25]. We have estimated, assuming a Boltzmann distribution, an effective vibrational temperature for the formed $C_2$ of 2200 ± 200 K.

To confirm the presence of CH among the dissociation products that has been assigned in the SL spectrum, we have carried out LIF experiments filtering the fluorescence signal at 488 nm. When the probe dye laser is less than 6 μs apart from the photolysis laser the LIF signal is very weak and superimposed to a strong SL signal. Scanning the dye laser wavelength 8 μs after the $CO_2$ laser we have obtained the fluorescence excitation spectrum of Figure 7. A broad band with some rotational structure centred at 431 nm is obtained, corresponding to the ($A^2\ \Delta \rightarrow X^2\Pi$, $\Delta\nu$=0) transitions of CH. Some spiky structure corresponding to the Q branch of this band is also observed.

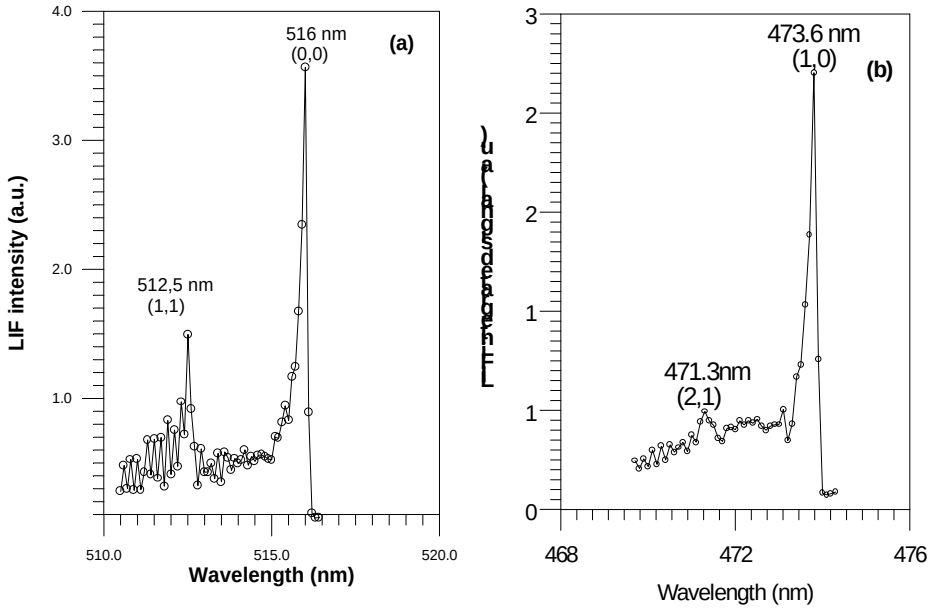


Figure 6. LIF excitation spectra following the irradiation of VBr filtering at 560 nm.

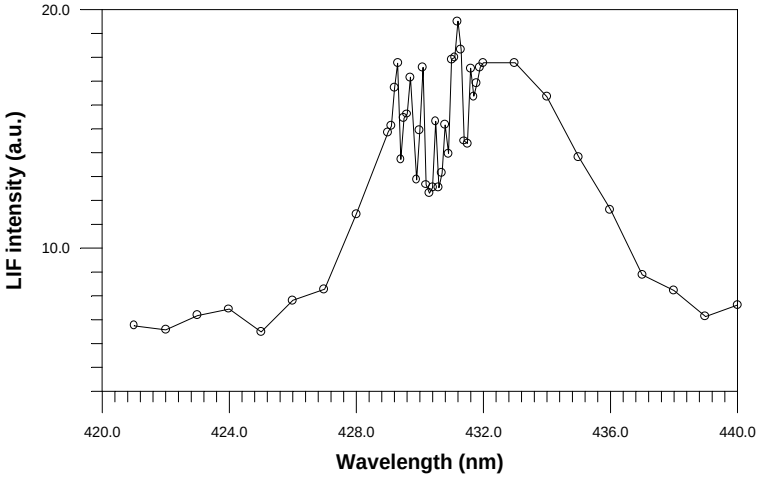


Figure 7. LIF excitation spectra following the irradiation of VBr filtering at 488 nm.

As it can be seen in the Figure 8 the addition of Ar up to 44 hPa significantly increases the amount of the detected $C_2$ signal. As it is well known, the addition of an inert buffer gas enhances the LIF detection of the produced fragments by controlling

the diffusion processes and inducing their vibrorotational relaxation. At 800 ns from the photolysis laser and at the VBr pressure used, the diffusion of $C_2$ out of the probed volume is quite small [26], scarcely contributing to the total increase. The SL signal recorded when the dissociation of VBr is carried out in the presence of Ar indicates that there is an increase in the amount of $C_2$ excited to the upper electronic states that is up to a factor of 6 for the smallest VBr pressure studied. We have assigned this increase to the existence of an effect of rotational hole filling (RHF) in the unimolecular dissociation of VBr. We assign then the high increase observed in the LIF detection of $C_2(a^3\Pi_u, v''=0)$ from the IRMPD of VBr in the presence of Ar as due to an actual increase in the formation of $C_2$ due to RHF in the dissociation of VBr, plus a large contribution from the relaxation of the initially formed rotational and vibrationally excited $C_2$. We have observed that up to the smallest VBr/Ar studied concentration (~ 1/600) no quenching of the $C_2$ ($d^3\Pi_g, v' = 0$) state have been detected, as has been already pointed out by other authors for smaller Ar concentration [27,28]. This result together with the different increase of the LIF and SL signals detected when Ar is added, suggests that, in the ground state, approximately five times more population is formed vibrorotationally excited than in the $v'' = 0$ level.

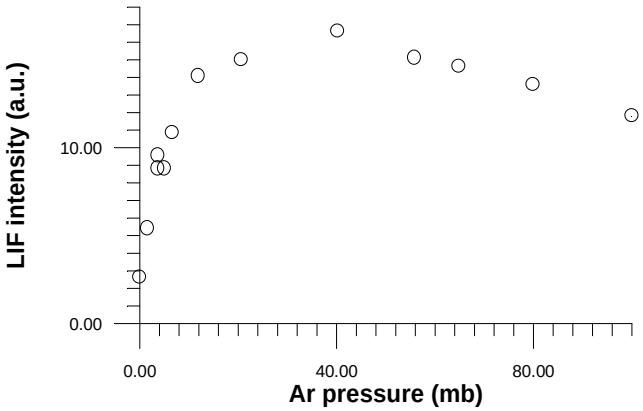


Figure 8. LIF intensity signal vs. the pressure of added Ar to 0.16 mb of VBr.

## CONCLUSIONS

We have reviewed the results obtained in the real time study of 2-chloroethenylsilane and vinylbromide by analysing the spontaneous luminescence emitted in the dissociation process and by applying laser induced fluorescence technique. In each of the molecules, the spontaneous emitted signal is due to a different origin. In CES it is produced by the relaxation of the $SiH_2$ fragments primary formed in the dissociation process, which are electronically excited through an inverse electronic relaxation process. In VBr the emission is due to the relaxation of

the excited $C_2$ and CH species collisionally formed from a previously produced precursor, probably vibrationally excited ecetylene. Laser induced fluorescence study of the fragments from the dissociation of both molecules indicates that these are produced vibrorotationally hot, estimating the vibrational temperature of the $C_2$ species from VBr in 2200 ± 200 K. In CES has been observed an accumulation of nascent rotational population in a selected set of states, while for the $C_2$ production in the ground state from dissociation of VBr in the presence of Ar there are approximately five time more population vibrorotationally excited than in the v" = 0 level

**ACKNOWLEDGEMENTS**

This work was carried out with financial support provided by the Spanish DGES under Project number PB96-0844-C02-02.

## REFERENCES

[1] W. Lupo and M. Quack, *Chem Rev*. **87** (1987) 181.
[2] J.C. Stephenson and D.S. King, *J. Chem. Phys*. **69** (1978), 1485.
[3] M. Santos, L. Díaz, J.A. Torresano and J. Pola, *J. Photochem. Photobiol. A:*, **104** (1997) 19.
[4] M. Castillejo, R. de Nalda, M. Oujja, L. Díaz and M. Santos, *J. Photochem. Photobiol. A:*, **110** (1997) 107.
[5] B. Samoudi, L. Díaz, M. Oujja and M. Santos, *J. Photochem. Photobiol. A:*, **125** (1999) 1.
[6] H. Schmidbaur, R. Hager, and J. Zech, in *Frontiers of Organosilicon Chemistry*, ed. A. R. Bassindale and P.P. Gaspar, The Royal Society of Chemistry, Cambridge, 1991, p. 62.
[7] J.M. Agulló, F. Fau-Canillac and F. Maury, *J. Mater. Chem*., **4** (1994) 695.
[8] L. Díaz, M. Santos, C.L. Sigüenza, S.A. Simeonov, P.F. González-Díaz, J.A. Domínguez, R. Fajgar, J. Pola, Z. Bastl and J. Tláskal, *J. Chem. Soc., Faraday Trans*. **89** (1993) 3907.
[9] M. Santos, L. Díaz, Z. Bastl, V. Hulínský, M. Urbanová, J. Vitek and J. Pola, *J. Mater. Chem*. **6** (1996) 975.
[10] S.C. O'Brien, J.R. Heath, R.F. Curl and R.E. Smalley, *J.Chem. Phys* (1998) 220
[11] Ehbrecht, M. Faerber, F. Rohmund, V.V. Sminov, O. Stelmakh and F.Huisken, *Chem. Phys. Lett*. **214** (1993) 34
[12] J.D. Campbell, M.H. Yu and C. Wittig, *Appl. Phys. Lett*. **32** (1978) 413.
[13] R. Fantoni, E. Borsella, S. Piccirillo, A. Giardini-Guidoni and R. Teghil, *Laser Chem.* **8** (1988) 385.
[14] Z. Li and J.S. Francisco, *J.Chem. Phys*. **96** (1992) 878
[15] C.R. Quick, Jr and C. Wittig, *Chem. Phys*.**32** (1978) 75.
[16] F.M. Lussier, J.J. Steinfeld and T.F. Deutsch, *Chem. Phys. Lett*. **58** (1978) 277.

[17] J. Pola, Z. Bastl, J. Suubrt, J.R. Abeysingher and R. Taylor, *J. Mater. Chem*. **6** (1996) 155.
[18] K. L. Kompa, H. Lamprecht, H. Schröder, A.A. Puretzky and V.V. Tyakht, *J. Chem. Phys*. **84** (1986) 2020.
[19] E. Borsella and L. Caneve, *Appl. Phys. B* **46** (1988) 347.
[20] M. Fukushima, S.Mayama and K. Obi, *J. Chem. Phys*. **96** (1992) 44.
[21] G. Duxbury, A. Alijah, and R.R. Trieling, *J. Chem. Phys.* **98** *(*1993) 811.
[22] J. W. Thoman Jr. and J. I. Steinfeld, *Chem. Phys. Lett*. **124** (1986) 35.
[23] D.M. Rayner, R.P. Steer, P.A. Hackett, C.L. Wilson and P. John, *Chem. Phys. Lett*. **123** (1986) 449.
[24] J.H. Hall, Jr., M.L. Lesieck and W.A. Guillory, *J. Chem. Phys*. **68** (1978) 2247.
[25] L. Danylewych and R.W. Nicholls, *Proc. R. Soc. Lond. A* **339** (1974) 197.
[26] C.R. Quick, Jr. and C. Wittig, *J. Chem. Phys*. **69** (1978) 4201.
[27] W. Bauer, K.H. Becker, M. Bielefeld and R. Meuser, *Chem. Phys. Lett.* **123** (1986) 33.
[28] M. Martin, *J. Photochem. Photobiol. A: Chem*. **66** (1992) 263.

# SURVEY ON ISOTOPE EFFECTS AND SEPARATION TECHNOLOGIES

## *REVUE DES EFFETS ISOTOPIQUES ET DES TECHNIQUES DE SEPARATION*

**MICHEL COUAIRON[(a)], STEPHEN GOLDSTEIN[(a)], EDGAR SOULIÉ [(b)]**

*[(a)] CEA/SACLAY, DCC/DPE, 91191-Gif Sur Yvette Cedex (France),*
*e-mail: rousseau@carnac.cea.fr*
*[(b)] CEA/SACLAY, DSM/DRECAM, 91191-Gif Sur Yvette Cedex (France),*
*e-mail: bsoulie@drecam.cea.fr*

This paper is a review of the main industrial processes and physical principles used for stable isotope separation on a production scale. It will be restricted to "classical" industrial technologies. Roughly speaking, only three types of technologies have been contemplated for today's production (apart from uranium enrichment, outside the scope of this review).

1. -*Chemical exchange processes for the lighter isotopes* $\left[D,T,{}^{7}Li,{}^{10}B,{}^{13}C,{}^{15}N,{}^{17}O\right]$. Operating processes such as exchange distillation and liquid-gas chemical exchange are based on isotope mass-differences in the free energy (vapour pressures, vibration frequencies) of molecular species. Insight into statistical thermodynamics gives low enrichment factors $\left(\alpha \le 1.O5\right)$ which have generally a $\left[\Delta m / m^2\right]$ ratio dependency. Although needing thousands of repetitive elementary operations, those low cost processes are well suited for large capacity production. Modern trends are now in solid-liquid chromatographic columns: polymer-crown complexes with large macro-cyclic rings have topological ability to pick up boron, lithium or caesium isotopes. Detritiation (on a small scale) with palladium solid-gas interface is a special case.
2. -*Thermal Diffusion process for the production of light rare gases* [ ${}^{3}He,{}^{22}Ne,{}^{36}Ar,{}^{86}Kr$ ]. While having a low separation factor for each stage, this process is still of topical interest for production of the rare gases with a high purity degree, and of ${}^{13}CH_4$ at the gram level of yearly production.
3. -*Ultra **G**as **C**entrifuge (**G.C.**) for medium and heavy nuclides.* This process is based on an increase of a small mass diffusion flux by a pressure gradient. Several counter-current thermal diffusion effects are added to reach higher separation factors $\left(\alpha \approx 1.5\right)$. The whole process results in a $\Delta m$ dependency. That allowed low cost units to separate xenon as well as metallic isotopes. The trend at Oak-Ridge and at the Kurchatoff-Institute is to replace the electromagnetic technique by **G.C.** for kilogram production of germanium, chromium, zinc or tungsten isotopes.

-*For the near future*, repercussions of laser research may occur in stable isotope production; they are extensively described in this meeting. Laser multistep AVLIS is a selective process developed for the nuclear fuel. Besides enriching $^{235}U$ or depleting $^{242}Pu$ it may succeed as a powerful process for the separation of rare-earth absorbers, such as $^{157}Gd$ or $^{167}Er$. **G.C.** could hardly be applied to the f-elements given that the volatility of the possible feed (diketonate) is very low. Ion Cyclotron Resonance could be a challenger if active research were resumed. Infrared multiphoton dissociation (IRMPD) has shown high separation factor and yield capacity for several light species like boron tribromine, halogenated hydrocarbons or silicon halides. Infrared tuning flexibility with a free electron-laser is a prerequisite to industrial developments. Single photon dissociation with ultraviolet wavelength was proven to be an efficient way to produce $^{13}C$ from formaldehyde: enrichment factors higher than 35 have been reached at Saclay ( see Alain Petit's abstract).

## I ISOTOPIC CHEMICAL EXCHANGE.

In a mixture of molecules $A'X$ *and* $AX$ where light and heavy isotopes are $A'$ and $A$, an isotopic chemical exchange is a reaction of the type $A'X + AY = AX + A'Y$ The molecules $A'X$ and $AX$ or $\left(A'Y \text{ and } AY\right)$ differ from each other by vibrationnal and sometimes rotational frequencies. Therefore the Gibb's free energies will also differ, and the equilibrium constant $K$ will slightly deviate from unity, resulting in the isotopic effect. $K$ is measured from $\Delta G = -RT \ln K$ or from the equilibrium concentrations $K = \frac{[AX]}{[A'X]} / \frac{[AY]}{[A'Y]}$. The separation factor $\alpha$ is related to K and to the symmetry number ratio of possible permutations in the two isotopic molecules, by $\alpha = K \prod_i \left(s_p / s_r\right)_i$ .Various types of exchange reaction are brought into play in industrial plants. Table 1, from [reference 1], displays the separation factor.

**Table 1**

| **INDUSTRIAL RESULTS** | **Isotopic Chemical Reactions** | | |
|---|---|---|---|
| **Separation** | **Exchange Reaction** | $\alpha$ | **Comment** |
| $^{14}N/^{15}N$ **Nitrox** | $^{15}NO(g) + H^{14}NO_3(l) = {}^{14}NO(g) + H^{15}NO_3(l)$ | 1.055 at 25 C | Spindel/Taylor process (1955) |
| **Monothermal Exchange** $H/D$ | $NH_3(l) + HD(g) = NH_2D(l) + H_2(g)$ | | Mazingarbe (1960) Roth process |
| **Dual temperature** $H/D$ | $H_2O(l) + HDS(g) = HDO(l) + H_2S(g)$ | 2.178; 32C 1.52; 138C | Girdler-Sulfide (Savannah River |
| $^{10}B/^{11}B$ **Exchange Distillation** | $^{10}BF_3(g) + C_6H_5OCH_3.{}^{11}BF_3(l) =$ $^{11}BF_3(g) + C_6H_5OCH_3.{}^{10}BF_3(l)$ | 1.028; p=0.5 Mpa 288 K | Anisole system Moscow-U (1997) |

Chromatographic Exchange Technology is promoted by the following last decade laboratory results:

| LABORATORY | Chromatographic Exchange Results published in the Proceedings [ 3, 4, 5 ] | | |
|---|---|---|---|
| $^{10}B/^{11}B$ **Anion exchange resin** | $R\text{–}^{11}B\left(OH^-\right)_2 + {}^{10}B(OH)_3(\text{aq}) =$ $R\text{–}^{10}B\left(OH^-\right)_2 + {}^{11}B(OH)_3(\text{aq})$ | 1.022 at 80 C | (n-methyl-NMG glucamine) resin of aminated type |
| $^{6}Li/^{7}Li$ **Anion exchange resin** | $R-\left(SO_3{}^{-7}Li^+\right)+\left[{}^{6}Li^+(CH_3COO)^-\right](\text{aq}) =$ $+R-\left(SO_3{}^{-6}Li^+\right)+\left[{}^{7}Li^+(CH_3COO)^-\right](\text{aq})$ | 1.0038 | Ion exchange on sulphonated DVB |
| $^{6}Li/^{7}Li$ **Benzo-15-crown-5 System** $Li(CCl_3COO)$ $-B15C5(CHCl_3)$ | $\left[{}^{7}Li^+ - (B15C5(CHCl_3))^-\right](\text{org}) + {}^{6}Li^+(CCl_3COO)^-(\text{aq}) =$ $\left[{}^{6}Li^+ - (B15C5(CHCl_3))^-\right](\text{org}) + {}^{7}Li^+(CCl_3COO)^-(\text{aq})$ | 1.054 | Ion exch. with aqueous and liquid benzo-15-crown-5 ethers at 0.5C |
| $^{32}S/^{34}S$ **Anion exchange resin** | ${}^{34}SO_2(\text{aq}) + H\,{}^{32}SO_3^-(\text{resin}) = {}^{32}SO_2(\text{aq}) + H\,{}^{34}SO_3^-(\text{resin})$ | 1.017 | Ion exchange on sulphonated DVB EG&G mound |
| **T/H Exchange on Metal hydride** | $H_2 + [2T - Me] = T_2 + [2H - Me]$ | 3.03 | $H/T$ Exhange on $PdH_{0.4}$ hydride |

Chemical exchange gives relatively low separating factors but multiplication of the elementary process is achieved by liquid-gas countercurrent contacting flow or by percolation with adsorption on solid phases in chromatographic exchange. In most cases, those processes need packed columns with refluxing systems at the product end. If heating the liquid phase to feed the vapour stream is the way to do refluxing, then the process is referred to exchange distillation. Boron separation with anisole system is the industrial example now enhanced to $\alpha = 1.028$ by Russian Institutes [2]. Sometimes it may be impossible to get economic phase change at both ends, otherwise than having a dual temperature operation such as in the Girdler-sulfide process. That is the industrial way chosen by Canadian AEC to produce more than 5000 Tons of heavy water a year for CANDU reactors. Extraction from ammonia synthesis (E.Roth process) is an alternate for deuterium production that had been operating in the late 1960's at Mazingarbe.

Nowadays chemical exchange processes are optimised for complexation of metallic ions in chromatographic separation columns packed with small size (10 $\mu$) fixed resins. Metallic ions are extracted from percolating aqueous solutions with adsorption on resins bearing the exchanger complexes: [3]

- With aminated resins such as n-methil glucamine (NMG), boron separation ability has been proven. Structural affinity between the tetrahedral $\lfloor NH : BO_3 \rfloor$borne

in resin phase and the trigonal planar $[B(OH)_3]$ in solution phase is the prevailing phenomenon. The separation factor may reach 1.02

- With sulphonated polystyrene dicetyl benzene (DVD), hydrogen or alkalyne sulfite ion such as $LiSO_3^-$ are continuously exchanged between resin and aqueous phases, with a low separation factor (1.0038) between lithium isotopes. Nevertheless, the process may be applied to the alkaline family $\{Li, K, Rb\}$and also to alkaline earth metals $\{Mg, Ca, Sr\}$. The height of an equivalent theoretical plate (HETP) ranges from 0.3 to 0.6 cm for lithium system, that is enough to produce by the kilogram a year with a tenth-meters high column.
- With metal crown complex system such as polymer bound 18-crown-6, alcaline earth such as $Ca^{2+}$ may be extracted from a fluid phase. The complexing ligand formed may have a short stability and is strongly dependent of the choice of the ether binding the crown to the polymer solid support-like here $(C_2H_5OCH_2)_5$-The same phenomenon is studied in CEA for Caesium extraction [4].
- Promising separation factors have been measured in laboratory experiments for the extraction of lithium in two-phase water-organic systems with $\lfloor Li^+(CCl_3COO)^- \rfloor (\text{aq}) / [LiB15C5\,(CHCl_3)]\,(\text{org})$, a benzo15-crown5 ether (B15C5). The basic mechanism is a topological correspondence between crown ether hole and metallic cation radius. To be efficient, the ring size must be large enough to allow the cation to enter the hole but not so large as to allow the ring to wrap around the cation. In this case, separation factors may reach 1.054 for lithium isotopes-Knyazev and alii p 313 in [5].
- The table below goes to show the ability of chemical exchange in enriching the heaviest isotopes as Uranium in the Asahi ion exchange ACEP and in the French CHEMEX pilots.

| | | | |
|---|---|---|---|
| $^{235}U/^{238}U$ **CHEMEX** | $^{235}U(III)(aq, HCL) + {}^{238}U(IV)(TBP) = {}^{238}U(III)(aq, HCL) + {}^{235}U(IV)(TBP)$ | 1.0030 at 300 K | CEA/Grenoble and Pierrelatte pilots |
| $^{235}U/^{238}U$ **ACEP** | $^{235}U(IV)(\text{aq}, HCL) + {}^{238}U(VI)(\text{anion resin}) = {}^{238}U(IV)(\text{aq}, HCL) + {}^{235}U(VI)(\text{anion resin})$ | 1.0014 at 313 K | Japanese Asahi Chemical Industry pilot |

Biegeleisen [6] has explained chemical exchange processes with a cell model for the condensed phase in the harmonic approximation, with temperature independence of the condensed volume. Many systems are well described by this model, in which the equilibrium constant is expressed in terms of the Q molecular partition functions: $K = (Q_{AX} / Q'_{A'X}) / (Q_{AY} / Q'_{A'Y})$. The Q ratio of two isotopic molecules with only translation (classical) energy is $(Q/Q')_{cl} = (s/s') \prod_i \left( m_i / m_i' \right)^{\frac{3}{2}}$. Thus the

separation factor $\alpha$ may be reduced by introducing a convenient **R**educed **P**artition **F**unction **R**atio noted as the ratio $\frac{s}{s'} f \equiv (Q/Q')_{qm} / (Q/Q')_{cl}$ where $qm$ and $cl$ indexes refer respectively to the quantum and the classical partition function ratio of two isotopic molecules. Therefore for the separation factor $\ln\alpha = \ln\left[\left(\frac{s}{s'}\right) f(AX)\right] - \ln\left[\left(\frac{s}{s'}\right) f(AY)\right]$. If AY is a free gaseous atom, then the last term is zero and the RPFR of the condensed phase is just the separation factor. The Q's may be expressed with the reduced frequency of normal mode vibrations $u_i = h\nu_i / kT$ and the reduced rotational momentum for a diatomic molecule $\sigma = hcB/kT$ Both $\nu_i$ and $B$ are measured by spectroscopy. One gets for the RPRF with classical rotation $\frac{s}{s'} f = \prod_i^{3n-6} \frac{u_i}{u_i'} \frac{e^{-\frac{u_i}{2}}}{e^{-\frac{u_i'}{2}}} \left( \frac{1-e^{-\frac{u_i'}{2}}}{1-e^{-u_i}} \right)$. For small $\Delta u_i = u_i' - u_i$ (light isotopes save for hydrogen) it may be expanded in a function series of $G(u) = 1/2 \coth(u_i/2) - 1/u_i$ with $\ln\left[\left(\frac{s}{s'}\right) f\right] = \sum_l^{3n-6} G(u_i)\Delta u_i$. From which $\ln\left(\frac{s}{s'}\right) f = \sum_i^{3n-6} \left[ \frac{\Delta u_i^2}{24} - \frac{\Delta u_i^2}{2880} \right]$ as an asymptotic value. Expressing the first term with the force constant $a_{ii}$ corresponding to a departure of the i'th atom from its equilibrium position gives the fundamental Biegeleisen's law: $\ln\alpha = \frac{1}{24}\left(\frac{\hbar}{kT}\right)^2 \sum_i \left(\frac{1}{m_i'} - \frac{1}{m_i}\right) [a_{ii}(AX) - a_{ii}(AY)]$. According to which:

1. **The fractionation factor decreases with $1/T^2$ and the mass dependence is $\Delta m/m^2$**: isotopic chemical exchange is more efficient for light isotopes than for heavy ones.
2. **$\alpha$ increases with the strength of the chemical bonds to the element involved in the isotopic exchange where the heavy isotope concentrates.**

**Application to exchange distillation** [7]**.** Fractional distillation is the oldest process unit operation to separate the light isotopes in liquid mixtures of deuterium, boron, carbon, nitrogen, or oxygen. The basic physical principle is the difference in vapour pressure between isotopic substances at low temperature: the zero point energy ratio between condensed phases has an inverse mass dependency. Therefore the lighter isotopic species has the lower latent heat of evaporation and is generally the most volatile of the mixture. Ex $H_2{}^{16}O \uparrow$ and $H_2{}^{17}O \downarrow$. The enrichment capacity is assessed by the separation factor which is the fraction of the desired component in the phase where it concentrates (generally the vapour) divided by the corresponding fraction in the liquid. For a majority of mixtures, except that

of $H_2, D_2, or\ HD$, ideal solution law applies and the separation factor $\alpha$ is just measured by the ratio of the vapour pressures of the pure substances, at the temperature of the liquid. Values of $\alpha$ for some mixtures are shown in table 2. It has be seen that the vapour pressure differences become very small at temperatures about 100 K because as the temperature is raised the thermal energies contribution tends to prevail and to cancel isotopic differences. Below, most substances obey closely the law $[\alpha - 1] \approx \frac{1}{T^2}$ and have conspicuous differences in vapour pressures. A laboratory method for measuring the pressure ratio is mass spectrometry analyses with free evaporation in vacuum (molecular distillation): for molecular weight $M_H, M_l$, Knudsen law gives $\alpha_M = \frac{P_l^0}{P_H^0}\left(\frac{M_H}{M_l}\right)^{1/2}$; the alternative way is a continuous Rayleigh distillation until obtaining a small residue.

**Table 2**

**Vapour pressure ratio in some mixtures as separation factor**

| Compounds | $\alpha$ | Temperature K | Compounds | $\alpha$ | Temperature K |
|---|---|---|---|---|---|
| $[H_2 / HD]$ | **3.61** | 13.76 (TP) | $BCl_3$ | **1.003** | 286 (BP) |
| $[NH_3 / ND_3]^{1/3}$ | **1.08** | 195.46 (TP) | $BF_3$ | **1.0082** | 171.5 (BP) |
| $[H_2O / D_2O]^{1/2}$ | **1.12** | 273.16 (TP) | $(CH_3)_2OBF_3$ | **1.001** | 338 (BP) |

Distillation has been used in many industrial plants since Urey (1932). The compounds listed in table 2 for boron separation were experimented during the Manhattan project. If only distillation is taken into account the separation factor are very low; nevertheless an industrial plant was build for the methyl ether-borane as some enhancing dissociation with efficient chemical exchange at $\alpha = 1.016$ had proven to occur. That is slightly lower than the best $\alpha = 1.032$ listed in table 1 for exchange distillation in industrial anisole systems. With pure distillation, quite expensive cryogenic refluxing systems are often required.

Experiments have verified the Bigeleisen's law for simple monatomic substances, with $m_H, m_l$ for the masses of the substituted isotopes $Ln\left[\frac{p_H}{P_l}\right] = \frac{A}{24}\left(\frac{\hbar}{kT}\right)^2\left(\frac{1}{m_H} - \frac{1}{m_l}\right)$ This formula indicates a reduction of the vapour pressure ratio when increasing the masses of the isotopes or with substitution of a heavy to a light atom. With the $NH_3$ and $NHD$ mixture the law for the geometric mean has also been established:

$$P^0_{NH_2D} = \left[P^0_{NH_3}.P_{NHD_2}\right]^{\frac{1}{2}};\ P^0_{NHD_2} = \left[P^0_{ND_3}.P_{NH_2D}\right]^{\frac{1}{2}} \text{ and } \frac{P^0_{NH_2D}}{P^0_{NH_3}} = \left(\frac{P^0_{ND_3}}{P^0_{NH_3}}\right)^{\frac{1}{2}}.$$

In many *diatomic and polyatomic substances* there are some effects of internal vibrations and differences on the latent heat of the isotopic species. That may lead to abnormal behaviour at high temperature where the species that include the heavier isotope happen to become the more volatile. $C_6D_6$ is more volatile than $C_6H_6$. Ditto for $\left({}^{11}BCl_3\uparrow,{}^{10}BCl_3\downarrow\right);\left({}^{11}BF_3\uparrow,{}^{10}BF_3\downarrow\right)$. If a real gas is considered with a first virial coefficient noted $B_0$ and a condensed molar volume $V_C$ then one gets for the RPFR: $\ln\alpha=\ln\frac{f_c}{f_g}=\left[1+P'T\left(B_0-\frac{V_c}{RT}\right)\right]\ln\frac{P'}{P}-\ln f_{rot}^{g}$ .The measure is approximated by $A/T^2-B/T$ . The A coefficient is the above high temperature vibrations term $A\equiv\frac{1}{24}\left(\frac{hc}{kT}\right)^2\sum\left(\nu_i^{2,l}-\nu_i^{2,H}\right)$ and B is identified to the low temperature zero point energy shifts upon condensation, noted $B=\frac{1}{2}\frac{hc}{kT}\sum\left[\left(\nu^l-\nu_i^H\right)_g-\left(\nu^l-\nu_i^H\right)_c\right]$. The abnormal behaviour of deutero-benzene may be due to an increase of the condensation volume and on a prevailing B-term with blue (instead of red) shifts upon H/D substitution.

## II-THERMAL DIFFUSION SEPARATION:

Thermal diffusion [T.D] is an operating process for separation of isotopes of the rare gases. If a temperature gradient is applied to a liquid solution or a quiescent gaseous mixture with initially uniform concentration and pressure, then a relative motion of the components may occur which leads to the development of concentration gradients. This type of diffusion is called thermal diffusion (T.D).

**T.D phenomena** were first studied by Ludwig in $Na_2SO_4$ solutions in 1856, then by Soret in 1879 with $KCl\ and\ KNO_3$ solutions. From there, the so called "Soret effect" for liquid T.D. Dufour in 1873 has observed the reverse diffusion thermo-effect of generating a temperature gradient by mixing two gases. Enskog(1911) and Chapman (1916) have studied more general laws showing that mass transport may be induced by concentration gradient, pressure gradients or by a force field $\mathbf{F}$: all diffusion phenomena are included in the relative diffusion velocity for a binary mixture:

$$\mathbf{v}_1-\mathbf{v}_2=D\left[-\nabla Ln\left(\frac{C_1}{C_2}\right)-(C_2-C_1)\nabla LnP+\frac{\rho}{P}\left(\frac{\mathbf{F}}{m_1}-\frac{\mathbf{F}}{m_2}\right)+\alpha_T\nabla LnT\right]$$

Ordinary concentration diffusive transport acts to cancel the concentration gradient (first term). Pressure diffusion (second term) causes heavy and light gases to move towards region of high and low pressure respectively. Forced diffusion (third tem)

only appears under an external force field. Thermal diffusion (the final term) sets up a gradient concentration as it causes the larger and generally the heavier molecules to migrate towards the cooler regions of the flow.

In 1938 Clusius and Dickel succeed in separating chlorine isotopes in a long column. The gaseous mixture was confined inside a narrow long vertical tube (a 3 stages cascade of 29 m-length). A central hot wire was used to heat the mixture whereas the external wall was maintained at a temperature T= 290 K. Due to basic T.D effect, the light isotopes first concentrates in the hot inner zone. Then a convective flow sets up an upward stream flow for light isotope near the hot wire and a downward stream for the heavy isotope, adjacent to the cold outer wall. From initial abundancy 75.4 % $^{35}Cl$ and 24.6 % $^{37}Cl$, the Clusius and Dickel column has produced liters of HCl, with 99.6 % $^{35}Cl$ at the upper end and 99.4 % $^{37}Cl$ at the bottom.

**T.D Separation factor**. Let us consider two bulbs reservoirs $(T_1,V_1)$ and $(T_2,V_2)$ linked by a capillary tube; if only first and last terms are considered in the above velocity expression, a steady state is possible and the T.D separation factor $\alpha$ may be established as $\ln\alpha = \alpha_T \ln\frac{T_2}{T_1}$; final concentrations in the bulbs gives $\alpha$ as the ratio $[C_1/C_2]_{V2} / [C_1/C_2]_{V1}$. Therefore, this method is the simplest way to measure the thermal diffusion coefficient $\alpha_T$, which may also be calculated as an intrinsic property of the gas via the intermolecular potential. It is usually expressed in a reduced form with the corresponding value for the first Chapman-Cowling approximation for rigid sphere molecules $\alpha_{HS} = \frac{105}{118}\frac{m_2 - m_1}{m_2 + m_1}$, ratio ranges from 0.1 to 0.7. In the Lennard-Jones 6-12 potential approximation, an asymptotic reduced value of $0.627\,\alpha_{HS}$ is reached at temperatures above 5 $\varepsilon/k$. Therefore if $\frac{\Delta T}{T}$ and $\alpha_{HS} \le 1$ the maximum separation factor may be estimated by $\alpha - 1 \approx \frac{8}{15}\frac{m_2 - m_1}{m_2 + m_1}\frac{\Delta T}{T}$. Measured values for the T.D coefficient is given in table 3, from [8].

**Table 3**

| | $^3He/^4He$ | $^{20}Ne/^{22}Ne$ | $^{36}Ar^{40}Ar$ | $^{83}Kr/^{84}Kr$ | $^{131}Xe/^{132}Xe$ | $^{16}O_2/^{16}O^{18}O$ | $^{12}CH_4/^{213}CH_4$ |
|---|---|---|---|---|---|---|---|
| $\alpha_T$<br>Sep factor | 0.07<br>0.0762 | 0.026<br>0.0254 | 0.023<br>0.0281 | 0.0019<br>0.0032 | 0.0011<br>0.00202 | 0.015<br>0.00161 | 0.011<br>0.00161 |
| Natural abundance | | Ne-22<br>9.21 | Ar-36<br>9.21 | Kr-86<br>17.5 | Xe-136<br>8.9 | O-18<br>0.204 | C-13<br>1.09 |
| Cascad sep factor | | 12500 | $3.3.10^6$ | 940 | 810 | $2.10^5$ | 45000 |

Table 3 shows that the separation factor for T.D. is very low, of the order of 0.005; but if a long column is used, the overall cascade separation factor may be very high, as noted in the last line. This efficiency is really due to an infinity of repetitive basic separation effect inside the Clusius-Dickel countercurrent.

Since 1936, many experiments from tritium to krypton have been designed with simple laws for binary mixture separation in C.D. columns. The mass transport equation for steady state operation or transient modes has been resolved in 1937 by Furry, Jones and Onsager. A slab of transverse thickness w, length L and breadth $B = 2\pi\bar{r}$ approximates the gas layer; gas properties are combined into some characteristic constants: H for the thermal diffusion effect and $K = K_C + K_D$ for remixing effects of convection ($K_c$) and longitudinal diffusion ($K_d$). The ratio $K/H$ is homogeneous to a characteristic length of the column noted $\lambda$; $C$ is the relative concentration of the component being enriched; $\mu$ is the mass of gas per unit length and $\eta$ the gas viscosity; $\sigma$ is the constant rate of withdrawal of the enriched gas:

Constants $H = \frac{g}{6!}\frac{\rho^2}{\eta}\alpha w^3 B\left(\frac{\Delta T}{T}\right)^2$ $K_c = \left(\frac{g^2}{9!}\right)\frac{\rho^3}{\eta^2 D_{1,2}} w^7 B\left(\frac{\Delta T}{T}\right)^2$ $K_d = \rho D_{1,2} wB$

Mass transport $\tau = HC(1-C) + \sigma C - K\frac{\partial C}{\partial z}$; Equation of continuity: $\mu\frac{\partial C}{\partial t} = -\frac{\partial \tau}{\partial z}$;

$\alpha_z = \exp\frac{z}{\lambda}$ is the separation factor at z position (at equilibrium);

Profile $C(z) = \frac{1}{2}\left[1 - th\frac{(z - z_0)}{\lambda}\right]$;

Rate enrichment $\mu\frac{\partial C}{\partial t} = -H\frac{\partial[C.(1-C)]}{\partial z} + K\frac{\partial^2 C}{\partial z^2}$; Relaxation time $\tau = \frac{4\mu\lambda}{H}\left[1 + \frac{4\pi^2\lambda^2}{L^2}\right]$.

The $UF_6$ separation factor was so estimated to be 1.00076 in thermal diffusion: it is smaller than in gaseous diffusion (1.0043). Nevertheless, an operating plant was built at Oak-Ridge during War II time with 2100 columns with liquid phase T.D process. The cascade produced U with 0.86 % enrichment for the calutrons.

Nowadays T.D effect is mainly used to separate middle isotopes of the rare gases with large cascades or long columns to get a high overall separation factor. When small amounts are needed, as for tracers or labelled compounds, T.D process may be useful. G.Muller has recently calculated the possibility to separate the

radioactive krypton from seven isotopes-fission product $^{85}Kr$ -in a 136-m-long column with closed ends [5]. The fraction profile evolution is evaluated with the transport equations for $C_i$ and the hydrodynamic equations.

$$\mu\frac{\partial C_i}{\partial t} = K\frac{\partial^2 C_i}{\partial z^2} - \frac{\partial}{\partial z}\left[H_0 C_i \sum_{k=1}^{l} m_{i,k} C_k + \sigma C_i\right] \quad \text{i=1,l. and} \quad \frac{1}{r}\frac{\partial}{\partial r}\left(r\eta\frac{\partial v}{\partial r}\right) = \frac{\partial p}{\partial z} + \rho.g \ .$$

## III-GAS CENTRIFUGATION (G.C).

This process is applied to Xenon, Krypton as well as metallic fluorides that have high vapour pressures near room temperature. The ability to separate is generally applied in the molecular range from 50 to 250. A high-speed rotor provides angular velocity to the processed gas introduced into a vacuum casing (to reduce rotor drag). The feed port is in the middle of the stationary centre column. Heavier molecules concentrate at outer wall and lighter at centre due to the differences in centrifugal forces exerted on the two species. Gas exits through two stationary extractors: one scoop for the lighter molecule near the axis and the other for the heavy ones, on the wall-side. Because of the sharp pressure gradient, most of the gas is in a thin shell near the external wall. The local separation equilibrium factor $\alpha(a,r)$ for a binary mixture of gases in a cylinder of radius a is: $\alpha(a,r) = \exp\left[\frac{\Delta m V^2}{2RT}\left(1-\frac{r^2}{a^2}\right)\right]$ with $\Delta m = m_2 - m_1$ The separation factor in the G.C thus depends on the difference between the molecular weights instead of the ratio $\Delta m / m^2$ in chemical exchange or $m_2 / m$ in gaseous diffusion. Table 4 (ex $UF_6$) shows that G.C is more attractive for heavy molecule separation than gaseous diffusion with $\alpha = 1.00429$.

**Table 4**

$UF_6$ **Local separation factors** $\alpha(a,r)$ **for various peripheral speed V**

| $r/a \downarrow$ *and* $\rightarrow V$ | 400 m/s | 500 m/s | 700 m/s |
|---|---|---|---|
| 0.8 | 1.035 | 1.056 | 1.112 |
| 0.9 | 1.018 | 1.029 | 1.058 |

The separative capacity is enhanced by an axially counter-current flow stream with a smaller velocity component –by 2 orders of magnitude less than the radial one- It is directed downward near the wall and upward at a few centimetres inside, near the internal boundary of the gas layer. The counter-current flow pattern is established by a combination of a temperature difference between the upper lid and the bottom floor and an inner re-intake of heavier gas-trough the bottoms baffle. The ratio of the flow rate at the upper scoop to the feed rate is referred as the cut $\theta$; a greater enrichment of the light isotope can be achieved by withdrawing a smaller cut at the top extractor. Streamlines and separative performance of U.C are

evaluated at SACLAY/DCC [9] with a finite-elements code for the vorticity equation, a finite-volume method for species diffusion fluxes, DSMC Monte Carlo calculations for nearly molecular flow singularities, and Monte Carlo optimisation for $\delta U$. The stream function equation in the Onsager's approximation is resolved with: $\frac{\partial^2}{\partial x^2}\left[e^x \frac{\partial^2}{\partial x^2}\left(e^x \frac{\partial^2 \chi}{\partial x^2}\right)\right] + \frac{Re^2}{\alpha^6}\left(\frac{\Omega^2 a^2 \mu}{\kappa T_0} + 4\right)\frac{\partial^2 \chi}{\partial y^2} = S(x,y)$ where $\chi$ is the potential for the stream function $= \alpha^{-1}\int \psi dx$; $\alpha$ is the gas compression ratio or stratification parameter, and $S(x,y)$ some external driving sources of mass, momentum or energy. The separative capacity is given in operating systems by $\Delta\delta \quad \delta U = E_I E_C E_F \left(\pi\rho D(\Delta m)^2 V^4 / 8(RT)^2\right)_L$. For $UF_6$ the product of the 3 first efficiency (ideal*circulation*flow pattern) is less than 0.4472. The overall separative capacity is near 10 kgU SWU/year at an optimum circulation rate, and only $V^{2,.2}$ dependent.

Reliable modern centrifuge design is an optimisation task constrained by three problems: mechanics of the rotor spinning, development of high-strength and bulk-modulus composite materials compatible with fluorine corrosion, multi-component mixture dynamics. Table 5 sum-up the feed gases processed at Kurchatov Institute:

**Table 5**

GAS CENTRIFUGE FEED (Kurchatov Institute) [10]

| | |
|---|---|
| Fluorides | $SF_6$, $M_0F_6$, $WF_6$, $OsF_6$, $GeF_4$, $SiF_4$, $VF_5$, $SbF_5$, $SeF_6$, $TeF_6$, $BF_3$, $NF_3$, $PtF_6$ |
| Oxyfluorides | $OF_2$, $CrO_2F_2$, $OsO_4$, $PoF_3$ |
| Halides | $ClF_3$, $BrF_3$, $TiCl_4$ |
| Carbon fluorides | $C_7F_{14}$, $CF_4$, freons |
| Boron Hydrides | $Zr(BH_4)_4$, $Hf(BH_4)_4$ |
| Inert gases | $Xe$, $Kr$, $Ar$, $Ne$ |
| π-complexes | $Fe(CO)_5$, $Ni(PF_3)_4$, $H_2Ru(PF_3)_4$, $HIr(PF_3)_4$, $HRe(PF_3)_5$ |
| Metal-organic compounds | $Sn(CH_3)_4$, $Pb(CH_3)_4$, $Hg(CH_3)_2$, $Cd(CH_3)_2$, $Zn(CH_3)_2$, $Ga(CH_3)_3$, $In(CH_3)_3$, $Tl(CH_3)_3$ |

## IV-INFRA-RED MULTI-PHOTON DISSOCIATION (IRMPD). [11]

This paragraph is only to catch a glimpse on the integration of laser processes in stable isotope production. The IRMPD process is the absorption of many infrared photons from an intense laser beam. The absorbed photon energy

increases density of vibrational states until reaching a quasi continuum region where density mixing allows for interaction of the laser radiation with a much larger number of states than those in the pumped vibrational mode. Dissociation may then occur in a similar manner as thermal dissociation. Diatomic molecules hardly dissociate with IRMPD and for polyatomic fluoroforms, the threshold fluency is from 2 to 10 J/cm$^2$. The energy absorbed generally increases linearly with laser fluency up to some saturation degree point followed by a 2/3-power region. In the region of onset of dissociation, the break-up probability has a 4$^{th}$ power fluency dependence. Generally, lowering the cell temperature improves the isotopic selectivity by reducing the population of higher vibro-rotational states. As for the dissociation of $CF_3Br \rightarrow CF_3 + Br$, efficient enrichment requires chemical scavenging of at least one of the reaction products. Scavengers are generally gases whose quick reactions with free radicals prevent scrambling recombinaisons. Here the chosen scavenger was $Br_2$ which produce $CF_3Br$ with the $CF_3$ radical. Then a staging enrichment process simply consists to recycle the $CF_3Br$ product. We sum-up in table 6 the best-known experiments with IRMPD for separation of light isotopes.

**Table 6-IRMPD FOR LIGHT ISOTOPES**

| **Isotope** | **Feed species** | $\nu(cm^{-1})$ | $\alpha$ **enrich factor** | **Reference** [12]**:** |
|---|---|---|---|---|
| **D** | $CDF_3$ | **979.7** | $\geq$ **2000** | **Evans,1982** |
| **T** | $CTF_3$ | **1057** | $\geq$ **10000** | **Makide,1982** |
| **T** | $CTCl_3$ | **828** | $\geq$ **15000** | **Herman,1984** |
| $^{10}B$ | $^{10}BCl_3$ | **979.7** | $\geq$ **5** | **Ambartsumyan, 1976** |
| $^{10}B$ | $^{10}BBr_3$ | **1208;1226** | $\geq$ **5** | **Kazuya.SUZUKI, 1994** |
| $^{12}C$ | $CF_3Br$ | **1077.3** | $\geq$ **150** | **Borsella,1983** |
| $^{13}C$ | $CF_2HCl$ | **1041.3** | $\geq$ **100** | **Gautier,1982** |
| $^{13}C$ | $CF_3I$ | **1041.3** | $\geq$ **100** | **Cauchetier,1983** |
| $^{13}C$ | $CF_2HCl$ | **1031.5** | $\geq$ **200** | **Hackett,1984** |
| $^{18}O$ | $CF_3OCF_3$ | **942.4** | $\geq$ **95** | **Tetsuro MAJIMA,1994** |

IRMPD may be a plausible intermediate component in a detritiation plant. Ontario Hydro was recently planning to process $HTO$ (10 Ci/kg) with a continuous feed of 500 kg /h to extract 0.5g/h of tritium gas. A four components system was studied:

1. Tritium transfer from water ( $HTO$ )to trifluoromethane ( $CTF_3$ and $CHF_3$ **)** by a liquid exchange.
2. IRMPD of $CTF_3$ to $TF$ *and* $C_2F_4$.

3. Adsorption of $TF$ on sodium fluoride beds and conversion with hot calcium to $T_2$.
4. Final purification by cryogenic distillation of $T_2$.

Equivalent systems for boron or lithium separation may appear after a first enrichment from ion exchange chromatography in organic phase- [13] till [16]. Laboratory research is now on silicon-30 for chips industry.

| | | | | |
|---|---|---|---|---|
| $^{30}Si$ | $Si_2F_6$ | **956** | $\geq$ **10** | **OKADA Yoshiku 1994** |
| $^{34}S$ | $SF_6$ | **934.9** | $\geq$ **5** | **Fuss,1979** |

Recent breakthrough in free electrons lasers [M.Hashida, 17] is convincingly renewing the ability of infrared processes to enrich boron and various elements.

AVLIS technology has recently been applied for the production at a laboratory scale of ytterbium 168 [18].

## REFERENCES

[1]-Etienne Roth, Critical evaluation of the use and analysis of stable isotopes**,** *Pure and Appl Chem*, Vol **69**, N°.8, pp. 1753-1828; 1997 [©1997 IUPAC].

[2]-Katal'nikov, S. Gsizov, Anisole system under pressures of 0,1-0,8 Mpa as applied to boron separations. Zh. Fiz. Khim. (1997)-71(7), 1165-1169.

[3]-M.G. Albert,Yves Barre, Roger Neige, La chromatographie ionique, p. 178-186, Workshop INSTN des 24 et 25 novembre 1993 sur les isotopes stables [S. Goldstein, P. Louvet, E. Soulié]- Edition CEA/Saclay.

[4]-V.Lamare, J.F.Dozol, S.Eymard, Calixarènes-couronnes pour l'extraction du Césium-DCC, Rapport Scientifique-1997.CEA-R-5801.

[5]-Proceedings of the international Symposium on isotope separation Nov 1990 Tokyo - p 313 / Y Fujii, T Ishida, K Takeuchi, Editors-Tokyo Institute of Technology.

[6]-J.Bigeleisen: *The Relative Reaction Velocities Of Isotopic Molecules*. J.Chem.Phys. **17**, n°8, 675-678, 1949

-J.Bigeleisen: *Isotope Separation Practice*, p1 et p192 in Isotope effects in chemical processes; R.F.Gould, ed-Advances in chemistry series n° 89 [ACSP]

-J.Bigeleisen: *Nuclear Size Effects in Chemistry of the Heavy Elements* J.Am Chem.Soc. 1996, **118**, 3676-3680

[7]- H.London: Separation of isotopes (1961) (G.Newnes Ltd, London)

[8]-The thermal diffusion column, Gheorghe Vasaru, G.Muller, G.Reinhold, T.Fodor. (D Verlag- Berlin 1969)

-Gheorghe Vasaru: Thermal diffusion. A bibliography (period 1965-1995) ITIM,Cluj-Napoca, (Romania) and Nagoya University (Japan), April 1996.

[9]-Frédéric Doneddu, Philippe Roblin, H.G. Wood- Application of the Pancake model to the "Iguaçu machine" Sixth workshop on separation phenomena in Liquid and Gases, NAGOYA (Oct 1998)- Society of Chemical Engineers and the Laser Society of Japan.

[10]-V.N. Prusakov. On the progress in stable isotope separation-p 169-177 in [3].
[11]-V.S. Letokhov. Non Linear Laser Chem Multiple-Photon Excitation. (1983)-Springer Series in Chem-Phy n°22-
[12]-J.L.Lyman-Laser-induced molecular dissociation- LA-UR-84-1407
[13]-R.J.Jensen, IRMPD of trans-2-chloroethenyl dichloroborane-US Patent 4,447,303-May,1984.
[14]-M.Cauchetier, M.Luce, C.Angelie: *Isotopic selectivity in the I.R.M.P.D*-Chem.Phys.(1994), **182** (2-3), 375-98.
[15]-G.Akhalkatsy,T.Abzianidze-IRMPD of alkenylboron halides- Soobshch.Akad.Nauk Gruz (1991), **144** (1), 45-48.
[16]-Suzuki,Kazuya-Separation of boron isotopes by infrared laser-JAERI Conf (1995), **95-005** p 1019.
[17]-M.Hashida, M. Matsuoka, Y.Nagaya, M.Ayabe, Y.Izawa - Multiphoton dissociation and boron separation by FEL. Williamsburg **FEL 98 Conference**, August 16-21, 1998, Williamsburg VA.
[18]-S.I Yakovlenko Main physical problems of AVLIS technology in producing ytterbium-168 in weighable amounts. *Laser and particle beams (1998), vol 16, n°.4.pp.541-568*

# THE ISOTOPE EFFECT IN GADOLINIUM AMALGAM SYSTEM

**D. AXENTE[(a)], M. NOMURA[(b)], Y. FUJII[(b)]**

*[(a)] Institute of Isotopic and Molecular Technology, R-3400 Cluj-Napoca 5, P.O. Box 7OO, ROMANIA, email: axente@s6.itim-cj.ro*
*[(b)] Tokyo Institute of Technology, Research Lab. for Nuclears Reactors, O-okayama, Meguroku, Tokyo 152, JAPAN, email: yfujii@nr.titech.ac.jp*

## INTRODUCTION

Gadolinium is a neutron absorbing material and has been used as a burnable poison contained in the U fuel pellets for LWRs [1].

Amoung the 7 isotopes of gadolinium, $^{157}Gd$ has a special large neutron absorption cross section of 254,000 barn.

In order to increase the burn-up rates of the U fuels for LWRs, the higher concentration of Gd burnable poison is necessary and therefore the use of gadolinium enriched in $^{157}Gd$ is of interest

Taking into account that the enrichment by laser processes would be costly for commercial use of $^{157}Gd$, we suggest the utilization of the chemical exchange between $Gd^{3+}$ (in solution) and Gd amalgam with this purpose.

In this paper gadolinium isotope single stage separation factor for isotopic exchange between $Gd^{3+}$ (in solution) and gadolinium amalgam (GdHg) is determined.

## EXPERIMENTAL

Shvedov and Antonov [2], [3], David and Bouissières [4], and Marsh [5] have experimentally determined the optimum conditions for Gadolinium amalgam obtaining by electrolyse on mercury cathod.

By electrolyse of aqueous solutions containing gadolinium acetate and lithium citrate as complexant agent, using the ratio $[Li^+] / [Gd^{3+}] = 12$, gadolinium amalgam was prepared. In Fig. 1 is presented the experimental device utilised in this case [4], [6]. Inside diameter of the first electrolyser utilised was 40 mm, the surface area 12.56 $cm^2$ and current density 0.032 $A/cm^2$.

**Experiment No. 1**

By electrolyse of 7.5 ml 0.02 M gadolinium acetate ($Gd(AcO)_3$), 4.5 ml 0.4 M Lithium citrate ($Li_3Cit$), 3 ml $H_2O$ and 10 ml Hg as cathode and Platinum as anode, a part of gadolinium passed into mercury, gadolinium amalgam (GdHg). The GdHg was stirred with 1N HCl solution and $Gd^{3+}$ is precipitated as oxalate at weak acid pH (5¸ 6) and then converted into $Gd_2O_3$: 0.010 g, SAMPLE No. 1. The

remained gadolinium in acetate solution, (after electrolyse), was also precipitated as oxalate and converted into $Gd_2O_3$: 0.0059 g, SAMPLE No. 2. The yield of GdHg formation was 37%.

**Experiment No 2** 7.5 ml 0.02 M Gd $(AcO)_3$
4.5 ml 0.4 M $Li_3Cit$
3 ml $H_2O$; 10 ml Hg
T = 25°C

In Table 1 are presented the operation parameters of the electrolyser for experiment No. 2.

**Table 1**

| Time (min) | Current Intensity (I) (A) | Voltage (U) (V) | Observations |
|---|---|---|---|
| 0 | 0.25 | 13 | Start |
| 50 | 0.44 | 14 | |
| 110 | 0.38 | 13.2 | |
| 180 | 0.34 | 13.5 | |
| 220 | 0.35 | 14.3 | |
| 230 | 0.43 | 15.15 | Stop |

In the same way like in Exp. No. 1, from GdHg resulted 0.0076 g $Gd_2O_3$, SAMPLE No. 3 and, from gadolinium remained in aqueous solution, resulted 0.0016 g $Gd_2O_3$, SAMPLE No.4. The yield of GdHg formation was 28%.

SAMPLE No. 5 is 0.160 g $Gd_2O_3$, of natural isotope abundance supplied by " Johnson Mathey Rare Earth Products", England.

**Experiment No.** 3 7.5 ml 0.02 M Gd $(AcO)_3$
4.5 ml 0.4 M $Li_3Cit$
28 ml $H_2O$; 20 ml Hg
T = 25°C

In Table 2 are presented the operation parameters of this experiment.

**Table 2**

| Time (min) | Current Intensity (I) (A) | Voltage (U) (V) | Observations |
|---|---|---|---|
| 0 | 0.42 | 17.5 | Start |
| 15 | 0.39 | 15.0 | |
| 35 | 0.42 | 14.9 | |
| 70 | 0.40 | 14.1 | |
| 110 | 0.40 | 14.5 | |
| 140 | 0.40 | 14.5 | |
| 200 | 0.42 | 15.0 | |
| 230 | 0.40 | 14.1 | Stop |

The Gd of GdHg was converted into $Gd_2O_3$, 0.0131 g, SAMPLE No. 6. The remained Gd in acetate solution was converted into $Gd_2O_3$, 0.0124 g, SAMPLE No. 7. The yield of GdHg formation was 48%.

**Experiment No. 4** 3.75 ml 0.02 M Gd $(AcO)_3$
2.25 ml 0.4 M $Li_3Cit$
14 ml $H_2O$; 10 ml Hg
T = 25°C

In Table 3 are presented the operation parameters of this experiment.

**Table 3**

| Time (min) | Current Intensity (I) (A) | Voltage (U) (V) | Observations |
|---|---|---|---|
| 0 | 0.4 | 23 | Start |
| 16 | 0.4 | 22.5 | |
| 25 | 0.4 | 17 | |
| 75 | 0.4 | 18 | |
| 105 | 0.38 | 18.2 | |
| 160 | 0.38 | 18 | |
| 195 | 0.41 | 19.5 | |
| 220 | 0.4 | 19.5 | |
| 240 | 0.4 | 19.2 | Stop |

The Gd of GdHg is converted to $Gd_2O_3$, 0.0102 g, SAMPLE No. 8. The yield of GdHg formation was 75.5%.

**Experiment No. 5** A new electrolyser of 53 mm i.d., the surface area 22 $cm^2$ and current density 0.027 $A/cm^2$ was utilised.
3.75 ml 0.02 M Gd $(AcO)_3$
2.25 ml 0.4 M $Li_3Cit$
14 ml $H_2O$; 10 ml Hg
T = 26°C

In Table 4 are presented the operation parameters of this run.

**Table 4**

| Time (min) | Current Intensity (I) (A) | Voltage (U) (V) | Observations |
|---|---|---|---|
| 0 | 0.47 | 27.5 | Start |
| 10 | 0.6 | 33 | |
| 25 | 0.6 | 30 | |
| 35 | 0.5 | 30 | |

| Time (min) | Current Intensity (I) (A) | Voltage (U) (V) | Observations |
|---|---|---|---|
| 75 | 0.5 | 30 | |
| 115 | 0.51 | 29.5 | |
| 155 | 0.5 | 29.1 | |
| 215 | 0.53 | 27.9 | |
| 235 | 0.53 | 27.3 | Stop |

Gd of GdHg is converted into $Gd_2O_3$, 0.0121 g, SAMPLE No.9. The yield of GdHg formation was 89.6%.

**Experimentt No.6** 3.75 ml 0.02 M Gd $(AcO)_3$
2.25 ml 0.4 M $Li_3Cit$
14 ml $H_2O$; 10 ml Hg
T = 26°C

In Table 5 are presented the operation parameters of this run.

**Table 5**

| Time (min) | Current Intensity (I) (A) | Voltage (U) (V) | Observations |
|---|---|---|---|
| 0 | 0.5 | 25.1 | Start |
| 35 | 0.5 | 24.1 | |
| 120 | 0.51 | 32 | |
| 150 | 0.5 | 30.5 | |
| 210 | 0.5 | 26.9 | |
| 265 | 0.5 | 26 | Stop<br>Was added 3.75 ml 0.02 M Gd $(AcO)_3$ and 2.25 ml 0.4 M $Li_3Cit$. |
| 275 | - | - | The two phases were separated. |

When $Gd^{3+}$ is passed into GdHg (after 265 min), the electrolyse was stoped and in the liquid phase was added 3.75 ml 0.02 $Gd(AcO)_3$ and 2.25 ml 0.4 M $Li_3Cit$. After 10 minutes of contact, (the mercury stirring was not stoped) the two phases were separated. Gd of GdHg is converted into $Gd_2O_3$, 0.0097 g, SAMPLE No. 10. The yield of GdHg formation was 71.7% .

**Experiment No. 7** 3.75 ml 0.02 M Gd $(AcO)_3$
2.25 ml 0.4 M $Li_3Cit$
14 ml $H_2O$; 10 ml Hg
T = 26°C

In Table 6 are presented the operation parameters of this run.

**Table 6**

| Time (min) | Current Intensity (I) (A) | Voltage (U) (V) | Observations |
|---|---|---|---|
| 0 | 0.5 | 33 | Start |
| 30 | 0.5 | 27 | |
| 60 | 0.5 | 25 | |
| 90 | 0.5 | 36 | |
| 140 | 0.5 | 34 | |
| 205 | 0.5 | 34 | Was added 3.75 ml 0.02 M Gd $(AcO)_3$ in electrolyse conditions. |
| 235 | 0.52 | 40 | The two phases were separated. |

After 205 minutes when $Gd^{3+}$ is passed into GdHg, in the aqueous phase was added 3.75 ml 0.02 M $Gd(AcO)_3$ and, after 30 minutes of contact in electrolyse conditions, the two phases were separated. $Gd^{3+}$ is converted into $Gd_2O_3$, 0.0114 g, SAMPLE, No. 11 and Gd of GdHg is also converted into $Gd_2O_3$, 0.0114 g, SAMPLE No. 12. The yield of GdHg formation was 84,3%.

**Experiment No. 8** 15 ml 0.02 M $Gd(AcO)_3$
9 ml 0.4 M $Li_3Cit$
56 ml $H_2O$; 30 ml Hg
T = 20°C

In Table 7 are presented the operation parameters of this run.

**Table 7**

| Time (min) | Current Intensity (I) (A) | Voltage (U) (V) | Observations |
|---|---|---|---|
| 0 | 1.5 | 37 | Start |
| 50 | 1.0 | 41 | |
| 170 | 0.65 | 41.5 | |
| 260 | 1.55 | 50 | Was added 15 ml 0.02 M $Gd(AcO)_3$ and 9 ml $Li_3Cit$, 0.4 M in electrolyse conditions. |
| 290 | - | - | The two phases were separated. |

When $Gd^{3+}$ is passed into amalgam, in the aqueous phase were added 15 ml 0.02 M $Gd(AcO)_3$ and 9 ml 0.4 M $Li_3Cit$ and electrolyse was continued for 30 minutes. Then the two phases were separated. GdHg is divided in two equal parts of 15 ml each: Gd of first part is solubilised with acetic acid 1M and this solution is added to the second part of GdHg and electrolysed 30 minutes in the electrolyser of 40 mm i.d. (Fig.1).

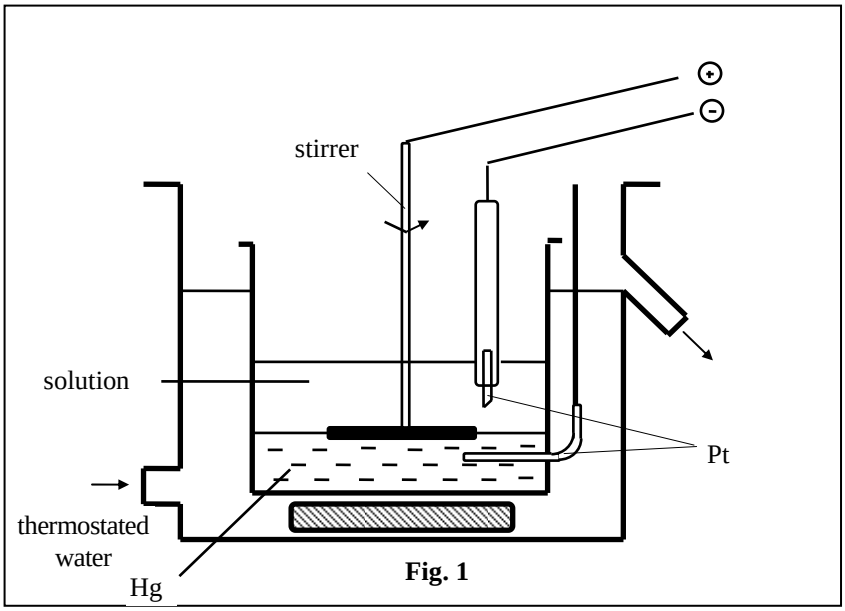


**Fig. 1**

The electrolyse parameters were: I = 0.28 A; U = 41 V; T = 25°C. After that the two phases were separated. Gd of GdHg is converted into $Gd_2O_3$, 0.0157 g, SAMPLE No. 13. The yield of GdHg formation is 58%. $Gd^{3+}$ from solution is converted into $Gd_2O_3$, 0.0169 g, SAMPLE No. 14. The yield of $Gd_2O_3$ formation was 62.6%.

**Experiment No. 9** 15 ml 0.02 M $Gd(AcO)_3$
9 ml 0.4 M $Li_3Cit$
56 ml $H_2O$; 30 ml Hg
T = 32°C

A new electrolyser of 86 mm i.d., the surface area of 59 $cm^2$ and the same current density as in Experiment No. 5 was utilised.After 100 minutes, when $Gd^{3+}$ is passed into GdHg in the aqueous phase were added 15 ml 0.02 M $Gd(AcO)_3$ and 9 ml 0.4 M $Li_3Cit$ and, after 30 minutes of contact in electrolyse conditions, the two phases were separated. GdHg is divided in two equal parts of 15 ml. Gd of first part is solubilised with acetic acid 1 M and the solution is added to the second part of GdHg and electrolysed 30 minutes in the electrolyser of 40 mm i.d. (Fig. 1). In the solution was added also 4.5 ml 0.4 M $Li_3Cit$. The electrolyse parameters were: I = 0.13¸0.16 A; U = 46 V; T = 34°C. After that the two phases were separated; Gd of GdHg was converted into $Gd_2O_3$, 0.0122 g, SAMPLE No. 15. $Gd^{3+}$ of solution was converted into $Gd_2O_3$, 0.0158 g, SAMPLE No. 16. The scheme of Experiment No. 9 is presented in Fig. 2.

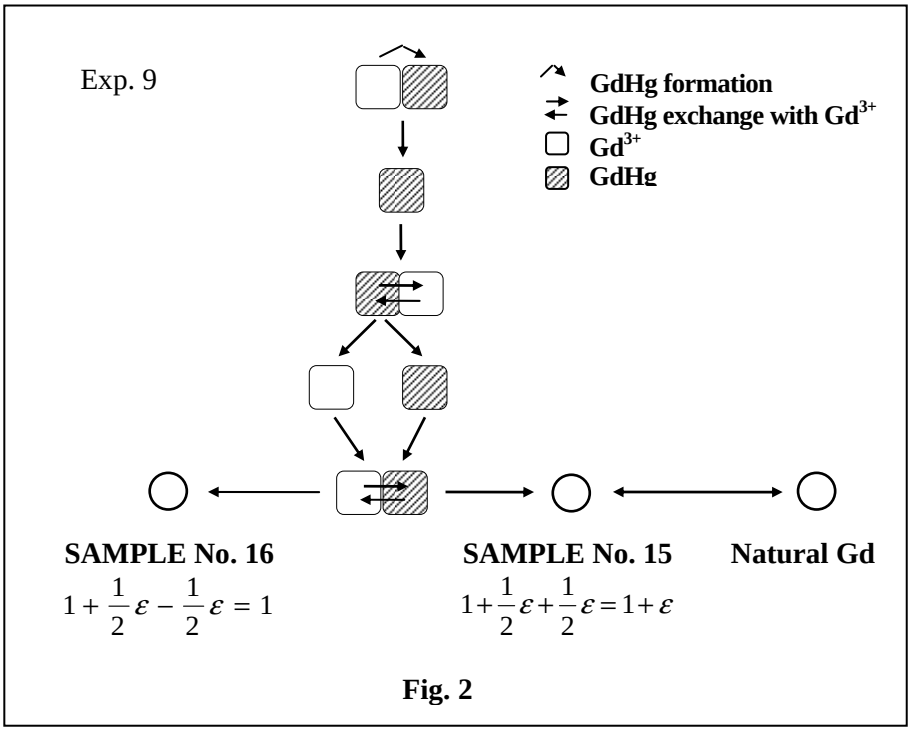


**Fig. 2**

The isotopic separation between SAMPLE 15 and Gd of natural isotopic abundance is $\alpha = 1 + \varepsilon$, (1 stage). $\alpha$ is the single stage separation factor and $\varepsilon$ is the enrichment coefficient.

**Experiment No. 10** 15 ml 0.0133 M $Gd(AcO)_3$
2 ml 0.4 M $Li_3Cit$
12.5 ml $H_2O$; 10 ml Hg
T = 25°C

In this experiment was utilised the electrolyser of 40 mm i.d. (Fig. 1).

0.0242 g $Gd_2O_3$, from GdHg, obtained from 3 experiments in conditions of the Experiment No. 9, is solubilised with acetic acid 1M. The solution is divided in two equal parts: first part of 5 ml 0.0133 M $Gd(AcO)_3$ is electrolysed. When $Gd^{3+}$ is passed into GdHg ( 150 min.) the electrolyse was stoped and in the aqueous phase was added the second part of 5 ml of 0.0133 M $Gd(AcO)_3$, and after 30 min. of electrolyse the two phases were separated. Gd of GdHg was converted into $Gd_2O_3$, 0.0135 g, SAMPLE No. 17. $Gd^{3+}$ from solution is converted into $Gd_2O_3$, 0.0120 g, SAMPLE No. 18.The scheme of Experiment No. 10 is presented in Fig. 3.

The isotopic separation between SAMPLE No. 17 and Gd of natural isotopic abundance is $\alpha^{1.5} = 1 + 3/2\ \varepsilon$; (1.5 stages).

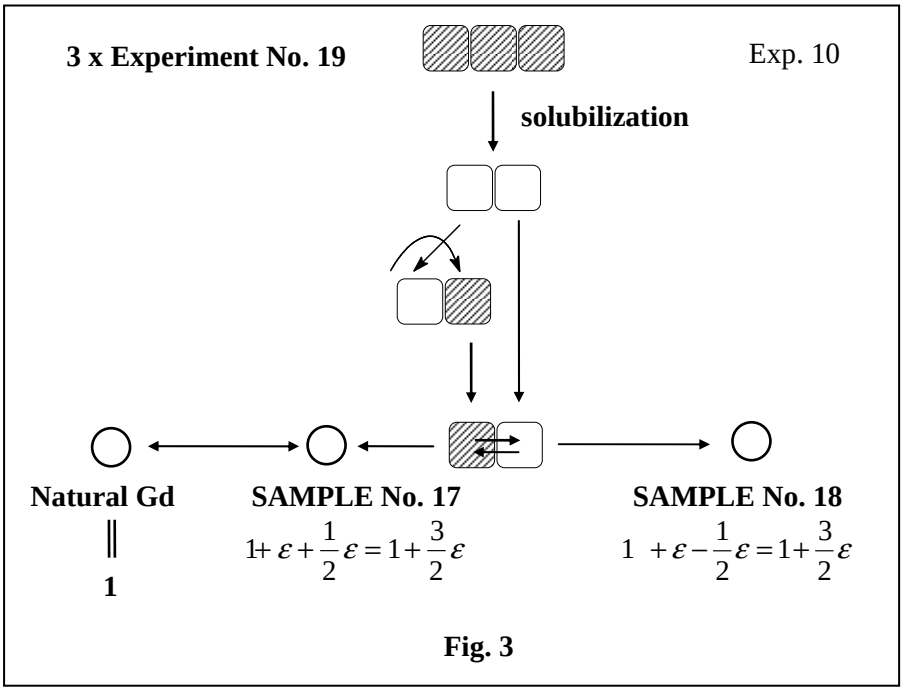


**Fig. 3**

The isotope analyses for gadolinium were made by mass spectrometry using MAT 261 equipped with a thermal ionization source. The gadolinium amalgam experiments data are presented in Table 8 and 9.

**Table 8**

| Exp. No. | Aqueous Phase Sample | | | Gd-amalgam Phase Sample | | | Single stage separation factor α** |
|---|---|---|---|---|---|---|---|
| | Sample No | Weight (mg $Gd_2O_3$) | Isotopic* Ratio | Sample No | Weight mg $Gd_2O_3$ | Isotopic* Ratio | |
| 1 | 2 | 5.9 | 0.9643 | 1 | 10 | 0.9485 | 1.0023 |
| 2 | 4 | 11.6 | 0.9482 | 3 | 7.6 | 0.9494 | 1.0013 |
| 3 | 7 | 12.4 | 0.9425 | 6 | 13.1 | 0.9468 | 1.00456 |
| 4 | - | - | - | 8 | 10.2 | 0.9465 | 1.00424 |
| 5 | - | - | - | 9 | 12.1 | 0.9465 | 1.00424 |
| 6 | - | - | - | 10 | 9.7 | 0.9481 | 1.0059 |
| 7 | 11 | 11.4 | 0.9472 | 12 | 11.4 | 0.9484 | 1.0013 |

* Isotopic Ratio: $^{156}Gd/^{160}Gd$; $\Delta M = 4$.

** Single stage separation factor $\alpha = R_{am} / R_{aq}$, where $R_{am}$ refers to the isotopic ratio of the GdHg phase contacted with the aqueous phase, for which the isotopic ratio is expressed by $R_{aq}$.

The isotopic ratio in the present paper is always calculated with the light isotope over the heavy isotope. Thus, if the light isotope is preferentially enriched in the GdHg phase, the α value will be greater than unity and ε will be positive.

For Exp. No. 4; 5 and 6 we calculate the α value taking as isotope ratio in aqueous phase: 0.9425, measured for experiment No. 3.

**Table 9**

| | Sample No. | Isotopic Ratio | | | | |
|---|---|---|---|---|---|---|
| | | $^{154}Gd/^{160}Gd$ | $^{155}Gd/^{160}Gd$ | $^{156}Gd/^{160}Gd$ | $^{157}Gd/^{160}Gd$ | $^{158}Gd/^{160}Gd$ |
| Exp. 8 | 13(GdHg) | 0.101650 | 0.687524 | 0.947731 | 0.722320 | 1.143161 |
| | 14($Gd^{3+}$) | 0.101441 | 0.686869 | 0.946447 | 0.721691 | 1.142001 |
| α | 13/14 | 1.00206 | 1.00135 | 1.00135 | 1.00085 | 1.001016 |
| ε/ΔM | 13/14 | $3.43\times10^{-4}$ | $1.9\times10^{-4}$ | $3.375\times10^{-4}$ | $2.833\times10^{-4}$ | $5.08\times10^{-4}$ |
| Exp. 9 | 15(GdHg) | 0.100485 | 0.681275 | 0.941122 | 0.718025 | 1.137497 |
| Natural abundance Gd | 5 | 0.100526 | 0.681062 | 0.940701 | 0.718561 | 1.138667 |
| α | 15/5 | 0.999592 | 1.00317 | 1.00044 | 0.999254 | 0.998972 |
| Exp. 10 | 17(GdHg) | 0.101510 | 0.687606 | 0.948975 | 0.722132 | 1.142473 |
| | 18($Gd^{3+}$) | 0.101241 | 0.687056 | 0.948016 | 0.721278 | 1.141919 |
| α | 17/5 | 1.0065 | 1.0064 | 1.0058 | 1.00331 | 1.00222 |
| ε/ΔM | 17/5 | $1.0833\times10^{-3}$ | $1.28\times10^{-3}$ | $1.45\times10^{-3}$ | $1.103\times10^{-3}$ | $1.11\times10^{-3}$ |

The α (15/5) Experiment No. 9 and α (17/5) Experiment No. 10 were calculated versus natural abundance gadolinium. α (17/5) has the best accuracy because of the experimental conditions used to get a 1.5 stages isotopic separation.

## CONCLUSIONS

The single stage separation factor (α) of gadolinium isotopes has been experimentally determined for GdHg - $Gd^{3+}$ exchange system the light isotope being preferentially enriched in gadolinium amalgam phase.

The enrichment coefficient (ε) are two order of magnitude larger than that observed in the resin/aqueous solution equilibrium systems for gadolinium isotopes [1].

The yield of GdHg formation has increased from 37¸ 75.5% for the electrolyser of 40 mm i.d., to 89.6% for electrolyser of 53 mm i.d.

After 30 minutes of contact (in electrolyse conditions) between $Gd^{3+}$ and GdHg phase there is not an important passage of Gd and, in these conditions, the isotopic exchange of Gd can be studied.

Agitation of the mercury surface is necessary to prevent formation of a crust of solid amalgam and to keep the cathode clear of any basic salts or sediments which might form.

The electrolyser must be thermostated at 25 ÷ 35°C.

## REFERENCES

[1] Chen J., Nomura M., Fujii Y., Kawakami F. and Okamoto M., J. Nucl. Sci. Technol., 29(11) 1086 (1992).

[2] Shvedov V.P. and Antonov P.G., Radiohimia, 5, 581 (1964).

[3] Antonov P.G., Shvedov V.P., Radiohimia, 11 306 (1969).

[4] David F., Bouissières G., Bull. Soc. Chim. France, 4, 1001 (1965).

[5] Marsh J.K., J. Chem. Soc., 398, 523 (1942).

[6] Chang Z., "The isotope effects in some alkali and alkaline earth metals in the amalgam system", Ph. D. Thesis, (1996), Research Lab. for Nuclear Reactors, Tokyo Inst. of Technology.

# THE ROLE OF THE ISOTOPOMERS IN THE VIBRATIONAL SPECTROSCOPY

**FERENC BILLES**

*Department of Physical Chemistry, Budapest University of Technology and Economics, H-1521 Budapest, Budafoki út 8., Hungary, e-mail: billes.fkt@chem.bme.hu*

**ABSTRACT.** The aim of this work is to introduce the applicability of isotopomers in the assignment of the vibrational spectra. The connection of the isotopomer vibrational modes was demonstrated with the product and sum rules. Several isotopomer spectra of pyrrole were simulated based on quantum chemical calculations. The isotope shifts were investigated and compared with the experimental ones.

Keywords: isotopomers, vibrational spectra, simulations.

## 1. INTRODUCTION

This work deals with the importance of the isotopomers in the vibrational spectra, their application in this area of this science and the possibility of the simulation of their spectra.

Isotopomers are applied already in the vibrational spectroscopy in the ‘40s of our century. Lord and Miller published the infrared spectra of some deuterated isotopomers of pyrrole in 1942 [1]. This paper was followed by several articles used the isotopomers for the better assignment of the vibrational spectra. The problems concerning their application was summarized by Wilson, Decius and Cross [2]. Later, the development of the computers and the calculation methods made possible the computer simulation of the vibrational spectra of isotopomers.

## 2. THEORY

The molecular vibrations of the majority of the molecules have the following properties: they have small amplitudes, their anharmonicity is small, vibrational quantum numbers change only $0 \rightarrow 1$. If the vibrations meets these conditions, the classical theory of harmonic vibrators is applicable to the description of vibrational motions of the molecule.

The N atoms of the molecules change their $x_i$ original equilibrium positions during the vibrations: with $\Delta x_i = X_i - x_i$ $(i = 1,2,...,3N)$. The change in potential energy has the form (harmonic, small-amplitude approximation):

$$2\Delta V = \sum_{i=1}^{3N}\sum_{j=1}^{3N} f_{ij}\Delta x_i \Delta x_j \qquad (1)$$

while the corresponding kinetic energy will be

$$2\Delta T = \sum_{i=1}^{3N} m_i \left(\Delta \dot{x}_i\right)^2 \tag{2}$$

The dynamic equation of the system is

$$\frac{d}{dt}\frac{\partial \Delta T}{\partial \Delta \dot{x}_i} + \frac{\partial \Delta V}{\partial \Delta x_i} = 0 \tag{3}$$

Its solution leads to the eigenvalue equation

$$\left|\mathbf{gf} - \lambda \mathbf{E}\right| = 0 \tag{4}$$

with $\lambda_i = 4\pi^2 c^2 \tilde{\nu}_i^{\,2}$ $i = 1,2,...,3N-6$ $\lambda_i > 0$

Matrix **g** is diagonal containing the inverse atomic masses, **f** contains the $f_{ij}$ force constants.

Two important equations connect the vibrational frequencies of the isotopomers

*The product rule* [3,4]. According to Equ. 4

$$\left|\mathbf{gf}\right| = \left|\mathbf{f}\right| \prod_{i=1}^{3N} \left(m_i\right)^{-1} \tag{5}$$

Since we assume the same matrix **f** and equilibrium geometry for all isotopomers, applying Equ. 5 for two isotopomers of a molecule, denoted one of them without, the other with prime, and taking into account translations and rotations (for translations stands a factor of the ratio of the molecular masses (M), for the rotations a factor of the ratio of the principal inertial moments ($I_x$, $I_y$ and $I_z$)):

$$\prod_{i=1}^{3N-6} \frac{\tilde{\nu}_i^{'2}}{\tilde{\nu}_i^{2}} = \prod_{i=1}^{3N} \frac{m_i}{m_i^{'}} \frac{M^{'3}}{M^3} \frac{I_x^{'} I_y^{'} I_z^{'}}{I_x I_y I_z} \tag{6}$$

*The sum rule* [5,6]. Let

$$\sigma \equiv \left|\mathbf{gf}\right| = \sum_{i=1}^{3N} m_i^{-1} \sum_{j=1}^{3N} f_{ij} \tag{7}$$

Let us choose r isotopomers then if for all the $m_i$ atom types the $n_k m_{ik}^{-1}$ expressions are zero

$$\sum_{k=1}^{r} n_k \sigma_k = \sum_{k=1}^{r} n_k \sum_{i=1}^{3N} m_{ik}^{-1} \sum_{j=1}^{3N} f_{ij} = \sum_{k=1}^{r} \sum_{i=1}^{3N} n_k m_{ik}^{-1} \sum_{j=1}^{3N} f_{ij} = 0 \tag{8}$$

where $n_k$'s are the stoichiometric numbers.

Here is a very simple example for the water isotopomers:

$$\sigma(HOH) + \sigma(DOD) - \sigma(HOD) - \sigma(DOH) = 0$$

Mainly the product rule is applied. Sometimes, if there exists strong association between the molecules, the product rule gives only approximate values.

## 3. APPLICATIONS

*The isotope substitution*. The calculations for the determination of characters of the vibrational modes apply the so-called (chemical) *internal coordinate system*. The 3N-6 coordinates of this system are the changes in the geometric parameters of the molecule: changes in bond lengths, valence angles, dihedral angles and torsional angles. For distinguishing the quantities in this system from the corresponding ones in Cartesian system they are denoted with capital letters.

The substitution of the molecules with isotopes helps the vibrational spectroscopist. It changes only the atomic masses (**G** matrix), the molecular geometry and the **F** matrix are regarded as constant. Band shifts can be calculated helping the interpretation of the spectra and proving the reality of the force field.

Two different types of the isotope substitution can be distinguished:

1. *Deuteration of mobile hydrogen atoms*. This process is easy but leads to an equilibrium. We have a mixture of the original and the deuterated compounds. Therefore it is difficult to yield pure compounds. This deuteration decreases the association. Sometimes the deuteration of a ring NH group gives surprising results. If the number of the nitrogen atoms is more than one in an aromatic ring the CH bands of the ring may get loose and the hydrogen atom of the CH groups will be deuterated, too. This is the case e.g. for the 1,2,4-triazole [7]. After its deuteration a sharp band appears in the IR spectrum at 2350 $cm^{-1}$, indicating the deuteration of CH groups:

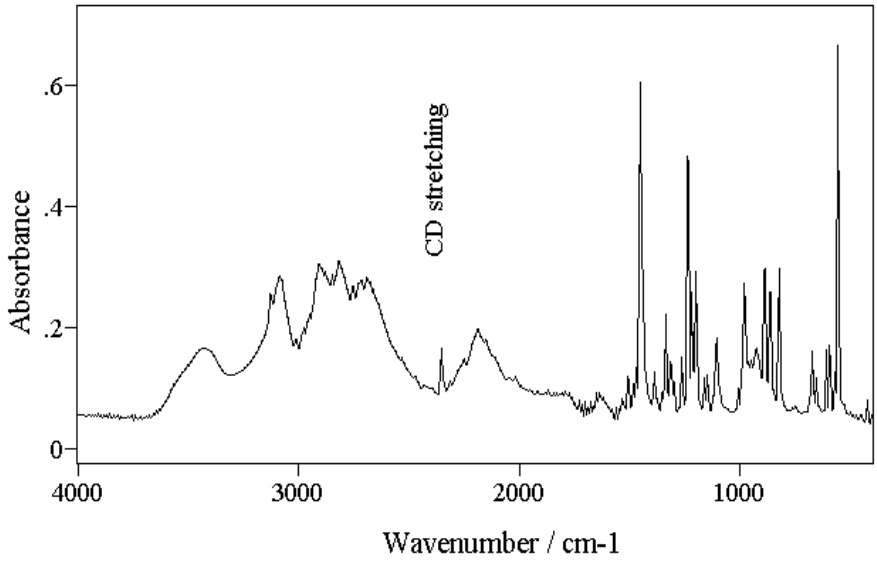


**Fig. 1.** Part of the IR spectrum of 1,2,4-triazole the deuterated with heavy water

2. *Other types* of isotope substitution are complicate and used less frequently in the vibrational spectroscopy. They have the advance of the nearly 100 % substitution but they are more expensive.

### 3.2. FERMI RESONANCE

Sometimes the isotope substitution helps in the interpretation of vibrational spectra in a very special case. If the frequency of a fundamental mode of a molecule is very close (practically equal) to a combination or an overtone of other fundamental modes, with equal symmetry (they belong to the same species) and they are active in infrared and/or in Raman spectrum, Fermi resonance will be observed.

In this case the two energy levels move away from one another and their corresponding band intensities will be nearly balanced. Sometimes the appearances of new bands are observed since the combinations having originally low intensities are frequently unobservable. The isotope substitution shifts unequally the fundamentals and therefore there is no longer Fermi resonance.

**Example:** the benzene molecule. Three bands are observed in the IR spectrum of $C_6H_6$ in the 3000 to 3100 $cm^{-1}$ (aromatic CH stretching) region (Fig. 2), while in the similar spectrum of $C_6D_6$ in the 2200 to 2300 $cm^{-1}$ (CD stretching) region only one.

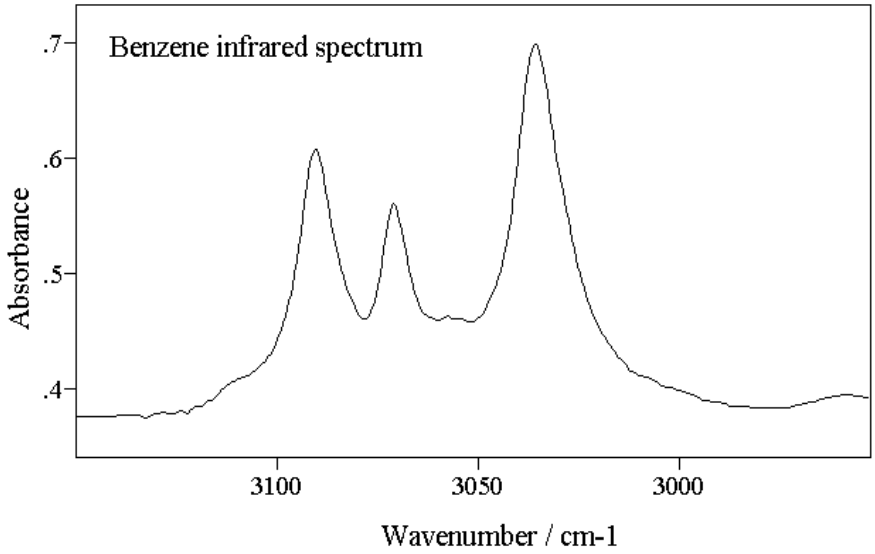


**Fig. 2.** Part of the infrared spectrum of benzene

The appearance of these three bands refer to Fermi resonance since according to the $D_{6h}$ symmetry of the benzene molecule it has only one infrared active vibrational mode. The Fermi resonance bands appear with coincidence of the following combinations (species in parentheses):

combination: 993 $cm^{-1}$ ($A_{1g}$) + 606 $cm^{-1}$ ($E_{2g}$) = 1599 $cm^{-1}$ ($E_{2g}$)
fundamental: 1599 $cm^{-1}$ ($E_{2g}$)

The combination of these levels with the fundamental appearing at 1482 $cm^{-1}$ ($E_{1u}$) yields the triple Fermi resonance of the bands: 993 + 606 + 1442 = 3081 ($E_{1u}$), 1599 + 1482 = 3081 ($E_{1u}$), 3081 ($E_{1u}$).

## 4. SIMULATION OF THE ISOTOPOMER SPECTRA

For the simulation of the isotopomer spectra a computer program was elaborated. The following conditions had to be considered: the molecular geometry and the scaled force field is constant for all isotopomers; the integrated intensities are the results of the quantum chemical calculations; the band shapes and the FWHH's (full width of half height, $\delta\tilde{\nu}$ ) of the bands are arbitrary.

*Band profiles.* The following band profiles are used in the praxis: the *Lorentz* profile:

$$I(\tilde{\nu}) = I_{\max} \frac{(\delta\tilde{\nu})^2}{4(\tilde{\nu} - \tilde{\nu}_{\max})^2 + (\delta\tilde{\nu})^2} \tag{9}$$

and the *Gaussian* profile:

$$I(\tilde{\nu}) = I_{\max} \exp\left[\frac{-\ln(32) \times (\tilde{\nu} - \tilde{\nu}_{\max})^2}{(\delta\tilde{\nu})^2}\right] \tag{10}$$

Besides the application of these pure profiles their mixing is also possible.

According to the oven-mentioned conditions the experimental and the simulated spectra can differ in the band shapes, intensities and FWHH's but they are in spite of these facts very good and demonstrative presentations of the results of the calculations.

*Example.* The example is the *pyrrole*. This molecule is planar and has $C_{2v}$ symmetry.

The following shorthands will be used for the isotopomers. PYL: the parent compound, PYD1: N**H** is deuterated, PYD5: pentadeuterated, PYN: $^{14}N$ is substituted with $^{15}N$, PYC4: all $^{12}C$ atoms are substituted with $^{13}C$, PYND1: N**H** is deuterated and $^{14}N$ is substituted with $^{15}N$, PYC4D1:N**H** is deuterated and all $^{12}C$ atoms are substituted with $^{13}C$, PYNC4D1: N**H** is deuterated, $^{14}N$ is substituted with $^{15}N$ and all $^{12}C$ atoms are substituted with $^{13}C$, PYND5 pentadeuterated and $^{14}N$ is substituted with $^{15}N$, PYC4D5: pentadeuterated and all $^{12}C$ atoms are substituted with $^{13}C$, PYNC4D5: pentadeuterated and $^{14}N$ is substituted with $^{15}N$ and all $^{12}C$ atoms are substituted with $^{13}C$.

The IR and Raman spectra of PYL, PYD1 and PYD5 were recorded. The IR and Raman spectra of all 12 molecules were simulated. The simulations were based on our quantum chemical calculations on pyrrole [8]. These calculations were carried out with the Gaussian 94 program package [9] applying the density functional theory with the Becke3P86 functional and 6-311G** basis set. All other computer programs are home made.

The same part of all 12 simulated infrared spectra of pyrroles are introduced in Fig. 4 (the region from 960 to 1100 $cm^{-1}$). This spectral series demonstrates how radical changes may occur as result of the isotope substitution.

Since the molecules associate with NH...N bridges, the *product rule* is only approximately valid. The positions of the bands do not correspond to those of the free molecule, for the experimental spectra:

| Isotopomers | Experimental | Theoretical |
|---|---|---|
| PYL/PYD1 | 6.13026 | 5.88016 |
| PYL/PYD5 | 12597.05 | 140321.07 |

The following figures introduce some interesting details of the simulated spectra. The most important property is the isotope shift.

The regions of the NH (ND) and CH (CD) stretchings of the infrared spectra of the 12 pyrroles are presented in Fig. 3. The primary shifts in the simulated spectra are effected by the deuteration. It is clearly seen that shifts of second order of the NH (ND) stretching frequencies depend only on the isomeric change of nitrogen atom while those of the CH (CD) stretching frequencies depend only on the isotope change of the carbon atoms.

Similarly, the same part of the infrared spectra of all 12 simulated of pyrroles are introduced in Fig. 4 (the region from 960 to 1100 $cm^{-1}$). This spectral series demonstrates how radical changes may occur as results of the isotope substitution.

The isotope effect of the wavenumber and the potential energy distribution (PED) is presented in Fig. 5 on the example of a vibrational mode belonging to the $B_1$ species of pyrrole. The experimental and the calculated frequencies are very close to one another. The wavenumber shifts are determined by the deuterations other isotope substitutions act hardly on them. The PED's of the non-deuterated molecules are nearly constant. The ring stretching ($\nu$ring) and the CH in-plane deformational ($\beta$CH) motions are of the same magnitude and their participations in PED are larger than that of the $\beta$NH motions.

After the deuteration on the ring nitrogen the $\beta$CH motions dominate and the following carbon change causes the domination of the $\beta$ND motions. Nitrogen changes do not have large effects on the PED.

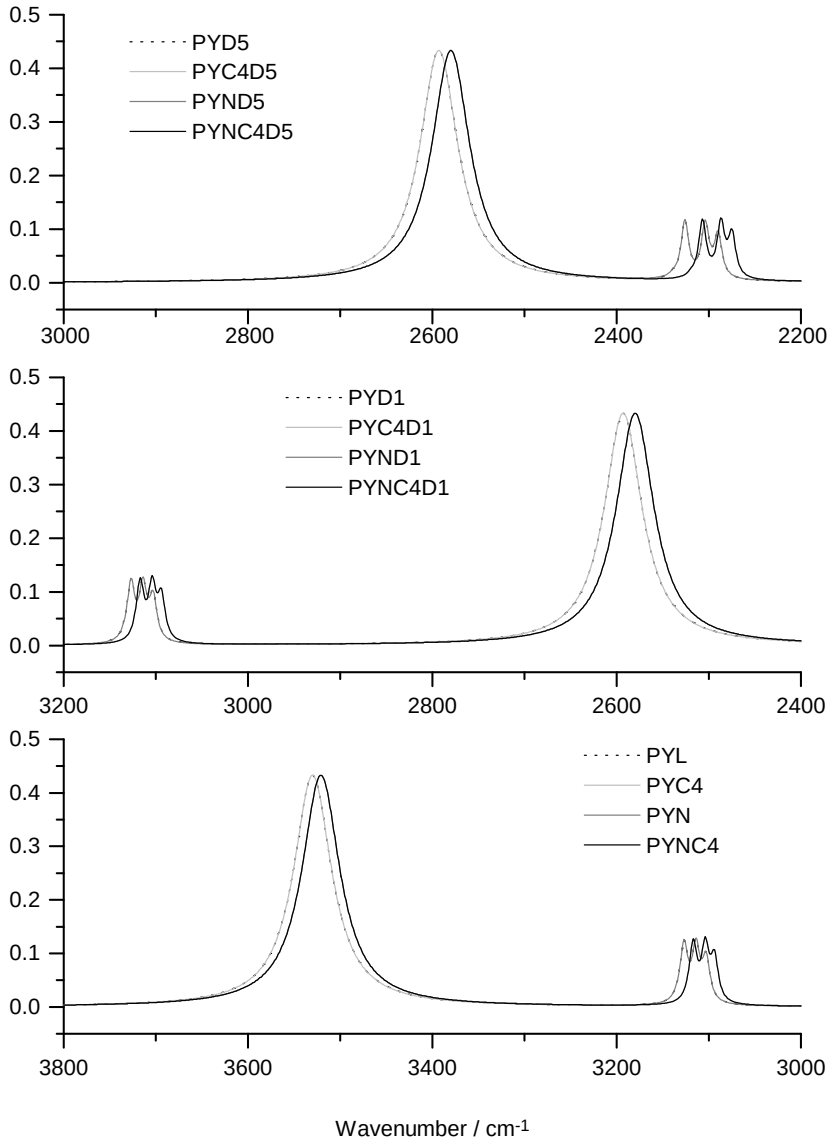


**Fig. 3.** Parts of simulated IR spectra of pyrrole isotopomers: the NH (ND) and CH (CD) stretching regions (ordinates: intensities, arbitrary units)

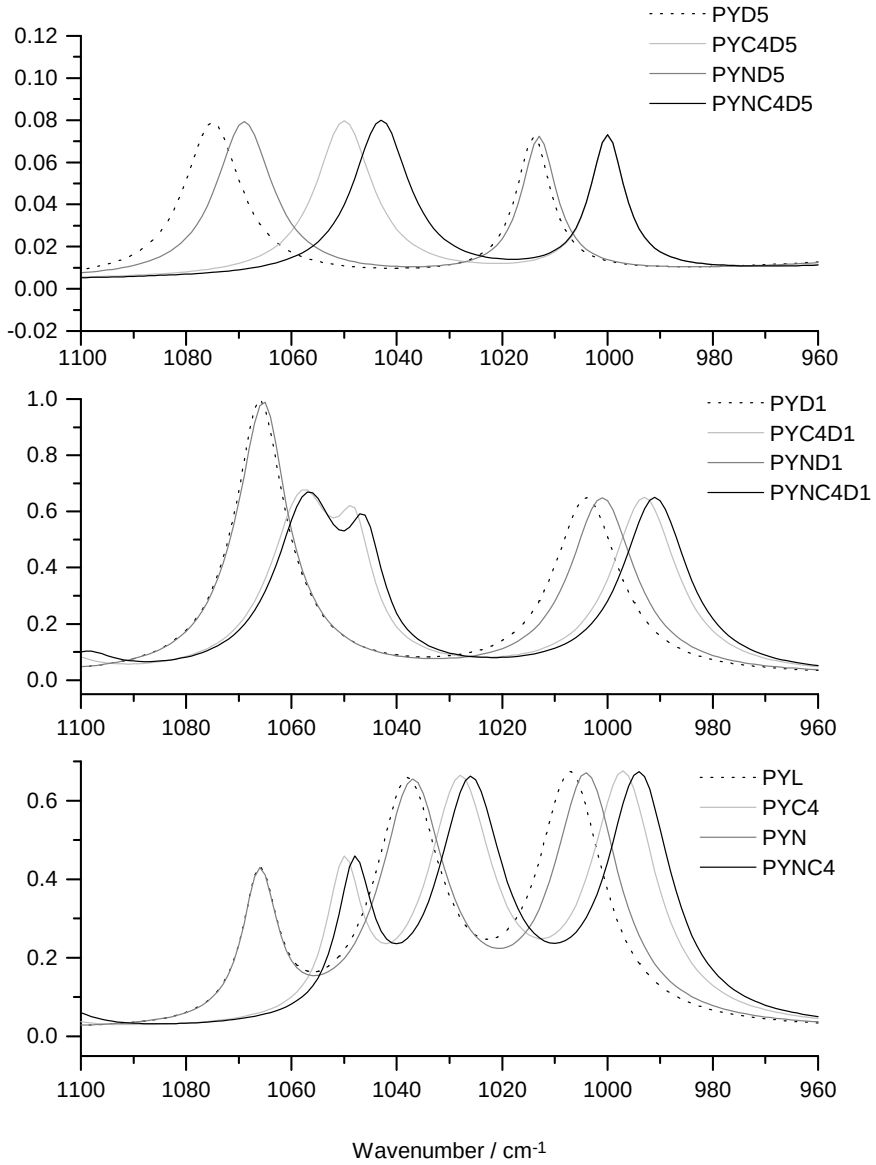


**Fig. 4.** Parts of simulated IR spectra of pyrrole isotopomers (ordinates: intensities, arbitrary units).

The pentadeuteration enlarges the βNH participation in the PED. If the change of the carbon atoms follows the deuteration the βCD motions dominate. The change of the nitrogen atom has similarly a very small effect on the PED.

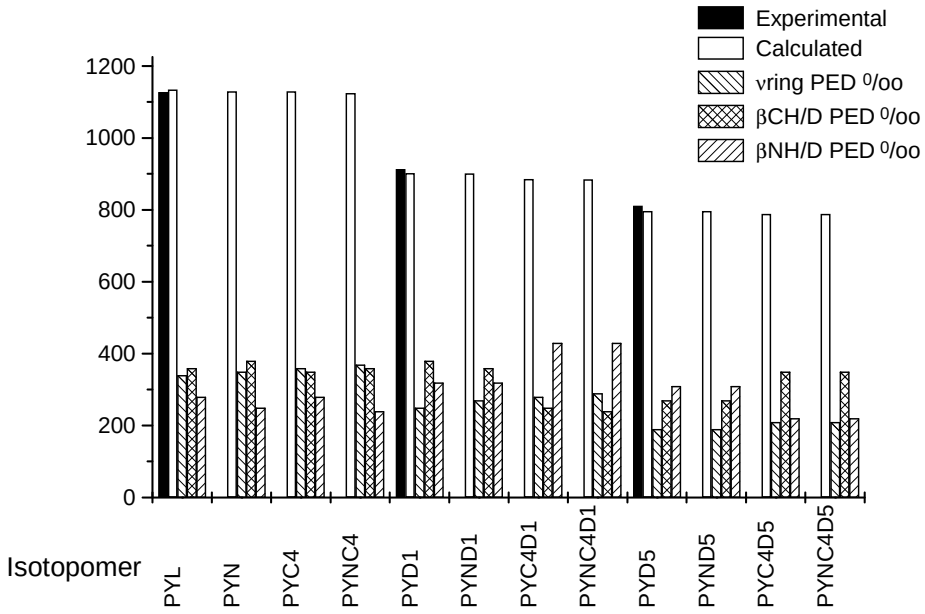


Fig. 5. Isotopomer dependence of the vibrational frequency and the potential energy distribution (PED) of a $B_1$ type vibrational mode of pyrrole (ordinate: wavenumber/$cm^{-1}$ and PED in 0/00, respectively )

## CONCLUSIONS

The isotope effect of the spectra is important in several cases for the good interpretation of the vibrational spectra. They can help in the control of the vibrational force fields, in the clearing up the Fermi resonances.

Based on the quantum chemically calculated and fitted force field and the calculated intensities the isotope shifts of the vibrational bands can be estimated.

Applying this effect one can choose from the fundamental modes those that have nearly the same potential energy distributions independently of the isotope substitution. These are the *vibrational modes of stable character*. Of course, in the PED the corresponding types of motions must be taken into account (e.g. βCH must be substituted by βCD).

There exist bands in the vibrational spectra that do not change their positions as results of the isotope substitutions or, and this is more frequently the case their isotope effect is very small. These are *vibrational modes of stable position* and characterize the molecule in question and also its derivatives.

Summarizing, the investigation of the isotope effect of the vibrational spectra is a very good aid to the interpretation of the infrared and Raman spectra.

## REFERENCES

1. R. C. Lord, F. A. Miller, J. Chem. Phys., 10 (1942) 328.
2. E. B. Wilson, J. C. Decius, P. C. Cross: Molecular Vibrations, McGraw-Hill, New York, 1955.
3. O. Redlich, Z. Phys. Chem., B28 (1935) 371.
4. W. R. Angus , C. R. Baily, J. B. Hale, C. K. Ingold, A. H. Leckie, C. G. Raisin, J. W. Thomson, C. L. Wilson, J. Chem. Soc., (1936) 971.
5. J. C. Decius, E. B. Wilson, J. Chem. Phys., 19 (1951) 1409.
6. L. M. Sverdlov, Dokl. Ak. Nauk SSSR, 78 (1951) 1115.
7. F. Billes, H. Endrédi, G. Keresztury, THEOCHEM, 530 (2000), 183.
8. E. Geidel, F. Billes: J. Mol. Structure THEOCHEM, 507 (2000) 75.
9. Gaussian 94, Revision B.2, M. J. Frisch et al., Gaussian, Inc., Pittsburgh PA, 1995.

# OVERVIEW OF USES AND NEEDS OF SEPARATED ISOTOPES
## *SYNTHESE SUR LES ISOTOPES SEPARES: UTILISATION ET BESOINS*

**MICHEL COUAIRON[(a)], EDGAR SOULIÉ[(b)], JACQUES LAIZIER[(c)], ALAIN ALBERMAN[(d)]**

*[(a)] CEA/SACLAY, DCC/DPE, 91191-Gif Sur Yvette Cedex (France), e-mail: rousseau@carnac.cea.fr*
*[(b)] CEA/SACLAY, DSM/DRECAM, 91191-Gif Sur Yvette Cedex (France), e-mail: bsoulie@drecam.cea.fr*
*[(c)] CEA/SACLAY, DTA/DAMRI, 91191-Gif Sur Yvette Cedex (France), e-mail: jacques.laizier@.cea.fr*
*[(d)] CEA/SACLAY, DRN/DRE, 91191-Gif Sur Yvette Cedex (France), e-mail: alberman@dre.cea.fr*

This synthesis paper is a glance through present use and potential need for artificially separated isotopes. It was completed when an excellent report by the Nuclear Energy Agency became available [27]. We focus on stable isotopes since many enriched stable compounds are now required for their unique properties in several high value economic sectors:

1. ***In environmental and biological sciences***. Preferred isotopes remain $D$, $^{13}C$, $^{15}N$, $^{18}O$. The whole French consumption amounts to about five Metric Tons (T) for heavy water and to a few kg for the others, per year. Generic applications encompass a broad spectrum, from drug metabolism up to insecticide research against the bark beetle of spruce.
2. ***In health-care systems***. The need of radioisotopes for medical imaging is expected to increase in European countries (E.U.) by more than 3% a year. Several highly purified stable isotopes are required in order to produce the radioisotopes by neutron, gamma, or particle irradiations. Therefore, we could not raise a sharp fence between radioisotopes and their related stable precursors, such as [$^{203}Tl$, $^{124}Xe$] for cyclotron targets or $\left[^{88}Sr, ^{98}Mo, ^{185}Re\right]$ for irradiations in a high flux reactor.
3. ***In nuclear power industry***. $^{7}Li$ Lithium is used (ten kg per year) as a buffer for boric acid in many Pressurised Water Reactors (PWR). Boron $^{10}B$ could be used by many ways: as enriched boric acid for shim control in PWR; as liquid sodium pentaborate in the stand by control systems for Boiling Water Reactors (BWR); as a solid absorber B4C in the rod clusters for PWR using a mixed uranium-plutonium oxide or «MOX» nuclear fuel. Enriched lanthanide trioxides are potential burnable absorbers in the fuel; the need would amount to ca. forty kg a year, for every high burn-up Light Water Reactor (LWR). Heavy water is now used by five hundred tons in each

Pressurised Heavy Water Reactor (PHWR). For fusion pilots JET and ITER, deuterium and tritium inventory for new programs will gradually increase from about thirty to a hundred grams, with mixing with helium-3 by gram quantities. For a fusion reactor, tritium breeding in a blanket made of a liquid metal or of a Be-Li fluoride molten salt or a solid ceramic, will contain several hundred kilograms of $^{6}Li$ enriched lithium.

## I-ENVIRONMENTAL AND BIOLOGICAL SCIENCES [1]

1. *In the absence of isotope effects*, a few stable isotopes are used as tracers: $D$, $^{13}C$, $^{15}N$, $^{18}O$, $^{34}S$. In various fields related to environmental research, atoms or molecules are tagged with those spikes, the fates of which are followed through equilibrium reactions or transport phenomena. Flow rates may be measured. To retrieve the path of the tracer, one resorts to mass spectrometry analysis based on isotopic dilution method (IDMS). When less precise or routine task is concerned, optical methods may be used. When investigating transport in nature, (e.g. research on estuaries and hydro-geological systems or studies on the formation of uranium ores), it is sometimes possible to get measures from the *natural variations* of isotopic abundances. Studies on transfer through the atmosphere and the hydrosphere rely on measures of hydrogen, carbon and sulphur isotopic ratios, related with the greenhouse effect. In agricultural research, $^{15}N$ is used for comprehensive work on nitrogen assimilation by plants; other investigations aim at a better efficiency of fertilisers, or for pollution inhibitors preventing ammonium decomposition into nitric acid and nitrates.

2. *In the presence of isotope effects*, molecular structure investigations become accessible with N.M.R. analysis. Molecules labelled with deuterium are used in a large number of researches aiming at the analysis of site specific effects, mainly in pharmacology and biology. A unique insight into drug metabolism is possible when stable isotopes and radio-labelled tracers [$^{32}P$, $^{14}C$ …] are coupled. Kinetic as well as mechanistic aspects of the metabolism of therapeutic agents and short-lived toxic intermediates are efficiently investigated with liquid chromatography-tandem mass spectrometry.

   In the forensic sciences, authentication of the origin of products are made by site specific isotope analysis and mass spectrometric analysis of $^{13}C$, $^{18}O$. Control of ethanol species in wines or of flavouring agents in perfumes is growing fast in France.

Labelled molecules are used by a tens gram in a growing number of laboratories. The main supplier in France is EURISO-TOP for the process and marketing of deuterated solvents (ton per year) [2]. Typical applications are summarised in table 1.

| Example of use of stable isotopes (from [1] and [3]). | Table 1 Isotopes |
|---|---|
| Pollution mechanism of agricultural soils, drainage and ground water by conversion of excess N-fertilisers in nitric acid or nitrates. | $^{15}N$ |
| Mechanism of carbonate precipitation at high pH in concrete with atmospheric $CO_2$ and rainwater. | $^{13}C, ^{18}O$ |
| Eco- physiology of nitrogen assimilation by marine phyto-plankton | $^{15}N$ |
| Behaviour of insecticide against the bark beetle of spruce | $^{13}C$ |
| Advances in human nutrition with stable isotopes labelled compounds | $^{15}N, ^{13}C, ^{18}O$ |
| Drug kinetics and metabolism with Isotopic Ratio Mass Spectrometry diagnoses | $D, ^{15}N$ |
| Study of protein ligand complexes by NMR for anticancer or antibacterial research. | $D, ^{13}C, ^{15}N, ^{19}F$ |
| Applications of isotope labelling techniques to studies in drug metabolism and toxicity | $D, ^{13}C, ^{18}O$ |

## II-RADIOTHERAPY AND NUCLEAR MEDECINE IMAGING [4]

There is an increasing economic and political interest in those fields, which are to become of primary importance in the health care system. Several radioisotopes are produced with a high flux of neutrons in research reactors: Osiris at Saclay, BR2 at Mol in Belgium, HFR at Petten in the Netherlands; others can be only produced by irradiation under low or medium energy beam of a cyclotron. Targets have to be highly enriched with stable precursor isotopes. There are two main uses of radioisotopes: cancer therapy and nuclear imaging with tracers. Both fields are now covered in France by CIS-BIO International, which supplies the needed nuclides and EURISO-TOP to process the radio-pharmaceuticals.

### A-Radiotherapy.

The use of radiotherapy for the treatment of cancers includes various methods. Some of them are routinely used, some others are emerging. Table 2 records some gamma or beta emitting nucleides with their mean yearly consumption.

**Table 2**

**Radio-pharmaceuticals**

| Stable precursor | | Sr-88 | Re-185 | Sm-152 | P-31 | Y-89 | Er-168 |
|---|---|---|---|---|---|---|---|
| Radio isotopes | $^{131}I$ | $^{89}Sr$ | $^{186}Re$ | $^{153}Sm$ | $^{32}P$ | $^{90}Y$ | $^{169}Er$ |
| Half life | 8.02 d | 50.65 d | 3.77 d | 1.93 d | 14.32 d | 2.67 j | 9.40 d |
| Ci/year | 530 | 16 | 6 | 6 | 25 | 8 | 10 |
| Production reaction | Fission Pr | Reactor $^{88}Sr(n,\gamma)$ | Reactor $^{185}Re(n,\gamma)$ | Reactor $^{152}Sm(n,\gamma)$ | Reactor $^{31}P(n,\gamma)\ ^{32}S$ | Reactor $^{89}Y(n,\gamma)$ | Reactor $^{168}Er(n,\gamma)$ |

1. -*Teleradiotherapy* using the gamma rays of cobalt 60 is currently the most widely used technique, although it is now being supplanted by the use of electron accelerators.
2. -*Brachytherapy* is the treatment of tumours by inserting into it sealed sources, in the form of wires or seeds. Iridium 192 and caesium 137 are the most often used isotopes. A recent and important development is the use of seeds of palladium 103 and iodine 125 for the cancers of prostate.
3. -*Pain palliative treatments and synoviorthesis* uses mostly beta emitting radioisotopes, as indium 111, strontium 89, etc.
4. -*Metabolic therapy* uses systemic injection of radioactive sources radio-labelled to targeting radio-pharmaceuticals. It is an emerging technology which could completely modify the situation of cancer therapy in the future. It uses beta or alpha emitters.
5. -F*or deep brain tumours*: The alpha therapy also called **Boron Neutron Capture Therapy** »(BNCT) had been proposed in 1936 [5]. It developed slowly, essentially for brain tumours [6]. Still today, it requires much development in radiation physics (see for example [7]) as well as in boron biology. A research program of the European Union is conducted at the high flux reactor in Petten, Netherlands, in order to determine a «therapeutic window» for this technique. BNCT entails the selective loading of the tumour cells with a $^{10}B$ compound (in order to maximise the efficiency of the neutron flux, given that the amount of boron remains very low). Subsequent tissue irradiation with epithermal neutrons will provide $\alpha$ particles with the $^{10}B(n,\alpha)^{7}Li$ reaction. Then, $\alpha$ particles of 2,34 MeV are absorbed in a lesser than 10 $\mu m$ distance so that the tumour cells may be selectively destroyed. The best choice for the neutron beam flux at the patient-end surface seems to be about one billion $n/cm^2s$, neutrons with a spectrum ranging from 4 eV to 40 keV. Besides the therapeutic problems, some groups are studying miniaturisation of neutron sources; the way is to develop sub-critical neutrons assembly driven by a californium source [8].

On the other hand, cobalt 60 and caesium 137 are used in irradiators for blood poaches, to avoid immunological reactions of immuno-depressed patient after blood transfusion.

A variety of techniques have been described to provide a stent with an incorporated radioisotope, for local irradiation of coronary arteries, to prevent resthenosis after angioplasty for improving blood flow.

**B-Nuclear medical imaging.** Several tools are now indispensable in diagnostic imaging methods either for morphological study of organs or for kinetic biochemical investigations of the brain. Planar imaging, positron emission

tomography (PET) and single photon emission tomography (SPECT) need radioisotopes.

1. *For general imaging with a gamma camera*: the most used isotope is $^{99m}Tc$ [half-life = 6.01 h]. Traditionally produced from $^{99}Mo$ obtained by fission of highly enriched $^{235}U$ targets, it may also be produced by neutron capture of the stable $^{98}Mo$. The Kurchatov Institute in Russia has been successful in obtaining highly enriched molybdenum by **g**as **c**entrifugation (GC). The main producer of $^{99m}Tc$ is Nordion International, which operates in partnership with A.E.C of Canada. The CIS-BIO company supplies generators to about twenty nuclear medical centres in France.
2. *For SPECT imaging*: more than fifty radioisotopes are produced by means of medium energy cyclotrons. The most commonly used in the European Union centres (Saclay, Karlsruhe) are $^{67}Ga, ^{81m}Kr, ^{121}In, ^{123}I,$ *and* $^{201}Tl$. Table-3 summarises their properties. All stable precursors should be isotopically enriched.

**Table 3**
**Radioisotopes produced in low to medium energy cyclotrons [7].**

| Stable precursor | Need g/year | Radio-isotope | Organs | Important use |
|---|---|---|---|---|
| Mn-55 | 50 | Co-57 | | Calibration devices for camera |
| Zn-68 | 400 | Ga-67 | BONE | Tumour location(soft tissue), pain |
| Kr-82 | 0.3 litre | Kr81-m | LUNG | Lung function studies, breathing |
| Cd-112 | 100 | In-111 | KIDNEY | Monoclonal antibody infection imaging |
| Xe-124 | 1 litre | I-123 | THYROID | Thyroid studies |
| Tl-203 | 1600 | Tl-201 | HEART | Myocardial imaging |

| **Stable / Radioisotope** | | **Half-life** | **Decay-mode, (E, k eV)** | **Typical production reaction {E, MeV}** |
|---|---|---|---|---|
| Cr 52 | $^{52}Fe$ | 8.3 h | $\beta^+(511), EC$ | $^{52}Cr(^3He,3n)(30)$ |
| Fe 56 | $^{55}Co$ | 17.6 h | $\beta^+(511), EC$ | $^{56}Fe(p,2n)(28)$ |
| Mn 55 | $^{57}Co$ | 271 d | $EC(122)$ | $^{55}Mn(\alpha,2n)(24)$ |
| Cu 83 | $^{62}Zn/^{62}Cu$ | 9.1 h | EC/ $\beta^+(511)$ | $^{83}Cu(p,2n)(28)$ |
| Zn 68 | $^{67}Ga$ | 3.28 h | $EC(93)$ | $^{68}Zn(p,2n)(28)$ |
| As 75 | $^{75}Br$ | 1.63 h | $\beta^+(511)$ | $^{75}As(^3He,3n)(38)$ |
| Br 79 | $^{77}Br$ | 57 h | $EC(240)$ | $^{79}Br(^4He,2n)^{77}Kr \rightarrow (36)$ |
| Kr 82 | $^{81m}Kr$ | 13 s | $IT(190)$ | $^{82}Kr(p,2n)^{81}Rb \rightarrow (22)$ |
| Br 79 | $^{81}Rb$ | 4.58 h | $\beta^+(511)$ | $^{79}Br(^4He,2n)$ (20-28) |
| Cd 112 | $^{111}In$ | 2.82 d | $EC(173,247)$ | $^{112}Cd(p,2n)(22)$ |

| Stable / Radioisotope | Half-life | Decay-mode, (E, k eV) | Typical production reaction {E, MeV} |
|---|---|---|---|
| Xe 124 $^{123}I$ | 13.2h | $EC(159)$ | $^{124}Xe(p,2n)^{123}Xe \rightarrow (24)$ |
| Sb 121 $^{124}I$ | 4.2 d | $\beta^{+}(511)$ | $^{121}Sb(^{4}He,n)$ (10-38) |
| Au 197 $^{195m}Hg$ | 1.67 h | $EC, IT(200)$ | $^{197}Au(p,3n)$ (26-34) |
| Tl 203 $^{201}Tl$ | 3.04 d | $EC(167)$ | $^{203}Tl(p,3n)^{201}Pb \rightarrow ^{201}Tl(26)$ |
| Tl 203 $^{203}Pb$ | 2.17 d | $EC(279)$ | $^{203}Tl(d,2n)(12-15)$ |

3. *For PET imaging*: «baby cyclotrons» are housed in the medical centres for on site production of the five usual isotopes recorded in table 4. In oncology, the use of 2-(F-18)-fluoro-2-Deoxy-D-glucose or «2-FDG» appears as one of the most efficient techniques for the early detection of metastasis.

**Table 4**

**PET isotopes**

| Stable precursor | $^{11}B$ (p, n) or $^{14}N(p,\alpha)C^{11}$ | $^{13}C$ (p, n) | $^{15}N$ (p, n) | $^{18}O$ (p, n) | $^{78}Kr$ (p, 2n) $^{77}Rb$ |
|---|---|---|---|---|---|
| Radioisotope | $^{11}C$ | $^{13}N$ | $^{15}O$ | $^{18}F$ | $^{77}Br$ |
| Half-Live | 20.5mn | 10.1mn | 2.1mn | 1.87 h | 57h |

4. *Radioisotopes from high-energy particles accelerators* [10]. There were in 1994 about six high-energy accelerators worldwide engaged in isotope production in their lull time of particle physics research. Two were located in the US {Brookhaven Linac Isotope Producer (BLIP) and Los Alamos Physics Facility (LAMPF)}; TRIUMF is in Canada, Paul Scherrer Institute (PSI) in Switzerland, NAC in South Africa. It appears that several promising isotopes may be exclusively produced in this way: $^{22}Na, ^{47}Sc, ^{67}Cu, ^{82}Sr, ^{97}Ru, ^{117m}Sn, ^{127}Xe$ and also $^{188}Re, ^{227}Ac, ^{229}Th$. It has been shown that they can bind to monoclonal antibodies and they could bear a good potential for cancer therapies. The world-wide market may be of several hundred grams for each one.

Long term plan is debated in the U.S for a reliable domestic supply of high energy produced radioisotopes. A National Biomedical Tracer Facility has been outlined with a [100 MeV; 750μA] accelerator dedicated to year round isotope production. An alternate option is considered in the Neutron Spallation Source projects where an isotope production facility could be grafted on a multi-purpose protons accelerator while the main aims remains on waste transmutation, neutron, muon and material sciences [JAERI (Japan) and Oak Ridge projects ].

## III-NUCLEAR POWER SYSTEMS

- ***Deuterium and Tritium.*** Heavy water is the moderator and coolant for natural uranium PHWRs, mostly developed in Canada [under the name CANDU]. While the spreading out of this type of reactor has slackened down, the world-wide nuclear capacity of PHWR is expected to reach 30 GWe in 2010; about a third of this future capacity is now in construction in India and Argentina. The heavy water inventory in «CANDU» reactors is around 800 metric Ton with a yearly consumption of 8 T per GWe of installed power. A process based on an exchange $[H_2 / NH_3]$ was developed under the direction of E.Roth's [11] and used in an ammonia production plant located at Mazingarbe in France. This process is now used in Argentina (280 tons:year), India (40 tons/year) and China. The world's principal $D_2O$ production plants are located in Canada: five Ontario-Hydro's units with a $[H_2 / H_2S]$ Girdler-Sulfide process, each one with a capacity of 800 tons/year; they have been shut down in 1999. They would fulfil all of the world needs. However for an environmental tracer use of deuterium, a high degree of purity may be required: exchange-processes with heavy water stemming from the nuclear reactors may be unsuitable for those applications. The amount of $D_2O$ needed for the European countries is lesser than five T/year. Table 5 summarises the expected amounts.

**Table 5**

**Deuterium and Tritium**

| Isotope | 1 Reactor PHWR 1 GWe | 1 Reactor PWR 1 Gwe | Processing Plant-1500 tons heavy metal/year | 1 Fusion Pilot 50 MWth |
|---|---|---|---|---|
| Feed of Deuterium Gram/year | Feed: 8 T Heavy Water | | | 130 |
| Potential Tritium to manage (gram/year) | 130 | 0.06 | 100 | 210 |
| Comment on Tritium source | $D(n,\gamma)T$ parasitic capture in water | $^{10}B(n,\alpha)^{7}Li(n,n\alpha)T$ parasitic capture in water (cf. dissolved salt) | Fission-product in spent fuel | $^{6}Li(n,\alpha)T$ Lithium-6 film. |

- ***Detritiation units*** to remove tritium from heavy water are of major interest for treating the PHWR water circuits. No such a problem arises in PWR. For future applications to fusion and spallation sources, compact cryo-systems are needed: tritium and deuterium have to be recycled and must be purified before from helium and others impurities. A detritiation process was invented and patented by E.Roth at CEA [12] for the Laue-Langevin research reactor. Its capacity was about ten g/year. It has been later adopted in the Darlington plant. Tritium recovered in such quantities could be used for fusion reactors. Tritium

is also a source for helium-3, a rare isotope of helium, used both in dilution refrigerators and in nuclear magnetic resonance spectroscopy and imaging.

- ***Lithium.*** In PWR, lithium hydroxide LiOH is routinely dissolved in water in order to inhibit corrosion of steel vessels by boric acid used for reactivity control. Natural lithium contains 7,5 % of $^{6}Li$ whose absorption cross section amounts to 940 barns. In order to prevent the capture of thermal neutrons by this isotope, more than 99,99 % purity in $^{7}Li$ is necessary. The feed is 6 kg $^{7}Li$ /year for a 1 GWe reactor [13]. There are about 150 reactors in the European Union. Table 6 displays other potential needs for the next decades.

**Table 6**

**Lithium isotopes**

| Isotope | PWR/1GWe | Space generator | Waste transmutation | Tokamac or ICL |
|---|---|---|---|---|
| $^{7}Li$ | For 150 PWR in E.U 6 *150= 900 kg/y | Liquid Li-metal 50 kg of Li-7 | 8 $m^3$ FLIBE molten salt 2688 kg of Li-7 [ATW] | |
| $^{6}Li$ | | | | 10 $m^3$ FLIBE-loop 3360 kg of Li-6 |
| **USE** | LiOH buffer for 150 PWR (actual use) | Eutectic-alloy coolant for a compact 50 kWe reactor (possible use). | [LiF (65 mole %) with $BeF_2$ (29 %),$ZrF_4$ (5 %), $UF_4$ (1 %)] (possible use) | Breeding blanket by $^{6}Li[n,\alpha]T$ for a 1 Gwe reactor (possible use) |

- ***Boron.*** Natural boron is an interesting material because boron-10 is an excellent absorber of thermal neutrons and boron-11 an efficient scatterer of fast neutrons. The main use of natural boron nowadays is as boric acid dissolved in light water reactors. Sometimes, highly enriched $^{10}B$ control rod clusters are used in fast and BWR reactors. The mean consumption of *natural boron* for a standard one GWe PWR is 2 tons/year with 400 kg of $^{10}B$ included, without recycling. For the future, reactor-management goes towards extended burn-up cycles and towards MOX increased assemblies. This mode of operation will require the control of the moderator coefficient at the beginning of life and then optimisation of the core-wide radial power distribution. These requirements could be met with burnable absorbers in the fuel or alternatively with half of the control rods made of $HfB_2$ or $ZrB_2$ in which boron is enriched in $^{10}B$ at 90 %. Besides, in order to comply with core global draining and cooling accident criteria in cases where standard PWR would be operated with increased proportion of MOX nuclear fuel (larger than 50 %), the isotope enrichment of the soluble boron in $^{10}B$ could be required [14]. Assuming an efficient recycling of enriched boron, the plausible consumption for a 100 % MOX standard reactor could be less than 100 kg

$^{10}B$/year (rods and operating losses). Conversely, in fusion devices, highly enriched $^{11}B$ may be preferred for transparency properties of cladding or pushers materials. Moreover, in high temperature plasma around 100 keV as expected with confined micro-pellets, $^{11}B$ also could be a stellar fuel since the $^{11}B\left[H,2\ ^{4}He\right]^{4}He$ fusion reaction releases 8.68 MeV in the plasma.

Table 7 displays the potential needs for boron consumption.

**Table 7**

**Probable future needs for boron isotopes**

| ISOTOPE | Extended burn-up for 1 GWe LWR | 1-LWR with more than 50 % MOX 1 GWe | Fast Reactor (burner) 1 GWe | Medicine | Inertial Confinement Fusion |
|---|---|---|---|---|---|
| $^{10}B$ **kg/year** | Soluble boron with 40% $^{10}B$ ; **and** boron recycling, **P=100** | APWR control-rod (77*24) with 98% $^{10}B$ **P=100** | Control-rods with 98% $^{10}B$ **P=330** | BNCT 98% $^{10}B$ **P=0.1** | |
| $^{11}B$ **kg/year** | | | 98% $^{11}B$ in 133 diluent-pins **P=50** | $^{11}C$ product F=98% $^{11}B$ **100 gr./year** | Pusher or Fuel **P=10** |

- ***Lanthanide burnable poisons*** $^{155}Gd$, $^{157}Gd$, $^{167}Er$, $^{149}Sm$ **:** [15, 16]

  For easier control of BWRs, General-Electric and principal fuel suppliers have proposed for a long time natural gadolinium compounds as poisons. This option is now optimised for extended burn-up cycles and for MOX fuel control in PWR with two usable lanthanide's sesquioxides: $Gd_2O_3$ [BNFL, FRAGEMA…] and $Er_2O_3$ [ABB]. Poisons may be embedded with $Al_2O_3$ in about ten specific cells per assembly or may be homogeneously dispersed at 8-w % in the fuel. Hold down of reactivity at the beginning of a cycle can be adjusted by initial concentration of poisons while the kinetics of the capture chain must be optimised to give a low penalty to the residual reactivity at the end of the cycle. The dominating absorbers are $^{157}Gd$ and $^{155}Gd$. Flexibility can be increased with enrichment in $^{157}Gd$ or $^{167}Er$ isotopes, in UOX and MOX fuel, preferably. In the case of a spectrum of fast neutrons, $^{149}Sm$ could be a better poison than $^{157}Gd$. In all cases, the isotope separation costs should be compensated by extra gains on fissile fuel content (increased of 3-w % with enriched poisons in a standard PWR assembly) in order to extend the cycle length. Today, the indifference-cost (the overall economic balance) between the use of a natural or of an enriched gadolinium poison is at a very depressive low level [12$/kg] for a mean consumption of 15 kg $^{157}Gd$ /year, per one GWe reactor. Gas centrifuge still

is unsuitable for the lanthanide separation because no gaseous compound of lanthanides is available at low cost. Atomic vapour isotope separation (AVLIS) could be competitive; the plasma processes or cryptant extraction could be the outsiders. It must be emphasised that one valuable by-product of a nuclear LIS industry could be the extraction of the stable $^{152}Gd$ isotope, precursor of the radioactive [17] used in osteoporosis diagnosis.

- ***Miscellaneous*****:** $^{64}Zn$, $^{91}Zr$ *and isotopic clean up of the platinum group*

  ***Zinc****:* Cobalt 60 is a troublesome emitter to manage due to its high-energy $\gamma$ rays. Therefore, ways to inhibit the formation of this radioisotope as a corrosion product such as $Co_{0,5}Fe_{2,5}O_4$ in those parts of a nuclear reactor which are to be manoeuvred by personnel have long been sought in particular in Sweden and Germany [17]. In the case of BWRs, it was found that the addition of natural zinc to water would reduce the doses received by personnel when filters are removed. A zinc solution is used in the cooling circuits of the German PWR located at Biblis (unit B) [18]. However the $\gamma$ active $^{65}Zn$ isotope (half-life 243 days) will be formed by transmutation of the 48 % abundant stable $^{64}Zn$**.** Therefore the use of zinc depleted in Zn-64 is advantageous to minimise maintenance exposure. Cryptant isotopic extraction and plasma processes are well suited for a European need of 1,5 MT/year [19]. If zinc isotope separation were undertaken, a high valuable by-product would be the isotopic enrichment of $^{68}Zn$**,** from the natural abundance of 18.8 % to 98,5 % level. For $^{68}Zn$ is a precursor target [4] for the cyclotron production of the radioisotope $^{67}Ga$ $[T_{1/2} = 78{,}3\ h]$. The worldwide need amounts to 10 kg $^{68}Zn$ per year.

  ***Zirconium***: Zr alloys are widely used for fuel cladding in water reactors. The 11 % abundant $^{91}Zr$ is the main thermal neutron absorber in natural zirconium. If zirconium depleted in $^{91}Zr$ were used instead of natural zirconium, a significant reduction of the neutron absorption would occur and result in an improved neutron economy. In heavy water reactors where the reactivity margin is short (natural uranium), the isotope separation could be justified since the break-even cost is not too high. But with light water reactors, the advantage is almost questionable; for the elimination of the $^{91}Zr$ isotope would result in an increase of the neutron flux lesser than that due to an «over-enrichment» of 0,1 % in $^{235}U$ .

The *fission product* $^{93}Zr$ is always present in spent fuel. It would therefore be desirable to modify the shearing technique of nuclear fuel needles in order to separate at the outset the cladding hulls from the nuclear fuel itself in order to retrieve the hulls unscathed from the radioactivity of the nuclear fuel. If this were done, it would be most desirable to prevent the formation in the hulls of the

predominant long-lived *activation product* $^{93}Zr$ [h.l=1,5 E+6 years] by eliminating also its stable precursors $^{91}Zr$ and $^{92}Zr$. In other words, zirconium would mainly contain the $^{90}Zr$ isotope. The combination of these two actions would result in a simpler waste management of the cladding hulls and enable their reuse. So, the economic difficulty at the reprocessing plant would be to add an efficient decontamination process in order to clean the surface deposits on the depleted Zr cladding-hulls [transuranium traces, fission products, and tritium inclusions]. The laser processes (AVLIS) or the infra red dissociation of a metal complex molecule (Westinghouse patent), are well suited for Zr separations.

***Clean up of the platinum group metals in fission products:*** Industry commonly uses the high value metals palladium (Pd), ruthenium (Ru), and rhodium (Rh), extracted from South African ores. These rare metals are applied as catalysts for reforming petroleum products and for producing nitric oxide and glass fibres. They are also produced in nuclear reactors as fission products by kilogram quantities per cycle. Chemical processes or *electrolysis* [20] are now ready to extract them from high level wastes in the reprocessing plant, at a competing cost with natural ore-extraction. In order to recycle the noble metals, which must be composed principally of stable isotopes, the problem is to remove small amounts of very harmful radioisotopes like $^{106}Ru\,(h.l = 368\,d)$, $^{102}Rh\,(h.l = 2.9\,y)$ and $^{107}Pd\,(7.10^6\,y)$. The short half-life of $^{106}Ru\,(h.l = 368\,d)$ justifies a cooling time of only ten years. For the two other radioisotopes, AVLIS processes for nonzero nuclear spin isotopes such as the stable $^{103}Rh$ and the radioactive $^{107}Pd$ are usable at a cost estimated to 10 % of the final recovery.

## IV-OTHERS INDUSTRIAL OR RESEARCH APPLICATIONS [21]

***Chips memories and superconductors***. Germanium stable isotopes $^{70}Ge$ and $^{74}Ge$ are needed for transmutation into $^{71}Ga$ and $^{75}As$. They are used as dope in electronic devices. Ditto for Silicon $^{30}Si$. Lanthanide isotopes such as $^{155}Gd, ^{151}Eu, ^{169}Tm, ^{170}Yb$ are used for Mössbauer effect spectroscopy applied to the investigation of high temperature superconductors.

***Calcium in concrete, bones and cell proteins:***

Calcium has six stable isotopes. Among them, the heaviest, calcium-48 (natural abundance 0.18%) was needed in large quantities for the investigation of double beta disintegration. Only one isotope of the element has a non-zero spin, namely $^{43}Ca$ (natural abundance 0.145%). It is therefore the only isotope of calcium, which lends itself to nuclear magnetic resonance, and can serve as a local probe of

the chemical bonding of the element in a variety of materials. However, with a very low sensitivity and a line broadening which results from the quadrupolar moment associated with its spin of 7/2, $^{43}Ca$ NMR is difficult to detect and had required isotopically enriched samples. Calcium enriched in the 43 isotope with an abundance of the order of 40 to 60% is available in the United States and in Russia. The first $^{43}Ca$ NMR experiments were done with solutions [22]. The application of $^{43}Ca$ NMR to calciproteins would be of the greatest interest to biological research. However, experiments were far too lengthy (24 hours for a millimolar solution); these should be resumed on molecules isotopically enriched in $^{43}Ca$. Isotopic enrichment may be achieved by a plasma process [16]. For calcium compounds in solid phase, another difficulties arise, due to the so-called dipolar interactions between nuclear moments. The first observation of $^{43}Ca$ NMR pertained to high-Tc superconductors and was made in 1989 by a Russian team who took advantage from an batch of isotopically enriched calcium [23]. Experiments were later done on portlandite, a calcium carbonate and a sample of hydrated calcium silicate (in the latter, $^{43}Ca$ had an abundance of 40%) at Saclay by Ivan Klur [24]. Even though NMR of $^{43}Ca$ has recently been observed on solid samples at natural abundance [25], it is most likely that isotope enrichment will remain necessary for many interesting materials:

a) soils, the investigation of which is needed in order to understand the growth of plants
b) concrete, cement and clay, which play a crucial role in construction
c) biomaterials which contain calcium, such as bones and teeth. At stake is the understanding of mechanisms of calcium assimilation and elimination, as a function of diet and age.

The pace of progress in these investigations will therefore depend heavily on the availability of enriched $^{43}Ca$.

## Conclusion

The logic of resorting to stable isotopes is quite different in the various fields. Price plays a minor role in medical applications and a key role in the nuclear power industry. Although the market segments have very different features in such different fields, it is worth emphasising possible synergies associated with separation of different isotopes of the same element corresponding to completely different needs (e.g. nitrogen, zinc).

## REFERENCES

[1]-Etienne Roth – Critical evaluation of the use and analysis of stable isotopes, *Pure and Appl Chem*., Vol **69**, N°.8 (1997) 1753-1828
-Etienne Roth and René Létolle, Production and use of stable isotopes in France, pp. 252-257 in Synthesis and Applications of Isotopically Labelled Compounds; [E.Buncel and G.W.Kabalka, Editors] 1992 Elsevier Science Publisher B.V.

[2]-Alain Vanhove, Que peuvent apporter aujourd'hui les isotopes stables ? p. 357, Les isotopes stables. Applications-Production, INSTN à Saclay, 24 et 25 novembre 1993 [S. Goldstein, P. Louvet, E. Soulié]- Edition CEA.

[3]-Synthesis and Applications of isotopically labelled compounds 1994- Proceedings of the 5th International Symposium- June 20th-24th, 1994 - STRASBOURG. [J.Allen, R.Voges] J.Wiley&Sons Ltd, Chichester, England

[4]-Michel Bourdoiseau, Production d'isotopes radioactifs pour la médecine nucléaire, p. 203, Les isotopes stables. Applications-Production, INSTN à Saclay, 24 et 25 novembre 1993 [S. Goldstein, P. Louvet, E. Soulié]- Edition CEA.

[5]-G. L. Locher, Biological effects and therapeutic possibilities of neutrons, Am. J of Roentgenology, **36** (1936) 1

[6]- D. N. Slatkin, A history of boron neutron capture therapy of brain tumors: postulation of a brain radiation dose tolerance limit, Brain, **114** (1991) 1609
R. Gahbauer, N. Gupta, T. Blue, J. Goodman, R. Barth, J. Grecula, A.H. Soloway, W. Sauerwein, A. Wambersie, Boron neutron capture therapy: principles and potential, pp. 183-209 of « Fast Neutrons and High-LET Particles in cancer Therapy », eds. Rita Engenhart-Cabillic and André Wambersie, series « Recent Results in Cancer Research », Springer-Verlag, Berlin, Heidelberg, 1998.

[7]- Florence Colomb-Dolci, B.N.C.T. Etude spectrale d'un filtre à neutrons-DRN/DRE/ SIREN- Thèse de doctorat INSTN-17/12/1998. Rapport CEA-R-5832, 1999.

[8]-Do Heon Kim and Jong Kyung Kim, Conceptual design of a Californium based epithermal neutron beam for boron neutron capture therapy using a subcritical multiplying assembly; Nucl.Technol., **124** (1998) 175.

[9]-V. Bechtold, Isotope production with cyclotrons CERN 96-02-p329-4 March 1996.

[10]-Suresh C.Srivastava and Leonard F. Mausner: Production and Supply of Radio-isotopes with High Energy Particle Accelerators. Current Status and Future Directions. BNL-60141

[11]-Etienne Roth, Préparation de l'eau lourde sur un cycle d'échange monotherme ammoniac-hydrogène, brevet français n° 1.494.264 du 27.07.1966. This patent has been applied in three factories: Mazingarbe (France, 1967-1972), Baroda and Tuticorin (60-70 T/an), in operation in India. Another factory is currently under construction in Argentina for a production of 200 tons/year.

[12]-Etienne Roth, Traitement de l'eau lourde pour la purge du protonium et du tritium, brevet français n° 1.526.867 du 09.08.1966. This patent has been applied at the research reactor of Institut Max von Laue- Paul Langevin at Grenoble and at the Darlington nuclear plant in Canada.

[13]-Paul Desmoulins, Utilisation des isotopes stables dans les réacteurs de puissance, p. 117, Les isotopes stables. Applications-Production, INSTN à Saclay, 24 et 25 novembre 1993 [S. Goldstein, P. Louvet, E. Soulié]- Edition CEA.

[14]-André Puill, Sylvie Aniel-Buchheit, Full Mox Core for PWRs - International Conference on Future Nuclear Systems Challenge towards second nuclear era with advanced fuel cycles GLOBAL 97-, 5-10 october 1999 Yokohama, Japan. Proceedings, Vol. 1, pp. 274-280.

[15]-Marielle Asou, Jacques Porta, Quelques besoins en isotopes particuliers pour les réacteurs du futur, p. 125,Les isotopes stables. Applications-Production, INSTN à Saclay, 24 et 25 novembre 1993 [S. Goldstein, P. Louvet, E. Soulié]- Edition CEA.

[16]-Agnès Pailloux, Antoine Compant La Fontaine, Pierre Louvet- Separation of Gadolinium isotopes by the ion cyclotron resonance process; 6th workshop on separation phenomena in Liquid and Gases, NAGOYA (Oct 1998)- Society of Chemical Engineers and the Laser Society of Japan. Ed. Y. Yamamoto, University of Nagoya,Department of Nuclear Engineering, 1999. pp. 332-343

[17]-M.I. Mel'nik, E. A. Karelin, R. A. Kuznetsov, Methods for production, recovery and purification of gadolinium-153, Radiokhimiya, **37** n°2 (1995) 154-168; Radiochemistry, **37** n°2 (1995) 142-155

[18]-Christopher J. Wood, Radiation exposure: closing the gap with Europe, Power, august 1990, pp. 65-67

[19]-D. Nieder, U. Staudt, B. Stellwag – Zinc addition for radiation field reduction: status of and experience gathered in German PWRs, Actes du Colloque International Fontevraud IV contribution des expertises sur matériaux à la résolution des problèmes rencontrés dans les réacteurs à eau pressurisée, Volume 2, conférence organisée par la Société Française d'Energie Nucléaire, september 1998, pp. 973-988

[20]-Pierre Louvet, Antoine Compant La Fontaine, Michel Patris- Isotope separation of zinc by ion cyclotron resonance; 5th Workshop on Separation Phenomena in Liquids and Gases, 22-26 Sept 1996- Fos Do Iguacu-Brasil. Proceedings, ed. C. Schwab, CentroTecnico Aerospatial, Instituto de Estudos Avancados, Sao Jose do Campos (SP), Brasil, 1997. pp. 184-196

[21]-Masayuki Yoneya, Yukio Hanamoto, Kazuhiro Kawamura, Hiroshi Igarachi, Yoichi Miyamoto, Separation of palladium and ruthenium from simulated high-level liquid wastes by electrolysis – International Conference on Future Nuclear Systems Challenge towards second nuclear era with advanced fuel cycles GLOBAL 97, 5-10 october 1999 Yokohama, Japan. Proceedings-Vol 2-pp. 1501-1503.

[22]-René Létolle, André Mariotti, Thierry Bariac. Isotopes stables: Applications. / Laboratoire de Biogéochimie isotopique, Université ParisVI / ADIT, 2 rue Brûlée 67000 Strasbourg

[23]-K. J. Neurohr, T. Drakenberg, S. Forsén, NMR of newly accessible nuclei, volume 2, chapter 8: Magnesium 25 and calcium 43, editor Pierre Laszlo, Academic Press, New-York, 1983

[24]-A. Yu. Yakubovskii, V.I. Ozhogin, L. V. Shustov, V.P. Tarasov, V.I. Privalov, G.A. Kirakosjan, S.V. Verchovskii, Yu. I. Zhdanov, K.N. Michalev, B.A. Alelsashin, NMR of rare isotope $^{43}Ca$ in HTSC $Tl_2Ba_2CaCu_2O_8$, 25 ème Congrès Ampère sur la résonance magnétique et les phénomènes apparentés, Résumés étendus, edts. M. Mehring, J. U. von Schütz, H.C. Wolf, Springer-Verlag et Université de Stuttgart, 1990. p.292

[25]-Ivan Klur, Etude par RMN de la structure des silicates de calcium hydratés, thèse de doctorat de l'Université Paris 6, soutenue le 26 février 1996

[26]-R. Dupree, A.P. Howes, S. C. Kohn, Natural abundance solid state $^{43}Ca$ NMR, Chemical Physics Letters **276** (1997) 399-404

[27]-Agence de l'Energie Nucléaire, Usages bénéfiques et production d'isotopes, Paris, 1998. 63 p., ISBN 92-64-26953 -3

STUDIA UNIVERSITATIS BABEŞ-BOLYAI, PHYSICA, SPECIAL ISSUE, 2000

# LITHIUM ISOTOPE SEPARATION

**ILIE HODOR**

*National Institute for Research and Development of Isotopic and Molecular Technologies, 3400 Cluj-Napoca 5, Romania*

## 1. Introduction

In this paper, it is summarised the research made at INCDTIM concerning lithium isotope separation.

Natural lithium consists of two isotopes $^{6}Li$ (7.5 %) and $^{7}Li$ (92.5 %). Lithium isotopes have many uses but first of all they are important materials for nuclear fusion. Up to the present time, nuclear fusion was used only in weapons but it is believed that the fusion power reactors will become a reality in the first decades of the following century.

In weapons, lithium is used both as a means for storing deuterium (DLi contains more deuterium per unit volume as liquid $D_2$ does) and as an essential fusion fuel. Furthermore, the main way to produce tritium, a remarkable fusion partner, is the reaction $^{6}Li(n,\alpha)T$. The countries which have developed thermonuclear weapons, have developed technologies for the large scale $^{6}Li$ production. The separation technologies and production capacities are kept under secret.

In Romania, the domestic demand for lithium isotopes, used especially for research purposes, was of a few hundreds grams per year. This quantity was small but it could not be bought from foreign market because of embargo reasons. The decision was taken to achieve an installation capable to supply the domestic needs. In 1976, after a preliminary study, the isotopic exchange between Li-amalgam and aqueous LiOH was chosen as basic reaction for the separation process,

$$^{6}Li^{+} + {}^{7}Li(Hg) \leftrightarrow {}^{7}Li^{+} + {}^{6}Li(Hg) \quad (1)$$

The isotopic effect of this reaction at ambient temperature is $\varepsilon$=0.05 [1]. The multiplication of this effect by countercurrent exchange in a column has the advantage of simple refluxes but has the shortcoming that the side reaction (2) take place.

$$Li(Hg) + H_2O = Li^{+} + OH^{-} + \tfrac{1}{2} H_2 \quad (2)$$

Some years later it was disclosed that the same reaction (1) had been used in United States in Colex process for large scale $^{6}Li$ production [2]. This coincidence is very interesting and it is possible that some other countries had used the same reaction.

## 2. Separation unit

Every separation unit based on the reaction (1) should have the same main components: 1) separation column, 2) electrolyser, 3) column for amalgam decomposition, and 4) evaporator. The technological solution chosen for these components may be very different. It seems that for large-scale equipment some special packing columns were developed. In our case, the scale was small so that we used a spray column in which the aqueous LiOH moved up in an unpacked cylindrical tube and a fine spray of Li-amalgam fell down.

The separation unit is presented schematically in Figure 1. The isotope separation takes place in column 1, which is a simple vertical Pyrex glass tube. The amalgam dispersion is carried out in the electrolizer 2 by electrolysis of an aqueous LiOH and using mercury jet cathodes. At the bottom of the column 3, the amalgam and water are circulated countercurrently and the decomposition reaction (2) is catalyzed by austenitic stainless steel packing. The formed aqueous LiOH is introduced at the lower end of the exchange column. The mercury at the bottom of column 3 is replaced automatically with water, so that in the exchange column 1 the amalgam and the LiOH aqueous solution have the same flow rate. In column 1, the amalgam and electrolyte have the same Li concentration of 0.23 M to 0.5 M. An evaporator 4 maintains a high electrolyte concentration at the column top placed between 2 and 4.5 M, LiOH solubility in water being 4.8 M. The hydrogen formed by amalgam decomposition in 3 is removed automatically in such a way that the electrolyte flow through the column1 is little disturbed.

## 3. Mercury jet cathode and drop size distribution

The drop size distribution has a determinant role for the mass transfer, that is for the column efficiency. For a given amount of dispersed phase, the smaller the drops, the larger the interfacial area. On the other hand, the smaller the drop diameter, the smaller the drop fall velocity. There are many experimental and theoretical studies concerning the dispersion of a fluid phase into another one. Still, the amalgam spray is produced in such peculiar conditions that no appropriate data are available to permit the prediction of the drop size distribution.

In order to fulfill certain requirements for the considered spray column, several ways to produce mercury jets were tested. Finally, small orifices made in thin Plexiglas plates were used. As it is believed that the drop size has an important role in the process efficiency, we have studied experimentally the drop size distribution of lithium amalgam produced by mercury jet cathode [3].

The drop size distribution can depend on many geometrical and physicochemical parameters. To maintain the volume of the experimental work to an acceptable level, a limited domain of experimental parameters was taken into account. All experiments were done with a LiOH aqueous solution of 3 mol per

liter, and at a temperature of about 20 $^0$C. These values seemed to be suitable for practical purposes as the LiOH solubility in water is 4.8 mol/l, and the electrolysis is usually carried out at ambient temperature.

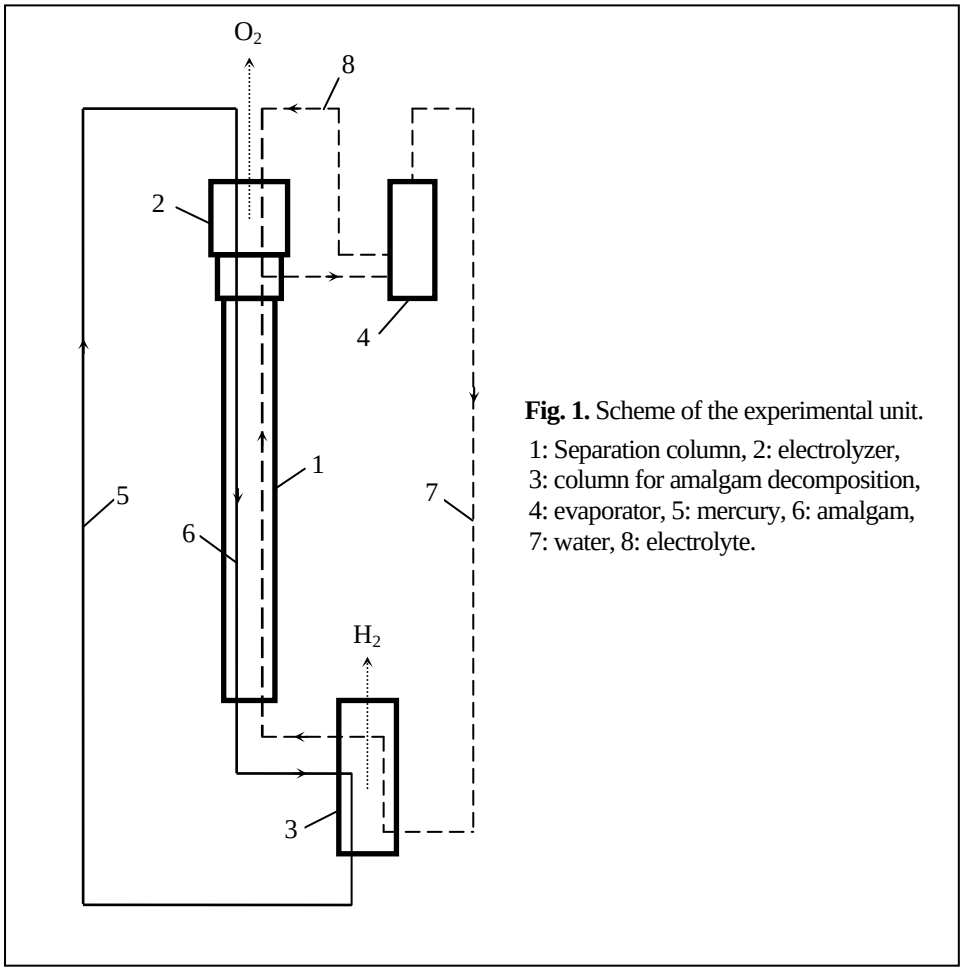


**Fig. 1.** Scheme of the experimental unit.
1: Separation column, 2: electrolyzer,
3: column for amalgam decomposition,
4: evaporator, 5: mercury, 6: amalgam,
7: water, 8: electrolyte.

Due to the conical form of the orifice, the diameter $\phi_m$ of the narrowest orifice end was the only geometrical parameter that has a determinant role in the jet hydrodynamics. We measured the mercury flow through orifices made in plates of thickness 0.1 to 0.3 mm and we found that the plate thickness had no influence upon the flow rate. At a given temperature, the diameter $\phi_m$ and the pressure drop through the orifice completely determined the mercury flow rate. The pressure drop was given by the hydrostatic pressure $p$ of the mercury that lay above the orifices.

For an isolated jet, the remaining parameters that could influence the drop size distribution are the diameter $\phi_m$, the pressure drop $p$, and the electrolysis voltage. The experiments were carried out with an orifice diameter varying from 28 to 70 μm, and with a pressure drop varying from 200 to 800 mmHg.

The voltage applied to the input wires of the electrolysis cell was 4.5 and 6 V. For an orifice with $\phi_m = 56.5$ μm, and in the experiment with three orifices, the measurements were also carried out for zero voltage.

For the electrolyses to occur, the applied voltage had to be larger than the reversible potential that is about 3 V. The voltage difference in excess of 3 V essentially represented ohmic losses in the electrolyte. As the surface of the thin mercury jet was small in comparison with the anode surface, the largest fraction of the ohmic losses was in the jet vicinity.

Lithium concentration in the amalgam depended on many parameters. For the experimental conditions mentioned above, at a voltage of 4.5 V, the lithium concentration in amalgam ranged between 0.23 and 0.45 mole/l. At a voltage of 6 V, the lithium concentration in amalgam was between 0.8 and 1.6 mole/l. The variation in that interval depended on the orifice diameter $\phi_m$, and on the mercury pressure $p$. Larger lithium concentration corresponded to smaller orifice diameter and to a lower mercury pressure.

Most experiments were done with isolated jets, that is with plates containing a single orifice. However, in a practical application [4] hundreds of orifices arranged in rows were used. Neighbouring jets could interact hydrodynamically between themselves and, on the other hand, around jets the symmetry of the electric field is disturbed. It follows that the number of jets and their spatial arrangement could influence the drop size distribution. For this reason two more plates were made and experimented. One plate contained two orifices having diameters $\phi_m$ of 58.1 and 59.8 μm, and the distance between the orifice centers of 0.5 mm. Another plate contained three orifices with centers placed in their corners of an equilateral triangle with sides of 1 mm, and orifice diameters $\phi_m$ of 60.2, 58.9 and 57.3 μm. When more then one jet was present, they screened one another reducing the access of the electrical field and lowering the Li concentration in the formed amalgam. For example at a voltage of 6 V and a pressure of 800 mmHg, Li-concentration was 0.79 mol/l for one orifice (diameter 59.3 μm), 0.61 mol/l for two orifices, and 0.44 mol/l for three orifices.

For drop size determination an optical method was developed [3]. A total of 51 distinct experiments were made. In the limits of experimental errors, the same drop size distribution was obtained for all experiments so that all results were put together, producing the general diagrams presented in Figure 2.

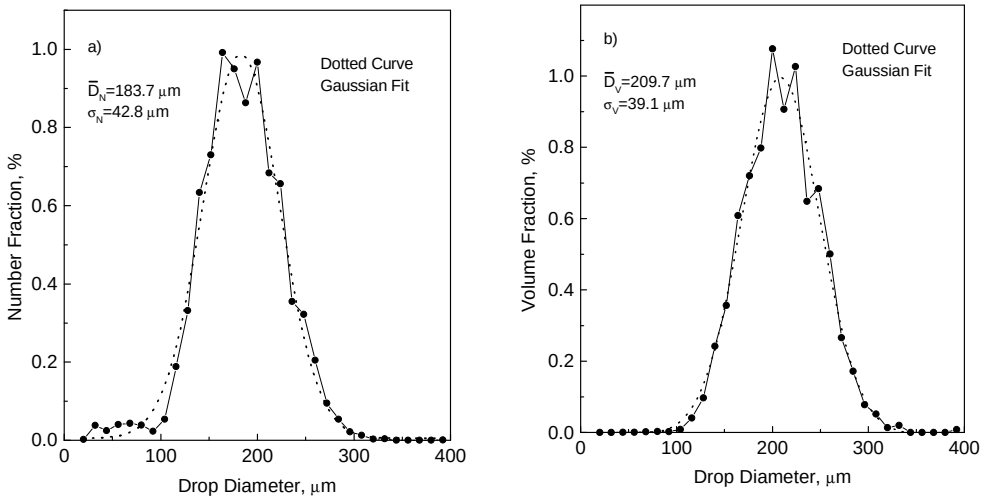


**Fig. 2.** General drop size distribution of all experiments.
The abscissa of an experimental point is the middle of an interval of 12 μm;
the ordinate cumulates the results from that interval.

The high preservation degree of the drop size distribution is a surprising result if one takes into account the large variation of the experimental parameters. The orifice diameter was increased more than two times; the pressure was increased four times. The independence of drop size distribution of the voltage is most curious. At zero voltage, the pure mercury jet was dispersed into droplets. At 6 volt, the jet was charged strongly at its surface with lithium, giving rise to a substance with different physico-chemical properties. In addition, over the usual surface tension, an electrostatic tension was superimposed.

It is noted that for small orifices, when the jet started with a diameter as small as 28 μm, the diameter of the mean drop volume was comparatively huge. The mean drop volume corresponds to a cylindrical jet segment having its height more then two hundred times longer than its diameter.

Some practical significance of the results is to be noted:

a) Varying the implied parameters in the experimented range can not modify the drop size distribution, given in Figure 7.

b) When orifices for a multiple jet cathode are made, it is not critical that the orifice diameters be made constant.

c) When a multiple jet cathode is operated, varying the mercury pressure above the orifices may modify the mercury flow rate, amalgam dispersion remaining unchanged. We have established empirically the following relationship for the mercury flow rate through an orifice

$$Q = 0.001253\,\phi_m^2\,\sqrt{p} - 0.1538\,\phi_m + 2.385 \tag{3}$$

where $Q$ is the mercury flow rate in ml/h, $p$ is the mercury pressure in cm Hg, and $\phi_m$ is the diameter of the narrowest orifice end in μm. Because of the interfacial forces, the mercury passes through an orifice only when pressure surpasses a positive threshold that depends on the orifice diameter and on the presence of the electrical field.

## 4. **Characteristics of the separation unit**

The separation unit has a series of important advantages:

a) favourable report between the velocities of reactions (1) and (2),
b) great separation power density,
c) small mercury inventory, and
d) small equilibration time.

The separation capacity of a column was 570 mol swu/year but we believe that a column with at lest 200 times greater capacity may be realised.

There are no published data regarding the plant capacity realised in other countries. Still, we can have an idea about that from the following information. A quantity of about 117 tone Hg was released in air and water at the lithium isotope separation plant at Oak Ridge, Tennessee, USA. The whole Hg quantity used in our separation unit was about 0.1 tone.

In the last time we have begun to consider some other separation processes based on Li complexation and on the combination of Li complexation with electromigration.

## REFERENCES

[1] A. A. Paklo, J. S. Drury and G. M. J. Begun, Chem. Phys. **64**, 1828 (1976).

[2] E. A. Symons, Sep. Sci. Technol. **20**, 633 (1985).

[3] I. Hodor, G. Mih¾ilescu, A. Chezan, and D. Radu, Chem. Eng. Comm. **177**, 231 (2000).

[4] I. Hodor, Proceedings of The International Symposium on Isotope Separation and Chemical Exchange Uranium Enrichment, Tokyo 1990, (Y. Fujii, T. Ishida, K. Takeuchi, eds., Bull. Res. Lab. for Nucl. Reactors, Tokyo Institute of technology, Tokyo, 1992), pp. 333-335.

STUDIA UNIVERSITATIS BABEŞ-BOLYAI, PHYSICA, SPECIAL ISSUE, 2000

# DETERMINĂRI SISTEMATICE DE TRITIU ŞI RADIOCARBON ÎN FACTORI DE MEDIU DIN ROMÂNIA

**AUGUSTIN TENU, FLORIN DAVIDESCU**

*Institutul Naţional de Meteorologie şi Hidrologie Bucureşti*

## 1. Introducere

Determinarea tritiului a început în actualul INMH în anul 1969 iar cea a carbonului-14 în anul 1977 fiind legate în principal de cercetarea hidrogeologică. În ambele cazuri, dezvoltarea acestor activităţi s-a făcut cu sprijinul AIEA sau în cadrul unor contracte încheiate cu acest organism.

Deşi AIEA împreună cu WMO au creat o reţea mondială de staţii pentru colectarea precipitaţiilor în vederea determinării izotopilor de mediu ($^{3}H$, D şi $^{18}O$), necesitatea de a se asigura cunoaşterea exactă a funcţiei de intrare în subteran a tritiului în România a condus la creierea unei reţele de 5 staţii care au funcţionat perioade de timp diferite. Prima dintre ele a fost instituită la Oradea în anul 1970; actualmente mai este în funcţiune numai staţia Bucureşti-Filaret.

România dispune aşadar de un şir practic neîntrerupt de măsurători ale concentraţiilor în tritiu în apele meteorice de 28 ani. Parţial ele au fost publicate ca atare (TENU et al., 1989) sau au stat la baza numeroaselor studii de hidrogeologie izotopică efectuate în ultimele trei decenii în ţara noastră.

În ceea ce priveşte radiocarbonul, măsurătorilor având iniţial scopul datării apelor subterane li s-au adăugat, din anul 1991 şi determinări efectuate pe $CO_2$-ul atmosferic.

Aceste determinări au început în România în cadrul unui Program naţional de cercetare privind "Schimbările climatice curente", iar din 1997 se derulează în cadrul unui Proiect de cercetare coordonat de AIEA privind gazele cu efect de seră.

Este cunoscut faptul că $CO_2$-ul, unul din componentele atmosferei, are un rol important în influenţarea balanţei eneregetice a Pământului. O mai bună cuantificare a $CO_2$-ului antropogen responsabil de aşa numitul "efect de seră" se poate obţine prin urmărirea variaţiei spaţiale şi temporale a izotopilor carbonului şi anume $^{14}C$ şi $^{13}C$.

Determinări neîntrerupte ale $^{14}C$ în $CO_2$-ul atmosferic există pentru staţia Bucureşti începând cu anul 1992; din anul 1995 s-a început probarea şi în zona Cernavodă pentru a se urmări eventualele modificări induse de intrarea în funcţiune a CNE în iulie 1996. Unele din rezultatele acestor măsurători au fost deja publicate (DAVIDESCU, 1996; TENU et DAVIDESCU, 1998).

În cele ce urmează ne vom referi aşadar la concentraţiile de tritiu din precipitaţii şi la cele de radiocarbon din $CO_2$-ul atmosferic.

## 2. Proceduri experimentale.

### 2.1. Probarea.

Probarea precipațiilor pentru determinările de ***tritiu*** s-a făcut în stații meteorologice care au fost dotate cu pluviometre construite astfel încât să se asigure, pe cât posibil şi în lunile cu precipitații reduse probe de peste 0,5 L. După colectarea tuturor precipitațiilor dintr-o lună într-un recipient etanş de sticlă, se prelevează o probă medie de 1 L care este adusă în laborator.

În ceea priveşte ***radiocarbonul***, extragerea $CO_2$-ului atmosferic necesar analizării s-a făcut pe cale chimică, prin tehnica absorbției statice în soluție NaOH 0,5N.

În timp de 14 zile, 1 L soluție diluată de NaOH expusă pe o suprafață de cca. 900 $cm^2$, permite formarea unei cantități de $Na_2CO_3$ suficientă pentru analizarea ambilor izotopi ai carbonului (cca. 4 gr. C).

Stocarea mai îndelungată a probelor în laborator se realizează printr-o tratare suplimentară în vederea încorporării carbonului într-o formă chimic stabilă. Pentru aceasta, soluției apoase conținând $Na_2CO_3$ şi $NaHCO_3$ i se adiționează o soluție saturată de $BaCl_2$, obținându-se un precipitat de $BaCO_3$ stocabil perioade îndelungate.

### 2.2. Preparare şi măsurare.

Deoarece conținuturile de ***tritiu*** din probele de apă naturală sunt în general foarte reduse, ca o etapă preliminră măsurării, laboratorul nostru a adoptat încă din 1969 tehnica îmbogățirii electrolitice fracționate monostadiale.

Plecând de la 200 c.c de apă şi asigurând o reducere volumetrică de 20 de ori se obține o îmbogățire în T de cca 13 ori.

Măsurarea activităților se face prin tehnica scintilației lichide utilizându-se în timp diverse aparate din gama Packard şi Beckman.

Limita de detecție maximă obținută prin acest mod de preparare-măsurare este de cca 2 TU, iar eroarea totală cumulată este cuprinsă în ecartul 5 - 10%.

Pentru determinarea ***radiocarbonului***, cea mai mare parte a cantității de $Na_2CO_3$ prelevat este transformat în benzen printr-o tehnică de laborator care presupune pe scurt următoarele etape succesive:

$$\mathbf{Na_2CO_3} \xrightarrow{H^+} \mathbf{CO_2} \xrightarrow{Li^+} \mathbf{Li_2C_2} \xrightarrow{H_2O} \mathbf{C_2H_2} \xrightarrow[600^0C]{\text{Perlcataliz}} \mathbf{C_6H_6}$$

Se obține de regulă un volum de 2-3 cc. care este măsurat prin tehnica scintilației lichide. Actualmente este folosit un aparat de măsură LS 5801 BECKMAN.

Precizia de determinare a valorilor $\Delta^{14}C$ poate fi estimată la $\pm$ 5‰.

### 2.3. Exprimarea rezultatelor.

Exprimarea rezultatelor de ***tritiu*** s-a făcut în unitatea special creată pentru acest radioizotop şi anume "unitatea tritiu - TU" care corespunde la o concentraţie de un atom de tritiu pentru $10^{18}$ atomi de hidrogen.

Conversia în activităţi corespunzătoare sistemului internaţional de unităţi, din ce în ce mai utilizat în ultimul timp, se poate face ştiind că 1 TU = 0,11983 Bq/L.

Rezultatele de ***radiocarbon*** sunt exprimate ca $\Delta^{14}C‰$:

$$\Delta^{14}C‰ = \delta^{14}C - (2\,\delta^{13}C + 50)\left(1 + \frac{\delta^{14}C}{1000}\right)$$

în care:

$$\delta^{14}C = \left[\frac{A^{*} - A^{0}}{A^{0}}\right] * 1000$$

cu următoarele notaţii:

A = semnifică activităţi în C-14;

* = desemnează proba;

° = desemnează standardul (adică activitatea carbonului modern de 13,56 dpm/gr carbon, dedusă din acidul oxalic NBS).

Notaţia $\Delta^{14}C‰$ include astfel atât compararea cu activitatea corectată a standardului de acid oxalic NBS cât şi "normalizarea" la acelaşi raport $^{13}C/^{12}C$ ($\delta^{13}C$ = -25 ‰); deoarece procedura noastră de probare nu este cantitativă, fiecare activitate $^{14}C$ exprimată ca $\delta^{14}C$ a fost corectată, în calculul formulei $\Delta^{14}C‰$, prin valoarea sa individuală $\delta^{13}C$.

## 3. Tritiul în apele meteorice.

Tritiul este produs şi introdus în atmosferă pe cale naturală şi artificială.

Calea naturală poate conferi precipitaţiilor conţinuturi de 5-20 T.U., situaţie întâlnită înainte de anul 1953.

Trebuie amintit faptul că ocurenţa tritiului şi căile sale de transfer din stratosferă în troposferă se face în funcţie de o serie de factori de natură geofizică, iar distribuţia sa la scară planetară este condiţionată de factori geografici şi meteoclimatici (TENU et al., 1971). Ca o consecinţă, aşa cum se poate vedea şi din Fig.1 care are ca subiect continentul european, distribuţia pe glob prezintă variaţii semnificative la un acelaşi moment de timp, iar cunoaşterea exactă pentru o regiune necesită determinări pe plan local.

Calea artificială de producere a tritiului se datoreşte exploziilor termonucleare începute în 1954 şi desfăşurate cu precădere în emisfera nordică. Ele au condus la creşterea treptată a conţinuturilor până la un maxim de cca 10.000 T.U. atins în primăvara anului 1963 în anumite puncte din America de Nord şi Europa. După

acordul de încetare a exploziilor termonucleare în atmosferă, tritiul artificial a început să descrească accentuat ca urmare a acțiunii combinate a dezintegrării şi spălării (TENU et al., 1989); explozii singulare efectuate după această dată de unele puteri nucleare s-au resimțit limitat, fiind de mai mică putere. Cele mai evidente situații sunt înregistrate în 1983 şi 1989.

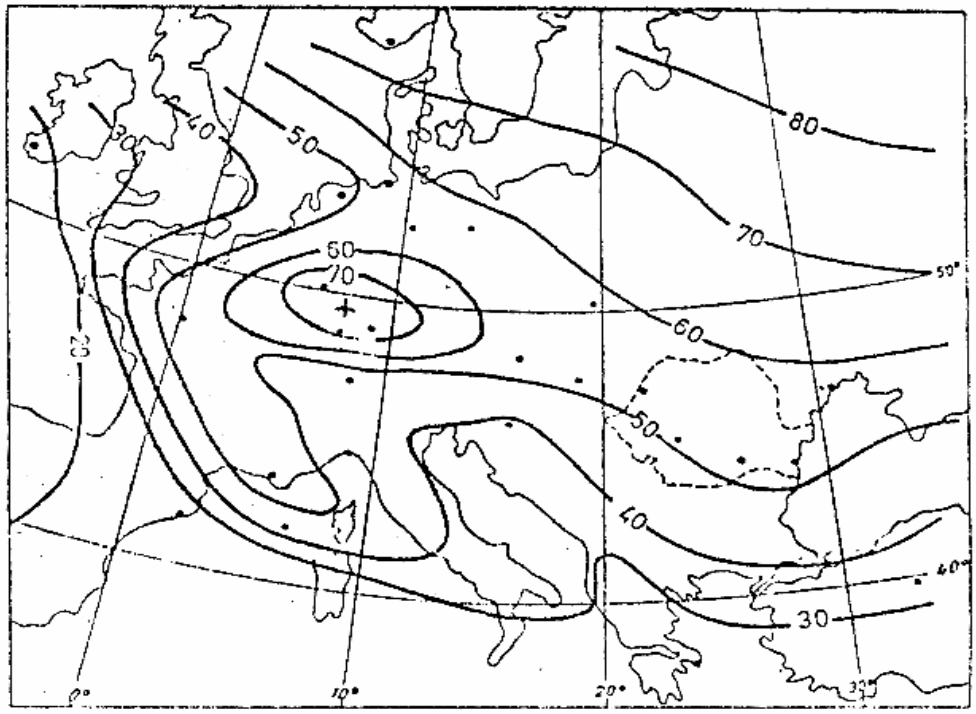


Fig.1 - Distribuția conținuturilor de tritiu în Europa, în anul 1979.

(după TENU et al., 1989).

In ultimul timp apare cu o pondere crescătoare tritiul artificial produs pe cale industrială şi în special în centralele nuclearo-electrice. In unele regiuni industrializate el este deja resimțit de peste două decenii, aşa cum se poate constata în Fig.1 pentru partea centrală a Europei Occidentale unde apare un maxim de concentrații dinainte de anul 1979.

Evoluția concentrațiilor de tritiu din emisfera nordică pe durata ultimilor 45 de ani, adică întregul interval de timp în care s-au efectuat determinări în apele meteorice, se poate vedea din Fig.2 în care am combinat rezultatele furnizate de patru stații şi anume: Ottawa (Canada), Viena (Austria), Oradea şi Bucureşti (România).

Valorile T.U. figurate reprezintă medii anuale ponderate, calculate conform relației:

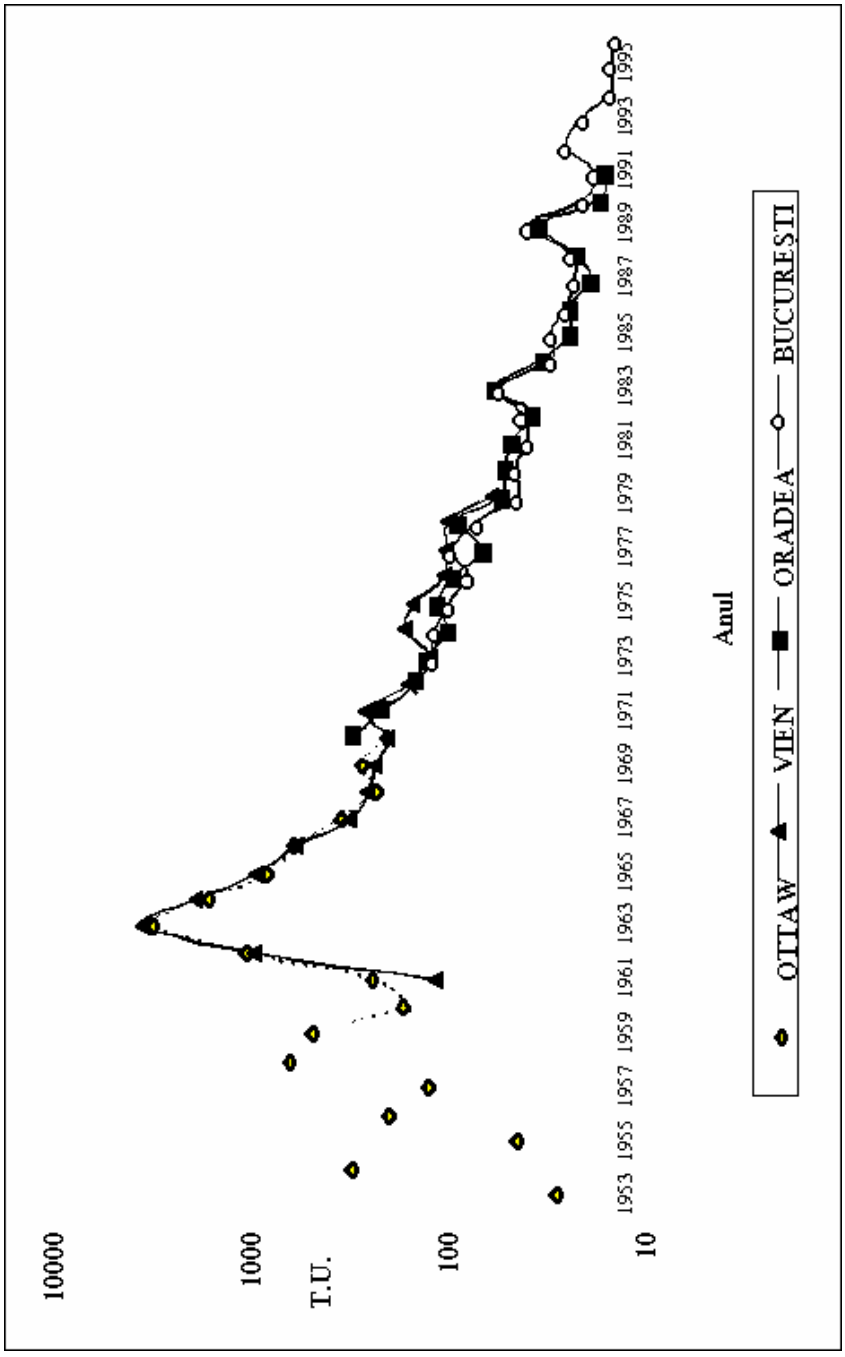


Fig.2. Nivelul şi evoluţia concentraţiilor medii anuale de tritiu (T.U.) în apele de precipitaţie din câteva staţii meteorologice din emisfera nordică.

$$Cw = \sum_{i=1}^{n} P_i * C_i / \sum_{i=1}^{n} P_i$$

în care $P_i$ şi $C_i$ reprezintă cantităţile lunare de precipitaţii şi respectiv concentraţia în tritiu a acestora.

Am adoptat această reprezentare pentru a facilita ilustrarea într-o singură imagine a unor aspecte ca:

- nivelul şi evoluţia multianuală a concentraţiilor de tritiu între cele două paliere de fond;
- succesiunea şi amploarea "inundaţiilor" de tritiu artificial termonuclear;
- gradul de corelare a unor valori medii anuale provenite din staţii situate în continente diferite, dar situate la latitudini aproximativ identice (Ottawa/Viena);
- influenţa factorului de continentalitate asupra rezultatelor din Europa Centrală (Viena/Oradea/Bucureşti);
- evaluarea factorului orografic prin compararea concentraţiilor din hinterland-ul şi vorland-ul carpatic (Oradea/Bucureşti) etc.

Aspectul unei diagrame ce redă variabilitatea lunară a tritiului este total diferit de cel din Fig.2. In Fig.3 am reprezentat concentraţiile lunare în patru staţii din România pentru diferite intervale de timp pentru a evita suprapunerea liniilor. Aspectul de "fierăstrău" al acestor linii face mai dificilă observarea tendinţelor şi legităţilor de variaţie deşi, calitativ, se poate constata o mai mare regularitate în cazul staţiilor Iaşi şi Constanţa comparativ cu staţiile Oradea şi Bucureşti.

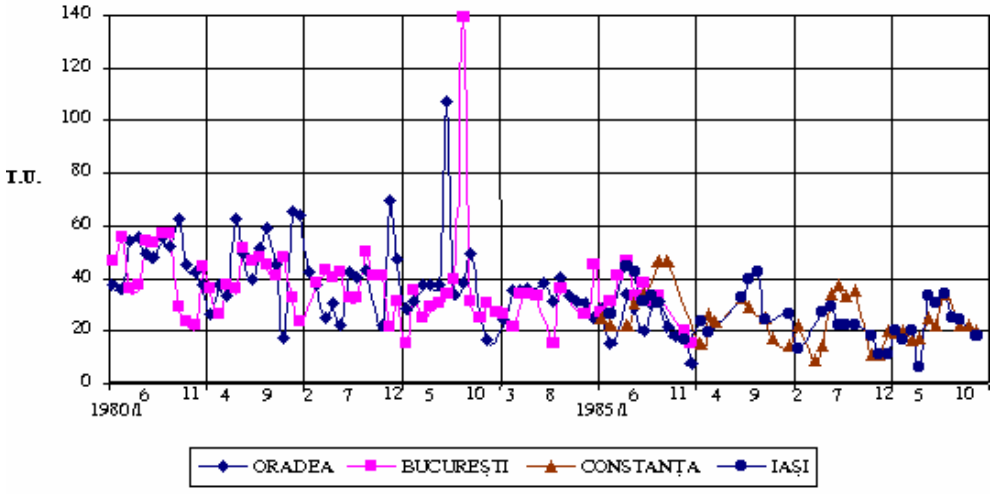


Fig.3 - Distribuţia concentraţiilor lunare de tritiu în precipitaţiile atmosferice colectate în staţiile: Oradea şi Bucureşti (intervalul 1980-1986 inclusiv); Constanţa şi Iaşi (intervalul 1985-1988 inclusiv).

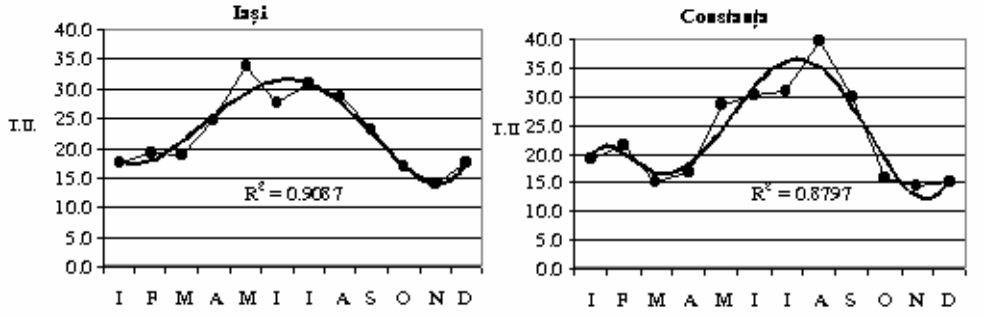


Fig.4 - Variația sezonieră a concentrațiilor medii lunare de tritiu, din intervalul 1985-1988 inclusiv, în Stațiile Iaşi şi Constanța

Analizând rezultatele de tritiu din aceste două stații pe perioada 1985-1989 prin calcularea mediilor lunare multianuale (Fig.4) este evidentă existența unei variații sezoniere, concretizată în valori crescute pe perioada de vară față de sezonul rece.

Curbele polinomiale de ordinul 6 prin care s-au aproximat distribuțiile pentru cele două stații indică existența unor minime diferențe atât în ceea ce priveşte luna de maxim cât şi valoarea lui $R^2$.

## 4. Radiocarbonul în $CO_2$-ul atmosferic.

Radiocarbonul poate fi produs, ca şi tritiul, pe cale naturală sau artificială.

Se admite că nivelul natural al radiocarbonului în atmosferă, existent înainte de 1953, avea valoarea $\Delta^{14}C = 0$ ‰.

Exploziile termonucleare au produs şi în cazul radiocarbonului un maxim ce a atins în anul 1963 valoarea de $\Delta^{14}C = 1000$‰; viteza de îndepărtare a sa din atmosferă este însă sensibil mai mică decât în cazul tritiului. Descreşterea conținutului de radiocarbon în atmosferă este consecința echilibrării $^{14}C$ provenit din testele nucleare cu cel din oceanele planetare şi din biosferă dar şi cu inputul datorit combustibililor fosili care aduc $CO_2$ fără $^{14}C$.

Este admis astăzi că activitatea actuală a $^{14}C$ atmosferic, indiferent de locul determinării, reprezintă un bilanț între activitatea naturală, activitățile antropice adiționale, diluția prin bioxid de carbon fosil, sursele locale de $^{12}CO_2$ şi schimbul dintre rezervoare. În acest context, factori importanți sunt şi latitudinea, altitudinea, distanța de ocean şi pattern-ul dinamicii regionale a atmosferei.

Seria de determinări de la Bucureşti are cel mai lung şir continuu de măsurători de acest gen din România (din februarie 1992 până în prezent) ceea ce permite integrarea lor într-un cadru regional şi discutarea evoluției globale a $^{14}C$. Stația Cernavodă a fost instituită în anul 1995 şi are o serie reprezentată de numai 38 valori lunare.

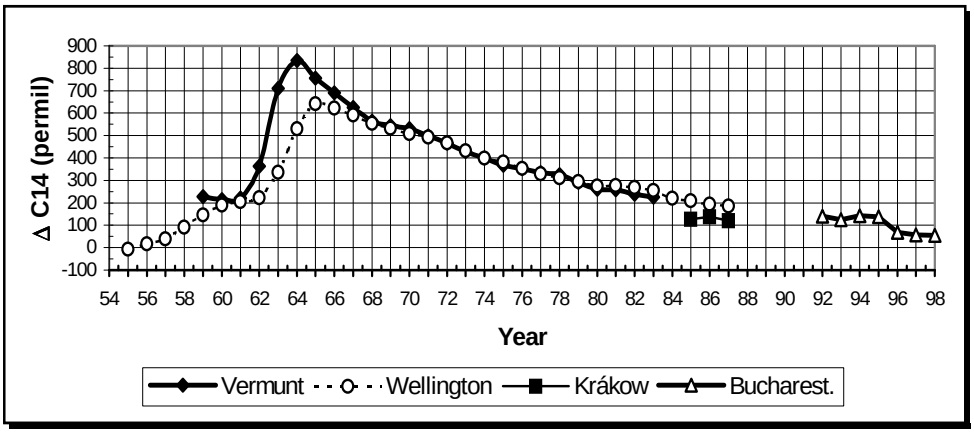


Fig. 5 - Variația în timp a $\Delta^{14}C$ (medii anuale) pentru unele date experimentale.

Ca medii anuale în intervalul 1992 - 1998, nivelul activității $^{14}C$ este situat la Bucureşti în ecartul 57 -142‰. Amplitudinea anuală a valorilor lunare $\Delta^{14}C$, calculate ca diferență între valorile maxime şi minime, este în general mare (frecvent între 100 şi 200 ‰ ) şi variază puternic de la un an la altul (247‰ în anul 1997 şi doar 74‰ în anul 1994

Pentru a evalua nivelul absolut al acestor rezultate la o scară globală, a fost întocmită diagrama prezentată în Fig. 5 în construcția căreia s-au folosit alături de datele proprii şi câteva serii experimentale publicate sub formă numerică.

Prin poziția lor în această diagramă rezultatele noastre din anii 1992-1995 sunt în continuitate şi în bună concordanță cu seriile Vermunt-Austria şi Wellington-Noua Zeelandă, dar sunt situate la acelaşi nivel absolut cu probele colectate în Polonia în intervalul 1985-1987 ($\Delta^{14}C \cong$ 120-140 ‰). Valorile medii pentru anii 1996 şi 1997 sunt mult mai scăzute, ca şi valoarea medie provizorie pentru anul 1998.

Amplitudinile mari şi ecartul larg de valori găsite la Bucureşti pot fi explicate, parțial cel puțin, prin poziția punctului de probare (în interiorul continentului) şi prin altitudinea sa redusă.

Pentru a evalua rezultatele noastre anuale ca tendință de evoluție am elaborat Fig.6 folosind nivelul activității de fond pentru $^{14}C$ în Europa, la scară multianuală.

″Europe clean air″ reprezintă o serie sintetică care poate fi considerată ca nivel reprezentativ background (neperturbat de combustibilii fosili) pentru $\Delta^{14}C$ la latitudinile medii ale emisferei nordice continentale, mai precis pentru Europa Centrală).

După cum se poate obseva, dreapta de tendință pentru ″Europe clean air″ în intervalul 1964-1992 poate fi aproximată bine printr-o ecuație de putere de tipul:

$$\mathbf{y = 6E + 11x^{-4,8937}} \qquad \mathbf{(R^2 = 0,998)}$$

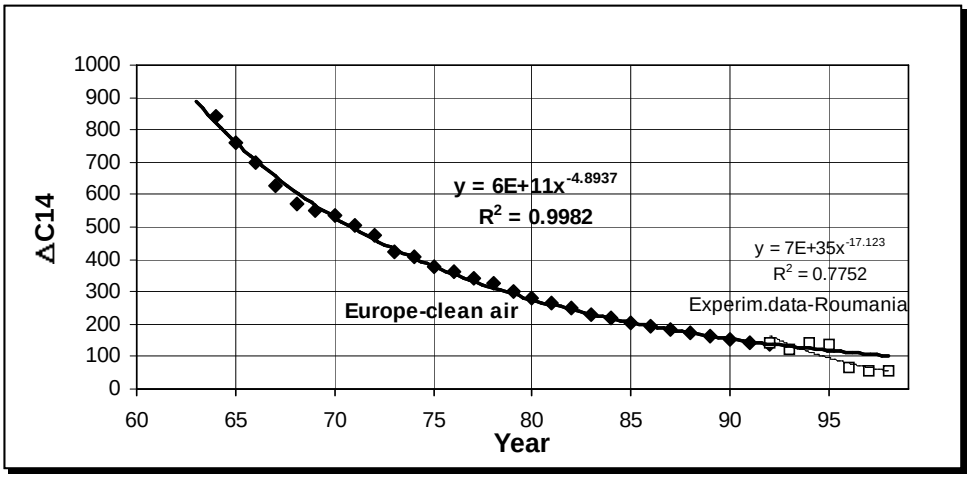


Fig.6 - Ecuația de putere a $\Delta^{14}C$ în Europa Centrală.

Folosind o ecuație exponențială, se poate deduce că activitatea $^{14}C$ se diminuează corespunzător unui $T^{1/2}$= 11 ani.

Datele experimentale de la stația Bucureşti se situează pe segmentul extrapolat al ecuației de putere pentru intervalul 1992-1995; valorile pentru anii 1996-1998 se situează însă cu mult sub cele în mod normal aşteptate.

## 5. Concluzii.

Ca urmare a acestei sumare prezentări de date experimentale privind ocurența în România a celor doi radioizotopi de mediu, se pot reține în principal următoarele:

**1.** Determinările de ***tritiu*** în apele meteorice, începute în anul 1970 şi continuate până astăzi într-un număr de 1-5 stații, au condus la cunoaşterea nivelului de concentrație local, a unor particularități privind distribuția lui teritorială şi au permis concluzii utile în ceea ce priveşte gradul de intercorelare cu alte stații de pe glob.

Ele au servit inițial cercetărilor privind circuitul apei în natură şi în principal celor hidrogeologice, dar se dovedesc astăzi extrem de utile şi aspectelor de mediu.

In ceea ce priveşte nivelul concentrațiilor, determinările au început în 1970 de la valori individuale de 500 - 600 T.U. (medii anuale ponderate de cca 300 T.U.) şi au ajuns astăzi la valori similare fondului. Această descreştere continuă, întreruptă de rare şi modeste creşteri artificiale, a avut o perioadă de "semi-diminuare" de 5-6 ani.

**2.** Determinările de ***radiocarbon*** în anhidrida carbonică din atmosferă au început, ca o activitate sistematică, din anul 1992.

Ele au contribuit la o mai bună cunoaştere a nivelului, variabilității şi tendinței de evoluție a $^{14}C$ în condițiile geografice şi de dinamică meteoclimatică specifice zonei de curbură carpatică.

Ele pot de asemeni contribui la discriminarea $CO_2$-ului antropogen şi la aprecierea cantitativă a acestui aport, fiind prin acesta utile în evaluarea efectului de seră.

**3.** Prin constituirea acestei "bănci de date" pentru ***ambii radioizotopi*** şi continuarea monitorizării, se poate decela cu promptitudine orice poluare artificială, chiar incipientă, manifestată prin alterarea conținuturilor situate în apropierea fondului natural. Astfel, în timp ce pentru tritiu standardul național de potabilitate admite un conținut în tritiu de 4000 Bq/L, adică $33*10^3$ T.U., determinările noastre permit decelarea unor variații de ordinul câtorva T.U.

Este motivul pentru care am instituit stația Cernavoda, cu determinări de $^3H$ şi $^{14}C$ în diferiți factori de mediu, măsurători începute dinainte de intrarea în funcțiune a CNE şi continuate lunar şi în prezent.

## BIBLIOGRAFIE

CONSTANTINESCU, T., TENU, A. (1971) - "Determinarea vârstei apelor subterane cu ajutorul tritiului". *Hidrotehnica*, Bucureşti, vol. 16, pp. 195 - 204.

DAVIDESCU,F., (1996) - "Determinări de radiocarbon în zona Cernavodă". *Mediul Înconjurător, vol. VII nr.4*, ICIM Bucureşti, pp.89-94.

TENU, A., DAVIDESCU, F., (1998) - "Carbon isotope composition of atmospheric $CO_2$ in Romania". *Isotope Techniques in the Study of Environmental Change*, IAEA - Vienna, pp. 19 - 26.

TENU, A., SLĂVESCU, A., DAVIDESCU, F., (1989) - "Level and evolution of the tritium concentrations in the natural waters of Romania". *Meteorol. and Hydrol. - Special Report*, INMH-Bucureşti, pp. 41-48.

*** * *** (1983) - "Environmental Isotope Data No.7: World Survey of Isotope Concentration in Precipitation (1976-1979)".*Technical Reports Series No.226*, IAEA, Vienna.

STUDIA UNIVERSITATIS BABEŞ-BOLYAI, PHYSICA, SPECIAL ISSUE, 2000

# THE RARE GAS ISOTOPES USED IN GEOPHYSICAL STUDIES FROM CERNA VALLEY

**C. COSMA*, D. RISTOIU***

***This work is dedicated to memory of Prof. Dr. Ioan Mastan at 10 years after he passed away (PIM 99/2000)***

**ABSTRACT.** In the Herculane Spa area (South –Western part of Romania) there is a long and deep fissure following the Cerna river canyon as well as many transversal fissures. The geothermal water sources (springs), always accompanied by large amounts of gases, are met where these fissures cross. The presence of granite rocks at the surface is another remarkable characteristic of this area. Between 1980-1986 a series of measurements were made, especially as regarding the helium concentrations in the gases emanated from these geothermal sources. Nitrogen and methane are the main components of emanated gases, and high helium and radon concentrations were also found. After 1990 year these studies were restarted especially regarding the radon concentrations in soil, waters and indoors. Between the fissure presence and radon exhalation rate a strong correlation was found. Also some data regarding the argon isotope composition are presented.

## Introduction

Herculane Spa (or the Bath of Hercules) is a well-known resort situated in Cerna Valley (South-Western part of Romania). The Cerna Valley is a deep and long canyon bordered by the Cerna mountains on the right and by Mehedinti Mountains on the left.

The geothermal waters from Herculane area, known since the period of the Roman Empire, have their origin in granite and sedimentary rocks (marl and limestone), the latter forming an impermeable roof for this hydrothermal deposit [1]. The waters of this deposit are permanently regenerated from three components [2]: a) uphill infiltration water from the Cerna Valley; b) deposit type waters; c) deep hot waters.

In the area of Herculane Spa, the Cerna corridor presents many transversal fissures. A big and deep fault also follows Cerna Valley. The geothermal sources can be located where these fissures cross. There are 24 sources, including 16 springs and 8 drillings, with a total water flow of 65000 l / 24 h.

Another remarkable fact is the surface presence of granite rocks at 2 km uphill from Herculane Spa. In the zone of the resort following Cerna watercourse sedimentary rocks progressively cover the granite rocks.

The most abundant components of emanated gases from the above mentioned sources [3-4] are nitrogen and methane, Table 1. Systematic studies of the chemical composition of the gases have also revealed considerable helium concentrations. There is another distinctive characteristic in the case of the Cerna Valley, related to their high radioactivity level (0.5 – 200 nCi/l NTP), which is generated by the presence of a granite massif in the area.

Many hypotheses were made regarding the origin of the gases in Cerna Valley. Because of their great radioactivity we advanced the idea of a radiogenic origin of helium and argon, but we did not definitely exclude the possibility of an inner origin for He and $N_2$ and even primordial for He. This fact is supported by the deep tectonic dislocations in this region [5].

**Table 1**.

Gas composition of emanated gases from Herculane area [3-4].

| **Place** | **Gas concentration ( % volume)** | | | | | | | |
|---|---|---|---|---|---|---|---|---|
| | $CH_4$ | $N_2$ | $C_2H_6$ | Ar | $O_2$ | $SH_2$ | $CO_2$ | $H_2$ |
| Ghizela (drilling) | - | 82.62 | - | 1.47 | 14.7 | - | 1.18 | - |
| Scorilo (drilling) | 2.87 | 95.12 | 0.16 | 1.73 | 0.12 | 0.04 | 0.07 | - |
| Sapte Calde | | | | | | | | |
| Dreapta (spring) | 1.77 | 96.28 | 0.04 | 1.66 | 0.16 | 0.01 | 0.05 | - |
| Neptun (drilling) | 60.47 | 35.41 | 0.81 | 0.57 | 0.02 | 0.41 | 0.30 | 1.72 |
| Dragalina (spring) | 67.61 | 28.75 | 0.57 | 0.31 | 0.05 | 0.61 | 0.11 | 1.85 |
| Decebal (drilling) | 70.88 | 25.54 | 0.84 | 0.47 | 0.04 | 0.15 | 0.08 | 1.98 |
| Sonda 5789 (drilling) | 64.77 | 32.13 | 0.60 | 0.36 | 0.02 | 0.01 | 0.02 | 1.68 |
| Traian (drilling) | 64.12 | 31.20 | 0.68 | 0.40 | 0.06 | 0.81 | 0.38 | 1.76 |
| Lime factory (drilling) | 59.51 | 37.06 | 0.69 | 0.60 | 0.15 | 0.03 | 0.66 | 1.43 |
| Coal Meh. mine | 12.01 | 8.05 | - | 0.17 | - | 0.14 | 79.63 | 0.31 |

## Experimental method

Gases emanated from mineral and geothermal water sources were collected using two special devices. Samples were gathered from the sources where the gas was always in excess, accompanying the water as gas bubbles. Helium and the main components of gases were measured with the Dempster mass spectrometer [6]. Argon isotopic composition was determined by means of an AMP-4 type mass spectrometer.

The small quantity of neon from these samples did not allow the determination the isotopic Ne ratios, because the contribution of $^{36}Ar^{++}$ to mass peak -20 ($^{20}Ne$) and the $CO_2^{++}$ contribution to mass peak -22 ($^{22}Ne$). For Ar the $H_2{}^{34}S$ contribution to mass peak -36 must be taken in account. This contribution was calculated by measuring the height (I) of mass peak 34 ($H_2{}^{32}S$). Also the presence of propane in the samples, evidently in mass peaks 41, 42, 43 and 44, requires a correction, which takes the fragmentation ratio $^{36}I/^{43}I = 0.01$ into account. An important contribution to mass peak 38 ($^{38}Ar$) is brought by propane $(^{38}I/^{43}I)_{propane} = 0.15$ and also by butane $(^{38}I/^{43}I)_{butane} = 0.02$.

The exhalation rate of the ground radon was measured through adsorption in activated charcoal (180g) from the 0.23 $m^2$ surface and for 12 h gathering time [7] The radon from water and emanated gases was measured in Marinelli geometry (0.5 l) using a large NaI (Tl) detector connected to a four – channel analyzer.

**Results and discussions**

Table 2 presents the results of Ar and Rn concentrations in emanated gases for nine of the main sources from Herculane and Mehadica areas. A high helium content was found, especially in Mehadica Valley, and a high radon concentration was detected, especially in the case of "Sapte Calde Dreapta" source. The high radioactivity of emanated gases may be explained through the presence of granite rocks at the surface, whereas helium can partially originate in the rocks from depth (even mantle).

**Table 2**.

Argon and radon concentration in emanated gasses.

| **Source** | | **Ar [%]** | **Rn [kBq.m$^{-3}$]** | **Main component [%]** |
|---|---|---|---|---|
| Sapte calde drapta | I | 1.66 | **6660** | $N_2$: 95.1 |
| Scorilo | O | 1.73 | 1110 | $N_2$: 96.3 |
| Neptun | N | 0.57 | 37 | $CH_4$ : 60 |
| Dragalina | M | 0.31 | 59 | $CH_4$ : 67 |
| Decebal | A | 0.47 | 16 | $CH_4$ : 71 |
| Sonda 4579 | S | 0.36 | 300 | $CH_4$ : 65 |
| Traian | T | 0.40 | 925 | $CH_4$ : 64 |
| Fabrica de var | A | 0.60 | 667 | $CH_4$ : 60 |
| Mehadica | N | 1.74 | 28 | $N_2$: 96 |

No correlation was observed between the helium content and the radon activity or the radon content. The presence of methane in the case of six sources in the Table 2 is probably related to the coal deposit of Mehadia, situated at about 10 km from the Herculane area.

To clarify the helium origin in these gases the ratio $^3He/^4He$ should be measured. The concentration of primary helium in gases can be found by the relation [8]:

$$C_p(He) = [(^3He/^4H4)_{meas} - (^3He/^4He)_{rad}] / (^3He/^4He)_p \quad (1)$$

where $(^3He/^4H4)_{rad} = 3\ 10^{-8}$ and $(^3H3/^4He)_p = 3\ 10^{-5}$.

Table 3 shows the results of radon exhalation for 1994 and 1995. The daytime values are generally smaller than night time ones and they are close to the average reference value (20mBq/$m^2$s), except Argus and Scorilo II, in which cases the higher values can be in direct connection with the transversal faults.

**Table 3**.

Radon exhalation rate in the Herculane Spa area.

| | Source | Radon flux values (mBq $m^{-2}$ $s^{-1}$) | | | | |
|---|---|---|---|---|---|---|
| | | Nov 1994 | | Mar 1995 | | Mean |
| | | Day | Night | Day | Night | value |
| 1 | Ghizela | 7.25 | 9.25 | - | - | 8.25 |
| 2 | Spate calde | 12.9 | - | - | - | 12.9 |
| 3 | Scorilo I | 32.6 | 38 | 28 | 26 | 31.15 |
| 4 | **Scorilo II** | - | - | 60 | 68 | **64** |
| 5 | Cascada | 18.1 | 24 | 21.3 | 26 | 22.35 |
| 6 | **Argus I** | 75.2 | - | - | - | **75.2** |
| 7 | **Argus II** | 156 | 190 | 193 | 240 | **194.82** |
| 8 | Pepa | 15.9 | 26.1 | 17 | 19.6 | 19.65 |
| 9 | Parc | - | - | 21 | - | 21 |
| 10 | Sirbu | 13.9 | 14 | 20 | 29 | 19.23 |

Table 4 presents the isotopic ratios for three sources from Cerna Valley and one source from Mehadica Valley. The high ratios $^4He/^{20}Ne$ prove the deep origin of these gases. The atmospheric ratio in the case of $^4He/^{20}Ne$ is 0.291. In the absence of radiogenic helium, the high ratio $^4He/^{20}Ne$ (higher than 400) is valuable information on the primary origin of helium. Such high ratios (150-500) were found in the case of geothermal gases from Japanese sources whereas the $^3He/^4He$ ratios for these Japanese sources were also much higher than the atmospheric ratio [9].

The $^4He/N_2$ ratios are almost identical for the Neptun, Mehadica and Abator sources ($1.2\ 10^{-2}$). In the case of "Sapte Calde Dreapta" this ratio is about between a half and a third of the ratios mentioned above.

**Table 4**.

Isotopic ratios for gases from Cerna and Mehadica Valleys

| Ratio | Neptun | Abator | S.C.D.* | Mehadica |
|---|---|---|---|---|
| $^4He/^{20}Ne$ | > 400 | > 400 | > 400 | > 400 |
| $(^4He/N_2).10^2$ | 1.25 | 1.09 | 0.45 | 1.15 |
| $^4He/^{40}Ar$ | 0.95 | 1.1 | 0.33 | 1.1 |
| $(^{40}Ar/N_2).10^2$ | 1.05 | 1 | 1.38 | 1.04 |
| $^{40}Ar/^{36}Ar$ | 333 | 344 | 301 | 280 |
| $^{38}Ar/^{36}Ar$ | 0.2 | - | 0.18 | 0.18 |

* Sapte Calde Dreapta

A similar behavior is shown by the ratio $^4He/^{40}Ar$, which in the case of "Sapte Calde Dreapta" is 1/3 of the ratio for the other water sources. The contribution of radiogenic argon must be considered for this source.

The $^{38}Ar/^{36}Ar$ ratios exhibit insignificant variations. The ratio $^{40}Ar/^{36}Ar$ varies rather considerably, being 280 in the Mehadica Valley, a smaller value than in the atmosphere. This resembles the situation of the gases in the Japanese volcanic sources, indicating a possible contribution of upper mantle argon with a lower isotopic ratio [10].

The ratio $^{40}Ar/^{36}Ar$ is higher than in atmosphere for the sources from Cerna Valley, similar to the gases in the Japanese geothermal sources, indicating the contribution of the radiogenic component. Differing from the Japanese sources, the ratio $^{4}He/^{40}Ar$ is five or six times higher.

## REFERENCES

1. A. Pricajan, S. Airinei, Hydrothermal riches from Romania, Bucuresti, Ed. Stiintifica si Enciclopedica, 1981
2. M. Visarion, A. Apostol, R. Stefanescu, St.Cerc.Geophys.12,135(1974)
3. I. Mastan, Helium in geothermal water sources Thesis, Cluj-Napoca, University Babes-Bolyai, 1987.
4. I. Mastan, C. Cosma, V. Znamirovshi, I. Pop, St. Cerc. Fiz., 33, 366, (1981)
5. M. Sandulescu, S. Veliciu, M. Visarion, A. Zamfir, General Tectonic Map of Romania, Bucuresti, 1976
6. I. Mastan, V. Znamirovschi, C. Cosma, St. Cercet. Fiz., 34,347(1982)
7. C. Cosma, D. Ristoiu, A. Poffijn, G. Meesen, Environ. International 22,383 (1996)
8. A.A.Aliev, A.I. Kabulova, Dokl.Acad.Nauk.Azerb., 36,52(1981)
9. K.Nagao, N.Takoka, O.Matsulabayashi, Earth Plan. Sci. Lett., 53, 175 (1981)
10. K. Nagao, Geochem. Journal, 14,139 (1980).

# SYNTHESIS OF $^{15}N$, $^{13}C$ LABELLED PURINES

**MARIA CHIRIAC, D. AXENTE, N. PALIBRODA**

*National Institute of Research & Development for Isotope and Molecular Technologies, 3400 Cluj-Napoca 5, P. O. Box 700, ROMANIA*

The heteronuclear NMR spectroscopy in the structural analysis of proteins and nucleic acids requires labelling with $^{15}N$ and $^{13}C$. These studies using oligonucleotides, specifically labelled with $^{15}N$ and $^{13}C$, may provide valuable informations regarding nucleic acid structure, drug binding and nucleic acid - protein interaction.

For this purpose, in the last years we prepared some purines labelled with $^{15}N$ and $^{13}C$ in different positions, which were requested by Institute Pasteur from Paris, where the labelled purines will be used in enzymatic syntheses of nucleotides - $^{15}N$,$^{13}C$.

This paper presents $^{15}N$ and $^{13}C$ labelling of the following purines:

1) [6 - $^{15}N$] ADENINE
2) [1,3,7 - $^{15}N$, 8 - $^{13}C$] XANTHYNE
3) [1,3,6,7 - $^{15}N$, 8 - $^{13}C$] ADENINE

**1) [6 - $^{15}N$] ADENINE** synthesis is presented in Scheme 1.

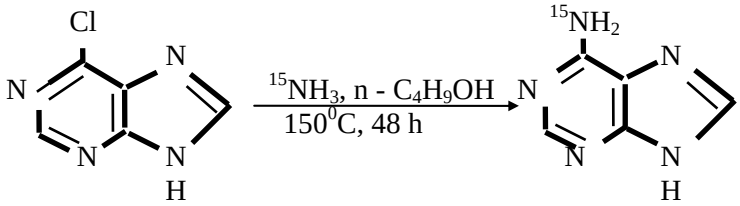


**Scheme 1**

A flask containing 1 l of $^{15}N$ enriched ammonia ( ~ 99 at. % $^{15}N$) was cooled to $-78^0C$, and 40 ml of 1-butanol was added. The resulting solution was heated with 2 g of 6-chloro-purine (a) in a sealed tube at $150^0C$ for 48 hours. Solvent was removed in vacuum, and the dark gray-green residue was taken up in 350 ml methanol and boiled with Dareo for 2 hr. Removal of solvent after filtration gave 1,5 g pure adenine - $^{15}N$ (b). Yield: 76% (based on $^{15}NH_3$) [1].

The structure and the purity of [6 - $^{15}N$] Adenine was confirmed using mass spectrometry and IR spectroscopy, and the isotopic label was determined by MS on the molecular compound.

**2) [1,3,7 - $^{15}$N, 8 - $^{13}$C] XANTHYNE** synthesis is presented in Scheme 2.

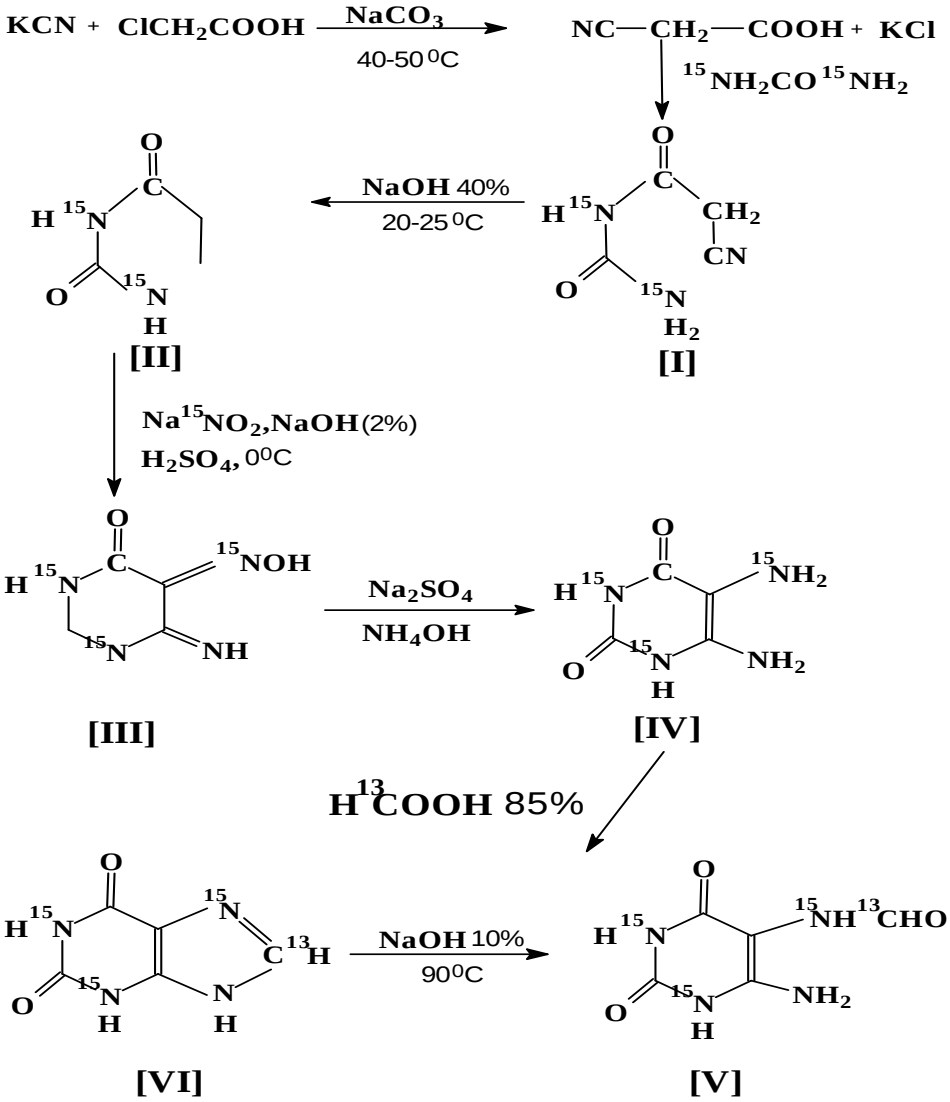


**[I] - cyanoacetylurea - [1, 3 - $^{15}N_2$]**
**[II] - Iminobarbituric - [1, 3 - $^{15}N_2$] acid**
**[III] - Iminovioluric - [1, 3 - $^{15}N_2$] acid**
**[IV] - 4,5 - diaminouracil [1, 3, 7 - $^{15}N_3$]**
**[V] - 4 - Amino, 5 - formylaminouracil - [1, 3, 7 - $^{15}N_3$, 8 - $^{14}$C]**
**[VI] - Xanthyne - [1, 3, 7 - $^{15}N_3$, 8 - $^{14}$C]**
**Scheme 2**

Chloroacetic acid (3.46 g) was dissolved in a minimum amount of water and neutralised by addition of anhydrous sodium carbonate. 1.97 g KCN in 10 ml water were added to the sodium chloroacetate solution and the temperature allowed to rise to $60^0$C. The reaction continued until the temperature ceased to rise, then the mixture was allowed to stand for twelve hours at room temperature. The resultant pale yellow solution was acidified and the excess of HCN, water and HCl were removed under reduced pressure at $50^0$C. The residue was taken up in absolute alcohol and the solvent removed.

A suspension of urea - $^{15}N_2$ (1.86 g) in freshly distilled acetic anhydride was added to the dried residue and was then added to the solution and upon cooling a crystalline solid was isolated, that proved to be cyanoacetylurea - 1,3 - $^{15}N_2$ (I), in 82% yield relative to urea. The melting point of the product is 211 - $2^0$C. [2].

The cyclisation of I to II was made with 40% NaOH solution. The mixture was stirred for 2.5 hours, keeping the temperature at 20-$25^0$C. Then the reaction mixture was neutralised with HCl 1:1 and allowed to stand for twelve hours in a refrigerator. The final product (2.72 g) II, was isolated by filtration. [3].

For the nitrosation compound II was dissolved in 2% NaOH solution and 2.18 g of sodium nitrite - $^{15}N$ was added. The mixture was cooled to $0^0$C and concentrated $H_2SO_4$ was added drop wise until the solution become dark violet.

After neutralization with ammonium solution the red precipitate obtained was isolated by filtration, yielding 3.23 g (84%). [4].

To the suspension of III in water were added 2.4 ml of 19% ammonium solution and 15.6 g sodium hydrosulfide. The mixture was heated to $55^0$C until the solution was decoloured entirely. After cooling, the product was filtrated and washed with water (the yield was 2.5 g of IV, 96%).

To the suspension of IV in 10 ml of water 1.5 ml of formic acid - $^{13}C$, 85% were added and the mixture was refluxed for 60 min. Then, the reaction mixture was allowed to stand for twelve hours at room temperature. The product was filtered, washed with water and dried at 60-$70^0$C, yielding 2.86 g of V (91%).

Compound V was suspended in 10 ml of water and 10% NaOH solution was added drop wise to pH = 9. Then, the reaction mixture was heated to $90^0$C and kept at this temperature until the solution become clear. After cooling to $0^0$C, the solution was neutralised with HCl 1:1 and allowed to stand for twelve hours in the refrigerator. Then, the product was filtered yielding 2 g of xanthyne (1,3,6,7 - $^{15}N_3$, 8 - $^{13}C$) (78%). [5].

### 3) [1,3,6,7 - $^{15}N_4$ , 8 - $^{13}C$] ADENINE

Because of the possibility to transform purines one into another, we prepared labelled adenine in the mentioned position, using [1,3,7 - $^{15}N$, 8 - $^{13}C$] xanthyne as starting material.

The steps of [1,3,6,7 - $^{15}N$, 8 - $^{13}C$] adenine synthesis, is presented on Scheme 3.

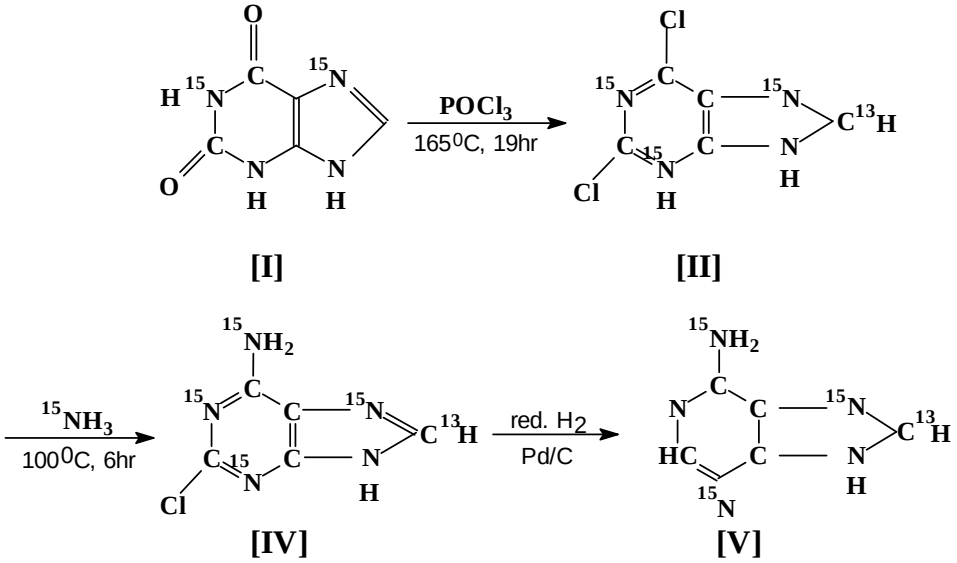


**[I] - [1,3,7 - $^{15}N$, 8 - $^{13}C$] Xanthyne**
**[II] - 2,6 - dichloropurine [1,3,7 - $^{15}N$, 8 - $^{13}C$]**
**[III] - 2-chloro, 6-aminopurine [1,3,6,7 - $^{15}N$, 8 - $^{13}C$]**
**[IV] - [1,3,6,7 - $^{15}N$, 8 - $^{13}C$] Adenine**
**Scheme 3**

For xanthyne chlorination to 2,6 - Dichloropurine, a mixture of [$^{15}N$, $^{13}C$] xanthyne and "pyrophosphoryl chloride" [6] are heated in a sealed glass tube at $165^0C$, for 19 hours. After cooling, the brown solution obtained was concentrate under reduced pressure, and then, form the sirupy residue the chlorinate purine was extracted with ether (yiled = 43%).

The amination of chloropurine was made by heating a mixture of 2,6 - Dichloropurine [$^{15}N$, $^{13}C$], with $^{15}NH_3$ in water, in a sealed glass tube at $100^0C$ for 6 hours (yield = 92%). [7].

The dechlorination of 2 - Cl - 6 - aminopurine is realised by catalytic hydrogenation on 5% Palladium - charcoal (at atmospheric pressure and $30^0C$) and [1,3,6,7 - $^{15}N$, 8 - $^{13}C$] adenine is obtained in 80% yield [8].

The structure of adenine - [$^{15}N$, $^{13}C$] synthesised by us, was confirmed by mass spectrometry and by NMR analysis [9].

The $^{15}N$ labelled compounds, $(^{15}NH_2)_2CO$, $Na^{15}NO_2$ and $^{15}NH_3$ used as starting material for the synthesis of labelled xanthyne and adenine, were obtained form $H^{15}NO_3$ 99 at. % $^{15}N$, produced at the National Institute of Research &

Development for Isotopic and Molecular Technologies, Cluj-Napoca, Romania. For the $^{13}C$ labelling of xanthyne, formic - $^{13}C$ acid 99 at. % $^{13}C$ from Sigma, was used.

## REFERENCES

[1] Leonard, Henderson, J. of the Amer. Chem. Soc., Vol. 97, p. 4990 (1975).

[2] J.W. Triplett, S.W. Moch, S.L. Smith, D. A. Digenis, J. of Lab. Comp., vol. XIV, No. 1, p. 35 (1978).

[3] D.I. Hmelevski, E.I. Abranova, Zhur. Obschei Khim., 28, p. 1970 (1958).

[4] H. Biltzu, W. Schmidt, Lieb. Ann., 431, p. 94 (1923).

[5] W. Traube, Chem. Ber., 34, p. 3035 (1900).

[6] G.B. Eliot, G. H. Hitchings, J. of Amer. Chem. Soc., Vol. 78, p. 3508 (1956).

[7] E. Fischer, A. Ach. Ber., 30, p. 2239 (1897).

[8] H. Bredereck, H. Herlinger, I. Graudums, Ber., 95, p. 54, (1962).

[9] Maria Chirac, D. Axente, N. Palibroda, J. of Lab. Comp. and Radiopharm., 42, 377-385, (1999).

STUDIA UNIVERSITATIS BABEŞ-BOLYAI, PHYSICA, SPECIAL ISSUE, 2000

# PROCEDEU SI INSTALATIE PENTRU PRODUCEREA APEI SARACITE IN DEUTERIU

**I. ŞTEFĂNESCU, GH. TIŢESCU**

*Institute of Cryogenics and Isotope Separation, P.O.Box 10, 1000-Rm.Valcea (Romania), e-mail: icsi@ns-icsi.icsi.ro*

Apa sărăcită în deuteriu este un produs biologic activ, cu numeroase posibilităţi de utilizare în agricultură, medicină şi alimentaţie. Calităţile sale sunt similare apei distilate, excepţie făcand concentraţia deuteriului care se situează sub concentraţia naturală de 144ppmD/(D+H).

Sunt cunoscute procedee de separare a unor structuri polimoleculare de apă conţinand şi apă biologic activă prin distilare simplă sau multiplă sau prin purificare chimică într-un lanţ de cascade de separare în care se realizează imbogăţirea şi separarea structurilor hidratate de structurile polimoleculare de apă, prin acţiunea concomitentă a unor campuri electromagnetice de 10…2500 V şi a unui camp ultrasonor de putere mică şi frecvenţă cuprinsă între 100 şi 1000 kHz care acţionează asupra campului propriu al moleculelor de apă, avand ca efect separarea a două fracţiuni de apă cu structuri moleculare diferite, una din ele avand proprietăţi biologic active. Aceste procedee nu reuşesc să realizeze o separare izotopică avansată, apa obţinută avand încă o concentraţie în deuteriu destul de ridicată. În plus, instalaţiile utilizate au o construcţie complexă şi necesită un consum energetic ridicat.

Procedeul şi instalaţia de producere a apei sărăcite în deuteriu brevetate de INC-DTCI-ICSI Rm. Valcea (Brevet nr. 112422 B1) permit obţinerea unei ape cu un conţinut de deuteriu foarte scăzut, situat în domeniul 2…80 ppm D/(D+H).

Acest procedeu constă în distilarea izotopică sub vid de 100 mm Hg a apei naturale sau a apei deşeu de la fabricarea apei grele, vidul folosit pentru evaporare asigurand şi alimentarea cu apă. Ca materie primă se poate utiliza apa potabilă, apa decarbonatată, condensul de apă demineralizată, apa distilată sau apa provenită de la fabricarea apei grele.

Instalaţia utilizată pentru obţinerea apei sărăcite în deuteriu este alcătuită dintr-o coloană (1) izolată termic, cu o înălţime de 15 m şi diametrul de 0,1 m echipată cu umplutură ordonată (2).

Coloana este dotată cu un colector de lichid (3) iar la bază este racordată la un fierbător pelicular (4) încălzit cu abur.

Fierbătorul pelicular (4) este racordat la un vas de alimentare cu nivel constant (5), pe traseu fiind prevăzute un rotametru (6), un robinet (7) şi un recuperator de căldură (8).

Colectorul (3) este conectat la un vas de colectare (9). Pe traseul ce conectează vasul de colectare şi colectorul coloanei sunt prevăzute un rotametru (10), recuperatorul de căldură (8) şi un robinet (11).

Coloana (1) are legătură la partea superioară cu o rampă de vid (15), pe traseu fiind amplasate în serie condensatoarele (12) şi (13) şi robinetul (14).

Condensatoarele (12) şi (13) sunt racordate la varful coloanei (10), pe traseu fiind prevăzut un rotametru (16), un schimbător de căldură încălzit cu abur (17) şi un alt traseu de legătură cu vasul de colectare a produsului (18).

Legătura între schimbătorul de căldură (17) şi vasul colector (18) este făcută prin intermediul rotametrului (19) şi al unui robinet (20).

Vasele de colectare (9) şi (18) sunt racordate la rampa de vid (15).

Întreaga instalaţie este confecţionată din oţel alimentar W1 4306.

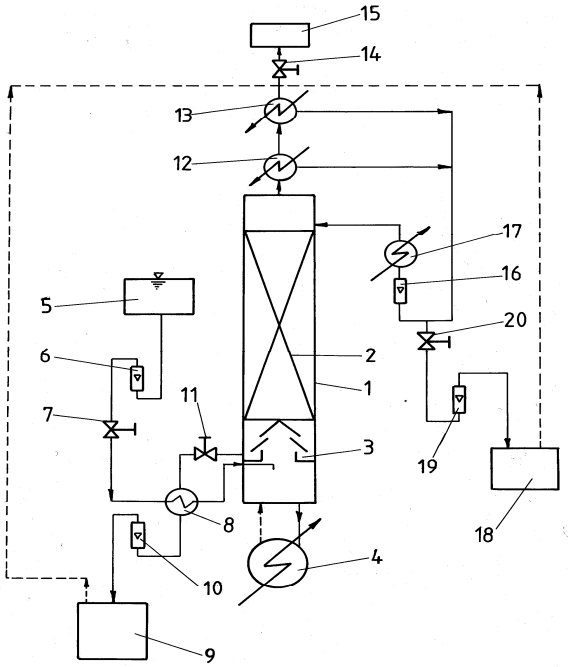


**Fig. 1.** Schema instalaţiei de producere a apei sărăcite în deuteriu

Aparatura de măsură şi control a temperaturii şi amplasarea acesteia este cea cunoscută pentru instalatiile clasice de distilare şi din acest motiv nu a fost figurată.

Umplutura ce echipează coloana de distilare este o umplutură ordonată confecţionată din plasă metalică, brevetată de INC-DTCI-ICSI Rm. Vâcea, brevet nr. 113543 B1.

Principalele caracteristici ale acestei umpluturi sunt următoarele:

| | | |
|---|---|---|
| Plasa | bronz fosforos tip $CuSn_8$ | |
| Compoziţie | Cu | 95,10% |
| | Sn | 4,23% |
| | P | 0,23% |
| Ţesătură | | 4 x 1 iţe |
| Nr. ochiuri | | 24 x 42 ochiuri/$cm^2$; |
| Dimensiune ochi | | 0,24 x 0,071 mm |
| Masa specifică | | 360 $kg/m^3$ |
| Suprafaţă contact | | 670 $m^2/m^3$ |
| Volum specific | | 0,048 $m^3/m^3$ |
| Fracţia de goluri | | 0,951 |
| Aria liberă | | 0,951 $m^2/m^2$ |

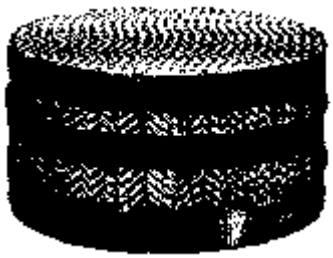

**Fig. 2.** Umplutură ordonată tip B7-INC-DTCI Rm.Vâlcea

Utilizarea acestui tip de umplutură determină o foarte bună amestecare şi omogenizare a fazelor pe orizontală şi o eficienţă de separare ridicată.

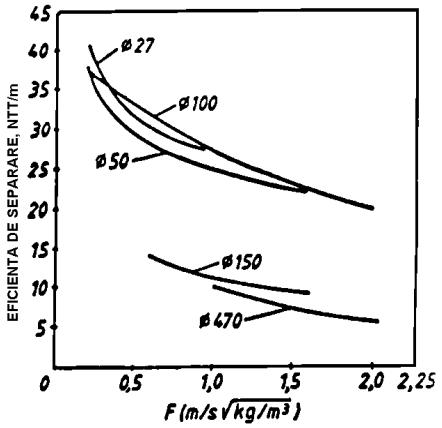


**Fig. 3.** Eficienßa (NTT/m) umpluturii B7 în funcţie de factorul de încărcare şi diametru (mm)

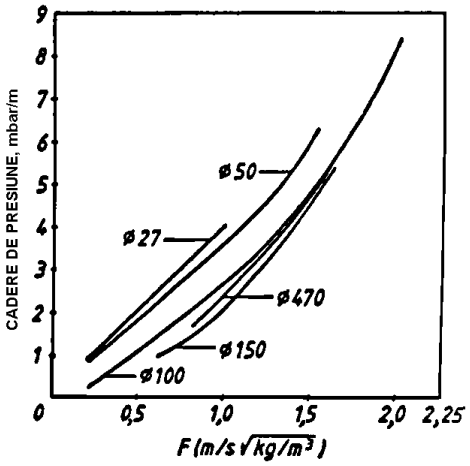


**Fig. 4.** Căderea de presiune(mbar/m) pentru umplutura B7 în funcţie de factorul de încărcare şi diametru(mm)

Prezentăm în continuare principiul de funcţionare a instalaţiei de producere a apei sărăcite în deuteriu.

După asigurarea condiţiilor de presiune de 100 mmHg, se alimentează fierbătorul pelicular cu un debit constant de apă naturală sau apă deşeu provenită de la fabricarea apei grele. Fierbătorul pelicular realizează evaporarea totală a debitului de alimentare.

Fluxul de vapori urmează un curs ascendent prin coloana de distilare şi ajunge în condensatoarele în care are loc transformarea în fază lichidă. Aceasta, după preîncălzire, se reintroduce în varful coloanei ca reflux, la o temperatură cat mai apropiată de cea din varful coloanei.

Fluxul de lichid descendent, datorită prezenţei umpluturii din coloană, are o suprafaţă foarte mare de contact cu vaporii. După ce străbate stratul de umplutură ajunge în partea inferioară a coloanei unde este acumulat ca reziduu în vasul de colectare, realizand totodată preîncălzirea apei de alimentare a instalaţiei.

În această situaţie, pe coloana de distilare se realizează un regim termic şi hidrodinamic stabil, determinat de valori constante ale gradientului de temperatură şi de stabilitatea debitelor.

Apa sărăcită în deuteriu se extrage cu un debit controlat astfel încat să aibă valori constante.

Procedeul şi instalaţia de producere a apei sărăcite în deuteriu prezentate asigură obţinerea unei ape cu concentraţie constantă situată în domeniul 2….80 ppm D/(D+H).

Caracteristicile calitative ale apei sărăcite în deuteriu sunt următoarele:

| | |
|---|---|
| Conținut deuteriu | 2 - 80 ppm D/(D+H) |
| pH | 6,5 - 7,5 |
| Conductivitate | max. 1,5 μS/cm |
| Consum $KMnO_4$ | max. 1,5 mg/l |
| $Cl^-$ | max. 0,1 mg/l |
| $SO_4^{2-}$ | max. 0,1 mg/l |
| $PO_4^{3-}$ | max. 0,1 mg/l |
| $Ca^{2+}$ | max. 0,1 mg/l |
| $Mg^{2+}$ | max. 0,1 mg/l |
| $Fe^{2+}$ | max. 0,1 mg/l |
| $Cu^{2+}$ | max. 0,1 mg/l |
| Examen bacteriologic | sterilă |

Procedeul şi instalația prezintă următoarele avantaje:

- asigură obținerea unui produs biologic activ cu utilizări multiple;
- instalația are un volum redus şi este lipsită de piese în mişcare, ceea ce-i conferă durabilitate;
- materia primă este ieftină şi foarte uşor de procurat;
- consumul energetic este redus.

Invenția a fost aplicată în cadrul INC-DTCI ICSI Rm. Valcea pe o instalație care include o coloană cu diametrul de 470 mm. Performanțele acestei instalații sunt prezentate în fig. 5.

| Concentraßie ppmD/(D+H) | Debit produs P,l/h | Reflux L,l/h |
|---|---|---|
| 80 | 18,21 | 220 |
| 70 | 16,69 | |
| 60 | 15,38 | |
| 50 | 14,22 | |
| 40 | 13,15 | |
| 30 | 12,1 | |
| 20 | 10,99 | |
| 15 | 10,35 | |

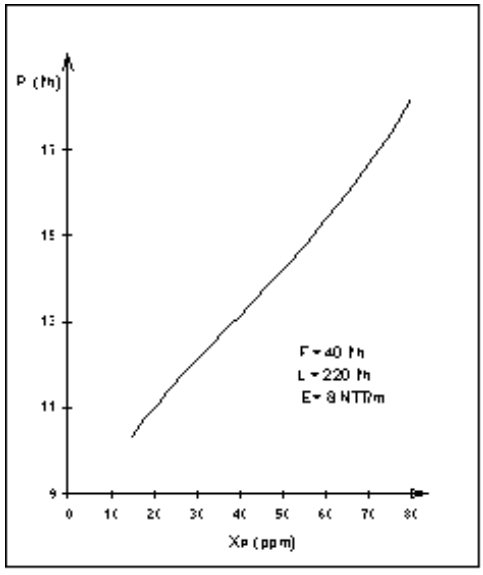


**Fig. 5.** Producția instalației de producere a apei sărăcite în deuteriu

În ceea ce priveşte utilizarea apei sărăcite în deuteriu, este cunoscut că după descoperirea deuteriului în apă, determinarea efectelor sale asupra organismelor vii a constituit o provocare pentru mulți oameni de știință. S-a observat că, în timp ce concentrațiile de deuteriu mai mici decat decat concentrația naturală144 ppm D/(D+H)) nu sunt toxice şi au efecte favorabile asupra organismelor vii, creşterea concentrației de deuteriu determină alterări structurale, metabolice şi funcționale de diferite grade.

Comparativ cu efectele biologice determinate de excesul deuteriului în apă, efectele reducerii concentrației deuteriului sub natural sunt mai puțin studiate. În acest sens, în ultimii ani, INC-DTCI-ICSI Rm. Valcea a inițiat colaborări cu institute specializate din țară şi din străinătate în vederea determinării efectelor biologice ale apei sărăcite în deuteriu.

Investigațiile realizate pană în prezent au condus la următoarele concluzii:

- animale tratate cu apă sărăcită în deuteriu au prezentat o creştere a rezistenței atat la doze subletale cat şi la doze letale de radiații gama, lucru ce sugerează o acțiune radioprotectivă a apei sărăcite în deuteriu;
- experimentele efectuate pe aminale de laborator cu inflamații cronice au demonstrat că înlocuirea apei de băut cu apă sărăcită în deuteriu produce o puternică stimulare a sistemului imunitar;
- apa sărăcită în deuteriu produce o creştere a tonusului bazal şi o potențare a efectelor substanțelor vasoconstrictoare;
- apa sărăcită în deuteriu ameliorează vizibil simptomele cauzate de diverse boli cutanate;
- apa sărăcită în deuteriu inhibă dezvoltarea celulelor canceroase şi poate duce chiar la dispariția tumorii;
- investigații privind reproducerea artificială a peştilor au relevat influența favorabilă a apei sărăcite în deuteriu, atat în stadii de dezvoltare embrionară cat şi în stadiile următoare de dezvoltare;
- apa sărăcită în deuteriu are o influență favorabilă asupra proceselor biologice din plante în diferite stadii ontogenetice.

Multitudinea efectelor benefice ale apei sărăcite în deuteriu asupra proceselor biologice sugerează că acest produs ar putea fi răspunsul la numeroase probleme nerezolvate pană în prezent. De mare interes este desigur posibilitatea utilizării apei sărăcite în deuteriu în profilaxia şi tratamentul diferitelor forme de cancer.

## BIBLIOGRAFIE

1. I. Ştefănescu, M. Peculea, Gh. Tițescu – Procedeu şi instalație pentru obținerea apei sărăcite în deuteriu, nr. brevet: 112422 RO
2. I. Ştefănescu, M. Peculea, Gh. Tițescu – Umplutură ordonată din plasă metalică, nr. brevet: 113543 RO.

3. Bild W., Stefanescu I., Haulica I., Lupusoru C., Titescu G., Iliescu - Research concerning the radioprotective and immunostimulating effects of deuterium-depleted water, Intern Symposium "Progresses in Cryogenics and Isotope Separation.", Calimanesti, 1998, Romania.
4. Haulica I., Peculea M., Stefanescu I., Titescu Gh., Todiras T., Bild W. - Effects of heavy and deuterium- depleted water on vascular reactivity, Romanian Journal of Physiology 1998, Volume 35, Issue 1-2.
5. Haulica I., Peculea M., Stefanescu I., Titescu Gh., Todiras T., Bild W. - Comparative study of heavy and deuterium-depleted water effects on vascular reactivity, XXXIII ICPS/IUPS, St.Petersburg, Russia, June 30- Iuly 5, 1997.
6. N.Maier, I. Stefanescu, Gh. Titescu - General Observation about the Possile use of the Deuterium Depleted Water in the Treatment of Some Skin Diseases, NR&DICIT Rm. Valcea, 1997.
7. Pricope F., Caraus I., Rujinschi R.I., Stefanescu I., Titescu Gh. - Deuterium-depleted water effects on reproduction of rainbow trout, MR&T Grant n$^o$ 3039GR/1997.
8. Titescu Gh., Stefanescu I., Pricope F., Caraus I. - Isotope composition for fecundated solutions, Patent n$^o$ 98-011296
9. Butnaru Gallia., Sarac I., Titescu Gh., Chirian C . - Deuterium-depleted water effect on AVENA SATIVA L.growth, Romanian Journal of Biological Sciences, 1997, 1, 5-6.
10. Butnaru Gallia - Organo-genesis in vitro on deuterium-depleted water environment, Experimental Report, 1998.
11. Somlyai G. & all - The Biological Effects of Deuterium-Depleted Water, a Possible New Tool in Cancer Therapy, J. of Oncol. 30, 4 (1998)
12. Somlyai G. & all – Pharmaceutical products for curing tumorous diseases and proceses for preparing same, HU 208084
13. Somlyai G. & all – Food products for preventing development of diseases and process for preparing same, HU 209787
14. Somlyai G. & all – Hygienic and cosmetic preparations for preventing and treating skin-diseases as well as a process for preparing same, P 9400833

STUDIA UNIVERSITATIS BABEŞ-BOLYAI, PHYSICA, SPECIAL ISSUE, 2000

# NUCLEAR MAGNETIC RESONANCE STUDY OF NAPROXEN AND IBUPROFEN INTERACTION WITH β - CD IN SOLUTION

**M. BOGDAN[1], S.I. FARCAS[1], M. BOJITA[2]**

[1] *National Research and Development Institute of Isotopic and Molecular Technologies, P.O.Box. 700, 3400 Cluj - Napoca, Romania*
[2] *Faculty of Pharmacy, University of Medicine and Pharmacy, 3400 Cluj - Napoca, Romania*

**ABSTRACT.** Inclusion of non - steroidal anti - inflammatory drugs (naproxen and ibuprofen), by β-cyclodextrin was investigated by proton NMR. The continuous variation technique was used to evidence the formation of soluble 1:1 complexes in aqueous solution. The effective association constants K, for each host / guest complex was calculated using a non- linear regression analysis.

**Key Words**: β - cyclodextrin, inclusion complexes, $^1$H - NMR, naproxen, ibuprofen.

## 1. Introduction

The non - steroidal anti - inflammatory drugs (NSAID) are one of the most commonly used class of drugs. However, at high-sustained dosages, most NSAID cause ulcerative side effects as gastric irritation and bleeding. Several approaches have been tested for preventing or reducing these side effects, including prodrug formation, microencapsulation and addition of neutralizing excipients [1]. One of the more recent methods tested is complexation of NSAID with cyclodextrins [2].

Cyclodextrins (CDs) are cyclic oligosaccharides containing six (αCD), seven (βCD) or eight (γCD) α - 1,4 - linked glucopyranose units with a hydrophylic hydroxyl group on their outer surface and a hydrophobic cavity in the center. The hydrophylic exterior of the CD molecules can make them water soluble, but the hydrophobic cavity provides an environment for appropriate sized non - polar molecules. In aqueous solution CDs are capable of forming inclusion complexes with many drugs by taking up a whole drug molecule or some part of it, into the cavity. These noncovalent complexes offer a variety of physicochemical advantages over uncomplexed drugs including increased water solubility and stability. In addition, CDs can be used to reduce or prevent gastrointestinal irritation, to eliminate unpleasant smells or tastes and to prevent drug - drug interaction. A complete characterisation of these complexes in terms of stoichiometry, stability and molecular conformation should contribute to a better understanding of the therapeutic properties. In this paper, we report a $^1$H NMR study of the complexes formed between naproxen, **1**, and ibuprofen, **2**, with β - cyclodextrin (β - CD),**3**, in aqueous medium. In particular a greater attention is paid to naproxen which is subjected to controversy with respect to its solubility limit in aqueous solution, its dissociation constant $K_a$, and the association constants, K, of the CD complexes with both the ionised and nonionised forms of the drug [4 - 9].

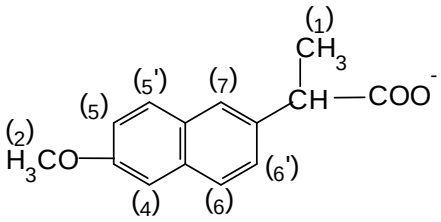

**1**

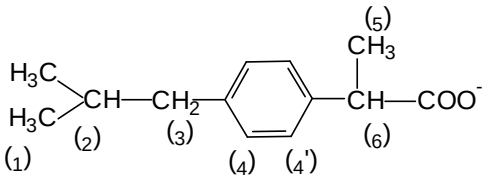

**2**

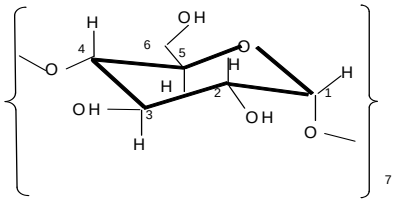

**3**

Analysis of our data by the continuous variation method confirm that the inclusion occurs and the complexes have 1:1 stoichiometry. The association constants for the 1:1 complexes were calculated by a non - linear least squares regression analysis of the observed changes the chemical shifts of the drugs and β - CD NMR lines as a functions of β - CD concentration.

## 2. Materials and Methods

β - cyclodextrin (β-CD) (water content 8 mol/mol), naproxen and ibuprofen sodium salts were purchased from Sigma Chemie GmbH (Germany) and $D_2O$ (deuterium content 99.7 %) from Institute for Cryogenics and Isotopic Separations (Rm. Vâlcea, Romania). Proton NMR experiments were performed at 300 MHz using a Varian Gemini spectrometer. The NMR spectra were recorded in $D_2O$ solution at room temperature and all chemical shifts were measured relative to external TMS. Typical conditions were 32 K data points, sweep width 4.5 KHz giving a digital resolution of 0.28 Hz/point. The pulse width was 4μs and the spectra were collected by co-addition of 32 or 64 scans.

## 3. Results and Discussion

3.1 *Determination of stoichiometry*

The formation of a complex involving one drug molecule and n β-CD, will be described by

$$G + nH \rightleftharpoons C \qquad (1)$$

where G, H and C are the drug, β-Cd and the $GH_n$ complex respectively for a 1:n stoichiometry. The association constant K is then :

$$K = \frac{[C]}{[G]\cdot[H]^n} \qquad (2)$$

where [G] and [H] are the concentrations of free drug and β - CD, respectively. In this study the stoichiometry was calculated by using the continuous variation method. This method is based on the difference in chemical shift, $\Delta\delta_{obs} = \delta_0 - \delta_{obs}$ between the free molecule ($\delta_0$) and the observed value ($\delta_{obs)}$ of that molecule in the presence of the other. Equimolar solutions of host and guest molecules were prepared and mixed to standard volume and proportions such that the total concentration remained constant $[G]_t + [H]_t = M$ and the ratio $r = [G]_t / M$ varied from 0 to 1.
In that case the free drug and β-CD species can be expressed as :

$$[G] = rM - [C] \tag{3}$$

$$[H] = M(1 - r) - n[C] \tag{4}$$

For a given value of r, [C] will reach a maximum value when d[C] / dr = 0. Based on eqs. (2), (3) and (4) we have :

$$\frac{d[G]}{dr} = M \tag{5}$$

$$\frac{d[H]}{dr} = -M \tag{6}$$

$$[H]\frac{d[G]}{dr} + n[G]\frac{d[H]}{dr} = 0 \tag{7}$$

These equations leads to single solution, namely the maximum complex concentration that is obtained for :

$$r = \frac{1}{1+n} \tag{8}$$

and does not depend on M or on the association constant [3].In the case of NMR, two situations may occur :
a) If the free and complexed forms of one component give rise to separated signals ( slow exchange), the ratio of the free and complexed forms can be measured directly by integration.
b) If only shifts of the spectral lines are observed due to fast averaging by the exchange between bound and free states, then, for a signal belonging to H for example, the quantity $\Delta\delta_{obs.}[H]_t$ will be proportional to [C]. As an example, the continuous plot of $\Delta\delta_{obs.}[H]_t$ against r for the most markedly affected protons of β-CD, in the presence of naproxen is presented in figure 1. The calculated quantities $\Delta\delta_{obs.}[G]_t$ with G = naproxen in the presence of β-CD are ploted against r in figure 2. The resulting continuous variation plots demonstrate that the β-CD- naproxen complex has 1:1 stoichiometry. The same result was obtained for ibuprofen.

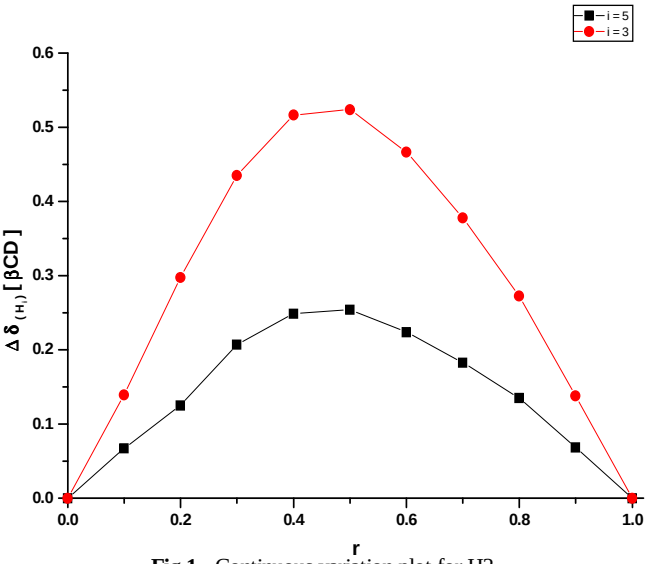


**Fig.1** - Continuous variation plot for H3 and H5 signals of the host (βCD).

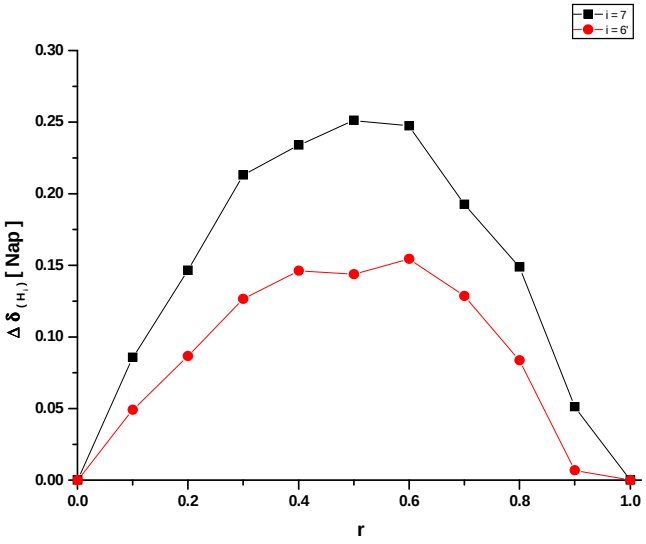


**Fig.2** - Continuous variation plot for H6' and H7 signals of the guest (naproxen)

*3.2 Determination of the association constant*

Various methods for the determination of the association constant have been described in the literature [10]. These are based on techniques such as conductometric titrations, potentiometric and spectroscopic methods, solubility studies.

The association constant K can be evaluated using NMR from the observed differences in chemical shift for drug or cyclodextrin molecules. Considering the tipical 1:1 equilibrium between G and H and expressing [H] and [G] in terms of the initial concentrations $[H]_t$ and $[G]_t$, the association constant can be written as

$$K = \frac{[C]}{\{[H]_t - [C]\}\{[G]_t - [C]\}} \tag{9}$$

The observed chemical shift difference, $\Delta\delta^{(X)}_{obs.} = \delta_X - \delta^{(X)}_{obs.}$, X being H or G, for the fast exchange inclusion equilibrium, is given by

$$\Delta\delta^{(X)}_{obs.} = \frac{[C]}{[X]_t}\,\Delta\delta^{(X)}_c \tag{10}$$

where $$\Delta\delta^{(X)}_c = \delta_X - \delta_c \tag{11}$$

Finally, substitution of eq. (10) into eq. (9) and solving for $\Delta\delta^{(x)}_{obs.}$ we obtain

$$\Delta\delta^{(x)}_{obs.} = \left\{ M + \frac{1}{K} - \left[ \left( M + \frac{1}{K} \right)^2 - 4[H]_t[G]_t \right]^{1/2} \right\} \frac{\Delta\delta^{(x)}_c}{2[X]} \tag{12}$$

Equation (12) involves no approximations and correlates the total concentrations of the guest and host molecules with the observed differences in chemical shift, $\Delta\delta^{(x)}_{obs.}$. We developed a computer program written in $C^{++}$ based on an interation procedure folowing specific algoritms in order to fit the experimental values of $\Delta\delta^{(x)}_{obs.}$ to the appropiate equation. The program is producing one single K value for the whole process and a set of calculated $\Delta\delta^{(x)}_c$ values. The program is quite flexible since both the guest and host can be observed for spectroscopic perturbations as a function of variable guest or host concentrations.

The obtained association constants and the relevant chemical shift differences $\Delta\delta_c$ (for a given proton) between the free β-CD, naproxen, ibuprofen and the pure complex are given in Table 1.

**Table 1**

Association constants, K ($M^{-1}$) and chemical shift differences (ppm) for Naproxen and Ibuprofen complexes with β - Cyclodextrin

| Complex / Proton | Naproxen - βCD K = 1619 | Ibuprofen - βCD K = 5714 |
|---|---|---|
| | β-CD | β-CD |
| $\Delta\delta_c$(H3) | 0.160 | 0.135 |
| $\Delta\delta_c$(H5) | 0.329 | 0.270 |
| $\Delta\delta_c$(H6) | 0.142 | 0.111 |
| | Naproxen | Ibuprofen |
| $\Delta\delta_c$(H4) | -0.054 | -0.163 |
| $\Delta\delta_c$(H5') | -0.053 | |
| $\Delta\delta_c$(H6') | 0.108 | |
| $\Delta\delta_c$(H7) | -0.177 | |

To summarize, it has been shown that NMR can be used to derive both the stoichiometry and the association constant of inclusion complexes. These experimental data can than be used to propose a molecular model of the inclusion complexes in solution.

## REFERENCES


1. T. Loftsson, J.J. Kaminski, N. Bodor, J.Pharm.Sci. **70,** 743 (1981).
2. K.D. Rainsfood, Drug Invest. **2 ,** 3 (1990).
3. Florence Djedaïni, S.Z. Lin, B. Perly and D. Wonessidjewe, J.Pharm.Sci. **79**, 643 (1987).
4. F. Melani, G.P. Bettinetti, P. Mura, A. Manderioli, J.Incl.Phenom. **22**, 131 (1995).
5. G.P. Bettinetti, P. Mura, A. Liguori, G. Bramanti, Il Farmaco **2**, 195 (1989).
6. G.P. Bettinetti, F. Melani, P. Mura, R. Monnanni, F. Giordano, J.Pharm.Sci. **80,** 1162 (1991).
7. S.E. Brown, J.H. Coates, C.J. Easton, S.F. Lincoln, Y. Luo, K.W. Stephens, Aust.J.Chem. **44**, 855 (1991).
8. F.J. Otero-Espinar, S. Anguiano-Igea, N. Garcia-Gonzales, J.L. Vila-Jato, J. Blanco-Mendez, Int.J.Pharm. **79**, 149 (1992).
9. I. Velaz, M. Sanchez, C. Martin, M.C. Martinez-Oharriz, A. Zornoza, Int.J.Pharm. **153** ,211 (1997).
10. W. Saenger, Angew.Chem.Int.Ed.Engl. **19**, 344 (1980).

STUDIA UNIVERSITATIS BABEŞ-BOLYAI, PHYSICA, SPECIAL ISSUE, 2000

# THE STRUCTURE OF THE FIRST SOLVATATION SPHERE IN TERNARY SOLUTIONS OF SOME CYCLOIMMONIUM YLIDS

**DANA ORTANSA DOROHOI**

*Al.I.Cuza University, Faculty of Physics,*
*Bd.Copou, nr.11, 6600 Ia¿i, Romania*

**ABSTRACT.** The average statistic weights in the first solvatation sphere of some cycloimmonium ylid ternary solutions were estimated on the basis of liquid cell model.

**Keywords**: pyridinium-, benzo-[f]-quinolinium- and pyridazinium- anilido-benzoyl methylids

## 1. INTRODUCTION

Cycloimmonium ylids are amphionic compounds [1,2] with an intramolecular charge transfer (ICT) electronic band in the visible range. This band is very sensitive to the solvent nature [3,4].

Van der Waals interactions in nonprotic solvents and specific proton donor-acceptor in the protic ones supplementary occur in the solutions of cycloimmonium ylids [5,6]. In the solvent mixture, the protic molecule compete to occupy the neighbourhood of the cycloimmonium ylid molecules.

## 2. THEORETICAL NOTIONS

Let’s consider the cell Takehiro Abe model [7] for a simple liquid, in which the central molecule is surrounded by concentric spheres, named solvatation spheres, full of fixed molecules. On the basis of this model it may be stated that the ratio of the interaction energies between the central molecule- cycloimmonium ylid molecule- and the first three solvatation spheres is 1:16:84. So, one can consider that solvatation energy of the spectrally active molecule is almost equal with the interaction energy between this molecule and its first solvatation sphere.

Let’s analyse now a ternary solution obtained by a cycloimmonium ylid - as spectral active molecule – in a two solvents mixture; ylid + solvent "1" + sovent "2".

The molecules of the solvent "1’ are protic and those of the solvent "2" are aprotic ones. Because the two solvents are spectrally inactive in the visible range,

their molecules remain in the ground state when the electronic absorption spectra of the ylid are recorded.

The ylid concentration in the ternary solution is very low ($10^{-4}$-$10^{-3}$ mol/L). That's why this solution may be devided in subsystems containing a spectrally active molecule and the solvent molecules surrounding it. The extinction in the electronic absorption spectra is proportional with the number of these subsystems [8]. Having in view the ratio of the intermolecular interaction energies between the ylid molecule and the solvatation spheres, one can extract only the first solvatation sphere from one subsystem.

The molecule number N in the first sphere is constant, but the numbers $N_1$ and $N_2$ of "1" or "2" type molecule are variable, satisfaying the relation:

$$N_1 + N_2 = N \tag{1}$$

The $N_1$ and $N_2$ modification is possible because in liquid, the energy of termic motion is of the same size with the energy of intermolecular interaction. In these conditions, the spectral shifts, measured in ternary solution related to gaseous state of the ylid, must depend on the average value of numbers $N_1$ and $N_2$. The average statistic weights, $p_1$ and $p_2$, are defined by;

$$p_1 = \frac{\overline{N}_1}{N}; \quad p_2 = \frac{\overline{N}_2}{N}; \quad p_1 + p_2 = 1 \tag{2}$$

depending on the average numbers $\overline{N}_1$ and $\overline{N}_2$ of the "1" respectivelly "2" type molecules in the first solvatation sphere.

The ylid molecule solvatation energies in the two states participating to the intramolecular charge transfer - $W_t^g$, $W_t^e$ - can be express by:

$$\begin{aligned} W_t^g &= p_1 \cdot N \cdot u_1^g + p_2 \cdot N \cdot u_2^g + W_s \\ W_t^e &= p_1 \cdot N \cdot u_1^e + p_2 \cdot N \cdot u_2^e + W_s \end{aligned} \tag{3}$$

where $u_j^g$ and $u_j^e$; j=1,2 are the energies of the pairs: one ylid molecule in its ground state + a solvent "j" molecule, respectivelly one ylid molecule in its excited state + a solvent "j" molecule and $W_s$ is the interaction between the solvent molecules. The last term from (3) does not change in the intramolecular charge transfer.

The spectral shift $\overline{\nu}_t - \overline{\nu}_0$ of the visible ICT band in the ternary solutions vs the gaseous state of the ylid can be expressed by:

$$hc(\overline{\nu}_t - \overline{\nu}_0) = W_t^e - W_t^g = p_1 N(u_1^e - u_1^g) + p_2 N(u_2^e - u_2^g) \tag{4}$$

One the other hand, the spectral shifts $\overline{\nu}_1 - \overline{\nu}_0$; $\overline{\nu}_2 - \overline{\nu}_0$ of the ICT band maximum in the binary solution realized with each of the two pure solvents vs. the ylid gaseous state can be expressed by the following terms:

$$hc(\bar{\nu}_1 - \bar{\nu}_0) = W_1^e - W_1^g = N(u_1^e - u_1^g)$$
$$hc(\bar{\nu}_2 - \bar{\nu}_0) = W_2^e - W_2^g = N(u_2^e - u_2^g) \quad (5)$$

where $W_j^e$ and $W_j^g$ are the solvatation energies in the excited (e), respectively in the ground (g) states of the cycloimmonium ylid in "j" (j=1,2) solvent.

From (4) and (5) it results:

$$p_1 = \frac{\bar{\nu}_t - \bar{\nu}_2}{\bar{\nu}_1 - \bar{\nu}_2}; \qquad p_1 = \frac{\bar{\nu}_1 - \bar{\nu}_t}{\bar{\nu}_1 - \bar{\nu}_2} \quad (6)$$

Relations (6) show that, in the limit of the cell models, the average weights may be estimated by the ICT band wavenumbers measured in the binary and ternary solutions.

Because the protic solvent can participate in intermolecular charge transfer with cycloimmonium ylids [5,6], one can estimate that the –OH strenght bound influences the ICT band frequency in the solvent mixture. The MNR signal of -OH proton measured in solvent mixture can estimate the proton unscreening, its capacity to participate in specific interactions [9].

If the mechanism of the proton change is realised at the ylid carbanion level [10,11], the statistic average weight of the –OH groups participating to it, can be calculated using the formula:

$$p_1^{OH} = \frac{\delta - \delta_0}{\delta_{100} - \delta_0} \quad (7)$$

where the chemical shift corresponding to the MNR signal of the –OH proton is noted $\delta$ for the solvent mixture and $\delta_{100}$ for the protic pure solvent. $\delta_0$ is the value obtained by extrapolation for $x_1 \to 0$ in the grafics $\delta$ vs. $x_1$.

## EXPERIMENTAL PART

The visible electronic absorption spectra - ITC band- in binary and ternary solutions of anilido benzoyl methylids having as heterocycle pyridine, benzo-[f]-quinoline and 3-(p-cumyl pyridazine) were recorded with a spectrophotometer Specord UV VIS Carl Zeiss Jena. The chemical shifts for the solvent mixture solvent "1"+solvent "2" with variable concentration $x_1$, have been measured from MNR spectra recorded with a Tesla BS-487C-spectrometer.

The solvents were purified by specific methods.

The parameters of the used solvents are listed in Table1. The cycloimmonium ylids: pyridinium anilido-benzoyl methylid (PABM); benzo-[f]-quinolinium anilido-benzoyl methylid (BQABM) and p-cumyl-pyridazinium

anilido-benzoyl methylid (CPABM) were prepared in Laboratory of Analitical Chemistry of "Al.I.Cuza" University from Ia¿i by known methods [12,13].The ylids were analyzed from point of view of structure and purity.

**Table 1**

Chemical shifts $\delta$ (ppm) in binary solvent Octanol +1,2 Dichloroethane, the ylid ICT wavenumbers $\bar{\nu}$ ($cm^{-1}$) in the corresponding ternary solutions and the average statistic weights

| Nr | $x_1$(%) | $\delta$ (ppm) | $p_1^{OH}$ | BQABM $\bar{\nu}$ ($cm^{-1}$); $p_1$ | | PABM $\bar{\nu}$ ($cm^{-1}$); $p_1$% | | CPABM $\bar{\nu}$ ($cm^{-1}$); $p_1$% | |
|---|---|---|---|---|---|---|---|---|---|
| 1 | 0 | (1.55) | 0 | 20550 | 0.0 | 22600 | 0 | 20110 | 0 |
| 2 | 2.5 | 1.72 | 4.7 | 20740 | 12.4 | 22780 | 11.3 | 20350 | 15.1 |
| 3 | 5.2 | 2.40 | 23.7 | 20960 | 28.1 | 22990 | 24.5 | 20580 | 29.6 |
| 4 | 14.1 | 3.43 | 52.5 | 21220 | 43.8 | 23160 | 37.3 | 20870 | 47.8 |
| 5 | 33.0 | 4.25 | 75.4 | 21620 | 69.9 | 23490 | 52.0 | 21250 | 71.6 |
| 6 | 59.7 | 4.72 | 88.5 | 21950 | 91.5 | 23900 | 86.6 | 21570 | 91.8 |
| 7 | 100 | 5.13 | 100 | 22080 | 100 | 24100 | 100 | 21700 | 100 |

**Table 2**

Chemical shifts $\delta$ (ppm) in binary solvent Benzene +1,2 Propane diol, the ylid ICT wavenumbers $\bar{\nu}$ ($cm^{-1}$) in the corresponding ternary solutions and the average statistic weights

| Nr | $x_1$(%) | $\delta$ (ppm) | $p_1^{OH}$ | BQABM $\bar{\nu}$ ($cm^{-1}$); $p_1$ | | PABM $\bar{\nu}$ ($cm^{-1}$); $p_1$ | | CPABM $\bar{\nu}$ ($cm^{-1}$); $p_1$ | |
|---|---|---|---|---|---|---|---|---|---|
| 1 | 0 | (4.95) | 0 | 20260 | 0.0 | 22250 | 0 | 19900 | 0 |
| 2 | 6.4 | 4.47 | 2.1 | 20490 | 11.1 | 22350 | 6.5 | 20150 | 14.6 |
| 3 | 12.6 | 4.50 | 5.3 | 20710 | 27.7 | 22560 | 25.8 | 20380 | 28.1 |
| 4 | 30.3 | 4.60 | 15.8 | 21520 | 60.9 | 22810 | 36.2 | 20660 | 44.4 |
| 5 | 56.6 | 4.85 | 42.1 | 22000 | 84.1 | 23150 | 58.1 | 21050 | 67.3 |
| 6 | 79.6 | 5.10 | 68.4 | 22150 | 89.9 | 23360 | 71.6 | 21340 | 84.2 |
| 7 | 100 | 5.40 | 100 | 22330 | 100 | 23800 | 100 | 21610 | 100 |

The results of the measurements are presented in Tables1 and 2, containing the molar rates $x_1$ of the protic solvent in the solvent mixture, the chemical shifts $\delta$ (ppm), measured in binary solvent, the frequencies $\bar{\nu}$ ($cm^{-1}$) in the ICT band maximum and the average statistic weights of the protic solvent, estimated with the relations (6) and (7). In the first line of these tables, the value of $\delta$ (ppm) for $x_1 \to 0$ were obtained through extrapolation in the graphic dependence $\delta$ (ppm) vs.$x_1$.

## RESULTS AND DISSCUSION

The use of the MNR spectra in the ternary solutions analysis has been suggested by the previous findings [5,6] that frequencies of the ylid ICT band in the binary protic solutions linearly depend on the chemical shift of the hydroxy group proton, measured in the pure solvent.Such a dependence points out that the protic solvents interact with the ylid molecules by specific proton donor- acceptor interactions. Bathochromic shift of the ICT band, by passing from gaseous state to protic solution of the ylid, suggests that the specific interaction between the protons and ylid molecule is less intense in the excited state, compared with its ground state.

From the Tables 1 and 2 data one can notice a linear dependence between the ICT band wavenumbers and the chemical shift of the hydroxy proton measured in solvent mixture. If one accept that the ICT process is realized from the carbanion to the heterocycle, the dependence mentioned above suggests that the specific interactions take place at the ylid carbanion.

The electronic absorption spectra have been registered at low concentrations of the ylid in ternary solutions. That's why one expect essential changes in the ICT band wavenumbers at the similar concentrations of the protic solvent in solutions. With the growth of the protic solvent concentration, concomitantly with the dimmer (protic molecule-protic molecule) increasing, the number of the protons implies in specific interactions with the ylid molecules also increases, determining an increasing of the solvatation energy of the ylid molecule. The process is saturated when the protic solvent concentration becomes equal with the ylid one.

This mechanism suggests that the ICT band frequencies measure both the solvatation energy of the ylid and the average number of the protic molecules in the first solvatation sphere. The $p_1$ values, computed on the basis of formula (6) and the data of Tables 1 & 2, show a higher protic solvent concentration in the first solvatation sphere vs. the solution left.

The values $p_1^{OH}$, determined using the relation (7), and the chemical shifts measured in the binary solvent "1" and "2" are smaller than the $p_1$ values for the ternary solutions, showing that the ylid molecule interacts with a hight number of protic molecules, while in the binary solvent only dimmer formation can appear.

From Tables 1 and 2 it results that the values $p_1^{OH}$ are higher than $x_1$ in the case of the alcohols and smaller than $x_1$ for the dihydroxy alcohols .

## CONCLUSIONS

1. The ICT wavenumbers in the ternary solutions linearly depend on the chemical shifts measured in the corresponding binary solvent.

2. The additional ICT shift measured in the protic solvents related to the aprotic ones can be explained by the proton transfer between the protic molecules and the ylid carbanion.

3. The proton exchange increases with the protic molecules number growth into the ternary solution.

4. There are differences between the average statistic weights and the molar rates in the solutions.

## REFERENCES

1. I.Zugravescu and M.Petrovanu N Ylid Chemistry, Academic Press, Mc Graw Hill, London 1976
2. G. Surpateanu, A. Lablache Combier, Heterocycles, 22 (1984) 2079
3. D.Dorohoi, D.Partenie and Do Nhat Van, An.St. Univ. Al.I.Cuza, Iasi, s.Ib, 26, (1980), 51 s Ib, 29,(1983), 28
4. Dorohoi, D.Partenie, J.Mol.Structure, 239,1-3 (1993), 129
5. D.Dorohoi, V.Holban, J.Mol.Structure, 239,1-3 (1993), 133
6.V.Pop, D.Dorohoi and V.Holban Spectrochimica Acta 50A,14, (1994), 2281
7. T.Abe, Bull. Chem. Soc. Jpn., 38,(1965),114; 39, (1966),939
8. T.Iu. Mazurenko, Opt.i. Spectr., 33, (1972), 1060
9. G.H.Pimmentel and A.L.McClellan, The Hydrogen Bond, L.Pauling editor, San Francisco, London, chap.4.1.5, (1960)
10. V.Pop, D.Dorohoi and M.Delibas, An.St.Univ Al.I.Cuza, s Ib, 32, (1986), 80
11. D.Dorohoi and V.Pop, An.St.Univ Al.I.Cuza, s Ib, 33, (1987), 79
12. Mai van Tri Thesis, Al.I.Cuza Univ., Iasi, 1976
13. Do Nhat Van, Thesis, Al.I.Cuza Univ., Iasi, 1977

STUDIA UNIVERSITATIS BABEŞ-BOLYAI, PHYSICA, SPECIAL ISSUE, 2000

# TIME-OF-FLIGHT MASS SPECTROMETER FOR FULLERENE AND RECOIL IONS: DESIGN AND CONSTRUCTION

**DANA DUMITRIU[*], D. IOANOVICIU[*], C-TIN CIORTEA[*], Z. SZILAGYI[*], G. BACIU[**], N. GLIGAN[**]**

[*] *National Institute for Nuclear Physics and Engineeering "Horia Hulubei", Bucharest-Magurele, Romania*
[**] *National Institute for Research and Development of Isotopic and Molecular Technologies, Cluj-Napoca, Romania*

## Introduction

Mass spectrometry was already involved in fullerene studies since their discovery [1]. The ionization methods as Laser Desorption, Electron ionization as well as Fast Atom Bombardment were used in these studies. Fullerene sputering from solid surfaces was obtained with ions of energies in the MeV range [2]. So $^{127}I$ ions of 72.3 and 55 MeV were used for the bombardment of polyvinyldenedifluorine and the ions were detected with a reflectron after acceleration in the range 3 to 15 keV [3]. The spectrum taken over 400 to 2500 u has resolved the peaks of $^{12}C_{60}^{+}$, $^{12}C_{59}{}^{12}C^{+}$. The interactions of $Si^{4+}$ ions of 2 MeV[4], of $Li^{+}$ [5] and of $H^{+}$ [6] ions with $C_{60}$ were studied with time-of-flight mass spectrometers.

The fragmentation of the fullerenes happens by photoionization [7], by electron impact [8], by ionic impact [9] and by collision with a gaseous target [10].

Various possible solutions for recoil ion analysis were suggested in [11].

## Focusing conditions and the adopted solution

The resulted ions have a temporal, spatial and velocity distribution. The simultaneous time focusing for space and velocity is not possible in time-of-flight mass spectrometry [12].

There are two possible solutions: the linear drift space geometry [13], [14], or the reflectron configuration including an electrostatic mirror [15], [16].

The geometry was so selected to ensure the exploration of two mass ranges: 1 to 200 u and 400 to 1000 u. The instrument length was selected to about 2 m to ensure a good temporal mass dispersion. A field-free space [17] of 2360 mm resulted for an extracting interval of 16.7 mm depth. An incidence angle of the ion packet to the mirror limit of two degrees ensures enough space between the collision chamber and detector to not interfere by their fields. The electrostatic mirror was constructed from 32 rings of 10TiNiCr180 stainless steel. Their inner

diameter is of 231 mm and each ring has a 20 mm length. The rings are sustained on three metalic bars connected to the rings by insulators. A grid limits the entry face of the mirror. Tolerrances of less than 0.02 mm were enforced to ensure relative differences in flight time shorter than $10^{-5}$.

The detector contains two channel plates in chevron assembly

The vacuum system ensures high vacuum levels by a turbomolecular pump backed in the first pumping interval by a rotary pump. A high vacuum gauge allows pressure measurements close to the detector assembly. The tube connecting the spectrometer to the collision chamber is 367 mm long while the main flight tube was constructed from two cylindrical chambers of 888 mm each.

A support ensures the location of the mass spectrometer at 1780 mm from the reference plane to be connected to the accelerator exit port.

**Outlook**

The next steps on the way to make this mass spectrometer a useful tool in fullerene an recoil ion investigation are: a cycle of vacuum tests, of electronic units including coincidence measurements and a program for the achievement of the needed mass resolution.

## REFERENCES

1. Kroto, Heath, O'Brien, Curl, Smaley, Nature 318 (1985) 162.
2. Bitensky, Brinkmalm, Demirev, Eriksson, Hakansson, Papaleo, Sundquist, Zubarev, Int. J. Mass Spectrom. Ion Processes 138 (1994) 159.
3. Brinkmalm, Hakansson, Kjelberg, Demirev, Sundqvist, Ens, Int. J. Mass Spectrom. Ion Processes 114 (1992) 183.
4. Itoh, Tsuchita, Miyabe, Imai, Imanishi, Nucl. Instrum. Methods Phys. Res. B129 (1997) 363.
5. Itoh, Tsuchita, Majima, Imanishi, Phys. Rev. A59 (1999) 4428.
6. Itoh, Nakai, Miyabe, Imanishi, J. Phys. B 31 (1998) 5383.
7. Graber, Hiss, Busman, Hertel, Z. Phys. D 24 (1992) 307.
8. Scheier, Mark, Phys. Rev. Lett. 73 (1994)54.
9. Walch, Cocke, Voehpel, Salzborn Phys. Rev. Lett. 72 (1994) 1439.
10. Erlich, Westerburg, Campbell, J. Chem. Phys. 104 (1996) 1900.
11. Wouters, Vieira, Wollnik, Enge, Kowalski, Brown, Nucl. Instrum. Methods Phys. Res A240 (1985) 77.
12. R. Stein, Int. J. Mass Spectrom. Ion Processes 132 (1994) 29.
13. J. Wiley, I. McLaren, Rev. Sci. Instrum. 26 (1955) 1150.
14. Time-of-flight mass spectrometry, Cotter R. Editor, Amer. Chem. Soc. Series 1994.
15. Bergmann, Martin, Schaber, Rev. Sci. Instrum. 60 (1989) 792.
16. Gohl, Laue, H. Wollnik, Int. J. Mass Spectrom. Ion Phys. 48 (1983) 411.
17. D. Ioanoviciu, Int. J. Mass Spectrom. Ion Processes 131 (1994) 43.

STUDIA UNIVERSITATIS BABEŞ-BOLYAI, PHYSICA, SPECIAL ISSUE, 2000

# SOLITONIC EXCITATIONS IN BIOLOGIC ONE-DIMENSIONAL MOLECULAR SYSTEMS

**D. GRECU[1], ANCA VIŞINESCU, A.S. CÂRSTEA**

*Department of Theoretical Physics, National Institute of Physics and Nuclear Engineering, Bucharest, Romania*

**ABSTRACT.** Several models of biological interest are reviewed. Special attention is given to the models of Davydov and Takeno, with a long-range interaction of Kac-Baker type (exponentially decaying). Solitonic excitations are obtained in the weak nonlinearity limit. The envelope solitons are studied in an approximation going beyond the usual nonlinear Schrodinger equation.

The quasi-one-dimensional molecular systems of biological interest are very complicated structures built up from complexes of atoms- we shall call them "molecules"- connected by hydrogen bonds. As an example we mention the complicated structure of α-helix mentioned above one distinguishes three coupled chains of the form

$$\cdots H - N - C\overbrace{=\underbrace{O}_{\chi}\cdots H - N - C=}^{J}O\cdots$$

and the first approximation is to consider only a simple chain, having the mentioned sequence (one chain approximation).

Each molecule is characterized by several intra-molecular vibrations, and we shall assume that only one of them plays an active role in the studied process. In the case of α-helix structure this corresponds to the amide I oscillation (C = O stretching). Between these excitations there are electromagnetic interactions of dipol-dipol type, and in spite of its long-range action character, usually one takes into account only the interactions between nearest neighbors, characterized by a coupling constant J (both these approximations can by -relaxed).

In the chain the molecules are oscillating around the equilibrium positions.

One considers only oscillations along the chain direction, described by an one-dimensional acoustic phonon field.

The intra-molecular excitation will induce a local distortion of the α-helix chain, which at his turn will react and try to trap the localized vibration. Consequently an interaction between the intra-molecular excitation and the phonon field has to be into account, interaction characterized by a coupling constant χ. It arises from the modulation of the amide I energy by stretching of the adjacent hydrogen bounds.

[1] *E-mail address:* dgrecu@theor. *1 theory. nipne.ro*

The Hamiltonian describing this very simple field picture is of Frohlich type [1]

$$H = H_{ex} + H_{ph} + H_{int}$$
$$H_{ex} = \sum_n (E_o B_n^+ B_n - J(B_{n+1}^+ B_n + B_n^+ + B_{n+1})) \quad (1)$$
$$H_{ph} = \sum_n \frac{1}{2M} \hat{p}_n^2 + \frac{1}{2}\omega((\hat{u}_{n+1} - \hat{u}_n)^2)$$
$$H_{int} = \chi \Sigma (\hat{u}_{n+1} - \hat{u}_n) B_n^+ B_n$$

Here $B_n^+$, $B_n$ is the creation, anihilation operator of the intra-molecular excitation, of energy $E_o$, in the site n, $\hat{u}_n$, $\hat{p}_n$ is the displacement operator of the n-th molecule and his conjugate momentum respectively, M the mass of the molecule, w the elastic constant and $\chi$ the coupling constant between the intra-molecular excitation and the phonon field.

Davydov [1] - [4] has used this Hamiltonian to discuss localized excitations of solitonic type in these structures. Davidov's basic hypothesis was a certain ansatz concerning the state vector associated to these excitation, namely:

$$|\psi(t)> = \sum_n a_n(t) B_n^+ \exp\left(-\frac{i}{\hbar}\sum_j (\beta_j(t)\hat{p}_j - \pi_j(t)\hat{u}_j)\right) |0> \quad (2)$$

Here |0> is the vacuum state both for phonons and molecular excitations.

The normalization condition for this state vector gives:

$$<\psi(t)|\psi(t)> = \sum_n |a_n(t)|^2 = 1 \quad (3)$$

and we can interpret $|a_n|^2$ as the probability to have the intra –molecular excitation on the n-th site. Also it is easy to show that:

$$<\psi(t)|\hat{u}_n|\psi(t)> = \beta_n(t)$$
$$<\psi(t)|\hat{p}_n|\psi(t)> = \pi_n(t)$$

which gives the interpretation for the coefficients $\beta_n$, $\pi_n$ as the mean values of $u_n$, $p_n$ on the state vector (2). The problem is reduced to the determination of the coefficients $a_n(t)$, $\beta_n(t)$, $\pi_n(t)$, which now are classical variables.

Davydov's procedure was to calculate first the average value of the Hamiltonian (1) on the state vector (2), <H>, and, after identifying conjugate coordinates and momenta, to use <H> in Hamilton's equation of classical mechanics to find equations of motion for $a_n(t)$, $\beta_n(t)$, $\pi_n(t)$. The following result is obtained:

$$i\hbar \dot{a}_n = E a_n - J(a_{n+1} + a_{n-1}) + \chi(\beta_{n+1} - \beta_n) a_n$$
$$M\ddot{\beta}_n = w(\beta_{n+1} - 2\beta_n + \beta_{n-1}) + \chi(|a_n|^2 - |a_{n-1}|^2)$$

Later the model was discussed by many authors [5] – [13], trying to improve it and eliminating some inconsistencies, but for our present purposes this simple model is sufficiently.

The system (4) represents a nonlinear system of coupled equations. It is very convenient to make an adiabatic approximation, and to assume $\beta_n = 0$. Then from the second eq. 4 we get:

$$\beta_{n+1} - \beta_n = -\frac{\chi}{\omega}\left|a_n\right|^2$$

which introduced in the first gives:

$$i\hbar a_n = Ea_n - J(a_{n+1} + a_{n-1}) - \frac{\chi^2}{\omega}\left|a_n\right|^2 a_n \qquad (5)$$

a typical equation for a discrete self-trapping system [14], [13], chapter V.

Let us consider now small nonlinearities. If $\chi = 0$ (linear case) eq. (5) has plane wave solutions:

$$a_n = Ae^{i(kln-\omega t)}$$

(l – lattice constant) with ω (k) given by the dispersion relation:

$$\hbar\omega(k) = E - 2J\cos kl$$

The cumulative effects of a small nonliniarity ($\chi$«1) manifest as a modulation of amplitude in the asymptotic region. To deal with process the multiple scales approximation (reductive perturbation method) is used [15]. One introduces the slow variables:

$$\epsilon = \varepsilon(ln - v_g t)$$
$$t_2 = \varepsilon^2 t, \qquad t_3 = \varepsilon^3 t, \ldots. \qquad (8)$$

and the solution is written as an asymptotic expansion in the small parameter $\varepsilon < 1$

$$a_n = \varepsilon^{i(kln-\omega t)} \sum \varepsilon^p A_p(\ ; t_2, t_3)$$

As a result the differential – finite difference equation (5) will be transformed into a partial differential equation, completely integrable, namely the nonlinear Schrödinger equation (NLS). The time derivative changes as:

$$\frac{\partial}{\partial t} \to \frac{\partial}{\partial t} - \varepsilon v_g \frac{\partial}{\partial \xi} + \varepsilon^2 \frac{\partial}{\partial t_2} + \ldots \qquad (9)$$

and also:

$$a_{n\pm1} = e^{i(kln-\omega t)} e^{\pm ikl} \sum \varepsilon^p \left( A_p(\xi, t_2, \ldots) \pm \varepsilon l \frac{\partial A_p(\xi, t_2, \ldots)}{\partial \xi} + \frac{1}{2}\varepsilon^2 l^2 \frac{\partial^2 A_p(\xi, t_2, \ldots)}{\partial \xi^2} \pm \ldots \right) \qquad (10)$$

Inserting (8), (9) and (10) in eq. (5) we shall equate with zero the coefficients of each powers of ε. In order ε we obtain, as it is expected, the dispersion relations (6). The order $\varepsilon^2$ defines the group velocity $v_g$:

$$\upsilon_g = \frac{2J}{\hbar} l \sin kl = \frac{d\omega(k)}{dk} = \omega_1 \tag{11}$$

The next order, $\varepsilon^3$, is relevant for the modulation process of the ware amplitude. It is found that the component $A_1$ in the expansion (8) has to satisfy the celebrated cubic nonlinear Schrödinger equation.

$$i\frac{\partial A_1}{\partial t_2} + \omega_2 \frac{\partial^2 A_1}{\partial \xi^2} + q\left|A_1\right|^2 A_1 = 0 \tag{12}$$

where:

$$\omega_2 = \frac{1}{2}\frac{d^2\omega(k)}{dk^2}, \qquad q = \frac{\chi^2}{\hbar\omega} \tag{13}$$

It is a generic equation describing the propagation of quasi –monochromatic waves in media with weak nonlinearities. It has appeared in many branches of physics: plasma physics, nonlinear optics, pulses propagation in nonlinear optical fibers, surface water waves, molecular crystals... [16] – [18]. It is a completely integrable equation, and can be solved by the inverse scattering transform (IST) method [16] – [18].

For $\omega_2 > 0$ it has bright soliton solutions, while for $\omega_2 > 0$ only dark solitons. For $\omega_2 > 0$, introducing the quantities:

$$\tau = \omega_2 t, \qquad \psi = \sqrt{\frac{q}{2\omega_2}} A_1 \tag{14}$$

it is transformed into the standard form:

$$i\frac{\partial \psi}{\partial \tau} + \frac{\partial^2 \psi}{\partial \xi^2} + 2\left|\psi\right|^2 \psi = 0 \tag{15}$$

We write down the expression of the one-soliton solution:

$$\psi = 2i\eta \frac{\exp i(2\zeta\xi + 4(\zeta^2 - \eta^2)\tau + \phi_0}{\cosh(2\eta(\xi - \xi_0 + 4\zeta\eta))} \tag{16}$$

describing an oscillatory localized excitation, propagating with the velocity $4\varsigma$ to the left. Here $z = \zeta + i\eta$ is the complex eigenvalue of the spectral problem associated to the NLS eq. In the IST method, and $\Phi_0$, $\xi_0$ are the initial phase and the initial position of the soliton.

Recently, in a paper [19] presented at the International Workshop on "Nonlinear Evolution Equations and Dynamical Systems", held in Kolymbari – Crete, 1999 (NEEDS-99) we used the multiple scales method to analyze a more complicated equation than (5)

$$L(\{y_n\}) = N(\{y_n\}) \tag{17}$$

L is a linear differential (time)- difference (space) operator, acting on a vibronic field $\{y_n\}$, and N is an algebraic nonlinear (cubic) operator. A model, elaborated several years ago by Takeno [11]-[12], to discuss localized excitations in nonlinear molecular systems, is at the origin of this equation of motion (17). For the $\alpha$-helix problem, the vibronic field is related to the amide I vibrations. The nonlinearity is introduced through the coupling of the vibronic field with the phonon field, and can be included also in the vibronic Hamiltonian. An harmonic long range interaction between vibrons, exponentially decayng (Kac-Baker model), was introduced to take into account the electromagnetic interactions between vibrons. We mention several conclusions resulting from our investigation.

• The time and space evolution of the first amplitude $Y_1$ of the asymptotic expansion of $y_n$ is given by the NLS eq., in the slow time-space variables.

• In the order $\varepsilon^4$, in order to eliminate a secular behavior of $Y_2$ (a linear growth in time of $Y_2$, which would invalidate the asymptotic expansion used), $Y_1$ is necessary to be also a solution of the next equation in the NLS hierarchy. This conclusion is in agreement with recent results obtained from a similar multi-scales analysis of certain partial differential equations [21], [22].

• For the first time in the context of nonlinear one/dimensional molecular crystals we analyzed the case when the second derivative $\omega_2$ is zero for a certain point in the Brillouin zone.

$$\omega_2(k_0) = \frac{1}{2}\frac{d^2\omega(k)}{dk^2}\Big|_{k=k_0} = 0 \tag{18}$$

This point is known as the zero dispersion point (ZDP) in the case of pulse propagation in optical fibers [22]. The NLS eq. is no longer valid and in order to find the relevant equation for this situation we have to modify the definition of the slow spatial variable, namely:

$$\xi = \varepsilon^{\frac{2}{3}}(an - \omega t) \qquad t_j = \varepsilon^j t, \quad j \geq 2 \tag{19}$$

and to consider k in the vicinity of $k_{0:}$

$$k = k_c + \varepsilon^{\frac{2}{3}} k_c \tag{20}$$

Then using the multiple scale method we find in order $\varepsilon^3$ the following equation:

$$i i\psi_T + 3\psi_{XX} + i\psi_{XXX} + q|\psi|^2\psi = 0 \tag{21}$$

Were $\Psi$,T,X are quantities conveniently scaled.

Finally let us make few remarks. The NLS eq. and its soliton solutions are obtained at the end of a sequence of approximations, some of them very questionable. In spite of this fact the soliton mechanism for the storage and transport of energy in molecular systems of biological interest is very attractive and deserve all the

attention. The present situation can be improved in many ways. We mention two such directions.

• To elaborate more complex models whish would take into account in a better way the complexity of the structure. In the case of α-helix structure it would be very interesting to consider a model of three coupled chains.

• A careful analysis of the mathematical problems risen by this simple model like the ZDP problem, and the influence of the higher order terms in the asymptotic expansion of the multiple scale method.

Works in both directions are in progress.

## REFERENCES


[1] H. Frohlich, Proc. Roy. Soc. (London) **A 215**, 291 (1952); Adv. Phys. **3**, 325 (1954).
[2] A.S. Davydov, N.I.Kislukha, Phys. Stat. Sol. **b 59**, 465 (1973); Zh. Eksp. Teor. Fiz. **71**, 1090 (1976).
[3] A.S. Davydov, Phys. Scripta **20,** 387 (1976); Usp. Fiz. Nauk **138**, 603 (1982).
[4] A.S. Davydov, "*Solitons in Molecular Systems"* (Reidel, Dordrecht, 1985)
[5] J.M. Hyman, D.W. McLaughlin, A.C. Scott, Physica **D 3**,23, (1981).
[6] A.C. Scott, Phys. Rev. **A 26**, 578 (1982)
[7] D.W. Brown, K. Lindenberg, B.J. West, Phys. Rev. **A 33,** 41104 (1986).
[8] W.C. Kerr, P.S. Lomdahl, Phys, Rev. **B 35**, 3629 (1987)
[9] Qing Zhang, V. Romero- Rochin, R. Silbey, Phys. Rev. **A 38**, 6409 (1988)
[10] M.J. Skrinjar, D.V. Kapor, S.D. Stojanovic, Phys.Rev. **A 38**, 6402 (1988)
[11] S. Takeno, Prog. Theor. Phys., **71**, 395 (1984); **73**, 853 (1985); **75**, 1 (1985)
[12] S. Takeno J. Phys. Soc. Japan **59**, 3127 (1990)
[13] P.L. Christiansen, A.C. Scott *"Davydov's Soliton Revisited, self-trapping of Vibrational Energy in Proteins"* (NATO ASI Series B 243, Plenum Press, New York, 1990), and references therein.
[14] J.C. Eilbeck, P.S. Lomdahl, A.C. Scott, Physica **D 16**, 318 (1985)
[15] S. Taniuti, Suppl. Prog. Theor. Phys. **55**, 1 (1974)
[16] M.J. Ablowitz, H. Segur, *"Solitons and the Inverse Scattering Transform"* (SIAM, Philadelphia, 1981);
[17] A.C. Newell, *"Solitons in Mathematics and Physics"* (SIAM, Philadelphia, 1985)
[18] V.E. Zakharov, S.V. Manakov, S.P. Novikov, P.L. Pitaevski, *"Theory of Solitons"* (Consultant Bureau, New York, 1984).
[19] D. Grecu, Anca Vişinescu, A.S. Cârstea, *"Beyond Nonlinear Schrodinger Equation Approximation for an Anharmonic Chain with Harmonic Long Range Interaction*" (NEEDS-(99) –to be published.
[20] A. Degasperis, S.V. Manakov, P.M. Santini, Physica **D 100**, 187 (1997);
[21] P.M. Santini *"Nonlinear Physics, Theory and Experiment*", Proceedings Galliopoli Workshop (eds. E.Alfinito et all, World Scientific, 1996) p.294.
[22] P.K.A. Wai, C.R. Menyuk, Y.C. Lee, H.H. Chen, Optics Lett.**11**, 464 (1986)
P.K. Wai, H.H. Chen, Y.C. Lee, Phys.rev. **A 41**, 426 (1990)
[23] M. Klauder, E.W. Laedke, K.H. Spatschek, S.K. Turisyn, Phys. Rev. **E 47**, R 3844 (1993)
[24] I.M. Uzunov, M. Goldes, F. Lederer, Phys.Rev. **E 52**, 1059 (1995).

STUDIA UNIVERSITATIS BABEŞ-BOLYAI, PHYSICA, SPECIAL ISSUE, 2000

# STRUCTURAL, OPTICAL AND TRANSPORT PROPERTIES OF II-VI NARROW-GAP SEMICONDUCTING THIN FILMS

**EMIL INDREA, IOAN BRATU, ADRIANA BARBU and XENIA FILIP**

*National Institute for Research and Development of Isotopic and Molecular Technologies, P.O. Box 700, 3400 Cluj-Napoca 5, Romania*
*Phone: 064 185027, Fax: 064 420042, E-mail: eindrea@L30.itim-cj.ro*

## 1. INTRODUCTION

The semiconducting $Hg_{1-x}Cd_xTe$ alloys are interesting because their tunable and narrow energy gap makes them ideal materials for infrared detector applications [1]. The accurate determination of actual structural parameters is of major practical importance for specific properties of this material owing to its band structure; *i.e.* the high intrinsic carrier concentration and the mobility of electrons are much higher than those of holes [2]. For many applications, a change of the near-surface region properties by large-scale impurity doping is needed. The most promising way of achieving such doping is the use of high-dose ion-implantations [3]. This phenomenon is used to produce $p \rightarrow n$-type conversion [4].

CdTe thin films have interesting physical properties for use in photovoltaic solar cells because they have a high absorption coefficient in the visible range of the solar spectrum and the band gap (≈ 1.45 eV) is close to the optimum value for efficient solar energy conversion and the availability of p- and n- type materials [5]. Since the difference between the lattice constants for CdTe and HgTe is only 0.3%, high-quality epitaxial layers of $Hg_{1-x}Cd_xTe$ solid solutions can be grown on CdTe substrates, very suitable for development of complex infrared detection devices [6].

Cadmium telluride is considered to be one of the most promising materials for the fabrication of solar cells. It has a high absorption coefficient in the visible range of the solar spectrum and its band gap (≈ 1.45 eV) is close to the optimum value for efficient solar energy conversion.

Thin film heterojunction cells made of CdTe and CdS are considered competitive in terms of solar energy conversion efficiency, low cost, long-term stability and possible production of large-area photovoltaic cells [7-9]. The heat treatment in the range from 400 to 500 $^0$C results in an improved efficiency of CdTe/CdS solar cells [10]. This is attributed to several processes including an increase in the grain size [11], surface and interface properties of CdTe/CdS/glass, heterostructures and changes in optical reflectance and refractive index [12].

## 2. Physical vapour deposited II-VI narrow-gap semiconducting thin films

### 2.1. Laser-assisted physical vapour deposited CdTe and $Hg_{1-x}Cd_xTe$ thin films

There are several preparing methods of semiconducting thin films, one of the most convenient presently being the laser-assisted physical vapour deposition (LAPVD) process [13]. In this process, a pulse laser beam is used to vaporize materials (target) in a vacuum cell (at a pressure of ~ $10^{-6}$ torr); the evaporant is deposited as a thin homogeneous film on a substrate at a rate of a few tenths of nanometers per pulse. In the LAPVD process multi-element materials can be deposited within the stoichiometric composition [14]. High purity evaporated material forward directed can be collected with high efficiency. CdTe and $Hg_{1-x}Cd_xTe$ thin films of various thicknesses were deposited on optical glass substrate using the LAPVD process [15]. A pulsed $CO_2$- TEA laser was used for the semiconductor samples vaporization. Laser pulse energy was kept at 5 J/pulse, while the repetition pulse frequency was 2.5 Hz. The incident laser beam was focused on the semiconductor target by means of a 20 mm focal NaCl spherical lens. The film substrate was external heating by a resistive element being in thermal contact with it. During the vaporization, the film substrate was continuously rotated in order to improve the film uniformity thickens. A better vacuum than $10^{-5}$ Torr was assured during the deposition processes. The thickness of the films ranged from 0.5μm to 3.0μm.

### 2.2. Heterojunction cells made of CdTe and CdS thin film

Thin films of cadmium sulphide have major applications in optoelectronic devices. CdS films could be combined with CdTe films in order to form heterojunctions that are valuable candidates for photovoltaic conversion of solar energy. The CdS thin films were prepared by chemical bath deposition (CBD) in multilayered form on optical glass substrate and they were post-growth annealed [16]. Prior to deposition the glass substrate was cleaned with chromic acid and distilled water. The presence of sodium citrate and thiourea in the chemical bath generate adherent and relative homogeneous CdS thin films. The structural and optical properties of as grown and annealed CdS thin layers have been used in order to select the best substrate for subsequent CdTe deposition. Thin CdTe films have been obtained through sublimation of CdTe polycrystalline grains (99.999% pure, obtained from Balzers, Switzerland) and deposition, in a vacuum of $10^{-6}$ Torr, onto heated CdS substrate. Films of different thickness were deposited at 230 $^0$C substrate temperature.

## 3. Structural characterization of the II-VI narrow-gap semiconducting thin films

The X-ray diffraction technique was used for structural characterization of the semiconductor materials deposited as thin films. The X-ray diffraction patterns were obtained by means of a standard DRON-3M powder diffractometer, working at 45 kV and 30 mA, and equipped with scintillation counter with single channel

pulse height discriminator counting circuitry. The Co $K_\alpha$ radiation, Fe filtered, was collimated with Soller slits. The data of the (111) CdTe profile were collected in a step-scanning mode with $\Delta 2\theta = 0.025^0$ steps and then transferred to a PC for processing.

From the X-ray diffraction patterns it was concluded that the crystallites of the LAPVD deposited CdTe films are preferentially oriented with the (111) plane parallel to the substrate. As the number of laser pulses increases, the X-ray diffraction of the CdTe films shows the representative patterns of a cubic zincblende structure polycrystalline material. The deposited compound has been confirmed to be CdTe with f.c.c. structure through X-ray analysis. The lattice constant ($a_0$ = 0.647 nm) is found to be quite close to the reported value.

The X-ray diffraction pattern of the $Hg_{1-x}Cd_xTe$ film contains (100) reflection, indicating a highly texturated film with [100] direction of the HgTe type structure.

The X-ray diffraction diagrams of the CdS substrate compared with ASTM charts showed that CdS films had a hexagonal wurtzite structure and their preferential growing planes are (101) and (002).

**Table 1**

Microstructural parameters for the CdTe/glass film and CdTe/CdS/glass film, respectively.

| | $D_{eff}$ (Å) | $\left\langle \varepsilon^2 \right\rangle_{111}^{1/2} \times 10^3$ | α |
|---|---|---|---|
| CdTe/glass | 140 | 6.01 | 0.074 |
| CdTe/CdS/glass | 308 | 2.27 | 0.028 |

The single (111) CdTe X-ray diffraction line was analyzed in order to determine the microstructural parameters of the semiconductor films. The structural information obtained by single X-ray profile Fourier analysis of polycrystalline CdTe films were: the effective crystallite mean size, the root mean square (rms) of the microstrains averaged along [hkl] direction, and the staking fault probability [17]. The crystallite size distribution function was determined from the second derivative of the strain-corrected Fourier coefficients by a method developed by Aldea and Indrea by a XRLINE [18] computer program.

Table 1 summarizes the microstructural parameters of CdTe/glass deposited (CTG) film and for CdTe/CdS/glass (CTSG) film, respectively. It can be observed (from the microstructural parameters presented in Table 1) that the CdTe film growth process on the CdS substrate favor the growth of polycrystalline CdTe films with larger crystallite size and lower crystalline imperfections. $D_{eff}$ is the effective crystallite size along the perpendicular direction to the (111) planes, $\left\langle \varepsilon^2 \right\rangle_{111}^{1/2}$ is the rms of the microstrain averaged along the [111] direction and α is the stacking fault probability. In polycrystalline structure grain boundaries have a dominant influence on the electrical and optoelectronic properties of the semiconductor film.

CdTe semiconductor compound exhibit both p- and n- type conductivity due to the formation of electrically active native point defects that are associated with deviations from the stoichiometric composition. The microstructure is dependent of the growth method, and very sensitive to the deposition parameters: the substrate temperature and film thickness [19]. Any of these factors may be used in modifying the electrical and transport properties. The 5μm thickness films grown at 600 K substrate temperature have a good structural quality: a high average effective crystallite size $D_{eff}$ = 48.3 nm, a small root mean square of the microstrain caused by distortions within the crystallites $< \varepsilon^2 >^{1/2} = 0.82 \cdot 10^{-3}$ and a stacking fault probability p= 0.27 %.

## 4. Local atomic structure in $Hg_{1-x}Cd_xTe$ narrow-gap semiconductor alloy

Extended X-Ray Absorption Fine structure (EXAFS) is a widely used technique for probing the structural local environment of atoms by using incident photons generated by a synchrotron radiation source [20,21]. The alloy used for this study was a n-type semiconductor grade of $Hg_{1-x}Cd_xTe$, $x$ = 0.21. The EXAFS measurements were performed at the Laboratoire pour l'Utilisation du Rayonnement Electromagnetique (LURE, Orsay, France), using the synchrotron radiation from the Dispositif de Collisions dans l'Igloo (DCI) storage ring operating with an positron-beam energy of 1.72 GeV and a maximum stored current of 180 mA [22]. The X-ray absorption spectra were collected over 800 eV above the mercury $L_{III}$ edge (12284 eV) using a conversion electron detector [23] working at liquid nitrogen temperature (78K) in order to reduce the thermal disorder in the probed material and consequently to increase the magnitude of the spectra oscillations. The monochromatisation of the incoming beam was achieved using Si (311) channel-cut monochromator. The EXAFS data were analyzed by means of standard methods described in details elsewhere [24]. The absorption threshold of the Hg $L_{III}$ - edge was taken at $E_0$ = 12284 eV. As a first step in data analysis, the energy scale is converted into a *k*-scale through the relation $k = \left[2m(E - E_0)\right]^{1/2} / \hbar$ using as reference energy $E_0$ for the outgoing electron the value obtained at the inflection point of the absorption coefficient. The interference EXAFS function is defined as [25] $\chi(k) = [\mu(k) - \mu_b(k)] / \mu_b(k)$, where $\mu_b(k)$ is the smooth atomic like background and $\mu(k)$ is the experimental corrected absorption coefficient (Fig. 1). The next step in the analysis consists in a fast Fourier transformation of the $k \cdot \chi(k)$ data to the *R* space. It yields to a radial distribution function *F(R)* which contains structural information about the absorbing atom [26]. The Fourier transform is actually given by:

$$F(R) = (2\pi) \cdot \int_{k_{\min}}^{k_{\max}} W(k) \cdot k^n \cdot \chi(k) \cdot \exp(2ik \cdot R) \cdot dR \qquad (4.1)$$

where $k_{min}$ and $k_{max}$ are the minimum and the maximum experimental $k$ data values. The factor $W(k)$ in equation (4.1) is a window function that converts the finite data set to an infinite one as it is necessary for Fourier transform. By inverse Fourier transform, the experimental EXAFS contribution $\chi_{\exp}(k)$ of the selected coordination shells was obtained. Based on an assumed structural model, the theoretical EXAFS spectrum $\chi_{th}(k)$ was calculated using the reported formula (24). The backscattering amplitude $|f_j(\pi,k)|$ and the total phase shift function $\Phi_j(k)$ were evaluated by taking into account the spherical-nature of the final photoelectron state in the full-curved-wave formalism of McKale [27]. The $k$ dependent backscattering amplitude and phase shift functions were taken from the FEFF5 code [28] at R = 0.280 nm for Te (Z = 52), and R = 0. 460 nm for Cd (Z = 48) and Hg (Z = 80). The amplitude and phase shift $k$ dependent features can be identified as a generalized Ramsauer-Townsend effect [29]. The calculated parametrised spectrum $\chi_{th}(k)$ was compared to the experimental filtered EXAFS function $\chi_{\exp}(k)$. All data were analyzed with a non linear least-squares fitting procedure by using the SEDEM computer code developed by Aberdam [30].

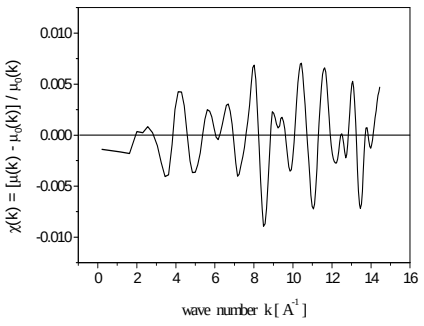


Fig. 1. The experimental normalized interference EXAFS function for the thin film composition Hg0.79Cd0.21Te related to the data obtained at the Hg $L_{III}$ edge.

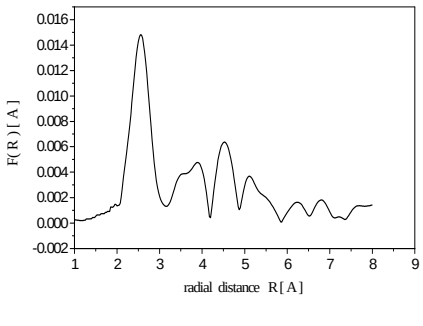


Fig. 2. The radial distribution function F(R) for the thin film composition Hg0.79Cd0.21Te related to the data obtained at the Hg $L_{III}$ edge.

In a first step, a one-shell model was used by filtering out the first peak of $F(R)$ (see Fig. 2) and back transforming it in the range 0.15 nm < $R$ < 0.32 nm $N_{ind}$ = 6. The fit of the related EXAFS signal leads to the value $R$ = 0.280 nm for the Hg-Te pairs, a distance that corresponds to that expected for this composition [31]. All these results have been obtain with a fixed values $S_0^2 = 1$ while $\Gamma$ has been found equal to the unity. In a second step, we have filtered the $F(R)$ distribution function in the

range 0.15 nm < $R$ < 0.42 nm ($N_{ind}$ = 12). We have then fitted the related EXAFS data using as free parameters the Hg-Te, Hg-Cd and Hg-Hg distances, the Debye-Waller factors, and the energy shift $E_0$ [32].

**Table 2.**

Values of the parameters related to the fits presented in Figure 3.

| | Atom pairs | N | Distance R (nm) | σ (nm) | Residual V |
|---|---|---|---|---|---|
| 1st shell | Hg - Te | 4 | 0.280±0.002 | $(5.3 \pm 0.5)^{-3}$ | $2.5 \times 10^{-3}$ |
| 2nd shell | Hg - Cd | 2.6 | 0.452±0.002 | $(6.7 \pm 0.5)^{-3}$ | |
| 2nd shell | Hg - Hg | 9.4 | 0.459±0.002 | $(10.0 \pm 0.5)^{-3}$ | |

The fitting parameters and the reliability factor V are listed in the Table 2. They agree quite satisfactorily with the experiments. The experimental results were fitted by minimizing the variance parameter V. The solutions reported in Table 2. were obtained when the variance parameter was less than twice of its minimum value. Such criteria provide an uncertainty of about $\pm 0.002$nm for the average interatomic distances as floating parameters. For the single crystal of $Hg_{0.79}Cd_{0.21}Te$ bulk composition we can see while ordering has been found for the first shell which consists in four tetrahedral coordinated Te atoms at 0.280 nm, the second shell (consisting in 12 cations) is split into two contributions at the bond lengths 0.452 nm for Hg-Cd and 0.459 nm for Hg-Hg pairs. In all cases, the coordination numbers have been fixed to the bulk composition. Based on EXAFS results, Mayanovic *et al* [33] suggest that the Hg-Te bond distance in $Hg_{1-x}Cd_xTe$ alloys is not different from the Hg-Te distance existing in the HgTe compound. Furthermore, no charge transfer occurs since no energy shift of the Hg-$L_{III}$ edge is observed. In our case, for the reference $Hg_{0.79}Cd_{0.21}Te$ sample, we found that the nearest neighbours (NN) Hg (cation) - Te (anion) bond length $R$ = 0.280 nm is like the one related to the binary zinc-blende HgTe compound. It means that the average NN distance is independent of the concentration $x$ parameter that hase been used. This result is in agreement with a "tetrahedral bond conservation rule" discussed extensively by E.Jaffe and A.Zunger [34]. As Mikkelsen and Boyce [35] pointed out, in the zinc-blende-type $A_{1-x}B_xC$ alloys, if the cation sublattice is too distorted, the average anion-cation distance must not differ significantly from the virtual crystal approximation (VCA) value. After implantation of the $Hg_{0.79}Cd_{0.21}Te$ alloys, a disordering process can be observed in the HgCd sublattice where the Debye-Waller disorder parameters increase with the ion mass. The lattice distortion results from the atoms displacements from their site position due to the influence of defect-generated fields.

## 5. Optical properties of II-VI narrow-gap semiconducting films

The photoacoustic (PA) spectroscopy have to be an extremely powerful technique [36] to analyze the absorption coefficient spectral shape of semiconductors, around them absorption edge. An experimental set-up was used in the so called

"open cell" configuration [37], consisting of 100W hallogen lamp, a mechanical chopper, a NaCl prism monochromator, a condenser microphone as detector and a lock-in amplifier. The incident radiation was chopped at 12Hz. The spectra were normalized and calculated by using a software developed by the authors. Each sample was mounted with a small amount of vacuum grease directly on the top of the microphone. The 0.5eV÷1.7eV spectral range was investigated, covered with a 10meV resolution. The spectral behaviour of the CdTe thin films was correlated with the classical NIR spectra recorded with a NIR Specord Photometer 68 covering the same spectral range. It was found an absorption edge of 1.45eV for the thin CdTe films, which are in good agreement with the NIR spectra recorded on Specord Photometer 68.

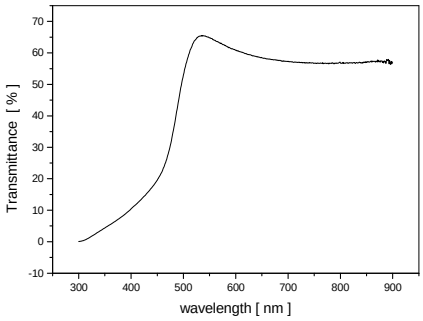


Fig. 3. Optical transmission spectrum of the CdS film was recorded on a Perkin Elmer 3B uv/vis spectrofotometer. The light beam was incident at the film side and the reference was the optical-glass substrate

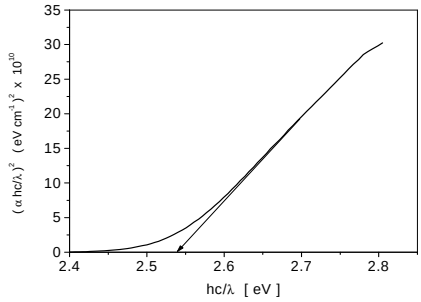


Fig. 4. The $(\alpha hc/\lambda)^2$ vs $(hc/\lambda)$ plot of the film of 0.65 μm thickness. The observed optical gap is $E_{go}$ = 2.48 eV.

Optical transmission spectrum of the CdS film was recorded on a Perkin Elmer 3B uv/vis spectrophotometer. The light beam was incident at the film side and the reference was the optical-glass substrate. Figure 3 shows the transmission spectrum of the CdS thin film. The high optical transmitance of the film at wavelengths longer than the absorption edge is similar to that of chemically deposited CdS thin films [38]. Figure 4 shows the $(\alpha hc/\lambda)^2$ vs $(hc/\lambda)$ plot of the 0.65 μm thickness film. The observed optical gap $E_{go}$ = 2.48 eV is slightly larger than $E_g$ = 2.42 eV which was observed for the CdS single crystal [39] at 300 K. This effect is attributed to very small grain size in the deposited film which leads to electrical isolation of individual grains, or quantum well structures [40].

## 6. Transport properties of II-VI narrow-gap semiconducting thin films

The electrical characterization of such structures is critical in the technological process. A method to determine the electrical conductance of semiconductor thin films that not require contacting electrodes is presented. This method, introduced by Sommer and Tanner [41], is based on measuring the amplitude and phase shift current of capacitive transmission line.

A setup consist of a three-electrode system above which the film is placed at a distance $d$ = 0.5 mm from the transmission line. An ac voltage ($V_c$ = 5 V) is applied to the first electrode. Using a lock-in phase amplifier, the current at the third electrode is phase sensitively measured. Since the capacitance of the air gap between the electrodes and the film is known, the method enables determination of the film conductance $\sigma_0$ of a sample by fitting the measured in-phase currents as a function of frequency. For a meaningful fit, it is essential that the peak in the phase current be measured.

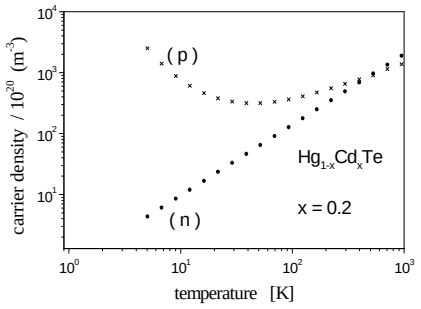


Fig.5. The experimentally obtained temperature dependences of the hole density $p$ and the electron density $n$ between 100 and 300K for the $x$ = 0.20.

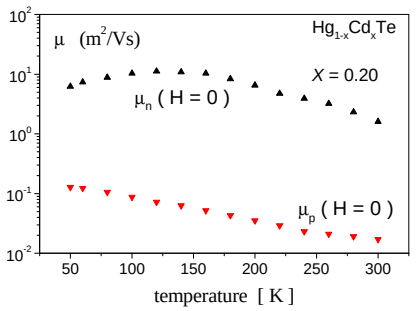


Fig.6. The experimentally obtained temperature dependences of $\mu_n$ and $\mu_p$ the mobilities of electrons and holes between 100 and 300K for the $x$ = 0.20.

The value for the angular peak frequency $\omega_{peak}$ can be expressed as [42] $\omega_{peak} \approx 8\sigma_0 / \alpha^2 \beta^2 \cdot \varepsilon_0 \varepsilon_r \cdot d$ , where $\alpha$ and $\beta$ are electrode geometrical factors and $d$ the gap distance between the electrodes and the film. From the peak frequency $\omega_{peak}$ = 10524 Hz, the calculated conductance of the CdTe/ Hg (1-x) CdxTe thin film heterostructure is $\sigma_0 = 3.2 \times 10^{-9}\ \Omega^{-1}$. Given a film thickness of 1μm, this means the conductivity is $\sigma_0 = 3.2 \times 10^{-5}\ (\Omega\text{cm})^{-1}$.

The Van der Pauw technique [43,44] was used to evaluate the film resistivity, free carrier concentration, and the Hall mobility. All Hall effect measurements were made in the temperature range from 100 K to 300 K, for $B$ = 0.6 T.

The CdTe/ Hg(1-x)CdxTe films were deposited into Van der Pauw clover leaf pattern, and the electrical contacts were prepared by Au evaporation. To express the resistivity explicitly we used the following relation [45]: $\rho = d/\ln 2\left(R_{AB,CD} + R_{BC,DA}\right)\cdot f\left(\frac{R_{AB,CD}}{R_{BC,DA}}\right)$ where $f$ is a form function [46]. The notation $R_{AB,CD}$ means the potential difference between contacts C and D when current is passed into A and return at B.

The Hall mobility can be determined by measuring the change of resistance $\Delta R_{AC,BD}$ when a magnetic field is applied perpendicular to the sample. The Hall mobility is then given by $\mu_H = \frac{d}{B}\cdot\frac{\Delta R_{AC,BD}}{\rho}$ where $B$ is the magnetic induction, $d$ the sample thickness, and $\Delta R_{AC,BD}$ the change of the resistance due to the magnetic field. The carrier density is given by $R_H = r\cdot 1/Nq$, where $r$ is a factor which depends on the band structure and the scattering mechanism, *i.e.* $r$=1.18.

The hole density $p$ and the electron density $n$ are [47]:

$$p = \frac{R_H\sigma^2 + \mu_n\sigma}{e\left(\mu_p^2 + \mu_n\mu_p\right)} \quad \text{and} \quad n = \frac{\sigma}{\mu_n e} - \frac{\mu_p p}{\mu_n}$$

with $R_H$ the Hall coefficient, $\sigma$ the electrical conductivity, $\mu_n$ and $\mu_p$ the mobilities of electrons and holes and $e$ the elementary charge, respectively.

Figure 5 shows the experimentally obtained temperature dependences of the hole density $p$ and the electron density $n$ between 100 and 300K for the $x$ value 0.20. Figure 6 shows the experimentally obtained temperature dependences of $\mu_n$ and $\mu_p$ the mobilities of electrons and holes between 100 and 300K for the $x$ value 0.20. According to [48] the experimentally obtained temperature dependence of $\mu_n$, the electron mobility should be dominated by phonon scattering above 100K. The experimentally obtained temperature dependence of $\mu_p$, the mobilities of holes should be dominated by a combined effect of ionized-impurity and optical-mode scattering [49].

## REFERENCES

1. G. Bunker, *Nucl. Instrum. Methods* **207**, 437 1983.
2. N. T. Gordon, S. Barton, P. Capper, C. L. Jones and N. Metcalfe, *Semicond. Sci. Technol.* **8**, S221 1997.
3. J. Marine and C. Motte, *Appl. Phys. Lett.* **23**, 440 1973.

4. J. Auleytner, *Phys. Status Solidi (a)*, **112,** 679 1989.
5. E. Indrea, M. Jaouen and P. Chartier, *Romanian Journal in Physics*, **43,** 251-259 1998.
6. R. H. Bube and K. W. Mitchell, *J. Electron. Mater*., **22,** 17-25 1993.
7. T. L. Chu, S. S. Chu, C. Frederics, J. Britt and C. Wang, *J. Appl. Phys.*, **70,** 7608-7612 1991.
8. E. Indrea, I. Bratu, Ileana Pop, Cristina Nascu and Violeta Ionescu, *Thin Solid Films*, **307** 240-244 1997.
9. D. –E. Arafah and R. Ahmad-Bitar, *Semicond. Sci. Technol.*, **13,** 322-328 1998.
10. S. A. Ringal, A. W. Smith, M. H. MacDougal, and A. Rohatgi, *J. Appl. Phys***., 70,** 881-889, 1991.
11. P. O. Vaccaro, G. Meyer and J. Saura, *J. Appl. Phys.*, **24,** 1886-1889 1991.
12. Z. C. Feng, H. C. Chou, A. Rohatgi, G. K. Lim, A. T. S. Wee, and K. L. Tan, *J. Appl. Phys.*, **79,** 2151-2153 1996.
13. J. Singh, *J. Mater. Sci***. 29**, 5232-5245 1994.
14. F. Beech and I.V. Boyd in: Photochemical Processing of Electronic Materials, E*ds. I.V. Boyd and R.B. Jackman* ( *Academic Press, New York, 1991* ).
15. E. Indrea, I. Deac, Adriana Barbu and Xenia Filip, *Appl. Surf. Sci.*, **106,** 70-74 1996.
16. Liana Pascu, Elisabeth-Jeanne Popovici, Rodica Grecu, Emil Indrea and Cristina Ciocan, Proceedings of the "2nd International Conference of the Chemical Societies", Athena, **Grece**, July 26-31, 2000.
17. J.G.M. van Bercum, A.C. Vermeulen, R. Delhez, T.H. de Keijser and E.M. Mittemeijer, *J.Appl. Phys.*, **27,** 345-353 1994.
18. N. Aldea and E. Indrea, *Comput. Phys. Commun.*, **60,** 155-159 1990.
19. E. Indrea and Adriana Barbu, *Appl. Surf. Sci.*, **106,** 498-501 1996.
20. E. A. Stern, "X-Ray Absorption Principles, Applications, Techniques of EXAFS, SEXAFS, XANES", Eds. D.C. Konigsberger and R. Prins, Wiley, New York, 1998.
21. J. J. Rehr and R. C. Albers, *Rev. Mod. Phys.*, **72,** 621-654 2000.
22. E. Indrea, M. Jaouen and P. Chartier, *Semicond. Sci. Technol.* **12**, 42-46 1997.
23. J. Mimault, J.J. Faix, T. Girardeau, M. Jaouen and G. Tourillon, *Meas. Sci. Techn*. **5,** 482, 1994.
24. P. Chartier, J. Mimault, T. Girardeau, M. Jaouen and G. Tourillon, *J. Alloys and Compounds* **194,** *77 1993*.
25. F.W. Lytle, D.E. Sayers and E.A. Stern, *Phys. Rev.* **B11,** 4825-4834 *1975*.
26. E.A. Stern, *Phys. Rev.*, **B10,** 3027-3034 1974.
27. A.G. McKale, G.S. Knapp and S.K. Chan, *Phys. Rev.* **B33,** 841-847 1986.
28. J. J. Rehr, J. Mustre de Leon, S. I. Zabinsky and R. C. Albers, *J. Am. Chem. Soc*. **113,** 5135, *1991*.
29. A.G. McKale, B.E. Veal, A.P. Paulikas, S.K. Chan and G.S. Knapp, *Phys. Rev.* **B38,** 10919-10244 1988.
30. D. Aberdam, "Software Package for EXAFS data Extraction and Modelisation", from author D. Aberdam, Lab. Cristallographie, CNRS, Grenoble, France 1997.
31. D. Long and J.L. Schmit, *Semicond. Semimet.* **18,** 18-22 1981.
32. A.G. McKale, B.W. Veal, A.P. Paulikas, S.K. Chan and G.S. Knapp, *J. Am. Chem. Soc.* **110,** 3763 1988.
33. R.A. Mayanovic, W.F. Pong, and B.A. Bunker, *Phys. Rev*. **B42,** 11174 *1990*.
34. E. Jaffe and A. Zunger, *Phys. Rev.* **B29,** 1882 1984.

35. J.C. Mikkelsen and J.B. Boyce, *Phys. Rev.* **B28,** 7130 1983.
36. A. Mandelis, in: "Photoacoustic and Thermal Wave Phenomena in Semiconductors" Eds. North-Holland, New-York, 1987.
37. O. Pesoa, L.C. Cesar, N.A. Patel, H. Vargas, C.C. Ghizoni and L.C. Miranda, *J. Appl. Phys.*, **59**, 1316 1986.
38. M.T.S. Nair, P.K. Nair, R.A. Zingaro and E.A. Meyers, *J. Appl. Phys.*, **75,** 1557 1994.
39. *CRC Handbook of Chemistry and Physics,* 70th ed., Eds. D.R. Lide (CRC, Boca Raton, FL, 1990.
40. G. Hodges, A.A. Yaron, F. Decker, and P. Motisuke, *Phys. Rev.* **B 36,** 4215 1987.
41. J. R. Meyer, C. A. Hoffman, F. J. Bartoli, D. A. Arnold, S. Sivananthan, and J. P. Furie, *Semicond. Sci. Technol.* **8,** 805- 814 1993.
42. E. Mounterrat, L.Ulmer, N.Magnea, and H.Mariette, *Semicond. Sci. Technol.* **8,** 261 1993.
43. Z. Dziuba, *Phys. Stat. Sol. (a)* **153,** 445-457 1996.
44. R. J. Severnes, H.J.M. Verhoven, M. Schaepkens, M.C.M. van de Sanden and D.C. Schram, *Rev. Sci. Instrum.* **67**, 3624-3626 1996.
45. L.J.Van der Pauw, *Philips Tech. Rev.*, **20,** 220-225 1958.
46. A.Mezerd, D. Sayah, I.J. Saunders and B.K. Jones, *Phys. Stat. Sol.* **119,** 487-494, (1990).
47. M. Winecke, M. Schenk and H. Berger, *Semicond. Sci. Technol.*, **8,** 299-302 1993.
48. J.J. Dubowsk1, T. Dietl, W. Szymanska and R.R. Galazka, *J. Phys. Chem. Solids,* 351-355 1981.
49. W. Scott, E.L. Stelzer and R.J. Hager, *J. Appl. Phys.*, **47,** 1408-1412 1976.

STUDIA UNIVERSITATIS BABEŞ-BOLYAI, PHYSICA, SPECIAL ISSUE, 2000

# THE EVOLUTION OF THE NATURAL MAGNETIC FIELD ENVIRONMENT AND ITS SIGNIFICANCE FOR TERRESTRIAL LIFE

**V.V. MORARIU**

*Department of Biophysics, National R&D Institute for Isotopic and Molecular Technologies, 3400 Cluj-Napoca, P.O.Box 700 and, E-mail: vvm@L40.itim-cj.ro and Babes-Bolyai University, Cluj-Napoca, Romania*

It has been established that the fluctuations of the geomagnetic field (GMF) may have a significant impact on the health (See for example the proceedings appearing in Biofizika, 1995 vol 40, No 4 and No 5). At the same time it is believed that GMF represents a environment factor thereby influencing to a great deal the terrestrial life. However this factor received much less attention compared to others which appear to be more stressing or even violent, with immediate consequences for the human kind and life on Earth in general. On the other hand the natural magnetic environment or GMF, is not a constant environment. At contrary it has a complicated dynamics if regarded on a wide span of time. The purpose of this work is twofold: 1) to point out this complexity and its influence on the terrestrial life and 2) to analyse the possible outcome of a magnetic polar reversal on the present status of life.

## The complexity of the geomagnetic field

The geomagnetic field has been a witness of the apparition and evolution of life on our planet. It is a sort of a common belief that terrestrial life depends on the existing GMF although systematic investigations and development of adequate interpretation have not substantiated this idea, at least on a grand scale of time. The starting point of this work is that GMF is not a constant environment. There are fluctuations which extends from a very short time scale of minutes up to very slow changes which extends over hundreds of thousands of years. They can be briefly summarised as follows:

-Micropulsations with amplitudes up to several tens of nanotesla

-Diurnal changes: GMF decreases from morning till noon and then increases again to the initial level. The amplitude is about 100 nanotesla.

-Magnetic storms more frequent during the spring and the autumn and lasting for a time interval of one or several days. The amplitude is of about several hundreds of nanotesla. The average global activity is estimated by the Ap index (fig.1).

-Increased geomagnetic activity during the maximum of solar activity which extends to a 11 years cycle ( fig.2).

- Time intervals of tens of thousands to hundreds of thousands of years when GMF varies very little which is followed by polarity reversals. Such a magnetic polarity reversal (MPR) is accompanied by a period of thousands of years when the GMF is practically zeroed. It has been suggested that such events may cause biological mass extinction (Harrison and Funnel, 1964; Watkins and Goodell, 1967). This is a dramatic claim which deserves much attention. The last MPR took place 780,000 years ago and the current period is known as the Brunhes chron. (fig.3). The previous time interval when the magnetic polarity was reversed is named Matuyama chron (fig.3). We notice that during a polar reversal the intensity of GMF decreases down to almost zero then increases again but polarity is reversed. At the same time the recovery of the magnetic field is much faster than the decrease in the previous period. Further it is estimated that ahead of us is a new MPR event, possibly to take place in about 1000-2000 years. GMF decreased by about 50% during the last 2000 years (fig.4). One can notice that more than 4000 years ago the intensity of the geomagnetic field was even weaker then at present. However no MPR occurred at the time. The present average value of GMF is around 0.5 Gauss (or 50,000 nanotesla) at mid latitudes.

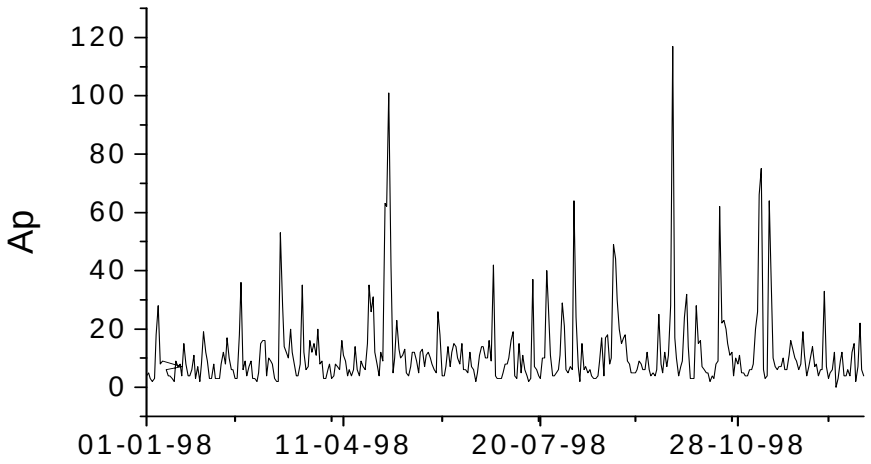


**Fig.1.** Geomagnetic activity measured by the Ap index during 1998. The scale of magnetic storms: Ap= 30-49, - minor storm; Ap= 50-99, - major storm; Ap= 100-400, - severe storm. One can notice that during the spring and the autumn there were two severe storms.

**Role of GMF for terrestrial life**

We know from the field of biomagnetism that weak to moderate fields may influence in a complex way the living matter.

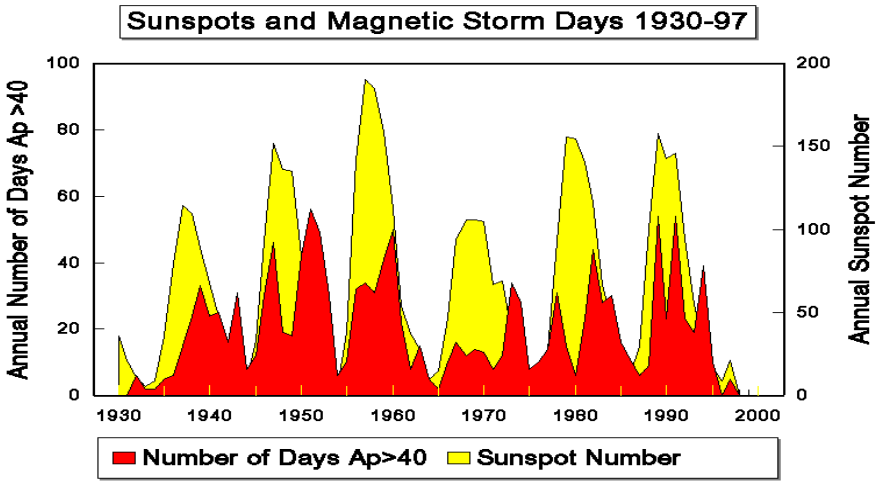


**Fig.2**. The years with increased solar activity (measured by the sunspot number) coincide with periods with increased number of days characterised by a higher geomagnetic activity. At present we are in new solar cycle which peaks up in the year 2000 (not shown in the figure).

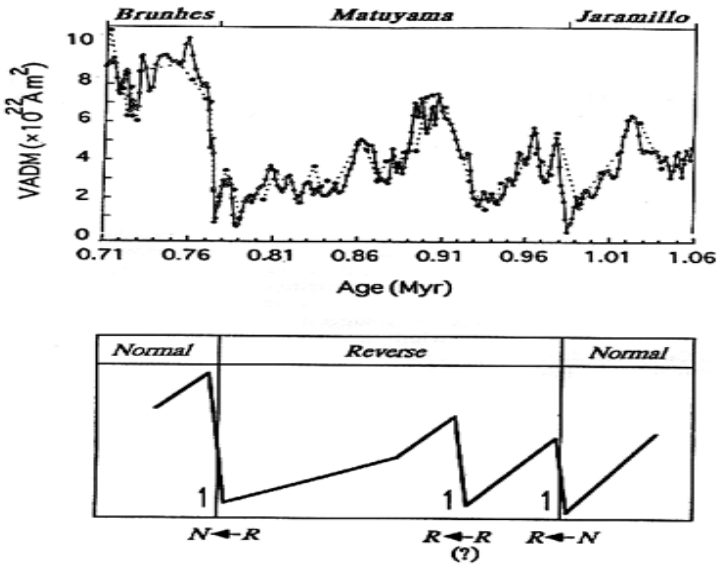


**Fig.3.** The last polar reversal occurred about 780,000 years ago. During the previous magnetic period (Matuyama chron), the polarity was reversed compared to the present time. The intensity of the field decreased slowly at almost zero, then polarity reversed (the present Brunhes period or chron) and the intensity increased much more rapidly than the decay of field during the previous period. One can notice a long-term asymmetric saw-toothed pattern: (above). Variations in relative paleointensity (expressed as VADMs, virtual axial dipole moments) across the normal-to-reverse (N -> R) Upper Jaramillo and reverse-to-

normal (R -> N) Matuyama-Brunhes reversals obtained from ODP Leg 138 sediments from the equatorial Pacific. Open and solid circles are U-channel and discrete sample measurements, respectively (Courtesy of J.-P. Valet and L. Meynadier); (below) Schematic diagram of the general intensity pattern suggesting that field revitalization occurs not only during successful reversals, but also during unsuccessful, or aborted reversal attempts (Hoffman, 1995).

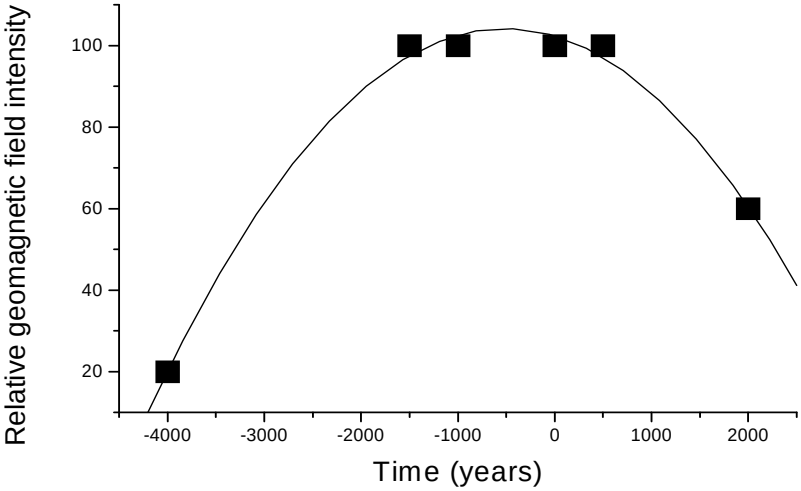


**Fig.4.** The current historical period of time and the evolution of the geomagnetic field. Data collected from the following sources: for the years 4000 BC and 0, from Merrill, 1990, and from Quing-Yung et al, 1987, for the rest of the data. The data in the graphic have been linked by considering their relative value.

-The micropulsations may involve variations with a frequency ranging between 0.1 mHz and 100 Hz. The lower the frequency the lower the field strength. For example micropulsations with a frequency of about 0.2 mHz have an amplitude of about 500 nT, at 3 mHz, an amplitude of about 50 nT, whereas beyond 0.1 Hz the amplitude is below 0.5 nT. Therefore only the infralow frequencies might have a significance in respect to the amplitude.

At present we do not know what is the influence of these kind of fields.

-The diurnal variations: this is also an unknown matter. In other words we do not know what is the influence of the absence of a such regular variations.

-The magnetic storms: There is a vast literature which proves that magnetic storms promptly triggers effects in living organisms. Many aspects of human health is negatively affected. There is also some evidence that non-equilibrium physicochemical processes may be affected.

-The geomagnetic activity extended over longer period of times (seasons, solar cycles): It is evident that increased number of days with magnetic storms during the spring and the autumn and during the maximum of solar cycles should enhance the deleterious effects.

The effects are sensed at individual level but also at populations levels including all kind of phenomena such as economical, political, sociological.

All the above phenomena refer to relatively short time variations of magnetic fields extending up to several days and their additive effects over periods of the order of years. They can be investigated in laboratory conditions and can be monitored in the every day life.

-The drift of the GMF over long period of times and magnetic polar reversals (MPR): This is a different matter compared to the above fast variations of GMF. The characteristic of the drift is a change of the static component of the GMF over hundreds of thousands of years therefore much slower than the modulation of GMF by the activity of the sun. At the same time the total change of the GMF intensity is much higher than the above class of changes. The lower limit is the nulling of the GMF, which occurs at the time of the MPR. Such a phenomenon cannot be simulated in laboratory. Exposing of a living system to a zero magnetic field in a laboratory device, does not in fact simulates the real situation. At the present time such an experiment involves a sudden drop of the magnetic environment from a field of about 0.5 gauss to a zero field. This can cause significant effects ( Morariu, 1999, Dorofteiu et al, 1995, Morariu et al.,2000, Ciortea et al., 2000). However the real situation will be achieved in about 2000 years which means a gradual and very slow decrease. In other words the stress imposed on a living creature by presently exposing it to zero magnetic field is indeed high, compared to the real situation which permits adaptation during many years of practically insignificant yearly decrease.

**Adaptation to the magnetic environment**

Is there any possible support from bioelectromagnetism for mass extinction during MPR? As suggested above this a matter of adaptation of the living systems to the ever changing GMF. These changes involve fluctuation (magnetic storms) superposed on a slow but significant drift of its intensity, culminating with the almost total annihilation during MPR. We can see that relative small fluctuations (such as those caused by magnetic storms) can cause serious health effects. However they represent rapid changes of the environment of the order of hundreds of nanotesla per day. The slow drift which occurs between MPR ( see fig.3) does not in fact represent a stress for terrestrial life or at least we are not aware of it.. It is estimated that the present rate of the GMF decrease of the intensity is about 0.02% per year (NASA information). Such a small variation would pass unnoticed while other fluctuations of the environment impose a much higher stress. The alternative is that there is possibly a threshold for the absolute value of GMF. However no total life extinction occurred on Earth during MPR, therefore we may

suspect that the gradual change of GMF permitted enough adaptation. If the rate of change of GMF intensity is the important matter then we could possibly imagine that a catastrophic impact of a MPR would only occur if it lasted for a very short of time. An abrupt change could possibly be regarded as a MPR which might have lasted several months. Such a ultrarapid MPR has been suggested to have occurred in the Steen Mountains, Oregon, 15.5 million years ago, but it is highly controversial (Coe and Prevot, 1989; Coe et al. 1995). Such a reversal could indeed cause a major biological effect on the mammals of our time, but we do not know what could have been the effect on the life 15.5 millions years ago. Any way, no major extinction has been recorded at the time. Mass extinction on a grand scale, are dated much earlier. The latest occurred 65 million years BP. While the extremlely slow change of the geomagnetic field towards a zero value may allow for adaptation of many biological processes one may ask what would be the effect of the zero magnetic field in the case of species which essentially depend on the magnetic orientation such as bees or migratory birds. The zero field period itself is not known exactly how long time it lasts but from fig. 3 it may be estimated to tens or hundreds of years at most. Such a zero field is not necessarily associated to a MPR. During the Matuyama chron a zero field was eventually reached without MPR. During such a period of time with a practically almost zero level of the geomagnetic field some species may be in serious trouble. For example the bees would not find the home and they would dissapear in a single year. We do not know the answer from paleontology but it is quite clear that bees have not dissapeared during the last MPR and neither the migratory birds have suffered such a dramatic event.

We should further consider the evolution of the magnetic field which follows the time interval of zero magnetic field, when the geomagnetic field increases very fast compared to the its evolution before the zero field. As seen from fig.3, this period may lasts for several thousands of years which is very little on the geological scale. However this again represents a large enough time interval to allow for adaptation. A change of the geomagnetic field from 0 to 4 Gauss in 2000 years would represent a change of 0.002%, even less then the present rate of change so that again we cannot expect any significant effect.

Therefore according to the present evaluation it is not likely that a MPR could have had a dramatic impact on terrestrial life, and cause extinction. MPR which involves a short period of zero magnetic field might pass unnoticed although it is not clear to what hapened to the species which vitally depend on the magnetic orientation. The paleontological record also do not seem to support a link between MPR and mass extinction's (Plotnick, 1985; D. Jablonsky, personal communication). According to Jablonsky, a revival of the idea of a link between MPR and mass extinction has been produced by Raup (1985) but it was quickly refuted by Lutz (1985) and Raup retracted his claim.

During the past 6000 thousands of years of history and prehistory, there was a relatively high value of GMF intensity (fig.4). This field decreased since the beginning of our era. Despite of a reduction of about 50%, it is not possible to associate this variation with any catastrophic event at biological level. Nevertheless we do not know what could

have possible been the impact of these changes extended over moderate time scales on the terrestrial life.

On the other hand, our own experiments showed that exposure to a magnetic field of double intensity, compared to present, it has a significant impact on the growth of plants (V.V.Morariu, unpublished results). This is, again, an effect resulting from exposure of the plants to a sudden stress.

A major problem in understanding the effects of various electromagnetic fields on living systems is the fact that the main body of experimental data reflect only effects after exposure for a given time interval to a certain field (intensity and frequency). The result is a frustrating incomplete picture; we do not know anything about the limits of the adaptation process for a given stress of the given living system.

There is a great need to have data concerning the effects of a given field intensity at various time intervals in order to understand the process: is it a simple dose-depended effect or it is a an adaptation effect ? In the case of an adaptation process, the effect increases in time, then decreases to the initial or somewhat modified level. Such experimental data are little available in the literature and are difficult to obtain. Therefore in the case of exposure to a magnetic field which is different to the present GMF, there are two alternatives: a) Either the effect is dose-dependent in a monotonous manner or, b) The effect is non-linearly dependent on the field intensity. Clearly the question is when is considered the effect, as in the case of an adaptation process, the effect varies with the time. If too long time is allowed for the exposure, little or no effect, could be observed. At intermediate time exposures, the effect may be important but the effect is only transient. I believe this aspect has been essentially missed in a large body of experiments in the field of bioelectromagnetism.

Our own experience in the field of zero magnetic field effects on living systems has occasionally suggested that the effect against field intensity is non linear, i.e. it shows, for example a minimum at GMF values whereas the effect is high, both at higher and lower fields.

This is suggesting an adaptation process. Despite the fact that the effect is qualitatively similar at higher or lower fields than the present GMF, the mechanism must be different as the field dependence of the effect has opposite signs in the two domains.

## Conclusions

The fluctuations of the geomagnetic field occurring during the magnetic storms cause a significant impact on the terrestrial life. These represent rapid variations extending over a time period of the order of days.

The change of the geomagnetic field over hundreds of thousands of years cover the magnitude of the field itself. When present living systems are exposed in laboratory conditions to such a change of the magnetic environment (which represents an abrupt change from 0.5 gauss to almost zero field, for example) then it causes very important effects. We hypothesise that in real conditions, the extremely slow change of the field

might allow for adaptation and therefore mass extinction is not likely to be caused. This might be valid both during the zero magnetic field and during the short period of several thousands of years which involve the return of the geomagentic field to a high intensity. However the zero magnetic field itself which may lasts for tens or hundreds of years might have an impact on the species which depends esentially on the magnetic orientation such as bees and many bird species. However there is no clear paleontological evidence for a such a critical event.

**Acknowledgements**

I thank Professor David Jablonsky, University of Chicago, for his advice.

## REFERENCES

1. Coe, R.S. and Prevot, M., 1989, Evidence suggesting extremely rapid field variation during a geomagnetic reversal. Earth and Planetary Science Letters, 92, 292-298.
2. Coe, R.S. et al. 1995, New evidence for extraordinarily rapid change of the geomagnetic field during reversal, Nature, 374, 687.
3. Ciortea, L., Morariu V.V., Todoran, A. and Popescu S., 2000, Life in zero magnetic field Part III Effect on zinc and copper during in vitro aging of human blood, Electro and Magnetobiology (in print).
4. Dorofteiu, M., Morariu, V.V., Marina C. and Zirbo, M. 1995. Life in zero magnetic field. Part I. The effects of near null magnetic field upon the leucoyte response in rats, Cytobios, 84, 179-189.
5. Harrison, C.G.A. and Funnel, B.M., 1964, Relationship of paleo magnetic reversals and micropaleontology in two late Caenozoic cores from the Pacific Ocean, Nature, 204, 566.
6. Hoffman, K.A., 1995, How are geomagnetic reversals related to field intensity? Eos, 76, 289-292.
7. Merrill, R., 1990, A slow moving field, Nature 345, 675-576.
8. Morariu, V.V. 1999, Life in zero magnetic field, http://www.L40.itim-cj.ro/Bio.
9. Morariu, V.V., Daniela Ciorba, Silvia Neamtu, 2000, Life in zero magnetic field Part I. In vitro aging of human blood, Electro and Magnetobiologiy 19, 271-278.
10. NASA Marshall Space Flight Center: The natural space environments; Geomagnetic field (WWW information).
11. Quing-Yung Wei, 1987, Geomagnetic intensity as evaluated from ancient Chiniese pottery, Nature, 328, 330.
12. Plotnick, R.E., 1980, Relationship between biological extinctions and geomagentic reversals, Geology, 8, 578-581.
13. Raup, D.,1985, Magnetic reversals and mass extinctions, Nature,314, 341-343.
14. -Watkins, N.D. and Gooodell, H.G., 1967, Geomagnetic polarity changes and faunal extinction in the southern ocean, Science, 156, 1983-1987.

STUDIA UNIVERSITATIS BABEŞ-BOLYAI, PHYSICA, SPECIAL ISSUE, 2000

# STUDY OF UNDERGROUND WATERS FROM NORTHEASTERN DOBROUDJA KARST USING DEUTERIUM AS NATURAL TRACER. CASE STUDY

**VICTOR FEURDEAN, LUCIA FEURDEAN**

*National Institute for Research and Development of Isotopic and Molecular Technologies*
*P.O.Box 700, 3400 Cluj-Napoca 5, Romania. E-mail: victor@l40.itim-cj.ro*

## 1. INTRODUCTION

The environmental isotopes are efficient physical indicators because they respond to the requests of the geologist to find a smaller anomaly in a greater or deeper study area. Deuterium in groundwater from karst is less prone to diagenetic alteration and is not affected during the isotope exchange between water and carbonate minerals being a sensitive indicator of water source and movement of water in under ground. Oxygen isotope exchange at low temperature (<100°C) has been observed to occur at reasonable rapid rate [1] where the dissolution and recrystallization of the carbonate dominate the isotopic exchange mechanism [2, 3]. This paper describes only the use of the deuterium as environmental isotope to determine the groundwater origin, the recharge of the shallow aquifer and deep aquifer, the mixing processes, the groundwater flow paths and the transport processes that induce the spatial distribution of deuterium in study area.

## 2. THE STUDIED AREA

The investigated region is located in the NE Dobrogea depression (Fig. 1). Information on the hydrological characteristics of the aquifer systems was obtained from [4, 5]. The main elements that define the hydrological conditions of the region are characteristic of a karst region. The rocks, which belong to the Middle Triassic formations, are situated on a Palaeozoic basement and are represented by dolomitic limestone with numerous impermeable breaks (clayey shells, sandstone). An important characteristic of these aquifers is the intrinsic heterogeneity of the infiltration and the distribution of the permeability that is reflected in the fluctuations of chemical and physical properties of the water.

Climate is semiarid with precipitation below 400 mm/year and the evapo-transpiration is close to the value of the precipitation. Consequently the climate has a small contribution on the underground. Groundwater from the Middle Triassic limestone is generally under pressure showing resurgence either at the contact with the impermeable rocks or in the fracture regions (Malcoci, Murighiol, and Plopu).

## 3. METHOD

The method described in a previous paper [6] is mentioned briefly:

- Monthly water samples (18 local fountains, 3 springs, 8 water wells) were collected from March to September 1993.
- Measurements of isotopic ratio of hydrogen from water were performed on THN 202 mass spectrometer (CEA-France) and expressed in delta units (δ) related to V-SMOW [7]. The analytical reproducibility for δD is ±0.5‰.
- The measurements of the density of water samples (Δdens) were made on DMA 02 C digital densimeter with an error better than ±1 %.
- Interpretation of the results. The spatial and time variability of input of the environmental isotopes in the hydrologic cycle and the construction of equipotential lines and flowlines set are the keys of interpretation in the investigations of isotopic hydrology.

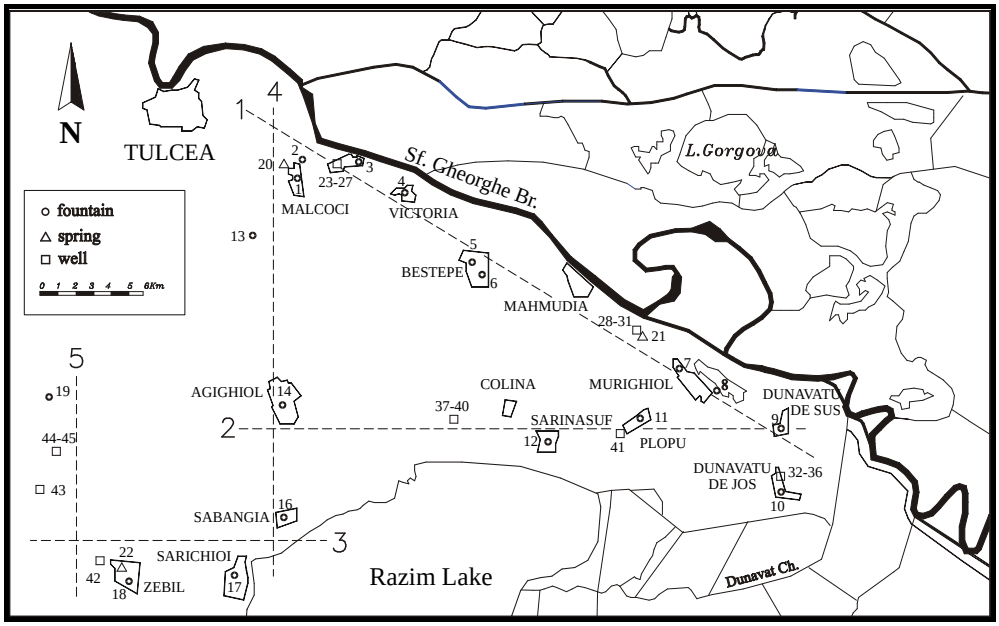


**Fig. 1.** Study area and the location of the sampling points.

## 4. RESULTS AND DISCUSSION

The average values of the measurements are plotted in Figure 2. The δD average values vary in the range from -87.5‰ to -54‰, those of all samples range from -92.8‰ to -49.5‰. For Danube River the δD average value is -75.2‰. The local infiltrating waters represent 81% of samples ranging from –75‰ to –65‰. Waters from high altitude (>1000m a.s.l) are depleting in deuterium having δD <-80‰ and

correspond to samples 16 and 40. The δD > –60‰ correspond to samples 18 and summer collecting samples from continental side of study area which present distinct seasonal characters. Δdens average values vary in the large range, the most samples having Δdens near 800 mg/l, typically for fresh waters, the samples 1 and 16 having Δdens >3000 mg/l.

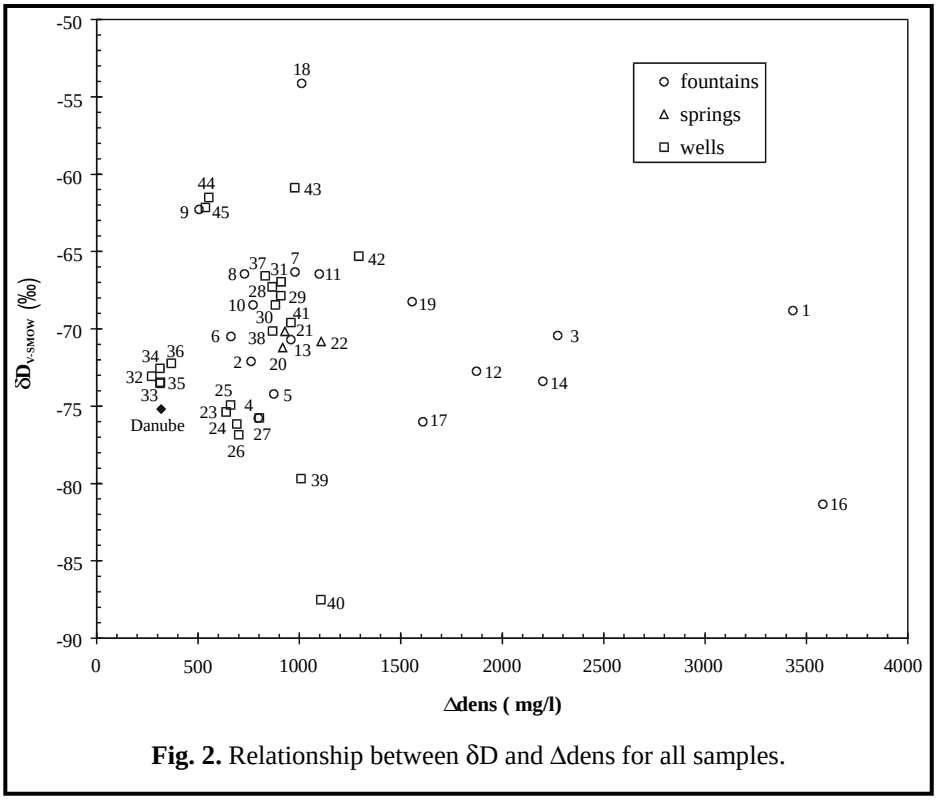


**Fig. 2.** Relationship between δD and Δdens for all samples.

Finally, the disposal of the samples values in δD-Δdens diagram suggests that the water from the most sampling sites results from both the local infiltration and mixing processes. There are a few samples (1, 16, 18, 40) that have δD and Δdens values well differentiated from the most samples.

**4.1. Wandering area.** On the δD-Δdens diagram, for one and the same sample, the suites of δD and Δdens values (monthly sampling) determine an area and we named it "wandering area". This area is proper for the water of each sampling point. Its slope indicates the predominant processes that determine variations of the δD and Δdens values. The upward inclination indicates the preponderance of evaporation-condensation processes and downward inclination indicates the preponderance of mixing processes.

The hooked shape of wandering line for samples 1 (Fig 3a) can be explained by following processes. One could be the evaporation of local infiltrating water, the other could be the rock-water interaction between the meteoric water with low δD recharged at high altitude and carbonates and finally the mixing between these two waters types.

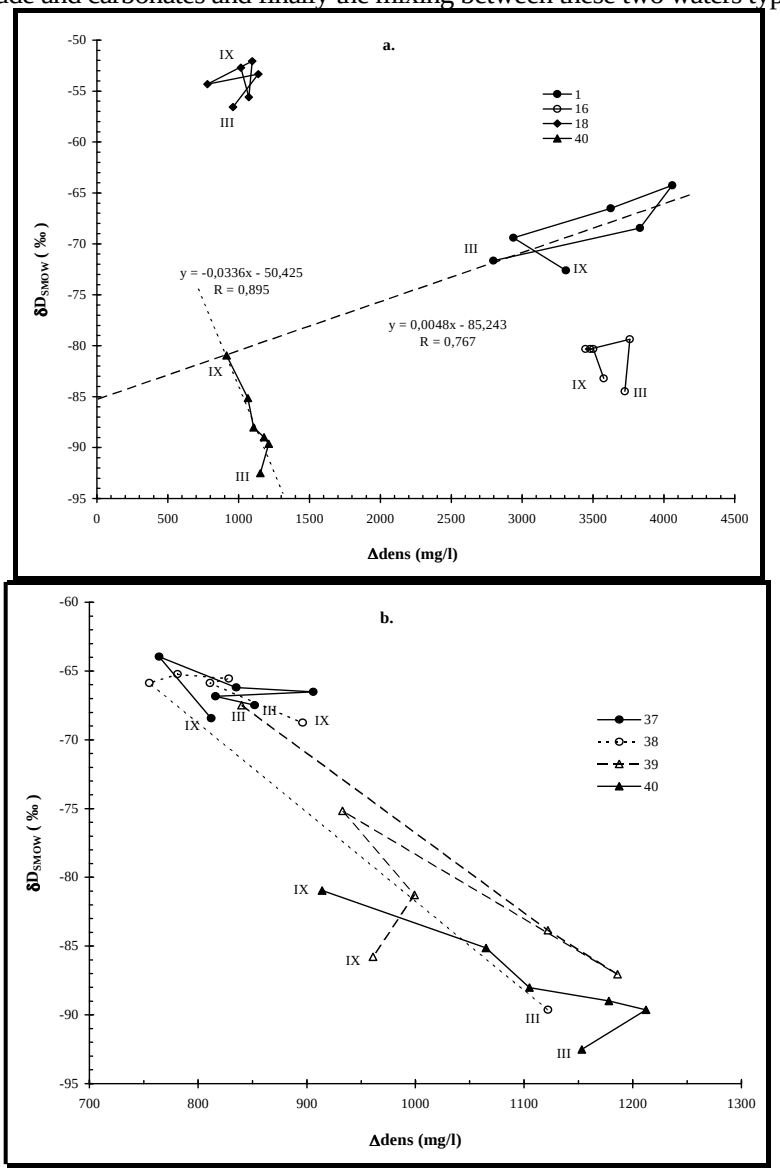


**Fig. 3.** Illustration of δD-Δdens values variation for samples from the fountains 1, 16, 18, 40 (a) and the well named km. 57 (b). The suites of δD-Δdens values were measured on monthly water samples collected from March (III) to September (IX).

Samples 40 and 16 are depleted in deuterium (δD< -80‰) relative to δD values of surface and groundwater in the geographic area from which they were collected (δD> -75‰). Feurdean and Feurdean [6] examined the processes that might alter D/H ratios within a basin and they proposed that altitude effects are predominant over paleoclimatic effect in depleting the deuterium. The low salinity and low δD from samples 40 suggest that fresh water-rock interaction is limited by one of the factors [8]: a) high flow rates through the carbonate aquifer that may not permit dissolution reactions to progress or b) flow through the fractures or karstic channels that are lined with carbonates that have previously been recrystallized and chemically equilibrated. The low δD and higher salinity values of samples 16 and its wandering area without the progressive deviation along a line of the δD and Δdens values can indicate the mixing processes involving two types of waters: the one with low δD and low Δdens and the anther with higher δD values (local infiltration water) and Δdens higher. The low δD and higher Δdens values are not a strict function of mixing processes because dissolved solids may be added to or removed from system by dissolution or crystallisation without affecting deuterium content [8].

For samples 18 the δD and Δdens values are not correlated, the wandering area (Fig 3a) can not indicate a distinct trend of its orientation. The wandering lines corroborated with evolution in time of δD values suggest that water of samples 18 could be from a reservoir without links with other aquifers.

**4.2. Variation in time of δD values.** The variability in time of δD values can be used in a qualitative way to identify the origin of water and to provide support for preliminary conclusions with respect to mixing waters [9]. Over a long period the δD values of precipitations represent a steady state input with random fluctuations about the mean. The original input variability is preserved to a considerable degree in groundwater that recharge appears to be directed into fractures and tubular opening and water moves rapidly through these openings. The damping of input variability in time-series δD values is reflected when the water travelled the great distance on underground reservoir. The small variation in time of δD values shows that the sampling point is supplied with water either from a closed reservoir or from an open one but with a rapid and well mixing of the whole source. The great variability is due either to the seasonal effect or to the strong influence of the mixing waters that have different characteristics. Two simple models of the flow system [10] can affect the evolution in time of deuterium concentration for the water from sampling site: the well-mixed reservoir model and the piston-flow model.

Based on deuterium variability in time the following water types were delineated:

**A.** Waters with variation of δD in time due to seasonal trend (the samples 1, 2, 9, 13, 16, 41, 43, 44 and 45). The seasonally isotopic gradient is more extent in the continental site (10 ‰ in the samples 43, 44 and 45) and dumped in vicinity of wet sites (5 ‰ for the samples 1, 2, 9 and 13).

**B.** Waters that have the variability of δD in time smaller than those of the Danube. The most of these samples are on NW-SE alignment and the small variability shows the interception of the ground layer in connection with Danube River. The samples 3, 6, 8, 10 and 21 perceive the influence of water with low δD during summer when the level of Danube waters is lower and its contribution is lesser important to recharge of aquifer [11]. It is reasonable to consider that waters from NW-SE transect is mainly subordinated to Danube waters and only secondarily to the groundwater depleted in deuterium from Triassic limestone.

**C.** Waters represented by the rest of samples that present great variability in time, due to the strong influence of mixing waters with different isotopic composition and/or different origins. For wells the depth of the intercepted water layer varies among 10m and 30m and the evolution in time of the δD values is similar for one and the same well, except the values of well Km 57. Their evolution in time and wandering lines for well Km 57 points out the supply from an endless reservoir (Danube) for 37 and a high altitude water for samples 40. For 38 and 39 the greatest variability indicate the preponderance of a mixing/dilution process of these two types of waters.

**4.3. Mixing lines.** The water mixing in underground can be pointed out by the measurements of the two additive properties of the water, as deuterium content and total dissolved salts content. The aligned points by one line with good correlation factor on the diagram of δD-Δdens average values suggest that the suite of samples belong to the mixing system of two water types endmembers.

The alignments of the samples suites corroborated with the evolution in time of δD values for the samples of residential fountain 14 (Fig. 4a) and for samples 12 (Fig. 4b) revealed that its water is originated in mixing processes between the water with different isotopic content. One of endmembers is heavier isotopic water that belongs to local recharged water or water coming from phreatic layer fed by Danube. The other endmember recharges at an altitude that is higher than 1000 m and can interact with rock and/or progressively mix with local meteoric water in its travel zone.

The distribution of the points 37, 38, 39, 40 and 7, 41, 39, 40 on δD-Δdens average values diagram (Fig. 4c) suggests a very good vertically mixing of the two isotopic types of the waters: one corresponding to the phreatic waters tributary to Danube and the other one corresponding to the high altitude water from Triassic limestone that was found at bottom of well km. 57. The water of samples 39 and 41 arises from two mechanisms responsible for confined delivery and the dewatering of unconfined aquifer. The levels corresponding to these samples discharge vertically and horizontally (artesian flow for water of site 41). The confined aquifer (sample 40) and the aquifer associated to samples 14 and 12 discharge in an area with water of type 17.

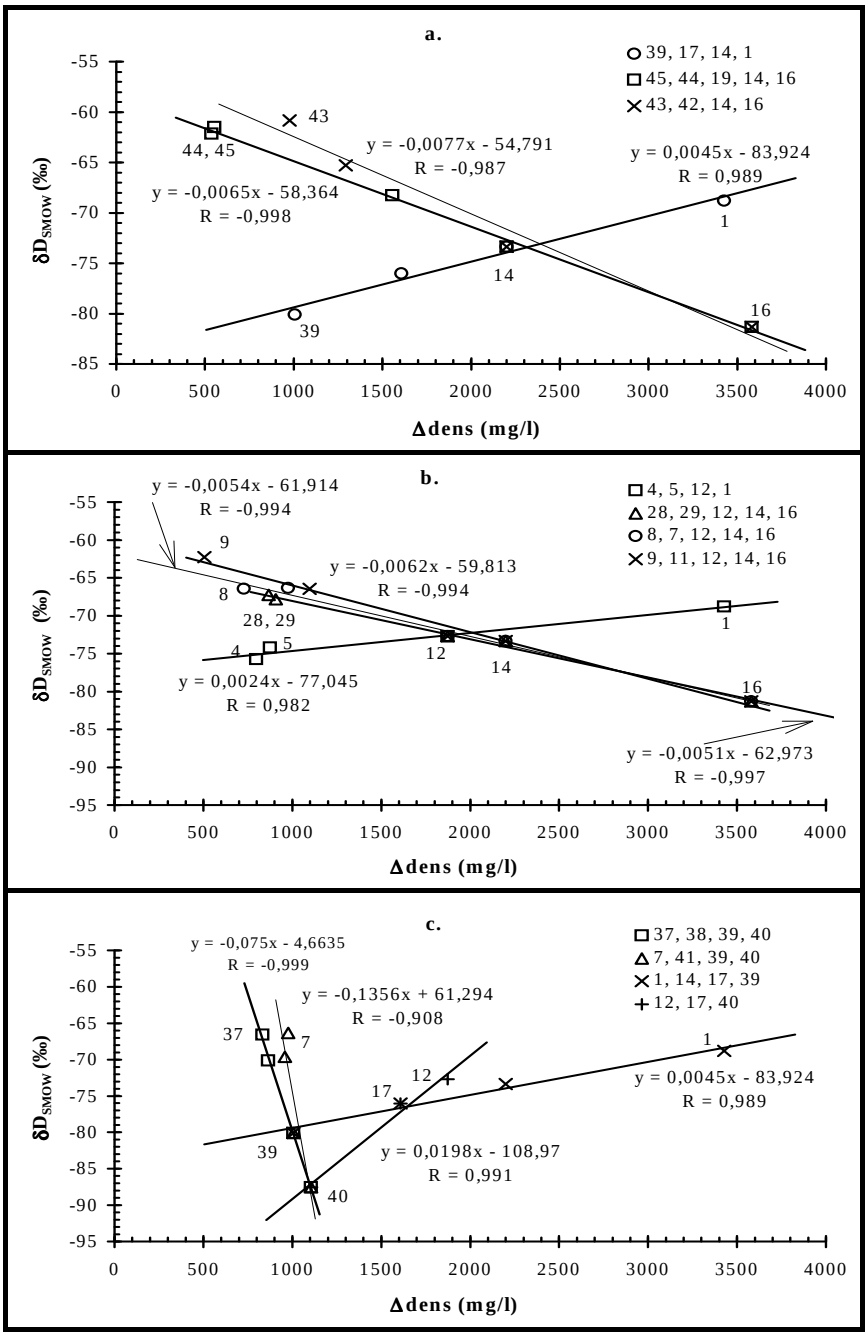


**Fig. 4**. δD-Δdens relationships in groundwater mixing. The mixing systems are for samples: 14 (a), 12 (b), and well km. 57 (c).

**4.4. Variations in space of the δD mean values**. The waters of sampling points by the NW-SE direction (transect 1) present a linearly increase of the δD values (Fig.5a). The isotopic shift towards higher values than of values of Danube of shallow groundwater (with about 12‰) can be due to two recharge components [12]. a) One is the influent that flows perpendicular to the cross-section of groundwater basin and can be explained by intense recycling of moisture within basin by the evaporation-condensation processes. b) The another is the effluent that flows parallel to cross-section.

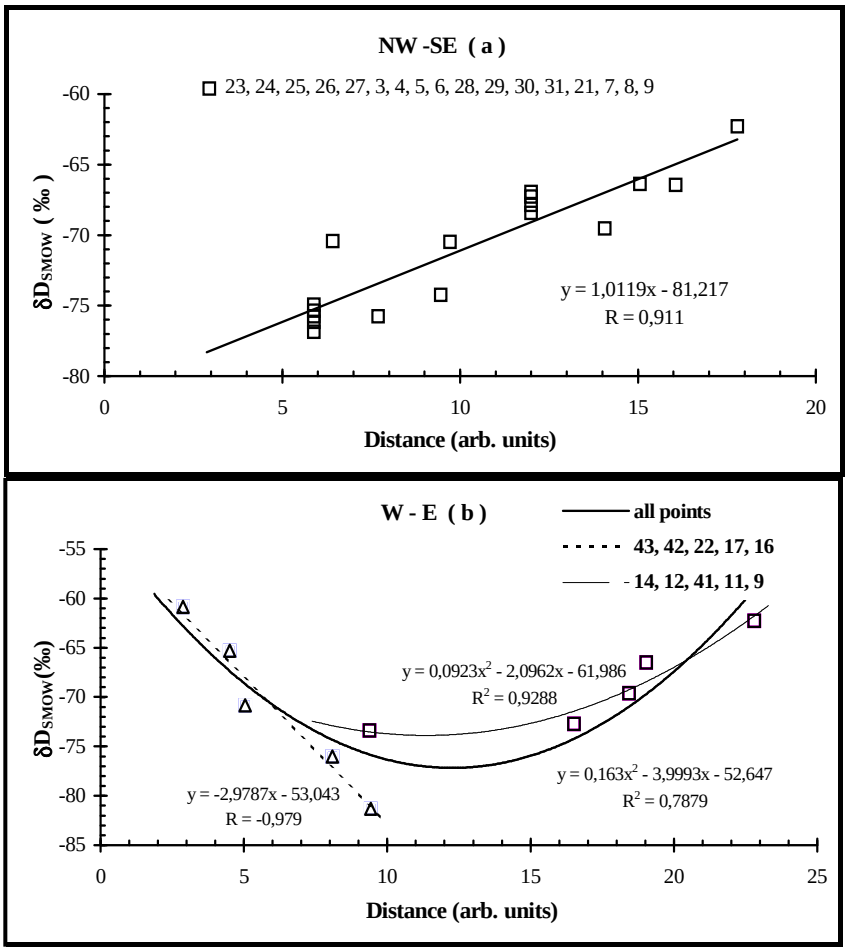


**Fig. 5.** Variations in space of the δD values for samples on the NW-SE transect (a) and W-E transect (b). The legend presents the samples ordered by increasing of distance (arbitrary units).

For the W-E direction (Fig.5b), δD average values present a parabolic evolution with a minimum of δD in the zone of the well Km 57 (not included in figure). δD average values decreases linear from west to east by the transect 3. The δD values slightly increase from west to east, towards the wet zone, by the transect 2. This different behaviour leads to the idea that there exists water with low δD that migrates in underground determining the waters mixing. Such water was identified at bottom of well km. 57 and in fountain 16.

**4.5. Isotopic patterns.** The deuterium content distribution as a result of the most important factors affecting transport behaviour can be examine by the isolines of equal deuterium mean content. The "isotopic relief" represents the isotopic gradients that may be an index of the groundwater movement velocity and the spatial variability in the hydraulic conductivity.

The spatial distribution of deuterium average content is given in Figure 6. The maps correspond to δD mean values of all samples associated with the δD mean values of four sampling levels for well km.57.

Three areas can delineate for which the relative configuration of isoline shape remains the same. A fourth area has a modified configuration of isolines. The substructures are:

1. Aquifer in the N part of the study area corresponding to site of the samples from Malcoci-Nufaru. In this substructure the percolation water contributes the most to limestone drainage and flow descending with different velocities on the flanks of the Tulcea-Mahmudia anticline. Light isotopic water appears in the fountains 2 and in the spring 20 either by diffuse flow or by vadose trickletes.
2. Aquifer situated in the SW part. For this aquifer the shape of the isolines is influenced by the source 18 that causes the appearance of a "peak" suggesting the absence of the links with the aquifers of study area (Fig. 6). The local infiltration waters feed the substructure. The underground streams seem to be local flows towards W. Here the percolation component moves likely slowly through texture soil, which cover limestone.
3. Phreatic aquifer tributary to Danube River. On the NW-SE direction the isolines do not change essentially their configuration (Fig. 6). The groundwater seems to move horizontal through homogeneous geologic materials towards the SE part. The cumulative effect of the lying groundwater stream on NW-SE direction and the vertical influx with higher δD can be the cause of the higher isotopic content. The isotopically lighter water, as input to the phreatic system during summer, traverses the flowpath without mixing by piston flow model [10] and modifies slightly the isolines shape without changing the direction of the streamline (samples 6, 8 and 21).

The displacement to the west of the isolines with lower δD for uppermost horizon (Fig. 6a, 6b) indicates that the phreatic water moves towards the zone of sink Colina. The region of sources 12-37 is one discharge area for phreatic system.

The mixing lines of the sources 12 are a support for this [6]. In the SE part the isolines tend to become almost parallel with E-W direction and the isotopic gradient increases. Groundwater meet impermeable barriers parallel to the direction determined by site 10 and 11. Geologists confirmed the hypothesis regarding the presence of a low permeability structure in the SE part [13] and the faults with NW-SE and SW-NE orientations that intersect and generate interconnected channels [14].

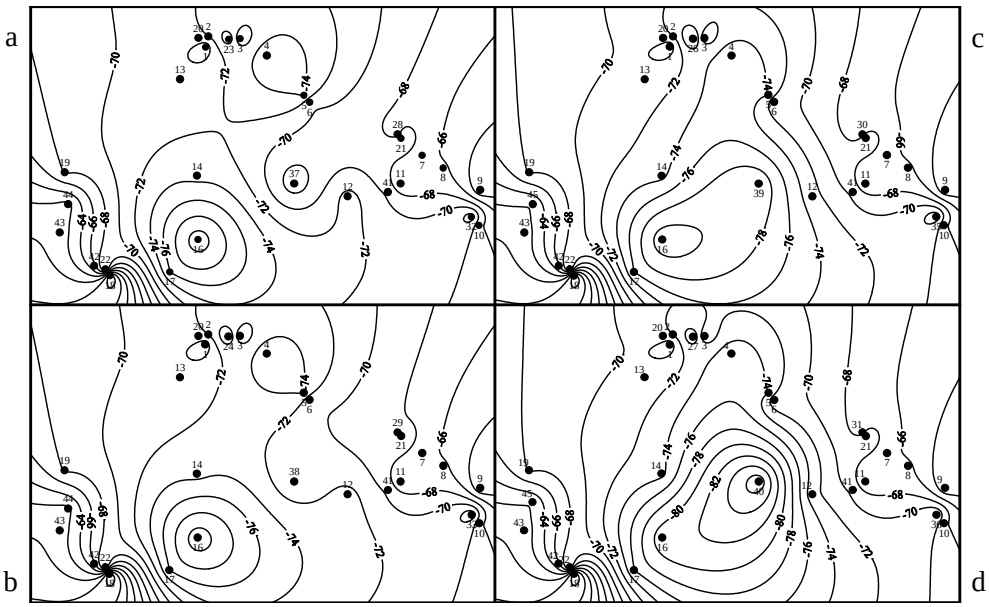


**Fig. 6.** The spatial distribution of deuterium average contents. The maps correspond to δD mean values of all samples associated with the δD mean values for samples from four levels of the water column corresponding to well km.57 (top-a, intermediate-b and c, bottom-d). The maps illustrate the effect of two aquifers leaky system (well Km 57) on deuterium distribution in space. Comparison of figures indicates that the unconfined aquifer with isotopic heavier water (at top of well) and the aquifer with isotopic light water from bottom of well have a vertical component of flow.

4. The last is the conduit aquifer and mixed aquifer. On the maps from Fig. 6 the points having low δD values and being originated from high altitude are represented by closed isolines (points 16 on Fig. 6a, b, c and 40 on Fig. 6d). In the 2-D flow domain, the tracer develops circular shapes of the isolines, causing a uniform flow through the system in all direction. In the two horizontal planes of the water layers (-8m and –10m depth) deuterium is uniform transported from fountain 16 to all direction and the water seems to move with the same velocities towards the sites of samples 14 and 17. For the follow depths (-15m and –20m) the isolines develop an elliptical shape in the direction of flow. The advance of the isotopically

light water from the fountain 16 is stronger directed to the SW-NE direction toward the N side of Razim Lake. For sample 40 an opposite direction is observed, towards SW, into the same side. The N side of Razim Lake is the discharge area of the aquifer with isotopically light water having the flow of conduit type and the phreatic tributary to Danube.

## 5. CONCLUSIONS

According to the δD values the following categories of waters were delineated:

- Waters depleted in deuterium (δD< -80‰) representing the intrusion of isotopically light water from high altitude (> 1000m). The discharge of this component occurs by conduits and diffuse flow.
- Waters tributaries to the Danube River (δD> -75‰) that have a small variability in time of δD values.
- Local infiltration waters (δD > -70‰), situated in the West of the investigated area towards the continental platform of the Dobrogea, with distinct seasonal effect.
- Waters originated in mixing processes between the waters with different isotopic content. The one endmember is heavier isotopic water that belongs to local recharged waters (local infiltration waters and waters tributary to Danube river) and the other endmember is the isotopically light water.

The correlation the spatial distribution of average of δD with water type and it origin indicates that the study area is compartmentalised in four hydrological subareas.

- The N part of the study area appears to act as a discharge area both for the local infiltration waters and for the isotopically light water from high altitude that discharges by diffuse flow
- The second is part of Southwest for which flow paths have a local character.
- The third is the phreatic system that recharges from the Danube River and move slowly towards Southeast. The sink Colina affects the flow direction of the phreatic and it discharges in Colina zone, too.
- The last is the conduit aquifer and mixed aquifer. The discharge of the aquifer associated to samples 14 and 12 of the mixed waters occur in an area with water of type 17 in the N part of the Razim Lake. The N side of Razim Lake is the discharge area of the aquifer with isotopically light water having the flow of conduit type, too.

## REFERENCES

[1] Friedman, I. & O'Neil, J. R. (1977). Compilation of stable isotope fractionation factors of geochemical interest. In Data of Geochemistry, 6th Edn, ed. M. Fletcher, U. S. Geol. Surv. Prof. Paper 440-KK.

[2] Sheppard, S. M. F. (1986). Characterization in isotopic variations in natural waters. Stable isotope in high temperature geological processes. Reviews in Mineralogy, 16, Ed. by J. W. Valley, H. P. Taylor Jr. & J. R. O'Neil Mineralogical Society of America: 165-183.

[3] Graham, C. M., Viglio, J. A. & Harmor, R. S. (1987). Experimental study of hydrogen-isotopic exchange between aluminous chlorite and water and hydrogen diffusion in chlorite. American Mineralogist 72: 566-579.

[4] Pascu, M. (1983). The underground waters from Romania. Technical Publishing House, Bucharest: 358-362.

[5] Cineti, A. F. (1990). Groundwater resources of Romania. Technical Publishing House, Bucharest: 95-96, 106-111.

[6] Feurdean, V. & Feurdean, L. (1999). Deuterium as natural tracer in groundwater from neighbouring area of Danube Delta Biosphere Reserve. Isotopes Environ. Health Stud., 35, 183-211.

[7] Hagemann, R., Nief, G. & Roth, E. (1970). Absolute isotopic scale for deuterium analysis of natural waters. Absolute D/H ratio for SMOW. Tellus, 22: 712-715.

[8] Banner, J. L., Wasserburg, G. J., Dobson, P. F., Carpenter, A. B. & Moore, C. H. (1989). Isotopic and trace element constraints on the origin and evolution of saline groundwater from central Missouri. Geochim. Cosmochim. Acta 53: 383-398.

[9] Mazor, E. & Vuataz, F. D. (1990). Hydrology of a spring complex, studied by geochemical time-series data, Aquarosso, Switzerland. Applied Geochemistry, 5: 563-569.

[10] Yurtsever, Y. (1983). Models for tracer data analysis, in Guidebook on Nuclear Techniques in Hydrolgy, IAEA Vienna, Tech. Rep. Ser., 91: 437 p.

[11] David, C., Gherghisan-Despina, C. & Condur, M. (1995). Pollution indicators-Ceatal Chilia 1991-1994. Sci. Ann. of Danube Delta Inst., IV/2: 153-158.

[12] Freeze, R. A. & Cherry, J. A. (1979). Groundwater. Prentice-Hall, Englewood Cliffs, New Jersey: 604 p.

[13] Besutiu, L., Nicolescu, A., Svoronos, D. & Vihristencu, M. (1994). Geological setting within Dunavatu-Dranov area according to the geographical data. Sci. Ann. of Danube Delta Inst., III/2: 321-328.

[14] Dimitriu, R. G. (1995). The contribution of the gravity survey in the Danube Delta regarding the limits within the sedimentary layer. The environmental audit of the gravity mapping. Sci. Ann. of Danube Delta Inst., IV/2: 35-48.

# OPERATION ANALYSIS OF THE DEUTERIUM DEPLETED WATER PILOT PLANT

**C. CROITORU, GH. TITESCU, I. SAROS**

*National Institute of Researche-Development for Cryogenic and Isotopic Technologies, ICSI Rm. Valcea Str. Uzinei nr. 4,Tel. 0040-050-732744, Fax 0040-050-732746, Romania*

**ABSTRACT.** The first stage of the pilot plant for the heavy water final concentration has been utilised for the deuterium depleted water production. Now the installation is fed in bottom of the second column with water of 144 ppm D/(D+H). The product of the plant, extracted at the top of first column, must be of 30 ppm D/(D+H), maximum. Simulation of steady state functioning of this plant has permit to establish the separation capacity in the plant operation conditions and the internal fluids flow that provides a significant increase of the plant production. It also has been analysed the influence of thermal feed state on the plant performances. On the basis of the unsteady state functioning simulation it has been established the evolution of plant production concentration in the period of setting in operation and after the changes of plant operation regimes.

**Key words:** deuterium depleted water, isotopic separation, vacuum distillation, mathematical model

## 1. Introduction

Deuterium depleted water is represented by water that has an isotopic concentration of 20-80 ppm D/(D+H), smaller than natural concentration, of 145 ppm D/(D+H). As a result of investigation's increasing in isotopic separation domain, NR&DICIT has elaborated and patented a method and an installation for deuterium depleted water yield. Beginning with 1996 NR&DICIT co-operated with Romanian specialised institutes for biological effects of deuterium depleted water.

The paper presents operation analysis of deuterium depleted water pilot plant.

In our institute deuterium depleted water (DDW) is produced in the first stage of the pilot plant for heavy water final concentration, by vacuum distillation. Fig. 1 shows installation scheme. The plant is fed at the bottom of the second column and the product extraction is make at the top of the first column. Installation production, for the first year of operation, is shown qualitatively and quantitatively in fig. 2 [1].

The analyse of DDW plant operation is based on simulation models, in order to establish the optimum values of operating parameters and to evaluate installation behaviour when it is operated in unsteady states.

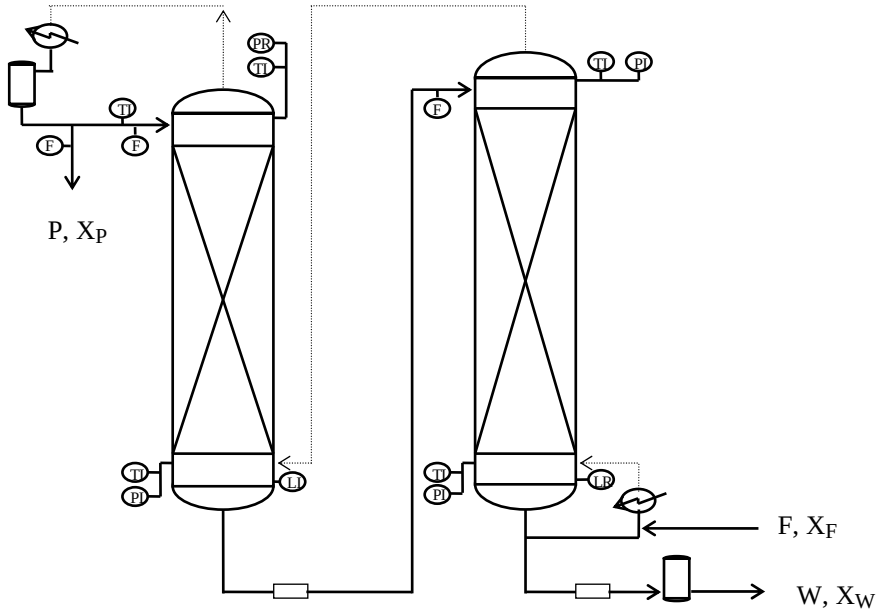


**Fig. 1.** Scheme of deuterium depleted water pilot plant

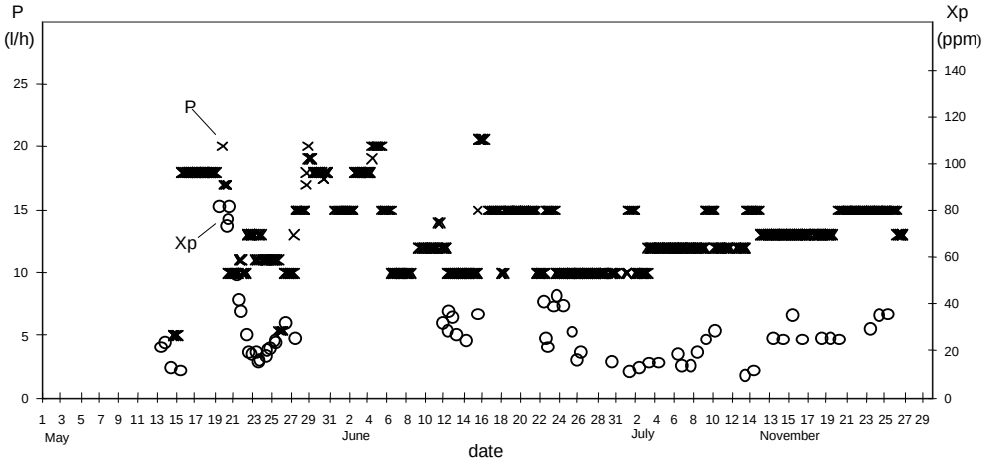


**Fig. 2.** Production of DDW pilot plant

## 2. Methods

The mathematical models used for simulation programs is composed of equation of isotopic equilibrium, equations for total mass balance and isotopic balance, in steady state, respectively unsteady state [2,3].

$$\alpha = \frac{x \cdot (1 - y)}{y \cdot (1 - x)} \tag{1}$$

steady state

$$\sum_{m=1}^{M} I_m - \sum_{n=1}^{N} E_n = 0 \tag{2}$$

$$\sum_{m=1}^{M} \left(I_m \cdot x_{I,m}\right) + \sum_{n=1}^{N} \left(I_n \cdot y_{I,n}\right) - \sum_{r=1}^{R} \left(E_r \cdot x_{E,r}\right) - \sum_{s=1}^{S} \left(E_s \cdot y_{E,s}\right) = 0 \tag{3}$$

unsteady state

$$\sum_{m=1}^{M} I_m - \sum_{n=1}^{N} E_n = \frac{\partial h}{\partial t} \tag{4}$$

$$\sum_{m=1}^{M} \left(I_m \cdot x_{I,m}\right) + \sum_{n=1}^{N} \left(I_n \cdot y_{I,n}\right) - \sum_{r=1}^{R} \left(E_r \cdot x_{E,r}\right) - \sum_{s=1}^{S} \left(E_s \cdot y_{E,s}\right) = \frac{\partial}{\partial t}(h \cdot x) \tag{5}$$

where:

I, E - feeding, outlet flow rate, kmol/h
x, y - isotopic concentration in liquid, vapour phase, mol fraction D/(D+H)
h - liquid hold-up, kmol/h

The model includes also relations for separation factor and fluids density calculation as a function of temperature, and relation for isotopic efficiency calculation as a function of vapour charge [4 ].

We make the assumptions that through distillation columns the temperature is constant and the vapour hold-up can be neglected. We solved the equation system using numerical methods.

## 3. Results

Using the program for steady state simulation, we determined, in the operating conditions for the first year, the plant separation capacity. The calculated values for product, flow rate and concentration, close to the values realised in installation. In analysed functioning period feeding flow rate has varied about 8–33 l/h.

Imposing for product concentration value of 25 ppm, we have determined the level whereat feeding flow rate influence is insignificant. Optimal feeding flow rate is about 40 l/h.

For optimal feeding flow rate we have determined the plant separation capacity, as a function of extracted product concentration. For extracted product flow rates takes in domain 10-12 l/h the plant production concentration lies in domain

20-30 ppm. Attempts to extract more products lied to product depreciation. These situations there is particularly in first period of plant functioning (fig. 2).

At present, in both plant columns, it can assuring maximum of liquid flow rate about 230 l/h. By simulation we have established that maximum charge supported by columns lie at level 400 l/h, value whereat package efficiency is 7,8 NTP/m, in comparison with 8,5 NTP/m at 220 l/h. Reflux doubling have as result production increasing with 67,7 %.

We have determined the influence of the thermal state of feeding, as a function of the feeding flow rate. The production increases in case of vapour phase feeding comparative with liquid phase feeding, but it is not significant (<1 %).

The prediction of unsteady state period, at plant start-up or at the modification of operating parameter, offers effective support in plant operation. With unsteady state simulation program, we have established that after two days from plant start-up, without feeding and extraction, isotopic concentration in product extraction zone reaches about 25 ppm.

Establishment of product flow rate at 11,5 l/h assures the obtainment of a concentration of 25 ppm. Simulation results, having at base May operating parameters, recorded in every other hour, evidence the correctness of mathematical description and liquid hold-up evaluation. Fig. 3 shows theoretical curve of temporal variation of product concentration and measured values of product flow rate and concentration.

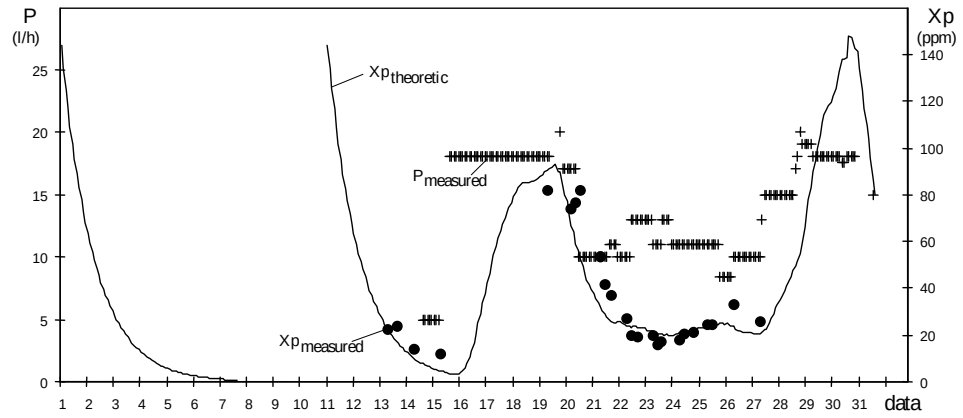


**Fig. 3.** Theoretical curve of temporal variation of product concentration and measured values of product flow rate and concentration

## 4. Conclusions

This paper present the analyse of installation operation, based on simulation models, in order to establish the optimum values of operating parameters and to evaluate the installation behaviour when is operated in unsteady states.

Using the program drawn up for steady state simulation, we have determined the separation capacity of the installation, in operating conditions of the first functioning year. The calculated values for product, flow rate and concentration approach the values realised in installation.

Having the confirmation that the model describe correct the isotopic separation process in steady state, we determined the level until which the influence of feeding flow rate is significant, the separation capacity of the installation as function of product concentration, product variation with the charge of vapours phase and the influence of feeding thermal state as function of the feeding flow rate.

Using the simulation program for unsteady state, we established the time of unsteady state at starting, function of extraction flow rate. The results of simulation, based on operating parameters registered every two hours, emphasise the accurate mathematical description of isotopic separation process in unsteady state as well as the correct evaluation of water hold-up from the installation.

## REFERENCES

[1] I. Stefanescu, M. Peculea, Gh. Titescu, Procedeu si instalatie pentru producerea apei saracite in deuteriu, Patent nr. 11422, Romania

[2] C. Croitoru, M. Dumitrescu, G. Isbasescu, Adaptarea si aplicarea modelelor si a programelor de calcul pentru proiectarea si simularea instalatiilor de distilare izotopica din cadrul C. Ch. Drobeta, S410/20.09.1988

[3] V. A. Kirillina, Tiajelaia, Teplofizischie cvoistva, 1973

[4] M. Pavelescu, M. Peculea, Schimbul izotopic $H_2O$ - $H_2S$. Proprietati termodinamice, Uzina "G", Rm. Valcea, 1975

STUDIA UNIVERSITATIS BABEŞ-BOLYAI, PHYSICA, SPECIAL ISSUE, 2000

# IMPROVING THE ACCURACY OF ISOTOPE RATIO DETERMINATION BY STATISTICAL TREATMENT OF DATA

**A. PAMULA, C. FLOARE, M. VERMEŞAN**

*National Institute for Research and Development of Isotopic and Molecular Technologies, Cluj-Napoca*

In a research concerning the study of the separation of uranium isotopes on ion exchanging resins, the problem of very precise isotopic analysis appeared. The existing instrument is a thermal ionisation mass spectrometer built in our institute in 1986. It is equipped with a two filaments ion source and a single ion collector based on a secondary electron multiplier. In 1986, during the homologation procedure, the accuracy was established to be 1% from the measured value. The aim of this work is to overpass this instrumental limitation.

## I. INTRODUCTION

Isotopic ratios measured with a thermal ionisation mass spectrometer are seldom the true ratios of a sample under study. Instrumental mass discrimination may arise from various sources. Ion-optics, analyser design and non-linearity in the measuring circuitry are some of them. The ion detection system can also introduce mass discrimination. The isotopic fractionation process at the same time will have his essential part of contribution at this effect. Below we will discuss some of the most important error sources encountered, and the methods used to avoid them.

## II. ISOTOPIC FRACTIONATION PROCESS

In thermal ionisation mass spectrometry, the main discrimination effect which may introduce low accuracy and low precision in an isotopic ratio analysis is the mass dependent, and consequently time dependent, isotopic fractionation process occurring in the ion source within the course of an analysis. The reason for this phenomenon is the mass dependent differential vaporisation of the isotopes from the heated sample filament, causing the lighter isotope to vaporise more rapidly. The usual trend is that at the beginning of an analysis the observed ratio favours the lighter isotope. During the vaporisation process, the higher evaporation rate of the lighter isotope leads to faster depletion of the sample in this isotope, and the ratio of light to heavy isotope decreases towards its true value and, eventually, below it.

Isotopic fractionation on the sample filament is a process, which must be carefully controlled; it is recognised as a major source of variable systematic errors limiting the accuracy of isotopic ratio measurements. Isotopic fractionation was

already observed in the early stages of thermal ionisation mass spectrometry by Brewer [1], followed by Hoff [2], Riik and Shukoliukov [3], Reutersward [4], Ordzhonikidse [5], Bentley *et al.* [6], Habfast [7], and Shields *et al.*[8]

Mass fractionation parameters which have to be considered are sample size, chemical composition and purity, sample loading procedures on the filament, the material of the ionisation and evaporation filaments, filament temperatures and the rate of sample heating and, finally, the time of data acquisition.

To control and avoid the consequences of this effect we tried to maintain constant as many as possible of these parameters. Hence, we use the same quantity of sample size at every analysis and we have developed a very precise sample loading procedure. The major limitation from this point of view remains the uranium concentration in the solution from which the sample is taken and its chemical purity.

We use multiple filament ionisation procedure, the sample is vaporised from the sample filament and the vapour is ionised with the aid of an ionising filament maintained at much higher temperature. The rate of filament heating and the final evaporation and ionisation currents are the same for all samples. Consequently, the final filaments temperatures for all samples are nearly the same.

We have increased the time of data acquisition to collect as many data as possible from the sample, in order to treat them statistically and we tried to develop a general idea about the time evolution of isotopic ratio.

## III. STATISTICAL TREATMENT OF DATA

One of the best ways to assess the reliability of a measurement in experimental sciences is to repeat it several times and to submit the whole set of accumulated results to a statistical analysis. Experimental uncertainty can be treated statistically only if it is a *random uncertainty*, i.e. a random error. Another type of error is *systematic uncertainty*, which cannot be revealed by statistical treatment. The average or mean of a set of measurements, the standard deviation of the mean, and the confidence interval are the basic parameters for the estimation of random errors. In the simple formulation of statistical treatment, it is assumed that the experimental data demonstrate a normal or Gaussian distribution.

To verify if our ratio data sets follow the normal (Gaussian) distribution, we apply the $\chi^2$*_test* (Hi square test) which is described below.

In its normalised form, the Gaussian distribution is bell shaped and centred on the mean value, which should also be the ‘true value’, provided that there are no systematic errors in the system under study. Even if the system does not exhibit any systematic errors, which may shift this value, it probably would be more correct to designate the mean value as the ‘best value’.

In our quest to improve, the statistical treatment of measured data, we have considered also the contribution of J.G. van Raaphorst et all. [9] and that of F. Scahaefer et all. [10]. At this level, we will describe the basic features of the statistical treatment of data as random and systematic errors, normal repartition of data, rejection of measurements.

## A. Random and Systematic Errors

Random errors in mass spectrometry arise owing to instability and fluctuations of the various instrumental components which produce, accelerate, mass separate and monitor the separated ion beam. It is clear that these errors will be larger for less intense ion beams. Possible sources of systematic errors are isotope fractionation effects in ionisation, ion source pumping systems, ion optics in the mass analyser systems, mass discrimination effects specific to electron multipliers, linearity and gain of the electronic measurement system. As already mentioned, the random errors are treated with statistical tools.

The systematic errors will be revealed by comparison with standard reference materials or standard reference measures. Our ruler had to be compared with a standard reference ruler, and the detection system tested with a standard reference current. Systematic errors in isotope ratio determinations are detected and corrected with isotopic standard reference materials (SRM's). It is generally accepted within the mass spectrometry community that the SRM ratio should be as close as possible to the studied ratio.

**Error sources in SMIT-1 mass spectrometer**:

- One of the most frequently encountered causes of severe random fluctuation in the ion current intensities, is vacuum instability. Because of the outgasing induced by thermal radiation of the incandescent filaments, and/or due to uncontrolled leaks of a complex bearing system, short term "burst" of the pressure in the ion source may occur. As the pressure increases, the transport phenomena became more important and the filaments are more efficiently cooled. Their temperature diminishes and consequently the ionisation efficiency is altered. To avoid, as much as possible, this effect, the spectrometer tube is intensively outgased during the night, to achieve a "clean" vacuum. A "finger" cooled with liquid nitrogen is placed in the proximity of the heated filaments in order to collect the unionised neutrals evaporated. We start data acquisition only when a high vacuum of $3 - 4 \cdot 10^{-7}$torr is established in the ion source.
- Modifications in the filament shape and position, caused by thermal dilatation, induce alteration of ion extraction efficiency and focussing performances of the ion source. This phenomenon produces a steady growing or decay of ion current intensities. Unfortunately, this effect is quite impossible to control. We adopted a special cross section profile of the ionisation region of the ion source in order to obtain an ion optics condition less dependent of filament position. A very low rate of increasing the temperature of the ioniser and sample is adopted to provide enough time to achieve a thermal equilibrium into the ionisation region. The situation will be sensibly improved by a system, which will permit the transversal movement of the filaments assembly while the source is running. This will realise a controllable maximisation of the ionic signal at the collector.
- The detection system is another source of error. It is a single collector based on a secondary electron multiplier. The use of a single collector means that the two ion currents of interest ($^{235}U$ and $^{238}U$) are measured alternatively. As

fluctuations are possible, we don't exactly know the intensity of the $^{235}U$ current while measuring the $^{238}U$ current.

Other authors, (E.L. Callis and R.M. Abernathey [11] from Analytical Chemistry Group, Los Alamos National Lab.) have been developed a method in which the entire sample is volatilised while simultaneously integrating the signal from each isotope, thus virtually eliminating the effects of isotope fractionation in the evaporation process. The method permits the analysis of samples much smaller than required for conventional techniques using Faraday collectors and is expected to have application in the analysis of many elements in addition to uranium and plutonium.

In our case, the mass spectrometry configuration doesn't permit such technique. To bypass the absence of double collector, we compare each peak with the mean of the two adjacent ones, assuming that, on short intervals; the dependence current versus time may be considered linear. In doing so, we must realise the scanning fast enough to avoid severe deviation from linearity, but slow enough to be compatible with the time constant of the electrometric system. This exigency is satisfied by adopting a magnetic scanning of single peak of interest followed by a "jump" to the other peak by a step - variation of the accelerating voltage.

- The secondary electron multiplier may induce other disturbing effects. The dynodes voltage is obtained via a chain of resistors, which divides the high voltage supplied by an electronic unit. If the ion flux on the first dynode is important, the secondary electron current may become comparable with the electric current in the chain of resistors. Consequently, the voltage applied on dynodes, which mean the gain of the multiplier, will become dependent of the incoming ion current intensity. It is difficult to estimate the importance of this effect. That is why, we tray to reach nearly the same intensity for the $^{238}U$ ion current for all the samples and natural standards.
- The secondary electron yield of the first dynode depends of the energy of the bombarding ions falling on it. As the $^{235}U^{+}$ ions are accelerated higher then the $^{238}U^{+}$ ions (one achieves thus the "jump" from one peak to the other) the gain of the multiplier is slightly higher for the lighter isotope. It is a systematic error source. The effect is compensated using natural standards with known isotopic content.

## B. Normal repartition of data - $\chi^2$ test (Hi square test)

One of the most commonly used method to determine if a set of experimental data follow a normal distribution is the *$\chi^2$ test*. This is a quantitative test.

As for majority tests, which verify the normality of the repartition of data, firstly we must group the data values on intervals of variation. Commonly the intervals dimensions are the same for all classes. Depending on how many data we have, we can determine the necessary number of classes using the Sturge's relation:

$$k = 1 + 3.322 \log (n) \quad (1)$$

where *n* is the data number.
After, we calculate the value:

$$\chi^2 = \sum_{i=1}^{k} \frac{(n_i - Np_i)^2}{Np_i} \quad (2)$$

where: $n_i$ – the number of values of class *i*; $N = \sum_{i=1}^{k} n_i$ - the total number of data;

k – number of classes; $p_i$ – the theoretical probability corresponding to frequency of apparition of value $x_i$

If the value calculated with relation (2) is greater than $\chi^2_{\nu,\alpha\,critical}$ we can say with certitude having the probability α that the function of the repartition of data differ from the normal repartition of data.

**Table 1.**

**Critical values $\chi^2_{\nu,\alpha\,critical}$ [a]**

| ν, α | 0.8 | 0.95 | 0.99 | 0.995 | 0.999 |
|---|---|---|---|---|---|
| 4 | 5.99 | 9.49 | 13.3 | 14.9 | 18.5 |
| 5 | 7.29 | 11.1 | 15.1 | 16.7 | 20.5 |
| 6 | 8.56 | 12.6 | 16.8 | 18.5 | 22.5 |
| 7 | 9.80 | 14.1 | 18.5 | 20.3 | 24.3 |
| 8 | 11.0 | 15.5 | 20.1 | 22.0 | 26.1 |
| 9 | 12.2 | 16.9 | 21.7 | 23.6 | 27.9 |
| 10 | 13.4 | 18.3 | 23.2 | 25.2 | 29.6 |
| 11 | 14.6 | 19.7 | 24.7 | 26.8 | 31.3 |
| 12 | 15.8 | 21.0 | 26.2 | 28.3 | 32.9 |

$\alpha$ - the level of trust; $\nu$ - the number of degree of freedom $\nu$

To effectively calculate the sum (2) we will follow the steps:

a) we calculate the mean $\bar{x} = \frac{1}{n}\sum_{i=1}^{n} x_i$ , and the mean square deviation

$$s = \sqrt{\frac{1}{n}\sum_{i=1}^{n} n_i (x_i - \bar{x})^2} \; ;$$

b) for all classes we calculate the value $t_i = \frac{x_i - \bar{x}}{s}$, where $x_i$ is the upper limit of the class;

c) we calculate the theoretical probabilities $p_i$:

$p_i = \Phi(t_i) - \Phi(t_{i-1})$, where $\Phi(t) = \frac{1}{\sqrt{2\pi}} \int_0^t e^{-t^2/2} dt$ is the integral probability function;

d) we evaluate the sum (2);

e) we compare the obtained value for $\chi^2$ with $\chi^2_{\nu,\alpha\,critical}$.

## C. Rejection of measurements

It may happen in a ratio determination that a value appears which departs considerably from the other values in the measurements. The appearance of an outlying value is not necessarily an indication that a serious error has been made. In a small group of values it can affect the mean and the standard deviation to such an extent that it may be reasonable to conclude that the mean ratio recalculated without the outlier would better represent the true value. Although there are cases where the rejection has definitive reasons, a statistical criterion of rejection is still important. Several such criteria exist, some quite complicated.

The Chauvenet rejection criterion is a simple and easily used test. It states that a value in a group of *n* values shall be rejected when the magnitude of its deviation from the mean of the group is such that the probability of occurrence of all deviations that large, or larger, is less than 1/2*n*.

**Table 2.**

**Chauvenet's criterion of the rejection of suspended measurements[a]**

| *N* | *P* | *n* | *p* | *n* | *p* | *N* | *p* | *n* | *p* |
|---|---|---|---|---|---|---|---|---|---|
| 2 | 1.15 | 7 | 1.80 | 15 | 2.13 | 40 | 2.50 | 250 | 3.09 |
| 3 | 1.36 | 8 | 1.86 | 20 | 2.24 | 50 | 2.58 | 300 | 3.14 |
| 4 | 1.54 | 9 | 1.91 | 25 | 2.33 | 75 | 2.71 | 400 | 3.21 |
| 5 | 1.65 | 10 | 1.96 | 30 | 2.40 | 100 | 2.81 | 500 | 3.29 |
| 6 | 1.73 | 12 | 2.04 | 35 | 2.45 | 200 | 3.02 | 1000 | 3.48 |

[a] *n* = number of measurements; *p* = ratio of the deviation of the measurement from the mean to the standard deviation

We compute

$$p = (r_{out}\text{-}R)/SD \quad (3)$$

where SD – standard deviation (an estimate of the uncertainty of a set of measurements);

For a set of isotopic ratio measurements the standard deviation is defined as

$$SD = \{[\Sigma_i(R\text{-}r_i)^2/(n\text{-}1)]\}^{1/2} \quad (4)$$

where $r_i$ is a measured ratio in a separate analysis of sample,

*n* is the number of measured ratios in the sample, and R is the mean of *n* ratios, $R = \Sigma r_i/n$ for one sample;

*p* is the number of standard deviations by which the suspected outlier differs from R.

The criterion is used as follows:

(a) R and SD are calculated for a set of r.
(b) The magnitude of *p* is determined for a suspicious r ($r_{out}$), using the equation.
(c) The observed magnitude of *p* from (b) is then compared with the value of *p* for the corresponding value of *n* in Table 1.
(d) If the observed *p* is greater than the value in the table, $r_{out}$ may be rejected.
(e) Finally, a new mean and standard deviation of *n-1* data points is calculated.

When the rejection procedure is completed, the resulting SD will be smaller than the original one. It may also happen that, with the new R and SD, more measurements may be considered for rejection. Because of that, most authorities agree that the Chauvenet criterion should not be applied again on the recalculated values of R and SD.

Several other more complex rejection criteria are known: Dixon's, Grubb's test, the coefficient of skewness test. In our analysis, we used the Chauvenet's criterion.

**Data processing.**

Complex software was developed to automatically acquire the ion current intensities. The computer analyses the slope of the function ion current versus time. When it becomes positive it means that a peak is going to be recorded, and the function is integrated until the slope becomes negative, then zero.

Data are stored in a file on disk. Once the acquisition accomplished, the normal distribution is checked (fig.1). If we get a normal distribution, then the Chauvenet criterion is applied and Student factor is calculated. We obtain a mean value and a confidence interval (fig 2. and fig.3). The same procedure is used with natural standard and unknown samples. The software estimates the systematic error and makes the necessary correction. Figure 4 shows some isotopic content determinations for several samples of uranium.

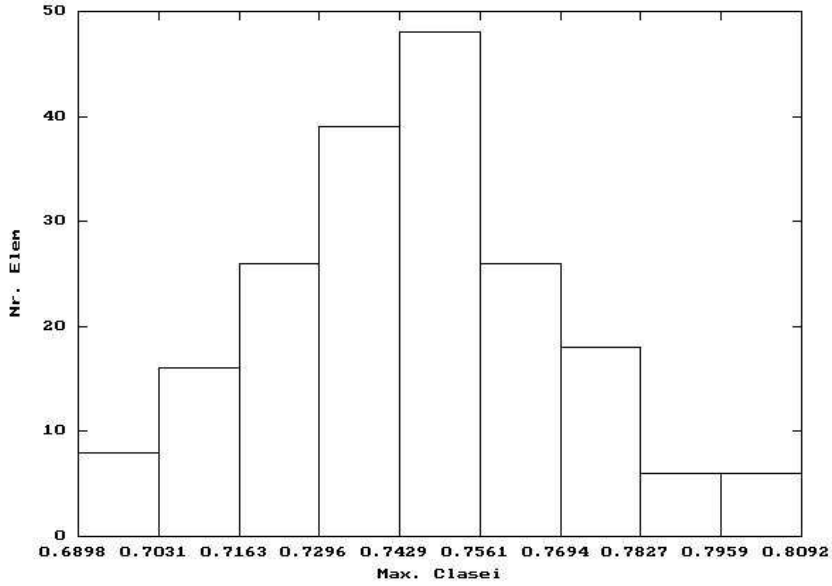


(a)

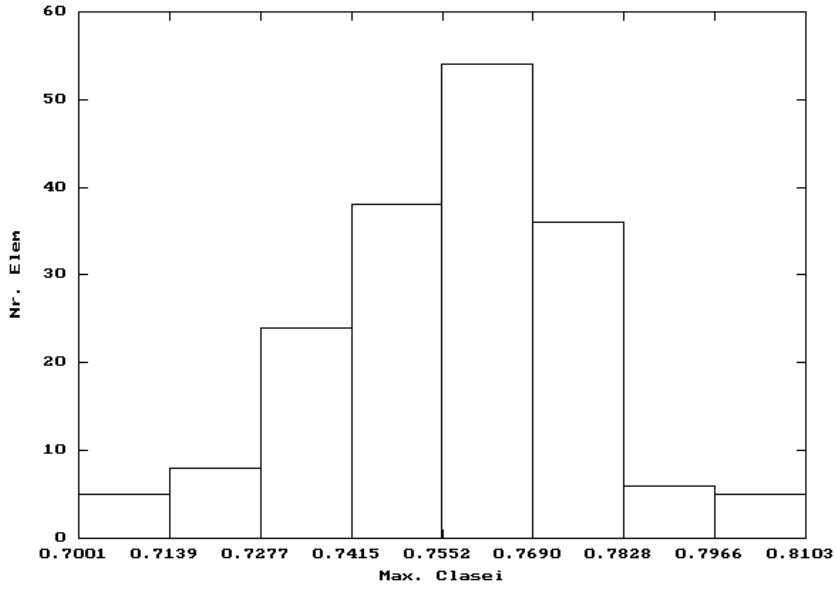


(b)

**Figure 1:** Testing the normal distribution of data: (a) – for a natural standard, (b) for a sample obtained from a separation experiment.

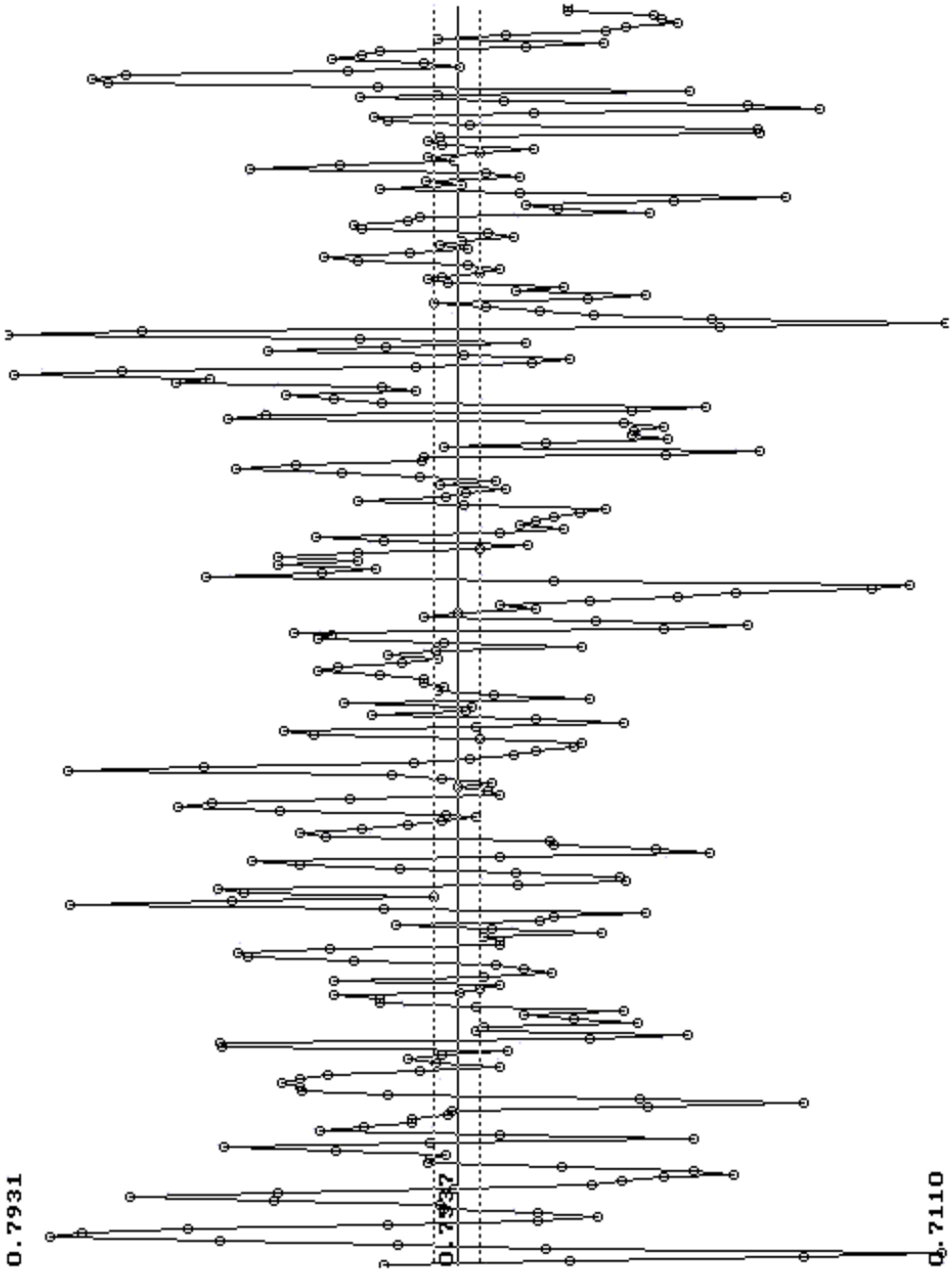


**Figure 2:** Acquired data in a natural uranium sample analysis. Points represent $^{235}U/^{238}U$ ion current ratio. With dotted lines: the confidence interval.

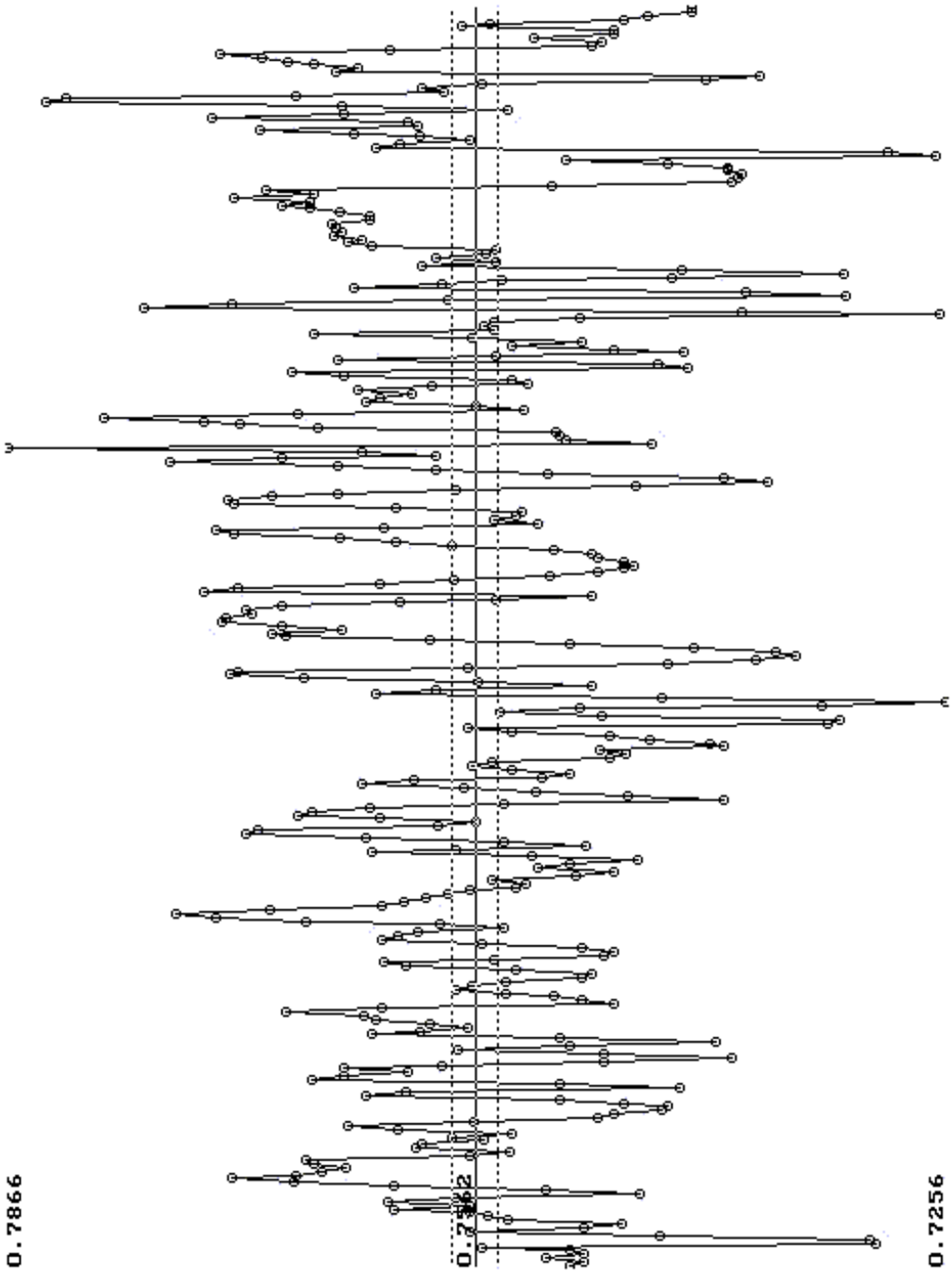


**Figure 3:** Acquired data for the sample from the separation experiment. Points represent $^{235}U/^{238}U$ ion current ratio. With dotted lines: the confidence interval.

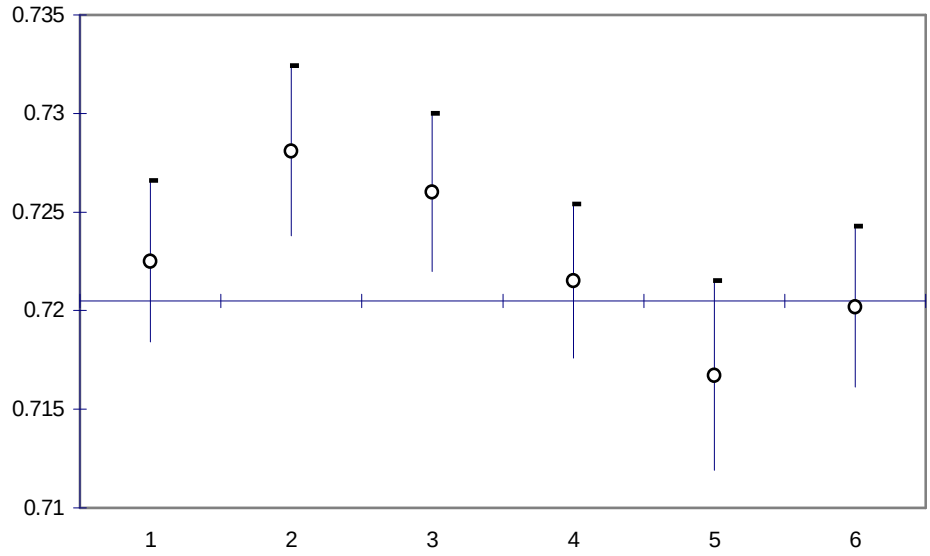


**Figure 4:** The $^{235}U$ (%) content in different samples of uranium, after a separation experiment

## Conclusions

- This work represents an attempt to compensate by software the "hardware" deficiency. The leak of a double collector system is overcome by a very tedious statistical treatment on a very large set of data.
- The performances obtained show, that an isotope separation effect can be observed even in these experimental conditions.
- To obtain higher accuracy, statistical treatment is not sufficient. Improvements of the ion source structure and a simultaneous detection of both isotopic species are the next steps in upgrading the mass spectrometer SMIT-1.

## REFERENCES

[1] A.K. Brewer, *J. Chem. Phys.*, **4**, 350 (1936).

[2] L. Hoff, *Phys. Rev.*, **53**, 845 (1938).

[3] G.R. Riik and Y.A. Shukoliukov, *Dokl. Akad. Nauk. SSSR*, **94**, 667 (1954).

[4] C. Reutersward, *Ark. Fys.*, **11**, 1 (1956).

[5] K. Orrdzhonikidse and V. Shutze, *Tarans. Theor. Phys. SSSR*, **29**, 479 (1956).

[6] P.G. Bentley, K. Bishop, D.F.Davidson and P.B.F. Evans, *J. Sci. Instrum.*, **36**, 32 (1959).

[7] K. Habfast, Z. Naturforsch., Teil A, **15A**, 273 (1960).

[8] W.R. Shields, E.L. Garner, C.E. Hedge and S.S. Goldich, *J. Geophys. Res.*, **68**, 2311 (1963).

[9] J.G. van Raaphorst at all., Int. Journ of Mass Spectr. and Ion Process., **31**, 65 (1979).

[10] F. Schaefer, P.D. P. Taylor, S. Valkiers, P. De Bievre, Int. Journ. of Mass Spectr. and Ion Process., **133**, 65 (1994) .

[11] E.L. Callis, R.M. Abernathey, Int. Journ. of Mass Spectr. and Ion Process., **103**, 93 (1991).

STUDIA UNIVERSITATIS BABEŞ-BOLYAI, PHYSICA, SPECIAL ISSUE, 2000

# THE USE OF RADON ISOTOPES IN RETROSPECTIVE EXPOSURE EVALUATION

**C. COSMA*, I. CHEREJI****

* *University of Babes-Bolyai, Faculty of Physics, 3400 Cluj-Napoca, Romania*
** *National Institute of Isotopic and Molecular Technology,3400 Cluj-Napoca, Romania*

**ABSTRACT**. Many retrospective studies regarding the long time exposure to radon ($^{222}$Rn) are based on the accumulation of $^{210}$Pb ($T_{1/2}$=22.3y) on the surface of glass objects or other materials and measuring the specific alpha activity of $^{210}$Po ($T_{1/2}$=138 d, $E_\alpha$=5.3 MeV) resulted by implanting of radon daughters, due to the alpha recoil. In the case of thoron ($^{22o}$Rn) this method is not applicable because there is not a long life time isotope to allow a significant accumulation of any descendant. The longest lifetime of the thoron descendants is $^{212}$Pb with a life time of $T_{1/2}$= 10.6 hours. But a study involving thoron daughters implanted at the surface of glasses or other materials (plastic, wood, paper, polyethylene, Plexiglas, Cu or Al foils) can be useful in the simulation of radon progeny implantation. This simulation is possible due to the equilibrium of implantation, which is obtained in a short time (about 50 h) compared to about 100 y in the case of $^{222}$Rn. The purpose of this work is to obtain the alpha and gamma spectra (especially alpha) for thoron daughters implanted at the surface of different materials and to show the possibility of this method to simulate the radon progeny implantation and thus to find some parameters used in the Jacobi model.

## Introduction

In order to estimate the risk of indoor radon in producing lung cancer, a lot of epidemiological studies were developed, using underground miners data. Extrapolating these results for the general public, based on the linear no-threshold relationship between radon exposure and lung cancer risk, is now a problem widely discussed by the scientific world [1]. In the United States, for example, the BEIR IV committee estimated that about 15,400 or 21,800 lung cancer death per year can be attributed to radon among eversmokers and neversmokers. Considering the results of the latest epidemiological studies, the BEIR VI committee, based on the uncertainties of these analyses, extended this interval to 3,000-32,000 deaths per year. However, the committee admits that it could not exclude the possibility of a threshold relationship between exposure and lung cancer risk at very low levels of radon exposure. To improve the results of the latest epidemiological case-control studies, and therefore to diminish the influence of the multiple parameters involved in the estimation in radon relative risk, an alternative would be a correct assessment of the past radon exposure to each case-control included in these studies.

This parameter is very important and the diminishing of its uncertainties can be done using dose reconstruction of past radon exposure [2,3]. Many retrospective studies regarding past radon exposure are based on the accumulation of $^{210}$Pb on the surface of glass objects or other materials, and measuring the specific alpha-activity of $^{210}$Po ($T_{1/2}$=138 d, $E_{\alpha}$=5.3MeV) resulting from radon daughters implanting due to alpha recoil. Because $^{210}$Pb have a lifetime of 22.3 years, the glass acts as a memory for the airborne radon activity over several decades. Another way to measure the specific surface activity of implanted radon daughters is the beta-activity measurement of $^{210}$Bi (parent of $^{210}$Po) [4] The measurement of implanted $^{210}$Po or $^{210}$Bi surface activity can be correlated to the average past exposure using the Jacobi room model [6-8]. In the case of thoron exposure ($^{220}$Rn) this method is not applicable because there is not a long life time daughter to allow a significant accumulation of any descendents. The longest life time of thoron progeny is that of $^{210}$Pb, ($T_{1/2}$=10.6 hours). But a study involving thoron daughters implanted on surface of glasses or other materials (plexiglass, paper, wood, copper, aluminum or other metals) can be useful for the simulation of radon progeny implantation and for the study of aerosol influence on this phenomenon. The desorption constant of the implanted atoms could be assessed by following the intensity modification of alpha or gamma peaks over time. This simulation is possible due to the equilibrium of implantation, which is obtained in a short time (about 50 hours) as compared to 100 years in the case of radon daughters. Many studies characterizing the adsorption and desorption of thoron daughters on aerosols have also been made [9-11].

The purpose of this work is to obtain alpha and gamma spectra (especially alpha) for thoron daughters implanted on surfaces of different materials and to find some characteristics of the implantation process.

## Experimental Methods

The obtaining of alpha spectra and the alpha counting were made by using a PIPS alpha-detector of Canberra type (900 mm$^2$) with 25 keV energy resolution operated under vacuum conditions and connected to a pulse height analyzer (ICA-70-Hungary). For gamma measurements we used a NaI (Tl) scintillator detector connected to the same pulse analyzer. For alpha energy calibration we used the internal standard pulses generated by the alpha spectrometer, and for gamma energy calibration we used a thorium source of Th $(NO_3)_2 5H_2O$. This thorium salt, in adequate quantity and simulating the same geometry as the samples with implanted thoron daughters, was directly placed on the NaI (Tl) detector. Comparing the calculated radioactivity of this salt to the activity of implanted sample below the 2610 keV photopeak of $^{208}$Tl, the equilibrium quantity of thoron progeny implanted in the samples could be found.

In the case of samples measured by alpha spectrometry, the detection efficiency was calculated taking into consideration the average solid angle under which the detecting surface (900 $mm^2$) is seen from sample surface (100 $mm^2$). The sample is placed on the detector axis, at 5 mm. The efficiency calculated in this way was 35.5%. Two hundred grams of $Th(NO_3)_2 5H_2O$ powder were put into a metallic box of 8.5 cm diameter and 5.0 cm height. This substance was purchased over 25 years ago; therefore the equilibrium between $^{232}Th$ and $^{234}Ra$ is almost reached (95%). A thin plastic sieve was placed on the thorium nitrate. The thickness of $Th(NO_3)_2 5H_2O$ layer was 2.9 cm and that of the layer of air above was 2.1 cm. Taking into account the very short life time of thoron (1 minute), its equilibrium concentration is quickly reached after closing the box. The amount of thoron was determined in a separate experiment by isolating the thorium nitrate in a 0.5 L plastic bottle hermetically closed, the thickness of thorium nitrate being the same. The equilibrium concentration of thoron above the thorium nitrate in the bottle was measured with the LUK 3A device [12] and the RnTh+ mode. Used in this mode, this device can measure both the radon concentration and the thoron concentration when their values are higher than 1 $kBq/m^3$. In our particular case we used the Janet syringe (annex of this device) to extract a determined quantity of air out of the plastic bottle. The extraction was done using this syringe (150 $cm^3$) fitted with a very thin medical needle and pricking the cork and lateral sides of the bottle. After determining the equilibrium concentration, the equilibrium activity of thoron was calculated multiplying this concentration by the volume of the bottle. The average of five extractions leads to a value of $1450 \pm 95$ Bq. Supposing that the same equilibrium quantity is to be found in the canister, the thoron concentration in volume is $A_0$=4.88 $MBq/m^3$. This value will be used to determine the implantation efficiency under equilibrium conditions. Considering the lifetime of the descendant with the longest life $^{212}Pb$ ($T_{1/2}$=10.65h), the implantation equilibrium could be reached in two days (48 hours). The determinations show that after this interval 95.6% of the equilibrium is reached. The samples exposed to implantation (glass, paper, polyethylene, aluminum etc.) are squares of 1-2 mm thickness and 1 $cm^2$ area, placed above the plastic sieve. In each case the implantation was measured on the upper side face.

## Results and Discussions

Fig. 1 represents the gamma spectrum obtained for the paper sample. The 2614 keV peak of $^{208}Tl$ and also the 238 keV peak of $^{212}Pb$ are well determined in the spectrum. In calculations the first photo-peak was used, because in the second case, at the energy of 238 keV, when comparing to the thorium nitrate sample, additional contributions of $^{228}Th$ and $^{224}Ra$ appear. Fig.2 shows the alpha spectrum obtained for the glass sample. The only spectrum peaks are those at the energy of 6.05 MeV and 8.78 MeV. The first peak is obtained from alpha disintegration of $^{212}Bi$ (36%) and the second from $^{212}Po$ disintegration generated by the beta disintegration of

$^{212}$Bi (64%). The 6.5 MeV, 7.5 MeV and 8.5 MeV peaks from this spectrum are peaks generated by the alpha spectrometer standard impulse generator, in order to be used at energy calibration. If the energy level is used for the energies $E_1 \geq 5$ MeV and $E_2 \geq 7$ MeV, the areas of these two peaks are obtained, and those areas can be well determined from $N_1$ and $N_2$, the number of impulses recorded for the two thresholds $E_1$ and $E_2$.

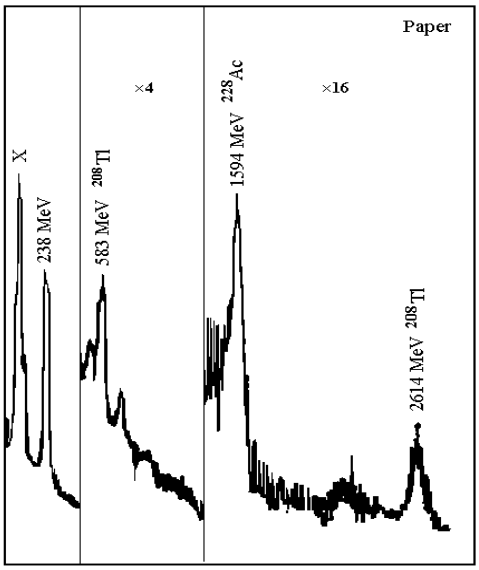


**Fig. 1.** Gamma spectrum for paper sample irradiated with thoron

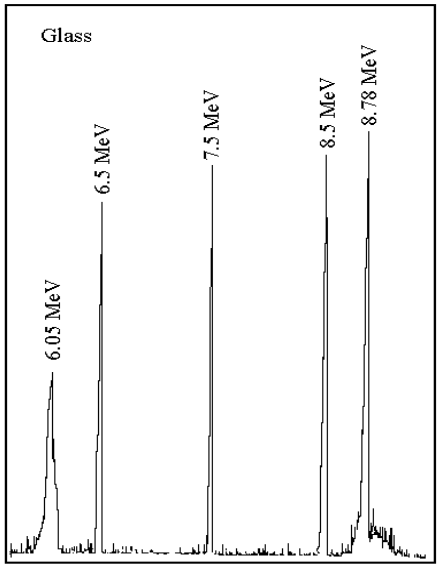


**Fig. 2.** The alpha spectrum obtained for the glass sample

$$\mathbf{A_1 = N_1 - N_2}$$
$$\mathbf{A_2 = N_2} \quad (1)$$

We can now calculate the weighting factors at the 212-Bi disintegration:

$$\mathbf{g(6.05\ MeV) = A_1/(A_1+A_2) = (N_1-N_2)/N_1}$$
$$\mathbf{g(8.78\ MeV) = A_1/(A_1+A_2) = N_2/N_1} \quad (2)$$

As this spectrum shows, the peaks are relatively narrow, especially the 8.78 MeV peak. The width of the peaks depends much on the degree of the surface roughness as it is presented in Fig.3 where the alpha spectrum for the Cu sample is represented, which was previously chemically cleaned using a $HNO_3$ solution. The width of the lines is in this case four times greater than that in the case of the glass sample. With mechanically polished Cu samples the lines are thinner.

A similar spectrum with that of the glass sample was obtained in the case of polyethylene, the widths of the lines being very alike, Fig.4.

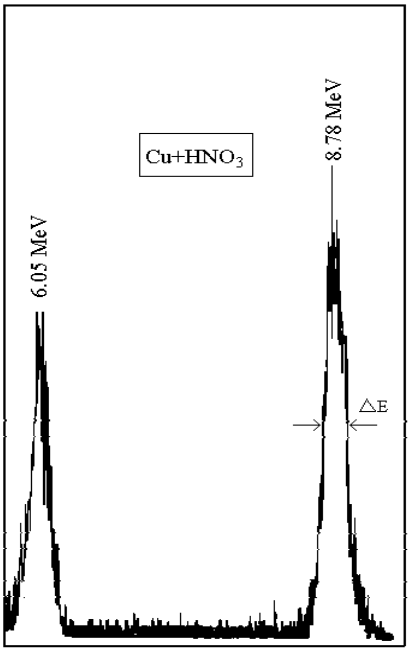


**Fig. 3.** Alpha spectrum of a copper sample cleaned with $HNO_3$

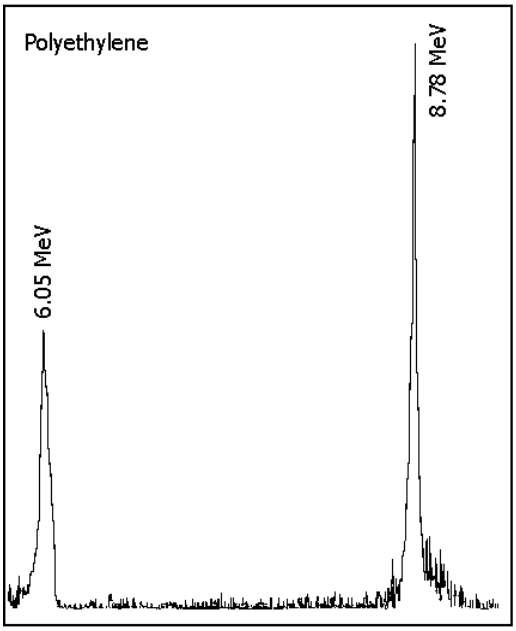


**Fig. 4.** Alpha spectrum for a polyethylene sample

Using the relations (1-2) the weighting factor for beta decay of $^{212}$Bi was found. The average value for our results is (63.25±0.95)% in good agreement with the standard. The width ΔE of the line depends on the nature and degree of material processing. The narrowest lines were recorded when working with glass and plexiglas materials with a very glossy surface. Taking for glass and Plexiglas an average width of 50 keV of the 8.78 MeV line and considering that the alpha detector protective cover introduces a supplementary width of the line, from 25 keV to 35 keV, we can calculate that the excess width of 15 keV is the result of a depth implantation of about 100 nm for $^{212}$Pb. Compared with other obtained data this value is almost 50% greater [13-14]. The excessive line width for the Cu sample treated with $HNO_3$ (221keV) suggests that the implantation of thoron and radon progeny could be used in the study of surface roughness. When mechanically polished, the same Cu probe gives approximately just half of the initial width, a value that can be also found for the Al sample. Another remark refers to glossy paper, with moderate values of the line width.

For glass, exposure was repeated placing the sample at four different heights: 2 mm, 6 mm, 10 mm, 16 mm from the thorium level in the box. The implantation result is observed in Fig.5. The quantity values of implanted $^{212}$Pb linear decreases, which may reflect the gravitational deposition of aerosols.

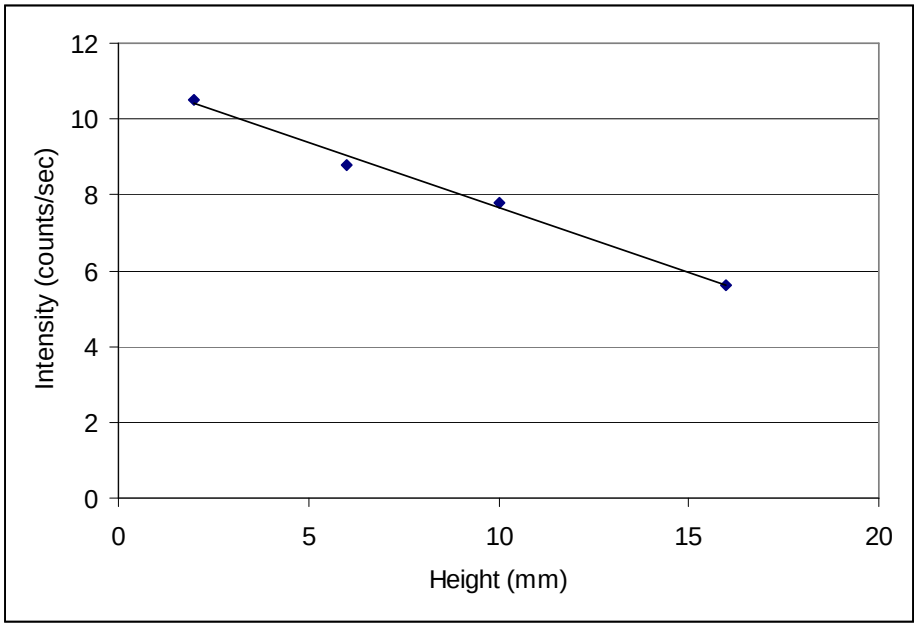


**Fig. 5.** Influence of gravitational deposition on the deposed and implanted $^{212}$Pb

The following experiment was made for the glass sample, consisting of 5 consecutive measurements. The first measurement was made after the sample was removed from the container, without touching the implanted surface (a). After that, the sample was carefully cleaned with a soft material and re-measured (b). The sample was again removed from the spectrometer chamber and cleaned with ethanol 95%, then re-measured (c). The operation (c) was repeated (d). This sample was measured again the next day, after 19 hours (e). The results are gathered in Table 1. In the first case (a) there is a great contribution of the aerosols gathered on a surface, which can be easily removed (b). A cleaning operation with ethanol (c) removes a part of the $^{212}$Pb and $^{212}$Bi atoms implanted even on the surface, but by repeating this operation the quantity implanted is hardly influenced. Calculating the lifetime of the implanted progeny, from the values (d) and (c) a value of T=10.55h is obtained, very close to the value of the lifetime of $^{212}$Pb.

**Table1.**

**The influence of surface cleaning on the implantation parameters**

| **Sample** | **(a)** | **(b)** | **(c)** | **(d)** | **(e)** |
|---|---|---|---|---|---|
| **Delay time** | 0 | 10min. | 20min. | 30min. | 19hours |
| **Intensity (c/s)** | 28.40 | 14.60 | 9.82 | 9.65 | 2.77 |

Also in the case of thoron progeny, the attachment to aerosols may be probably neglected due to short life time of $^{216}$Po ( 0.5 s ).

## REFERENCES

[1] J.H. Lubin, Health Phys., 75, (1998) 4.

[2] R.S. Lively, E.P. Ney, Health Phys., 52 (1987) 411.

[3] C. Samuelsson , Nature, 334 (1988) 338.

[4] J.Palfalvi, I. Feeher, M. Lorinc, Radiat. Meas., 25 (1995) 585.

[5] W. Jacobi, Health Phys., 22 (1972) 441.

[6] J.Cornelis, C. Landsheer, A. Poffijn, Appl. Radiat. Isot., 43 (1992) 1027.

[7] G. Meesen, A. Poffijn, J. Uyttenhove, Radiat. Meas., 25(1995) 591.

[8] P. Cauwels, A. Poffijn, in: Jozef Sobol editor, IRPA Regional Symposium on Radiation Protection in Countries of Central Europe, 1997, p. 102.

[9] I. Bigu, J. Aerosol Sci., 16, (1985) 157.

[10] J. Porstendorfer, A. Reineking, Radiat. Prot. Dosim., 45 (1992) 303.

[11] Y.S. Cheng, C.C. Yu, K.V. Tu, Health Phys., 66(1994) 72.

[12] J. Plch, Manual for operating LUK 3A ,Prague 1997, pp. 27.

[13] T.M. Semkow, Geochim. Cosmochim. Acta, 54 (1990) 425.

[14] J.Cornelis, H. Vanmarke, A. Poffijn, Health Phys., 65 (1993) 414.

STUDIA UNIVERSITATIS BABEŞ-BOLYAI, PHYSICA, SPECIAL ISSUE, 2000

# QUANTITATIVE AND QUALITATIVE ANALYSIS OF ACTIVE PRINCIPLES OF MENTHA PIPERITA L. AND HIPPOPHAE RHAMNOIDES L. BY GC/MS

**CARMEN GHERMAN, MONICA CULEA*, O.COZAR**

*Universitatea "Babes-Bolyai", Cluj-Napoca*
**S.C."Natex"S.R.L., Cluj-Napoca*

**ABSTRACT.** *The active principles in plants are the chemical organic substances synthesized in the vegetal cells.*

*Mentha Piperita L.* (*Libiatae* family) is a hybrid. The compounds identified in different types of the same plants of *Mentha Piperita L.*, extracted by liquid-liquid extraction (LLE) method, are presented. The extracts were analysed by GC and GC-MS. The gas chromatography-mass spectrometry analysis results prove the existence of some active principles of *Mentha Piperita L.* We show the quantitative and qualitative analysis of vegetal active principles from *Mentha Piperita L.*

This article presents also, the quantitative determination of vitamin E from *Hippophae rhamnoides L.* oil. It has been used the GC/MS method. The precision of the extraction method gave relative standard deviation lower than 3%. It has been used a calibration curve with cholesterol as internal standard. The results showed that *Hippophae rhamnoides L.* oil contains 0.05% vitamin E.

## Introduction

Previous studies have proved that the therapeutical activities of herba plants are not depending by their form, color, taste, and smell [1,2], but they are depending of some organic compounds called "*vegetal active principles*" [3]. The active principles in plants are the organic compounds synthesized in the vegetal cells. Their various chemical structures explaines their multiple therapeutical actions**.**

The vegetal active principles have physical and chemical properties. It is necessary to take care when a drug is prepared for a complete extraction of the active principles from plants, otherwise they can be destroyed in the extracting process with the diminuation and even the loss of therapeutical activity.

In the first part of this paper we show the quantitative and qualitative analysis of vegetal active principles from *Mentha Piperita L.* and the second part presents the quantitative analysis of vitamin E from *Hippophae rhamnoides L.* oil by using a GC/MS method. Vitamin E from *Hippophae rhamnoides L.*oil was determinated by using a regression curve.

## Experimental

The coupling gas chromatograph-mass spectrometer is useful for the analysis of some complex mixtures of organic compounds, with a large number of components [4,5,6]: the chromatograph is ideal for complete separation of the compounds of a mixture and the mass spectrometer is an ideal detector for the identification of each compound.

A Hewlett Packard 6890 gas chromatograph with flame ionisation detector (FID) and a Hewlett Packard 5989B mass spectrometer detector were used. It is used a fused silica capillary column (HP-5MS), 30m x 0.32 mm, 0.25 μm film thickness, in different temperature programs from 50°C (kept 2 minutes) to 250°C, with a rate of 8°C per minute for aroma compounds and from 70°C/min with 20°C/min to 100°C, then 30°C/min to 300°C/min (15min) for vitamin E determination. The injector and the detector temperature is 250°C, and the flow rate of He is 1ml/min.

The mass spectrometer has the electron energy of 70 eV, the electron emission 300μA, the ion source temperature 200°C, and the analyser temperature 100°C. The interface was kept at 250°C.

The quantitative and qualitative analysis of vegetal active principles from *Mentha Piperita L.* has been done by gas chromatography and gas chromatography-mass spectrometry methods. The liquid-liquid extraction (LLE) method was used.

The extraction process consists in: 1g from each dry and crushed plants sort mixed with 20 ml ethanol and 20 ml distilled water. For the experiment we used the flowers, the leafs and the stems of the plants. We kept 2 or 3 days these mixtures. Then one quantity of 0.6 ml from these mixtures was mixed with 0.2 ml solvent (ethyl acetate: hexane: methyl chloride, in a proportion of 5:1:1). The new mixure was agitated for 2 minutes, and 4μl was injected in the chromatograph. The separated compounds were identified with the mass-spectrometer.

The reagents used for this experiment are: ethanol, methyl chloride, hexane, ethyl acetate, and distilled water.

## Results and discussion

Five different samples were used for analysis: $P_1$ proceeds from a private herb shop, $P_2$ from a state herb shop, $P_3$ from harvest as white-peppermint from the forest, $P_4$ from harvest as green-peppermint from the forest, and $P_5$ from a private garden.

The extracts were analysed by the GC/MS. The gas chromatography-mass spectrometry analysis results prove the existence of some active principles in *Mentha Piperita L.* The compounds are:

1. Isobutyric acid
2. Menthone
3. Isomenthone
4. Guanidine
5. Carvone
6. Cis-piperitone oxid
7. Butyl-butyryl lactate
8. Heptadecane
9. 3 hexenyl fenylacetate
10. Ethyl myristate
11. Cis-3-hexenyl 2 aminobenzoate
12. Linalyl fenylacetate
13. Palmitic acid
14. Ethyl palmitate
15. Stearaldehyde
16. γ-undecalactone
17. Stearic acid
18. DOP (contaminant)
19. Ethyl linoleate

The figure 1 and figure 2 are presents the chromatograms of samples $P_1$, $P_2$, $P_3$, $P_4$, and $P_5$. The precision of the extraction method gave a relative standard deviation lower than 3%.The results were compared taking into consideration the same variables: the amount of sample, the extracting solvent volume, the extraction temperature, and the extraction time[7,8,9].

The range for vitamin E acetate in the regression curve was 0-250 μg when the same quantity of 250 μg of cholesterol the internal standard, was added. Vitamin E was determined in *Hippophae rhamnoides L.*oil.

Figure 3 presents the chromatogram of *Hippophae rhamnoides L.*oil sample and the vitamin E mass spectrum Figure 4 presents the comparison of the vitamin E and vitamin E acetate mass spectra and figure 5 presents theirs chemical formulae. The chromatogram of the mixture of known quantities of cholesterol and vitamin E acetate is presented in figure 6.

The second part of this article shows the quantitative analysis of vitamin E from *Hippophae rhamnoides L.* oil determinated by a GC/MS method. We are used a calibration curve with the cholesterol as internal standard. The regression curve is y=0.014x-0.20 and the correlation factor shows a good linearity (r = 0.99) (Figure 7).

**Conclusions**

In the *Mentha Piperita L.* case we observe that the plants provided from private garden keep the volatile compounds much better than the others samples.

The results show the presence of very different compounds for different types of the same plant, probably as a consequence climate, soil, and other factors.

The precision of the extraction method gave relative standard deviation lower than 3%. The results were compared taking into consideration the same variables: the amount of sample, the extracting solvent volume, the extraction temperature, and the extraction time. By using an appropriate mixture of solvents, a good recovery of the active principles were obtained by LLE method (81%).

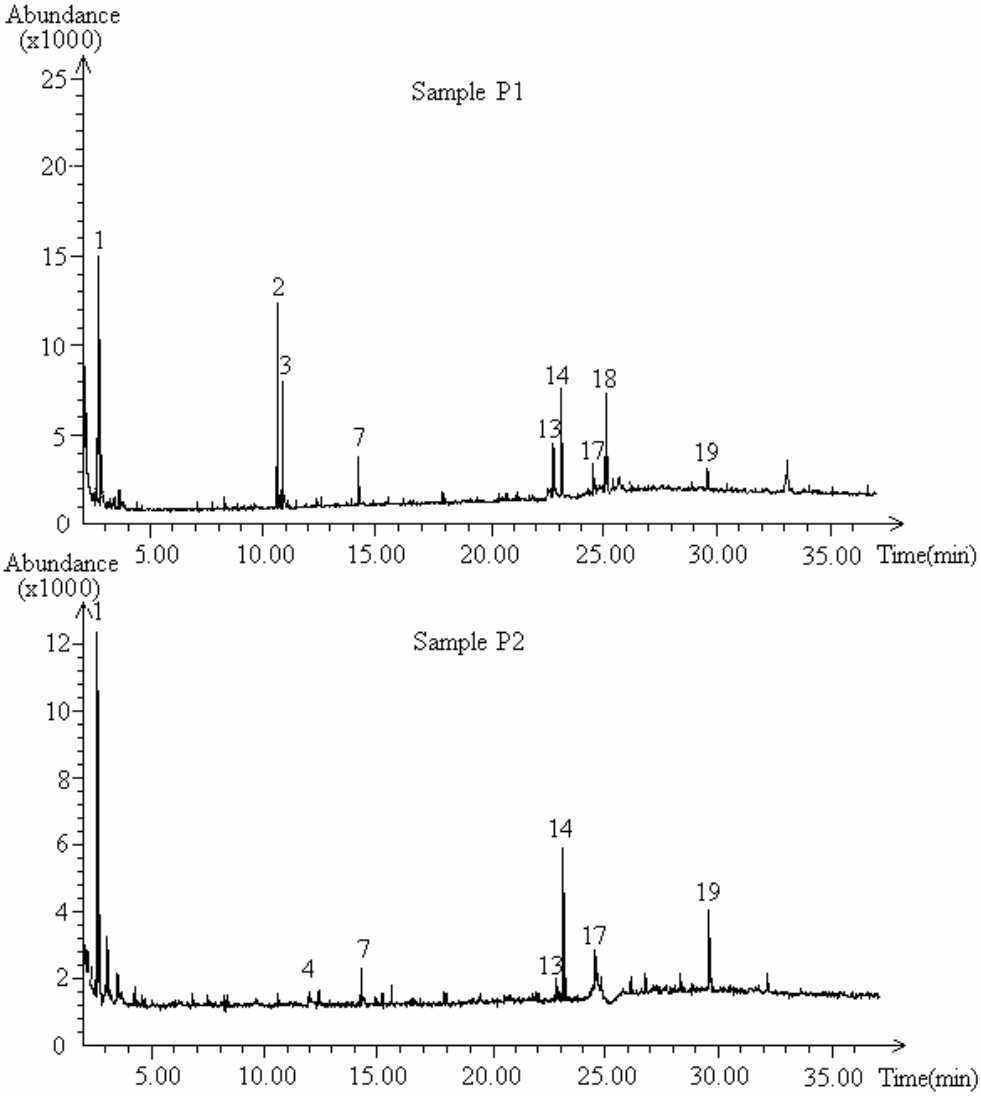


Figure 1. The chromatograms of Mentha Piperita L. ( samples: P1 ,P2 )

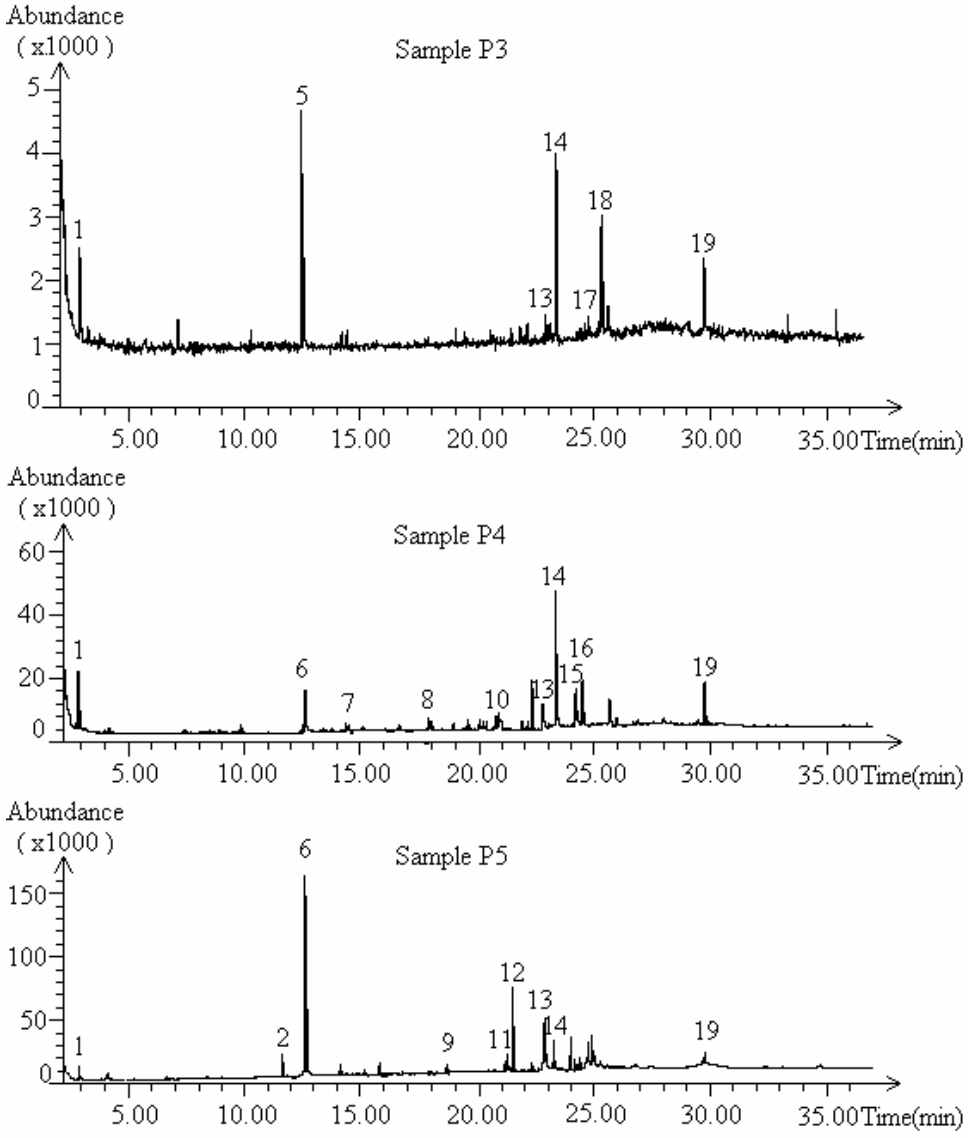


Figure 2.The chromatograms of Mentha Piperita L.(samples: P3, P4, P5 )

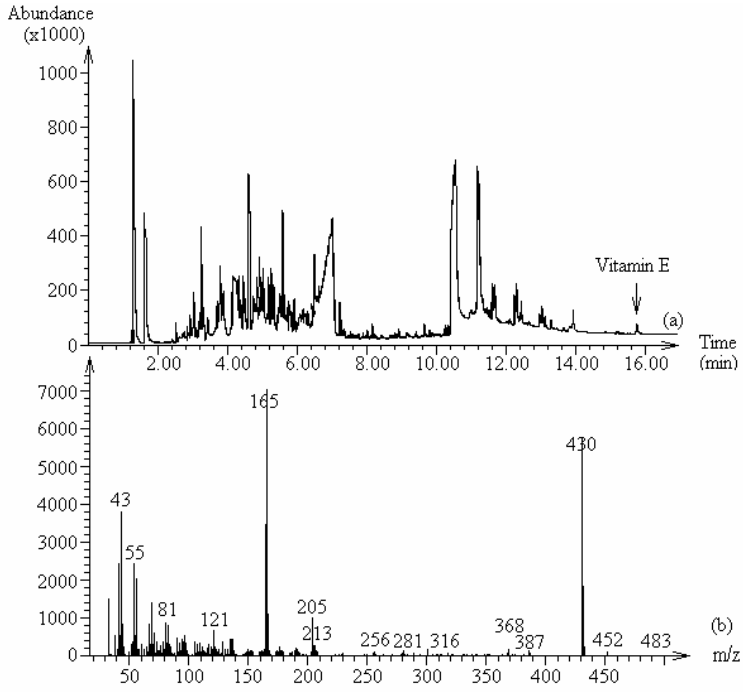


Figure 3. The chromatogram of Hippophae Rhamnoides L. and the vitamin E mass spectrum

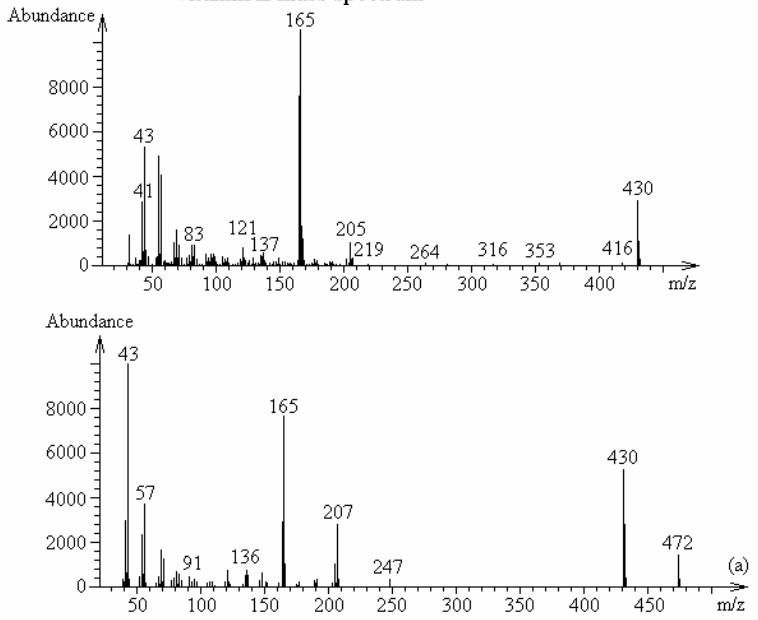


Figure 4. The comparison of vitamin E and vitamin E acetate mass spectra

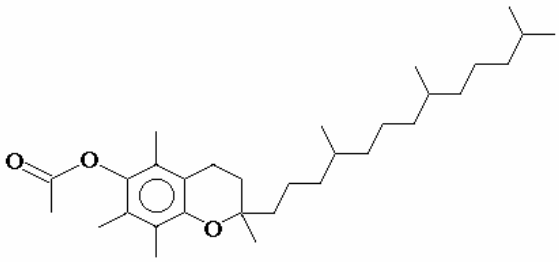

$C_{31}H_{52}O_3$

Vitamin E acetate

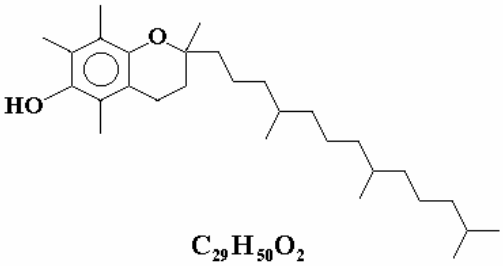

$C_{29}H_{50}O_2$

Vitamin E

Figure 5. The chemical formula of vitamin E and vitamin E acetate

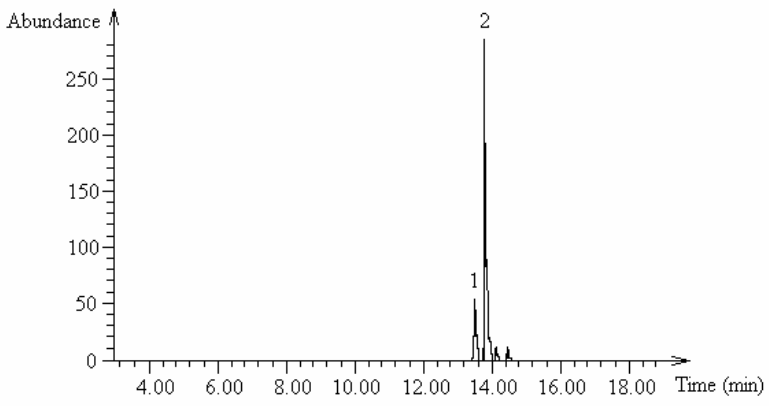


Figure 6. The chromatogram of the mixture of know quantities of cholesterol and vitamin E acetate

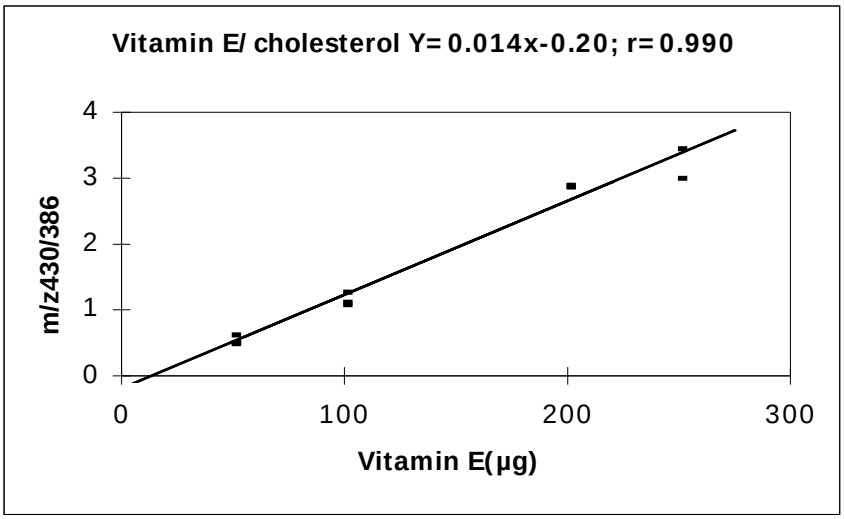


**Figure 7.** The regression curve for vitamin E quantity in Hippophae rhamnoides L oil.

It can be also observed that the herbs from private garden kept much better the volatile substances and they will have a good taste. Carvone is the only compount which is present in the forest variety of the plants.

The results also show that *Hippophae rhamnoides L.*oil contains 0,05 % vitamin E which is an antioxidant and takes an important function in nutrition, cardiovascular diseases, and muscular, nervous and glandular system aging process. The precision of measurements gave a relative standard deviation of 20 %.

## REFERENCES

[1] C.Popescu, C. Brăileanu, Indreptar farmaceutic, Ed.Ştiinţă şi Tehnică, Bucureşti 1974.

[2] R.Zitti, Farmacopeea romana,Ed.Humanitas, Bucureşti 1976.

[3] A.Agopian, Plantele medicinale din flora spontană şi substituirile lor, Ed. Humanitas, Bucureşti, 1975.

[4] V.Mercea, P.Ardelean, D.Ursu, Introducere în studiul spectrometrie de masă, Ed. Tehnică, Bucureşti 1978.

[5] J.V.Hinshaw, LC-GC Int., 6(10):606(1993).

[6] L.Jordan, LC-GC Int., 6(10):594(1993).

[7] L.Maignial, P.Pibarot, G.Bonetti, A.Chaintreau and J.P.Marion, J.Chromatogr., 606 (1): 87(1992).

[8] D.A.Moyler, Developments in Food Flavours (G.G. Birch and M.G. Lindley, eds.), Elsevier, London, 1986, pp.118-129.

[9] J.O.Bosset and R.Gauch, Int. Dairy J., 3:359(1993).

# QUANTITATIVE ANALYSIS OF CHOLESTEROL BY GAS CHROMATOGRAPHY AND GAS CHROMATOGRAPHY/ MASS SPECTROMETRY

**MONICA CULEA, GH. CIURDARU, LIDIA LUNCIAN, MIHAELA APETRI, LAURA FROMONDI, R. PODEA**

*Natex S.R.L., 3400 Cluj-Napoca, P.O.Box 374, Romania*

**ABSTRACT.** A method for quantitative analysis of cholesterol in egg yolk and tissues is presented. The internal standard was diosgenin, added 5mg/g of egg yolk or 1mg/g of tissue. The extraction was performed in dichloroethane: methanol in an optimization process of the amount of sample, extractant solvent volume, extraction temperature, extraction time. The extraction was followed by methylation of fatty acids and gas chromatographic and gas chromatography- mass spectrometric analysis. The extract was derivatized with methanol HCl 1M, at 60$^{o}$C, 1h for fatty acids. A HP-5 capillary column, 30mx0.32mm, 0.25µm film thickness, in a temperature program: 70$^{o}$C (1 min) to 100$^{o}$C with a rate of 20$^{o}$C per minute, then 30$^{o}$ C per minute to 310 $^{o}$C (10min) was used. The method was validated showing good analytical parameters. The method was applied for monitoring the cholesterol level in egg yolk or tissues for testing different functional food diet to chicken.

**Keywords:** cholesterol, gas chromatography; gas chromatography-mass spectrometry; egg yolk; tissue.

## Introduction

Cholesterol, indispensable substance to our body present in our cell membrane, is healthy to be intake in low quantities by food. It is present especially in egg yolk, meat and dairy products. In the last years many articles show the health benefits of different ingredients contained in foods. The influence of some of these functional foods could be observed in the variation of cholesterol level in biological matrices [1].

Several methods have been used to quantitate total cholesterol in multicomponent foods; eggs [2-6], meat [7-9], dairy products. Methods usually involve an organic extraction and a quantitative technique such as gas chromatography (GC) or liquid chromatography (LC). The organic extract is saponificated or not and the cholesterol sample is derivatized or not before GC analysis. Many collaborative studies are made for the optimization of the experimental design approach for obtaining the best recoveries, low solvent consumption and reduced extraction times [2-10].

The aim of this paper is to present a rapid method for cholesterol quantitation in egg yolk and tissues. Cholesterol was analysed without derivatization. The recovery of our method was compared with the recovery obtained by other methods [2]. Saponification was replaced by methylation for monitoring the total cholesterol and fatty acids levels too. The analytical technique chosen is gas chromatography (GC) with flame ionization detection (FID) and gas chromatography - mass spectrometry (GC/MS) for identification of the separated compounds.

## Experimental

### *Apparatus*

A Hewlett Packard GC 5890 couplet with a MS engine 5989B in the EI mode was used for compounds identification. The GC was equipped with an HP-5MS capillary column 30m x 0.25mm diameter, 0,25µm film thickness, in the temperature program: 70 $^{o}$C for 1 min, then increased to 100$^{o}$C with a rate of 20 $^{o}$C/min, followed by a rate of 30$^{o}$C/min to 310$^{o}$C(10min) at a helium flow rate of 1ml/min. A Hewlett Packard 6890 gas chromatograph was equipped with a HP-5 fused silica capillary column, 30mx0.32mm, 0.25µm film-thickness with the same temperature program.

Deactivation by treating the injector glass liner with 5% dimethyldichlorosilane in toluene gave a higher sensitivity. The GC/MS interface line and the ion source were maintained at 200$^{o}$C, and quadrupol analyser at 100$^{o}$C. Electron energy was 70eV and electron emission 300µA.

### *Reagents and chemicals*

Solvents (methanol, ethanol, methylen chloride, 1,2dichloroethane, purchased from Chimopar (Bucharest, Romania) were purified by distillation, when necessary. Acetyl chloride was purchased from Carlo Erba (Milano, Italy). Cholesterol (99% pure) and diosgenin (99% pure) were purchased from Sigma-Aldrich (Deisenhofen, Germany).

### *Procedure*

Six aliquots containing 50, 100, 150, 200, 250 and 300 µg cholesterol and the same quantity of 80 µg of the internal standard diosgen were prepared. 3 µl were injected two times from each alliquot by using the autosampler injector to obtain a regression curve for egg cholesterol determination in the range 0-300 mg. The relative integrated areas were plotted against the injected amount as the calibration curve.

For tissue cholesterol analysis the chosen range was 0-70mg; seven aliquots of 10, 20, 30, 40, 50, 60 and 70 µg cholesterol and the same quantity of 100 µg of the internal standard diosgen were prepared, then injected twice by using the autosampler injector. The relative integrated areas were plotted against the injected amount as the calibration curve.

The weight of boiled and dried egg yolk corresponding to 1g of boiled egg yolk (or 1 g well mixed tissue) was placed in a 10 ml screw cap glass centrifuge tube with 5 ml 1,2 dichloroethane:methanol (1:1). The extraction was performed at 50$^{o}$C, 30 minutes, agitating well every 5 minutes. The extract was cooled, centrifuged and the supernatant was removed. 0.5 ml were transferred was methylated with 0.5 ml methanol: acetyl chloride (10:1,v/v) at 60$^{o}$C for 1h. The reagent was removed under nitrogen. 0.5 ml 1,2dichloroethane and 5mg diosgenin/g in egg yolk or 1 mg diosgenin/g in tissues were added. Three extracts were made and each sample and injected twice.

### *Experimental design*

10 replicates egg yolk were analyzed by our method. 3 replicated dried egg yolk were analyzed by our method and by saponification [2] to compare the recovery obtained by the two methods.

## Results and discussion

### *Method validation*

Linearity in the range 0-300 mg cholesterol gave a good correlation coefficient of r=0.998 and in the range 0-70 mg cholesterol of r=0.999. The regression curve obtained for the two ranges were: y = 0.02x - 0.02 (Fig. 1) and y=0.01x - 0.01; precision of the method measured in the aliquots containing 50, 60 and 200 µg cholesterol gave R.S.D lower than 2% (n=9) and for egg yolk control 6.5% (n=10); accuracy showed better than 4 %; (Table 1) recovery gave 95% (Table 2); L.O.D was lower than 5ng at a signal-to-noise ratio of 10.

**Table 1**

Precision and accuracy characterization for cholesterol in egg yolk (n=9)

| Cholesterol(mg) | | precision | accuracy |
|---|---|---|---|
| added | measured | R.S.D. (%) | R.S.D. (%) |
| 200 | 201.85 | 0.04 | 0.92 |
| 50 | 48.27 | 1.39 | 3.49 |
| 60 | 59.36 | 1.16 | 2.71 |

R.S.D.= relative standard deviation

**Table 2**

Comparative recovery mean values for cholesterol in egg yolk (n=3)

| Procedure | S (%) | M (%) | US (%) | USM (%) |
|---|---|---|---|---|
| boiled and dried | 99.8 | 95.54 | 70.40 | 95.36 |
| boiled | 94.06 | 91.6 | | |

S=saponification[2]; M=methyilation(ours); US=unsaponification; USM=unsaponification and methylation

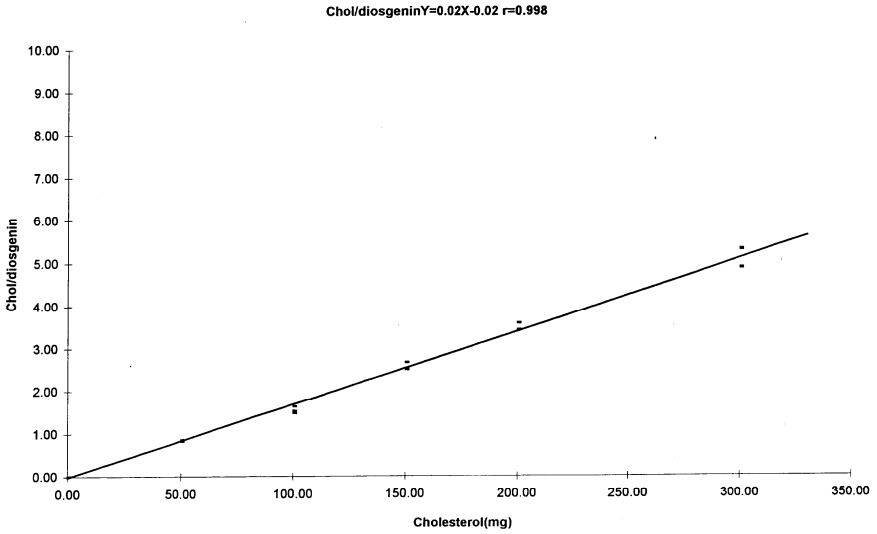


**Fig. 1.** Correlation curve for egg yolk cholesterol calculation

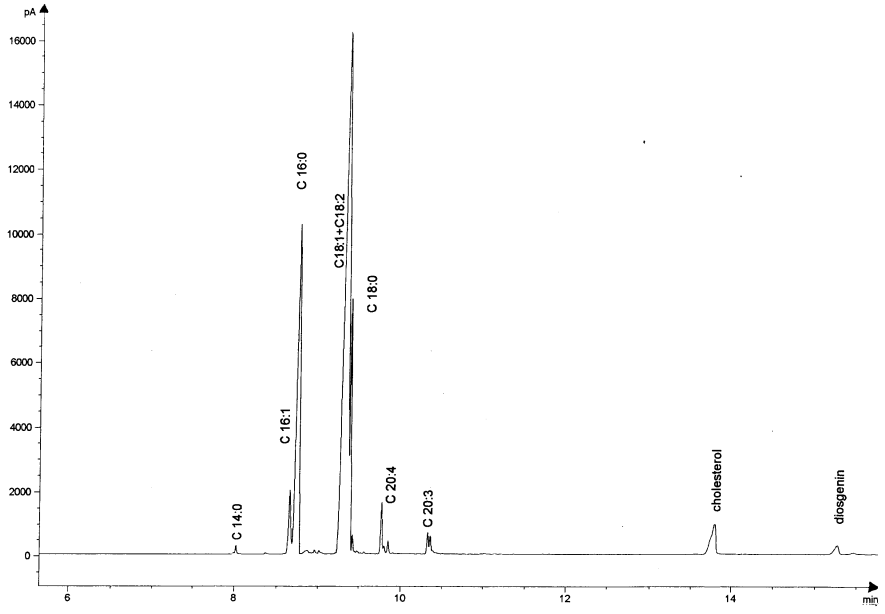


**Fig. 2.** The separation chromatogram of lipids in egg yolk. Fatty acids methyl esters (FAME) of: myristic acid (C14:0); palmitoleic acid (C16:1); palmitic acid C16:0); oleic acid (C18:1); linoleic acid (C18:2) ;stearic acid (C18:0); arachidonic acid( C20:4).

The chromatogram of separation of the compounds studied is presented in Fig. 2. The results of the precision, accuracy and recovery studies are presented in Tables 1 and 2. The average values are resulted from three extraction procedures and two injections of each extract. Precision and day-to-day reproducibility measured for 50 and 60 µg standards (n=6) showed relative standard deviation values bellow 4%. The mean values for the recoveries found for each method studied are compared. The best values for recovery were found for dried egg yolk (Table 2). Significant test studies showed no significant differences at the 0.05 level between the two methods (Table 3).

The mass spectra for cholesterol and diosgenin are shown in Fig.3. Diosgenin was a mixture of two isomers with the same mass spectrum and closed retention times.

**Table 3**

Comparative mean value for cholesterol by two different methods (n=3)

| Method | Cholesterol (mg) | S. D. | R.S.D. |
|---|---|---|---|
| M | 193.41 | 6.58 | 3.40 |
| S | 209.56 | 1.25 | 0.59 |

M=methylation; S=saponification; S.D.:standard deviation; R.S.D.:relative standard deviation

## Conclusions

This paper presents a method of cholesterol determination in egg yolk and tissues. The comparison between two extraction methods gave similar recovery results without significant differences of the mean values of cholesterol levels. The method was validated showing good analytical parameters: linearity in the range 0-300 mg cholesterol gave a good correlation coefficient of r=0.999; precision of the method gave R.S.D. 6.5% (n=10 in egg yolk; accuracy showed R.S.D. better than 3 %; recovery gave 95% comparable with the recoveries obtained with other methods (99%) [2]; L.O.D was lower then 5ng. The boiled and dried egg showed better analytical parameters.

The methods are suitable for the determination of cholesterol amount in food and biological matrices. The method is simple, rapid, accurate and suitable for cholesterol level variation study for testing the benefits of functional food diet.

The author thank the management, Director and colleagues, S. C. Natex s.r.l., for their co-operation in conducting this study.

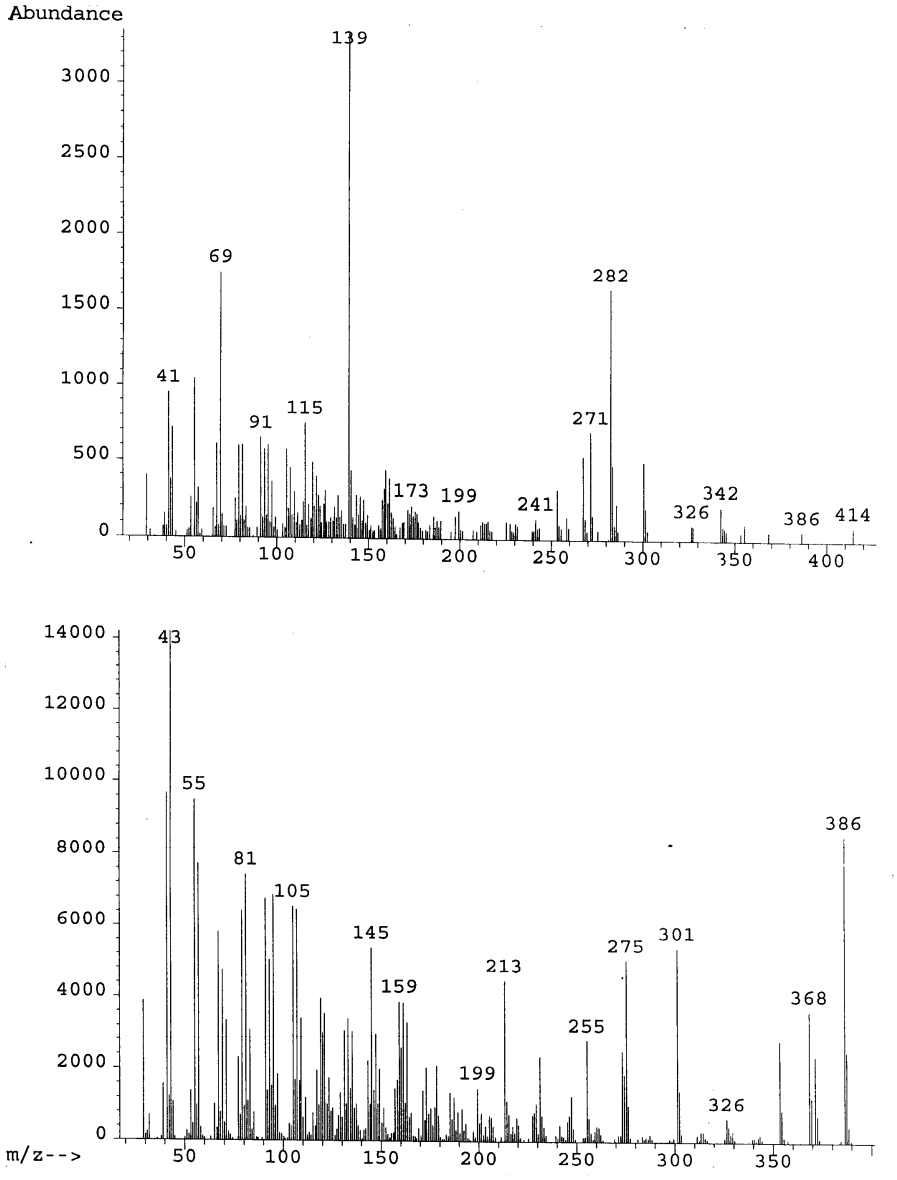


**Fig. 3.** Diosgenin (M=414) and cholesterol (M=386) mass spectra

## REFERENCES

1. C. M. Hasler, "Functional foods: Their role in diseases prevention and heath promotion" Food Tech. 52( 11) 1998, 63-70.
2. J J.D.Beyer, F.X. Milani, M. J. Dutelle, R.L. Bradley , "Gas Chromatographic determination of cholesterol in egg products"J. Assoc. Off. Anal. Chem. 72( 5) 1979, 746-748.
3. M. T. Rodriguez- Estrada, M. F. Caboni, A. Costa, G. Lercker, " Gas chromatographic analysis of cholesterol oxidation products on a thermostable medium polarity capillary column", J. High Resolut. Chromatogr. 21(9) 1998, 509-512.
4. G. Pasin, G. M. Smith, M. O'Mahony, "Rapid determination of total cholesterol in egg using commercial diagnostic cholesterol reagent", Food Chem. 61(1-2) 1998, 255-259.
5. M. S. Lai, J. I. Gray, M. E. Zabik, "Evaluation of solid-phase extraction and gas chromatography for determination of cholesterol oxidation products in spray-dried whole egg", J. Agric. Food Chem. 43(5) 1995, 1122-1126.
6. F. Guardiola, R. Codony, M. Rafecas, J. Boatella, "Selective gas-chromatographic determination of cholesterol in eggs", J. Am. Oil Chem Soc. 71(8) 1994, 867-871.
7. M. Fenton, J. S. Sim., "Determination of egg yolk cholesterol content by on-column capillary gas chromatography", J. Chromatogr. 540 (1-2) 1991, 323-329.
8. E. D. Naeemi, N. Ahmad, T. K. Al-Sharrah, M. Behbahani, "Rapid and simple method for determination of cholesterol in processed food", J. AOAC Int. 78(6) 1995, 1522-1525.
9. K. Duckett, D. G. Wagner, " Effect of Laidlomycin proprionate on bovine longissimus muscle fatty acid and cholesterol content", J. Agric. Food Chem. 45, 1997, 1725-1728.
10. M. Van. Boven, P. Daenens, K. Maes, M. Cokelaere, " Content and composition of free sterol free fatty alcohols in jojoba oil", J. Agric. Food. Chem. 45, 1997, 1180-1184.

STUDIA UNIVERSITATIS BABEŞ-BOLYAI, PHYSICA, SPECIAL ISSUE, 2000

# FLIGHT TIME MASS SPECTRA FROM ION PACKETS GENERATED ON THE SLOPE OF THE DEFLECTING PULSES

**D. IOANOVICIU, C. CUNA, A. PAMULA, N. PALIBRODA, V. COSMA, ST. KOVACS, ST. POPESCU, M. KAUCSAR, B. ERDELYI, L. SARKOZI, D. URSU, P. ARDELEAN**

*National Institute for Research and Development of Isotopic and Molecular Technologies, Cluj-Napoca, Romania*

## Introduction

With the purpose to built up new solutions in time-of-flight mass spectrometry ([1] is a general reference about this research field) an experimental model of this kind of mass spectrometer was constructed. This experimental set up was initially intended to work with a pulsed ion source able to store ions in the time lapse between two consecutive extracting pulses. The constructed ion source follows closely the design of Wollnik and his team [2]. The research performed in this direction has as main purpose to overcome the technical problems arising from a limited budget by trying to use an extended and diversified range of solutions.

## Tested solutions

To overcome the difficulties connected with the construction or the costs of a pulse generator with floating mass**,** the method of beam cutting (beam chopping) was used. The major inconvenient of this method is the use to the packet formation of only a small part of the ions delivered by the source in a continuous beam. The big advantage of the procedure is however the possibility to operate the ion source pulse generator at the ground potential. Therefore the ion source originally designed to work in a pulsed regime was operated with continuous voltages applied to their electrodes. First a function generator of the Hewlett Packard 8005 B type was used. This generator delivered trapezoidal pulses of 20 V maximal height. This limitation was somewhat aleviated by the construction of a pulse generator of 240 V flat top value. The ion source was operated in a continuous regime with the following set of typical values: electron accelerating voltage 70 V, electron reflector voltage -120 V, voltage between the ionization chamber and the ion gun 3-5 V, ion reflecting voltage 10.8 V.

The ion source geometry is completely determined by specifying the following dimensions: depth of the extraction space 2 mm, the portion of beam acceleration in homogeneous field 21.6 mm, between them being located a space of 9 mm.

The ion gun, having the purpose to create an electric field as homogeneous as possible was incorporated in a system of three electrodes fed through a voltage divider [3].

The length of the ion packets resulted by the continuous ion beam chopping was derived from a straightforward method in Ref. 4. More sophisticated applications of this method arose later as double gate devices [5], [6] and more recently as chopping devices with venetian blind [7].

Our chopping deflector was designed accounting for the limitations of the available instrumentation. The first burden was the need to deflect the beam quickly enough with reduced voltages applied on the plates, by using a small voltage pulse generator. The chopper's geometry can be defined by the length of its plates 122 mm and the gap between them 14 mm [8]. The width of the plates was selected in such a way that an acceptable field homogeneity is ensured in the space region where beam ions are passing.

The deflecting system can be operated in two modes. If the voltage impulse length can be conveniently selected the pulse flat top can be used entirely. Then one of the electrodes is polarized to a potential equal to the pulse height. On the opposite electrode the pulse is applied, during the time interval between two pulses being at the ground potential. By this procedure the ion beam from the source is deflected on one of the plates except the time lapse when the pulse acts, when the beam is passing undeviated. Therefore the length of the ion packets will be equal to the pulse flat top length. If the length of the available pulses is too long to obtain the desired length packets another procedure can be used. If a plate is polarized to a potential smaller than the height of the pulse, the ion beam will be deflected on the plate before the pulse beginning, on the opposite plate when the voltage increases approaching the flat top value. By this procedure the length of the ion packet can be reduced in principle how much it is wanted with the according loss of intensity, by reducing the width of the entry and exit slits of the chopping device. The unpleasant feature of this procedure is that the height of the applied pulse must be big enough to ensure the efficient deviation on both sides. The most efficient version of the method uses only the increasing part of the pulses to generate ion packets. The condition to be satisfied in this case is that the time the ion is tranziting the deflector must be shorter that the time lapse when the voltage increases or decreases. While the transit time of the ions can be reduced by shortenning the plates and by increasing the ion energy, the height of the pulses must be increased because the gap between the plates can not be reduced under a certain limit, set by the space needed to accomodate the beam delivered by the source. By fast transistorised high voltage swiches voltages of 5 kV can be established in 9 ns [9]. Even swiches of 65 kV [10] are available with increasing time lengths of 70 to 135 ns. Simple calculations allow to connect the basic electrical and geometric parameters of the deflecting system to the ion packet length. If the ions spend inside the chopper time intervals longer than the increasing time interval of the pulses, the ion packet length is given by the expression:

$$dt = (2^{1/2})D(F+f)/\{nL_d/v_z[(1+a)^2+a^2-(t_f v_z/L_d)^2/6]^{1/2}\}$$

where the symbols are:

D the distance between the chopper plates,
F the width of the ion beam approximately parallel,
f the width of the slit in front of which the ion beam is swift,
n=eV/U, +/- V the highest voltage applied to the chopper,
U the chopped ion energy,
$L_d$ the chopper effective length,
$v_z$ the average longitudinal ion velocity,
$a = L_f/L_d$, $L_f$ the longitudinal distance between the chopper and the slit,
$t_f$ the pulse front length.

For our device, operated with the Hewlett Packard function generator, the above procedure can be applied for the following geometric parameters and reducing the ion energy to 500 eV: D=0.014 m, $L_d$ = 0.122 m, $L_f$ =0.586 m, F=f= 1 mm, the packets result of $3.1x10^{-8}$ s (while for F=8 mm they should be of $1.4x10^{-7}$ s.) With the 240 V impulse height generator the possible length of the ion packets reduces to 1.5 and 6.9 ns respectively.

The length of the ion packets can be reduced to convenient values paying the price of the ion number los. Also it must be observed that the charge density along the ion packet is not constant. Even for a parallel primary beam, of constant charge density, the packet obtained by chopping will have a trapezoidal longitudinal charge profile. This is easy to understand as when the beam begins to cover the slit area, the transmited quantity of ions increases linearly, decreasing in the same way when the beam leaves the slit on way to the another plate.

The ion duty cycle can be improved significantly by operating the ion source in a storage mode and extracting the ion packets in bursts longer than the packet final length. In this way the ion packets will be adjusted by the deflecting system to the desired size. In this case the ion source needs a pulse generator with floating mass, working sinchronized with the chopper pulses.

Ther use of the ion packet production by chopping a continuous beam, from gaseous samples, eliminates the harmful effect of the turn-around time, on the time focusing of the instrument. The analyzer benefits in this way of the energy focusing ensured by the electrostatic mirror.

The tests were performed by the direct detection of the ion packets. The detector incorporates a pair of channel plates borowed from IFIN "HH" and is located at 1137 mm from the final grid of the ion source.

A single stage, homogeneous electrostatic field mirror [11] was constructed. It was assembled from metalic rings of 122 mm inner diameter. With this mirror mounted inside the vacuum system and with the detector relocated on the source side, the field-free space travelled by the ions was of 1425 mm, as it resulted from the condition of energy focusing in time, at first order, to have focused the ion packets leaving the source final grid. The reference ion turning point inside the mirror was placed at 356 mm from the mirror entry to ensure the unaltered homogeneity of the field all along the ion path.

Ion spectra were obtained for the residual vacuum. For the direct detection, with 400 V ion accelerating voltage, the measured flight time was of 6.18, 19.23 and 24.1 microseconds for the mass 2, 18, and 28 respectively. They are obtained from the mass scale $t = a + bm^{1/2}$ if the constants are taken a=-0.351 and b=4.618 respectively.

**Future improvements**

We expect a substantial improvement of the performances by the program in progress. The homogeneous single stage electrostatic mirror possibilities will be capitalized by the reduction of the ion packet length closely to the detection level of the spectrum peaks of interest. The parabolic field mirror will be also tested including improvements of the field distribution by using auxiliary electrodes. The obtention of a powerful pulse generator is planed to valorise the potential of the method of ion packet generation by chopping. In a next stage of the program the method of synchronized chopper and source operation will be applied.

## REFERENCES

1. R. J. Cotter, Time-of-flight mass spectrometry: Instrumentation and applications in biological research, ACS Washington DC, 1997.
2. R. Grix, U. Gruener, G. Li, H. Stroh, H. Wollnik, Int. J. Mass Spectrom. Ion Processes 93 (1989) 323.
3. D. Ioanoviciu, C. Cuna, A. Pamula, Analusis 20 (1995) 95 s abstract.
4. J. M. B. Bakker, J. Phys. E: Sci. Instrum. 6 (1973) 785.
5. H. Haberland, H. Kornmeier, C. Ludewigt, A. Risch, Rev. Sci. Instrum.. 62 (1991) 2368.
6. H. Haberland, H. Kornmeier, C. Ludewigt, A. Risch, M. Schmidt, Rev. Sci. Instrum. 62 (!991) 2621.
7. C. K. G. Piyadasa, P. Hakansson, T. R. Ariyaratne, D. F. Barofsky, Rapid Commun. Mass Spectrom. 12 (1998) 1655.
8. H. Matsuda, Int. J. Mass Spectrom. Ion Phys. 18 (1975) 367.
9. AVTECH Electrosystems Rev. Sci. Instrum. 70 (1999) A15
10. Behlke Electronic GmbH application note 1997.
11. S. Della Negra, Y. LeBeyec, Int. J. Mass Spectrom. Ion Processes 61 (1984) 21.

# SPECTRAL STUDY OF SOME 4-STYRYL-COUMARINE DERIVATIVES

S. FILOTE, M. COTLET, G. SINGUREL, TATIANA NICOLAESCU*, CATINCA SIMION*, R. GRADINARU* and DANA DOROHOI

*"Al. I. Cuza" University, Faculty of Physics, Bd. Copou 11, 6600 Iasi, Romania*
**"Al. I. Cuza" University, Faculty of Chemistry, Bd. Copou 11, 6600 Iasi, Romania*

**ABSTRACT**. The spectrometric study of some 4-styryl-coumarine derivatives is reported. $^1$H NMR and IR spectra were used in order to determine the compounds structure. Some spectral parameters determined from electronic absorption spectra in solution and diffuse reflectance spectra have been estimated. A chemical quantum calculation for these compounds was made to estimate electronic transitions and to compare with those obtained from spectra.

## INTRODUCTION

Coumarine derivatives are organic compounds with biological action due to the functional group or heterocycle introduced in the side chain of benzene in coumarine residue [1, 2]. Some coumarines derivatives are reported as strongly fluorescent compounds [3] or as pH sensors [4].

This paper deals with a study of spectral properties of some 4-styryl coumarine derivatives, in solutios and solid state.

## EXPERIMENTAL

4-styryl coumarine (4-SC) derivatives analyzed in this paper are presented in Fig.1 and Table I.

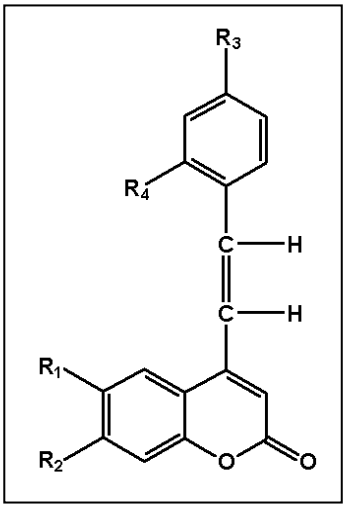


**Table 1.**

Substituents of the 4-SC derivatives

| Compound | Substituent | | | |
|---|---|---|---|---|
| | $R_1$ | $R_2$ | $R_3$ | $R_4$ |
| I | -H | -OH | -OH | -H |
| II | -H | -OH | $-OCH_3$ | -H |
| III | -H | -OH | -H | -Cl |
| IV | $-CH_3$ | -H | $-N(CH_3)_2$ | -H |
| V | -H | -OH | $-N(CH_3)_2$ | -H |

**Fig. 1.** Structural formula of the analyzed 4-SC

**Structural analysis.** In order to determine the 4-SC structure both chemical and spectroscopic analysis were carried out. The $^1$H NMR spectra were recorded in DMSO, at 80 MHz on a Bruker spectrometer. The IR spectra were recorded in KBr pellets on a SPECORD-71 apparatus. The structural elements yield from the spectral features are lised in Table 2 and 3.

**Table 2.**

$^1$H RMN signals (ppm) recorded in DMSO

| 4-SC | Chemical shifts δ (ppm) |
|---|---|
| I | 7.3-8.1 (m, 7H aromatic); 7.3 [d, 2H(-CH=CH-)]; 6.65 (s, 1H, $H_3$) |
| II | 7.2-8.1 (m, 7H aromatic); 7.2 [d, 2H(-CH=CH-)]; 6.65 (s, 1H, $H_3$) |
| III | 7.3-7.9 (m, 7H aromatic); 6.8 [d, 2H(-CH=CH-)]; 6.6 (s, 1H, $H_3$) |
| IV | 7.3-7.9 (m, 7H aromatic); 7.3 [d, 2H(-CH=CH-)]; 6.65 (s, 1H, $H_3$); 3.2 [s, 6H, $N(CH_3)_2$]; 2.4 (s, 3H, $CH_3$) |
| V | 7.3-7.9 (m, 7H aromatic); 7.1-7.3 [d, 2H(-CH=CH-)]; 6.65 (s, 1H, $H_3$); 3.2 [s, 6H, $N(CH_3)_2$]; 2.4 (s, 3H, $CH_3$) |

**Table 3.**

IR spectra in KBr pellets

| 4-SC | Wavenumbers $\bar{\nu}$ ($cm^{-1}$) |
|---|---|
| I | 3420 ($\nu_{OH}$); 1760($\nu_{C=O}$); 1620($\nu_{C=C}$); 1560, 1480 (aromatic ring); 980($\nu_{=C-H}$) |
| II | 3410 ($\nu_{OH}$); 1764($\nu_{C=O}$); 1620($\nu_{C=C}$); 984($\nu_{=C-H}$) |
| III | 3390 ($\nu_{OH}$); 1760($\nu_{C=O}$); 1625($\nu_{C=C}$); 980($\nu_{=C-H}$) |
| IV | 2995 ($\nu_{C-H}$ aliphatic); 1768($\nu_{C=O}$); 1625($\nu_{C=C}$); 1375 ($\delta_{CH3}$); 985($\nu_{=C-H}$) |
| V | 3420 ($\nu_{OH}$); 2900 ($\nu_{C-H}$ aliphatic); 1760($\nu_{C=O}$); 1620($\nu_{C=C}$); 1560, 1482 (aromatic ring); 1370 ($\delta_{CH3}$); 980($\nu_{=C-H}$) |

**Measurements.** The following spectra of the analyzed 4-SC were recorded:

-electronic absorption spectra (EAS) in solution, at room temperature (296K), in the range [45000-14000] $cm^{-1}$, using a SPECORD UV VIS spectrophotometer with Data Acquisition Sistem. Solvent used, ethanol (EtOH), from Merck, was spectral grade. The concentration of the solutions was under $10^{-4}$M $l^{-1}$. At this concentration, the eventually molecular associations between spectrally active molecules can be neglected.

-diffuse reflectance spectra (DRS) in solid pellets with MgO, at room temperature (296K), using a VSU–2P spectrophotometer adapted for measuring reflection factor. As standard diffuser was used a MgO pellet.

Precaution on solvent purity, weighting of compounds, preparation of solutions and pellets were considered.

**Calculations.** In order to build theoretically the electronic energy levels of the analyzed molecules and to compare with those experimentally obtained, quantum chemical calculations were performed using the AM1 (Austin Method) SCF (Self Consistent Field) method [5,6]. Optimization of the molecules geometry was performed before using Molecular Mechanics 2 (MM2) method.

## RESULTS AND DISCUSSION

The EAS of the studied 4-SC in EtOH were processed for determining frequencies and molecular extinction coefficients in the maximum of the bands. The processing was made in the following maner: the EAS spectra of 4-SC were deconvoluted [7], extracting the absorption bands $S_0$-$S_1$, $S_0$-$S_2$ and $S_0$-$S_3$. The frequencies in the maximum of these bands were estimated by deriving the corresponding extracted bands. In Table 4 are shown the wavenumbers and the molar absorptivities in the absorption spectra of 4-SC.

**Table 4.**

The wavenumbers $\bar{\nu}$ ($cm^{-1}$) and the molar absorptivity $\varepsilon$($lM^{-1}cm^{-1}$) in the absorption spectra of 4-SC

| Transition | I | | II | | III | |
|---|---|---|---|---|---|---|
| | $\bar{\nu}$ ($cm^{-1}$) | $\varepsilon$($lM^{-1}cm^{-1}$) | $\bar{\nu}$ ($cm^{-1}$) | $\varepsilon$($lM^{-1}cm^{-1}$) | $\bar{\nu}$ ($cm^{-1}$) | $\varepsilon$($lM^{-1}cm^{-1}$) |
| $S_0$-$S_1$ | 19420 | 762 | 18870 | 150 | 23360 | 5406 |
| | 20330 | 824 | 21190 | 300 | | |
| $S_0$-$S_2$ | 30400 | 12390 | 30490 | 14830 | 31150 | 7040 |
| | 35090 | 11490 | 36230 | 6176 | 35210 | 288 |
| | 39530 | 9940 | 39220 | 7360 | 37740 | 15764 |
| $S_0$-$S_3$ | 45250 | 18900 | 46950 | 24645 | 47620 | 27950 |

| Transition | IV | | V | |
|---|---|---|---|---|
| | $\bar{\nu}$ ($cm^{-1}$) | $\varepsilon$($lM^{-1}cm^{-1}$) | $\bar{\nu}$ ($cm^{-1}$) | $\varepsilon$($lM^{-1}cm^{-1}$) |
| $S_0$-$S_1$ | | | 23810 | 4960 |
| $S_0$-$S_2$ | 30770 | 7400 | 31060 | 7100 |
| | 34720 | 3270 | 34480 | 3180 |
| | 39680 | 1929 | 39370 | 2100 |
| $S_0$-$S_3$ | 46730 | 7900 | 47850 | 28100 |

The DRS recorded in MgO pellets give informations about the compounds in solid state. The DRS were deconvoluted in the same manner as EAS, obtaining the frequencies in the maximum of each $S_0$-$S_1$, $S_0$-$S_2$ and $S_0$-$S_3$ bands. On passing from the liquid solutions to solid state of the compounds I, II, III one can see a hypsochromic shift of the electronic bands. The wavenumbers in the maximum of the bands from DRS spectra of 4-SC are listed in Table 5.

**Table 5.**

The wavenumbers $\bar{\nu}$ ($cm^{-1}$) in the maximum of the bands from DRS spectra of 4-SC

| Transition | $S_0$-$S_1$ | $S_0$-$S_2$ | $S_0$-$S_3$ |
|---|---|---|---|
| I | 19.13 | 27.95 | |
| II | 18.08 | 27.91 | |
| III | 19.62 | 27.46 | |
| IV | 18.65 | 22.39 | 30.64 |

Table 6 contains the wavenumbers in the fluorescence spectra of 4-SC. The first two compounds have a fluorescent band with vibronic structure. The IV and V compounds, having -$N(CH_3)_2$ substituent, present the smallest values for wave-numbers of the fluorescence bands. The visible absorption and emission bands have mirror symetry [4].

**Table 6.**

The wavenumbers $\overline{\nu}$ ($cm^{-1}$) in the fluorescence spectra of 4-SC

| 4-SC | $\overline{\nu}$ ($cm^{-1}$) |
|---|---|
| I | 19380; 17300; 16580 |
| II | 19090; 17610; 16610 |
| III | 22570 |
| IV | 16590 |
| V | 16570 |

The total energy of the ground state, the ground state dipole moment and the wave numbers of the electronic transitions and the oscillator strenght for molecules considered in vacuum were estimated through the AM1 method [5,6]. In Table 7 are given the calculated values for the frequencies and the oscillator strength for the electronic transitions. The total energies and dipole moments for the ground state are presented in Table 8.

**Table 7.**

The frequencies and the oscillator strength for the electronic transitions

| 4-SC. | I | | II | | III | |
|---|---|---|---|---|---|---|
| | Transition Energy (1/cm) | Oscillator Strength | Transition Energy (1/cm) | Oscillator Strength | Transition Energy (1/cm) | Oscillator Strength |
| 1 | 27781.8 | 0.7783 | 26653.8 | 0.7321 | 28192.0 | 0.7273 |
| 2 | 32149.3 | 0.3987 | 32158.9 | 0.4116 | 31951.1 | 0.3630 |
| 3 | 37869.5 | 0.1729 | 35087.6 | 0.2399 | 42050.8 | 0.4232 |
| 4 | 38708.7 | 0.1219 | 37755.9 | 0.2306 | 42517.7 | 0.6191 |
| 5 | 42533.4 | 0.3541 | 41810.8 | 0.3111 | 43490.4 | 0.1344 |
| 6 | 42712.8 | 0.2695 | 42574.0 | 0.2777 | 43895.5 | 0.1546 |
| 7 | 43524.5 | 0.4410 | 43156.0 | 0.1284 | 48638.8 | 0.1091 |
| 8 | 45617.0 | 0.1214 | 45104.8 | 0.1075 | 50092.7 | 0.1140 |
| 9 | 51071.9 | 0.3409 | 46067.1 | 0.2029 | 52069.2 | 0.3413 |
| 10 | | | 51470.6 | 0.3240 | 52914.3 | 0.1214 |

| 4-SC | IV | | V | |
|---|---|---|---|---|
| | Transition Energy (1/cm) | Oscillator Strength | Transition Energy (1/cm) | Oscillator Strength |
| 1 | 25086.7 | 0.3345 | 25564.3 | 0.3129 |
| 2 | 33437.1 | 0.7325 | 33463.8 | 0.7704 |

| 4-SC | IV | | V | |
|---|---|---|---|---|
| | Transition Energy (1/cm) | Oscillator Strength | Transition Energy (1/cm) | Oscillator Strength |
| 3 | 43375.8 | 0.5094 | 34226.4 | 0.3038 |
| 4 | 44636.1 | 0.7396 | 43251.3 | 0.1253 |
| 5 | 45131.5 | 0.2552 | 44469.9 | 0.4748 |
| 6 | 48636.0 | 0.1947 | 45375.3 | 0.3803 |
| 7 | 52924.5 | 0.2535 | 47209.9 | 0.1077 |
| 8 | 55156.7 | 0.1127 | 53694.7 | 0.4489 |
| 9 | | | 56515.4 | 0.1003 |

**Table 8.**

The energies and dipole moments for the ground state

| 4-SC | Total energy (kcal/mol) | Ground state dipole moment (Debyes) |
|---|---|---|
| I | -83433.0960172 | 4.099 |
| II | -86795.1805889 | 8.139 |
| III | -84338.3175319 | 5.798 |
| IV | -84395.8684528 | 4.956 |
| V | -88290.7250287 | 6.043 |

Using the wave number values measured in the electronic absorption spectra and those computed by AMI method, a diagram of the electronic levels was performed, neglecting the shift of the fundamental level by passing from the gaseous state to the solution. From this diagram (Fig.2) it results that the first three compounds, 4-SC I-III, have similar computed and recorded spectra. They have visible bands in the ethanol solutions, while the computed spectra do not present visible bands. The last two compounds also have similar computed and recorded spectra. The compounds 4-Sc IV and V have a visible computed band, but do not have visible bands in the ethanol solutions.

In ethanol solutions, the electronic bands of the first three compounds 4-SC I,II and III shift hypsochromically, while for the last two compounds IV and V bathochromic shifts are registered. This fact shows that for I, II and III, the intermolecular interactions in ethanol are smaller in the ground compared with the excited state of the 4-SC compounds. In the case of the compounds IV and V , the spectral shift suggests that the intermolecular interactions in the ground state are higher than those in the excited state of these compounds.

Analyzing the values of spectral parameters of 4-SC derivatives in function of $R_i$ substituents nature, one can observe that the $R_1$ and $R_2$ substituents do not decisively influence EAS. The $R_3$ and $R_4$ substituents induce major modifications in electronic spectra. The replacement of H with an electronegative atom (Cl)

determines changes in the electronic charge distribution on the benzene ring to which $R_4$ is bounded.

The substitution in the $R_3$ position of -$N(CH_3)_2$ group leads to a bathochromic shift of the electronic bands and to a decrease of the recorded band number, compared with the compounds I-III.

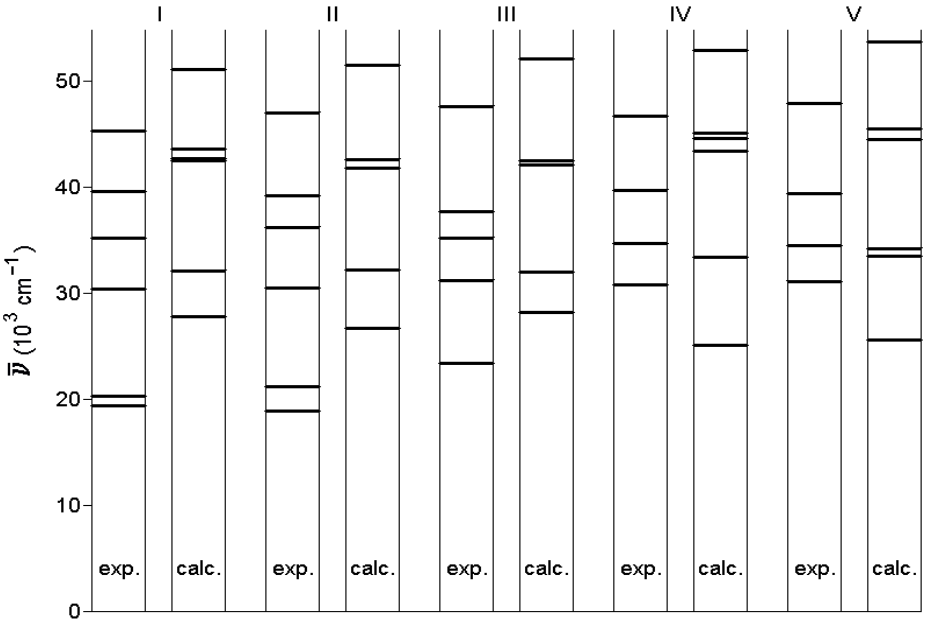


**Fig. 2.** Diagram of the electronic absorption bands recorded in EtOH solutions (exp.) and estimated by AM1 (calc.)

## CONCLUSIONS

1. 4-SC are spectrally active compounds with mirror symetry of the electronic spectra.
2. 4-SC participate in condensed medium to dipolar interactions.
3. A visible band forbidden in the case of isolated molecules becomes permitted in condensed state of the 4-SC I-III.
4. The substituent Cl in $R_4$ position induces major changes in visible EAS.
5. The substituent -$N(CH_3)_2$ in $R_3$ position determines an decrease of the numbers of recorded electronic absorption bands in ethanol compared with the corresponding spectra of I-III.

## REFERENCES

1. T. Nicolaescu, E. Nemitan and O. Ailiesei *An. St. Univ. Iasi*, I, S. Ch.,61, (1991)
2. T.Nicolaescu, E.Nenian and O.Ailiesei, *An. St. Univ. Iasi*, IV, S. Ch.,139, (1996)
3. N.K.Chadankar, S.D.Yoshi, S.Sequerie and S. Seshadri, *Indian J.Chem*., 26B, 427, (1987)
4. T.Nicolaescu, C.Simion, D.Barabula, D.Dorohoi and R.Gradinaru, *An. St. Univ. Iasi*, VI, s.Ch., 23 (1998)
5. R.Daudel, G.Leroy, D.Peeters and M.Sana, "Chimie Cuantica", Ed. Acad. Rom. (1988)
6. I.Humelnicu, I.Cretescu, C Ghirvu and M.Macovei *An. St. Univ. Iasi*, VI, S. Ch., 65 (1991)
7. H.H.Perkampus, "UV VIS Spectroscopyand its Applications", Springer Verlag, Berlin, (1991)

# DIPOLE MOMENTS OF SOME 3-(P-HALO-PHENYL) PYRIDAZINIUM PHENACYLIDS

**M. COTLET, DANA DOROHOI, S. FILOTE, I. MANGALAGIU[*] and G. SINGUREL**

*"Al. I. Cuza" University, Faculty of Physics, Bd. Copou 11, 6600 Iasi, Romania*
*[*]"Al. I. Cuza" University, Faculty of Chemistry, Bd. Copou 11, 6600 Iasi, Romania*

**ABSTRACT.** Evaluation of the dipole moments in the ground state for some pyridazinium ylids by two experimental methods and by chemical quantum calculation was performed. The dipole moments in the ground state were experimentally determined, both from the solvent influence upon the intramolecular charge transfer band of the studied ylids and from dielectric constant and refractive index measurements at infinite dilution. For quantum chemical calculation the CNDO and AM1 methods were applied. A correlation between these methods was made.

## INTRODUCTION

Carbanion monosubstituted 3-(p-halo-phenyl-) pyridazinium ylids (CMPPY) are organic compounds with large applicability in pharmacology [1]. They are amphyonic compounds in which a positive nitrogen, $sp^2$ hybridized, is covalently bonded to a negative carbon ion named carbanion. The hybridization of the CMPPY carbanion is between $sp^2$ and $sp^3$, depending on the nature of the attached substituent to carbanion [2]. The electronic absorption spectrum (EAS) in solution presents an intramolecular charge transfer (ICT) band in the visible range [3], very sensitive to the polarity of solution. The values of ground state dipole moments of two compounds from CMPPY class, using experimental and theoretical methods have been estimated.

## THEORETICAL ASPECTS

A. The ground state dipole moment can be experimentally estimated, in conformity with Bakhshiev theory [4] about the solvent influence on the frequency in the maximum of an EAS band in solution ($\tilde{\nu}_{max}^{sol}$) relative to those in vapor state ($\tilde{\nu}_{max}^{vap}$). Between these frequencies and the macroscopic parameters of the solvent there is a relationship of the following type:

$$\tilde{\nu}_{max}^{sol} = \tilde{\nu}_{max}^{vap} + C_1 \frac{\varepsilon - 1}{\varepsilon + 2} - C_2 \frac{n^2 - 1}{n^2 + 2} \qquad (1)$$

Here $C_1$ and $C_2$ are constants with significance of wavenumbers. Eq. (1) describes a linearly dependence between $\tilde{\nu}_{max}^{sol}$ and the macroscopic parameters of solvents. If the magnitude of the radius of molecular action sphere ( r ) is known, the ground state dipole moment ( $\mu_g$ ) can be estimated from the next relationship:

$$C_1 = \frac{1}{r^3}\frac{2n^2+1}{n^2+2}2\mu_g\left(\mu_g - \mu_e\cos\varphi\right) \tag{2}$$

$C_1$ is the same coefficient that intervenes in Eq. (1), $\mu_e$ is the dipole moment in the excited state and φ is the angle between $\mu_g$ and $\mu_e$. Because in ICT process the dipole moment of pyridazinium ylids decreases [3], one can approximate $\mu_e \to 0$ and the relationship (2) becomes:

$$C_1 = \frac{2}{r^3}\frac{2n^2+1}{n^2+2}2\mu_g^2 \tag{2'}$$

The Eq. (2) can be used to estimate the dipole moment in the ground state of CMPPY.

B. The ground state dipole moment can be also experimentally estimated, by dielectric constant and refractive index measurements. For a mixture composed from a non-polar solvent (1) and a solute (2), the global molecular polarization is given by the following relationship [5]:

$$P = P_1f_1 + P_2f_2 = \frac{\varepsilon-1}{\varepsilon+2}\frac{M_1f_1 + M_2f_2}{d} \tag{3}$$

Here $P_1, f_1, M_1$ and $P_2, f_2, M_2$ are the corresponding molecular polarizations, molar fractions and molar mass of the components (1) and (2) and $f_1 + f_2 = 1$. The macroscopic parameters $d$ (density), $\varepsilon$ (dielectric constant), and $n$ (refractive index) characterize the mixture. The contribution of the solute to the global molecular polarization will be:

$$P_2 = P_1 + \frac{P - P_1}{f_2} \tag{4}$$

Density and dielectric constant of a mixture vary linearly with the molecular fraction of the solute [6], i. e

$$\varepsilon = \varepsilon_1(1+\alpha f_2) \quad \text{and} \quad d = d_1(1+\beta f_2) \tag{5}$$

where:

$$\alpha = \left(\frac{\partial\varepsilon}{\partial f_2}\right)_{f_2\to 0} \quad \text{and} \quad \beta = \left(\frac{\partial d}{\partial f_2}\right)_{f_2\to 0} \tag{6}$$

Using relationships (4) and (5) for infinite dilution, when $f_2 \to 0$, the molecular polarization of the solute can be express as follows:

$$(P_2)_{f_2 \to 0} = P_{2\infty} = P_1 + \left(\frac{\partial P}{\partial f_2}\right)_{f_2 \to 0} = \frac{3\alpha\varepsilon_1}{(\varepsilon_1+2)^2}\frac{M_1}{d_1} + \frac{\varepsilon_1}{(\varepsilon_1+2)}\frac{M_2 - M_1\beta}{d_1} = A\alpha + B\beta + C \quad (7),$$

where A, B and C are constants.

Measuring the dielectric constant and density of solution for different concentrations of the solute, from the linear dependencies of the type (5) one can estimate the slopes $\alpha$ and $\beta$ and calculate $P_{2\infty}$ from (7). The ground state dipole moment (in Debye) for the solute molecule one can evaluate, using the following expression:

$$\mu_g = 0.0128 \sqrt{(P_{2\infty} - \frac{(n^2-1)}{(n^2+2)}\frac{M_1}{d_1})} \quad (8)$$

C. The ground state dipole moment of a molecule can be theoretically estimated using quantum mechanical calculations [7,8].

The average value of the associated operator of the dipole moment components in the ground state of a molecule is:

$$\mu_x = -e\sum_j \int \Psi^* x_j \Psi \, dv + e\sum_N Z_N X_N \ , \quad (9)$$

where *e* is the elementary electronic charge, $\Psi$ - the electronic wave function of the molecule, $x_j$ and $X_N$ - the coordinates of the $j^{th}$ electron, respectively of the N atom and $Z_N$ - the positive charge on the N atom. The wave function that intervenes in relationship (10) can be explicited by a self-consistent method of Hartree-Fock type, using configuration interaction. Depending on the approximations made at the evaluation of the coefficients which intervene in the Roothaan equations, there are some evaluation methods of the electronic wave function: CNDO (Complete Neglected Differential Overlap), INDO (Intermediate Neglect of Differential Overlap), AM1 (Austin Model 1) and PM3 (Parametric Model 3).

## EXPERIMENTAL

3-(p-halo-phenyl-) pyridazinium ylids analyzed here have the structural formula given in Fig. 1 and Table I.

**The compounds were synthesized and purified as previously described [1]. The purity was checked by elemental (C, H, N) and spectral (IR, $^1$H and $^{13}$C NMR) analysis.**

**Spectral measurements.** In order to determine the dipole moment from the study of the solvent influence on the position of the ICT band, EAS in different solvents, between 30000-14000 $cm^{-1}$, at room temperature (25°C), were recorded for each compound [3]. A SPECORD UV-VIS Carl Zeiss Jena spectrometer provided

with a Data Acquisition System was used. The solvents, from Merck, Aldrich and Fluka, were spectral grade. The recorded spectra were deconvoluted as previously described in [9].

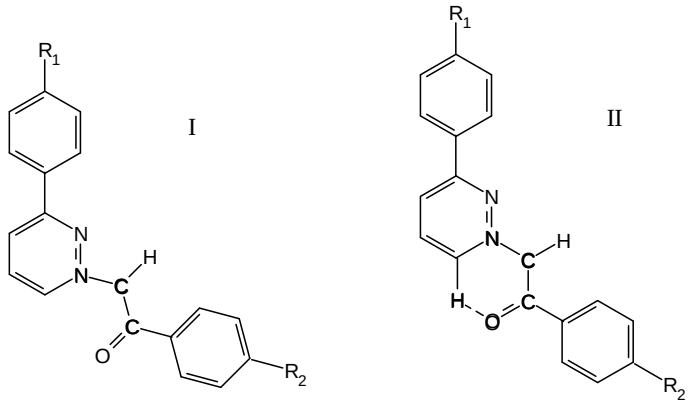


**Fig. 1.** Structural formula of the studied compounds.

**Table I.**

Name, notation and corresponding substitutes of the analyzed CMPPY.

| No. | Name | Notation | Substitute | |
|---|---|---|---|---|
| | | | $R_1$ | $R_2$ |
| 1. | 3-(p-chloro-phenyl)-pyridazinium benzoyl-methylid | $Y_1$ | Cl | H |
| 2. | 3-(p-bromo-phenyl)-pyridazinium benzoyl-methylid | $Y_2$ | Br | H |

**Dipolmetric measurements.** In order to determine the dipole moment from dipolmetric measurements, using the infinite dilution, there were measured dielectric constants, refractive indices and densities for solutions in benzene of compounds $Y_1$ and$Y_2$, for concentrations between $10^{-3}$ M and $10^{-4}$ M. Benzene with spectral purity, from Fluka, was treated with sodium to eliminate water traces. Determination of $\varepsilon$ at 25°C was made using a WAINE KERR Autobalance Universal Bridge B-641 (300 MHz) coupled with a TELMES TR-9701 dielectric cell for liquids, thermostated with a U-10 ULTRA THERMOSTAT (±0.2°C precision). The cell was washed with $CCl_4$ and dried before each determination. Precision in determination of $\varepsilon$ was about ±4 %. The refractive index of solutions was measured with a RPL Carl Zeiss immersion refractometer ($\pm 10^{-5}$ precision) thermostated at 25°C with the same thermostat used for $\varepsilon$ determination. Densities of solutions were measured with a 25 ml picnometer, using a METTLER MDB-5 balance ($\pm 10^{-5}$ grams). Picnometer was initially standardized with bi-distilled water.

**Theoretical calculations.** In order to compare the quantities obtained from experimental measurements they were also determined theoretically. MM2, the most general method for molecular mechanics calculations, developed principally for organic molecules was used for molecular geometry optimization and self-consistent field (SCF) methods for electronic properties. The dipole moments of the ylids were estimated with both CNDO (useful for calculating ground-state electronic properties of open- and closed-shell systems) and PM3 (for electronic properties, total energy). Also the charge on each atom was computed with PM3. Using SCF's there was selected RHF spin pairing. With PM3 were performed singly excited configuration interaction calculations with 45 configurations, maximum excitation energy (orbital energy) being 10 eV.

## RESULTS AND DISSCUTION

The Bakhshiev's theory was applied, in the approximation $\mu_e \to 0$, to the ICT band of the studied compounds. So, the ground state dipole moment was estimated with Eq. (2'). To determine $C_1$ coefficient which intervenes in Eq. (2'), a multiple linear regression [10] was applied to the values of $\tilde{\nu}_{max}^{sol}$, $\left(n^2-1\right)/\left(n^2+2\right)$ and $(\varepsilon-1)/(\varepsilon+2)$. The regression parameters $\tilde{\nu}_{max}^{vap}$, $C_1$ and $C_2$ are listed in Table II.

**Table II.**

The regression coefficients for Eq. (1)

| Ylid | $\tilde{\nu}_{max}^{vap}$ ($cm^{-1}$) | $C_1$ ($cm^{-1}$) | $C_2$ ($cm^{-1}$) | $r$ (A) |
|---|---|---|---|---|
| $Y_1$ | 21730 | 615 | 5258 | 6.4 |
| $Y_2$ | 21030 | 614 | 3639 | 6.4 |

From the length of the bonds implied in the structure of each compound the *r*-values were estimated (see Table II, the last column).

The $\mu_g$ values for the analyzed CMPPY were calculated, using Eq. (2') (see Table V-col. 2**)**. The values obtained from the solvent influence on the ICT band can be affected by errors coming both from the limits in which Bakhshiev's theory was developed and form the used approximation $\mu_e \to 0$.

DK-metric measurements were realized for solutions with [$10^{-5}$-$10^{-4}$] M $l^{-1}$ concentrations. The values obtained for ε and d through this method are listed in Table III A and Table III B. The values of $\alpha$, $\beta$ and $P_{2\infty}$ are listed in Table IV. Using relationship (8), the ground state dipole moments values were found and they are listed in Table V-col. 3. The small solubility of these compounds in non-polarizable and non-polar solvents, such as heptane, hexane or nonane (recommended in this method) determined us to use benzene as solvent, which polarizes solution, inducing some errors in the estimation of dipole moment [5].

**Table III A.**

Dielectric constant and density of binary solutions: $Y_1$ ylid in benzen

| $f_2$ | $\varepsilon$ | d (g $cm^{-1}$) |
|---|---|---|
| 0 | 2.28 | 0.7601 |
| $0.4 \cdot 10^{-5}$ | 2.28196 | 0.7611 |
| $1.026 \cdot 10^{-5}$ | 2.2891 | 0.7625 |
| $2.052 \cdot 10^{-5}$ | 2.2985 | 0.7638 |
| $3.896 \cdot 10^{-5}$ | 2.311 | 0.7652 |
| $4.10 \cdot 10^{-5}$ | 2.325 | 0.7666 |

**Table III B.**

Dielectric constant and density of binary solutions: $Y_2$ ylid in benzen

| $f_2$ | $\varepsilon$ | d (g $cm^{-1}$) |
|---|---|---|
| 0 | 2.2800 | 0.7601 |
| $0.4 \cdot 10^{-5}$ | 2.2820 | 0.76097 |
| $1.00 \cdot 10^{-5}$ | 2.291 | 0.7602 |
| $2.01 \cdot 10^{-5}$ | 2.3010 | 0.7633 |
| $3.01 \cdot 10^{-5}$ | 2.3120 | 0.7641 |
| $4.01 \cdot 10^{-5}$ | 2.32460 | 0.7663 |

**Table IV.**

$\alpha, \beta$ and $P_{2\infty}$ parameters.

| Ylid | $\alpha$ | $\beta$ | $P_{2\infty}$ |
|---|---|---|---|
| $Y_1$ | 1182 | 146 | 37600 |
| $Y_2$ | 1170 | 150 | 36966 |

In Table V-cols. 4 and 5 are also listed the values of $\mu_g$ for structure I (Fig.1) calculated by CNDO and PM3 methods. These data show that, the nearest values from the experimentally obtained, are those estimated by PM3. These values are also bigger than those experimentally obtained. This fact can be explained by the formation of an intramolecular hydrogen bond, (of the type II, Fig.1), in the case of carbanion monosubstituted ylids [3], which can reduce dipole moment values. These bonds were neglected in the initial theoretical calculations. The computed data, by CNDO and PM3 methods for the structure II dipole moment are summarized in Table V (cols. 6 and 7).

**Table V.**

Ground state dipole moments (in Debye).

| Compound | Spectral | Dipolmetric | I | | II | |
|---|---|---|---|---|---|---|
| | | | CNDO | PM3 | CNDO | PM3 |
| Y1 | 3.513 | 2.483 | 6.863 | 3.940 | 2.652 | 1.760 |
| Y2 | 3.510 | 2.460 | 6.684 | 3.979 | 2.228 | 0.735 |

Analyzing the data of Table V, cols. 3, 6 and 7, one can see that the experimentally determined dipole moments and those calculated by CNDO method for structure II are of the same order of magnitude.

In Fig. 2 are indicated the charges estimated by PM3 method as being located near the atoms of the ylid.

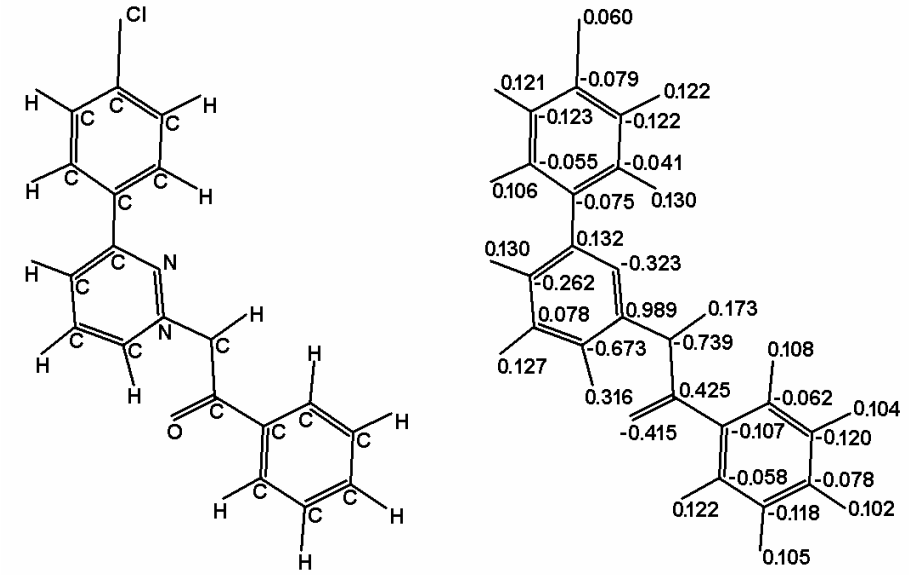


**Fig. 2.** Electric charges computed by PM3 on the ylid $Y_1$ atoms.

The values of dipole moments determined from the solvent influence on the visible electronic absorption band are affected by errors rising both from the Bakshiev's theory approximation and from the condition $\mu_e \rightarrow 0$ corresponding to the intramolecular charge transfer from the ylid carbanion to the heterocycle. In Bakshiev's theory the specific interactions that can act in protic solvent solutions are also neglected.

The most precise results are obtained by the DK-metric measurements in a non polarizable and non-polar solvent such as heptane, nonane. The small solubility of the ylids in such a solvent determined the use of the benzene that induces errors in the dipole moment estimation, by its polarizing effect.

The structures I and II were considered for theoretical estimation. The obtained data correspond to an isolated molecule included in condensed medium. The smallest dipole moments are theoretically estimated for the ylid with intramolecular hidrogen bond (structure II).

The dipole moment values determined from the solvent influence on the visible band of the ylids are bigger than those determined by DK-metric measurements.

## CONCLUSIONS

1. The values of the ground state dipole moments determined by the methods used in this work are of the same size order.
2. The big values of the dipole moments in the ground state indicate the amphionic nature of these compounds.
3. The theoretical estimations evidence the necessity to have in view the intramolecular hydrogen bond between the nearest hydrogen atom from the ylid nitrogen and the oxygen from the CO group of the carbanion.

## REFERENCES

1. I. Mangalagiu, I. Druta, M. Caprosu and M. Petrovanu, *An. St.Univ. "Al. I. Cuza" Iasi, s. Chimie*, **II**, 49, (1994).
2. D. Dorohoi, M. Caprosu and I. Mangalagiu, *J. of the Algerian Chem. Soc*", **8**, 2, (1998).
3. D. Dorohoi, D. Partenie, A. Anton and L. Chiran, *J. Chim. Phys. Biologique*, **91**, 419 (1994).
4. N. G. Bakhshiev, "*Spectroscopia Mejmoleculiarnov Vzaimodeistvii*", Izd. Nauka, Leningrad, 1972, p.178.
5. H. Federspiel, PhD Thesis, Univ. Clermont Ferrant-France, 1973.
6. I. F. Halvrstadt and W. D. Kumler, *J. Amer. Chem. Soc.*, **64**, 2988, (1942).
7. I. Humelnicu, I. Cretescu, C. Ghirvu and M. Macoveanu, *An. St.Univ. "Al. I. Cuza" Iasi, s. Chimie*, **VI**, 65, (1998).
8. Dana Dorohoi, G.Surpateanu and Livia Gheorghies, *Balkan Physics Letters*, **6**, 3, 198 (1998)
9. M. Cotlet, D. Dorohoi G. Singurel, M. Luca, T. Nicolaescu and C. Simion, *An. St.Univ. "Al. I. Cuza",s. Chimie*,**VII**, 1, 91 (1999).
10. G. Henrion, A. Henrion and R. Henrion, "*Beispiele zur Daten Analyse mit BASIC Programmen*", Berlin, (1988).

STUDIA UNIVERSITATIS BABEŞ-BOLYAI, PHYSICA, SPECIAL ISSUE, 2000

# SPECTRAL STUDY OF THERMAL 3 + 3 DIMERIZATION OF CARBANION MONOSUBSTITUTED - PYRIDAZINIUM YLIDS

**DANA DOROHOI[*], V. MELNIG[*], J. VATAMANU[**] and I. MANGALAGIU[**]**

[*] *Department of Physics, "Al. I. Cuza" University, Bd. Copou 11, R-6600 Iaşi, Romania*
[**] *Department of Chemistry, "Al. I. Cuza" University, Bd. Copou 11, R-6600 Iaşi, Romania*

**ABSTRACT**. The $10^{-3}$ mol/l solutions of carbanion monosubstituted BPPBM in benzene were spectrally studied. It is revealed the catalitic effect of light on 3 + 3 dipolar dimerization processes of carbanion monosubstituted pyridazinium ylid. It is proposed a loop kinetic mechanism of 3+3 dipolar thermal dimerization reaction for the studied ylid.

**KEYWORDS**: 3 - (p - bromo - phenyl) - pyridazinium benzoyl - methylid (BPPBM), 3+3 dipolar dimerization, electronic absorption spectra, intramolecular charge transfer.

## INTRODUCTION

Pyridazinium ylids [1,2] present a characteristic electronic absorption band in the visible range, assignable to an intramolecular charge transfer (ICT) from carbanion to heterocycle [3,4]. This band is very sensitive to the carbanion substituents as well as to the heterocycle structure [5]. ICT band is also strongly dependent on the solvent nature [6-8].

The absorption spectra of $10^{-3}$ mol/l solutions of carbanion monosubstituted BPPBM in benzene and ethanol were studied at room temperature. The decreasing of extinction in the case of monosubstituted pyridazinium ylid in an aprotic solvent can be explain by 3+3 dipolar dimerization of the ylid molecules in which the lone electron pair of the carbanion participates in covalent bond with the proton of - CH groups located near the nitrogen - atom from heterocycle [1]. The increase of dimerization efficiency in presence of light suggested us to study the 3 + 3 dipolar dimerization mechanism in lighting process.

## EXPERIMENTAL

The carbanion monosubstituted BPPBM was synthesized and purified as previously described [9]. The aprotic solvent - benzene - was Merck spectroscopic grade. The quartz cells were carefully dried and purified before use. The electronic absorption spectra from visible range [30000 - 14 000] $cm^{-1}$ were recorded with a Specord UV VIS Zeiss spectrophotometer equipped with a Data Acquisition System.

The **B**ouguer-**L**ambert-**B**eer (**BLB**) law [10] allows us to estimate the concentration of the spectrally active substance in a studied solution, if we know the extinction value:

$$E(\lambda) = \ln \frac{\Phi_0(\lambda)}{\Phi(\lambda)} = \varepsilon(\lambda)\, cl\ . \tag{1}$$

The product $\varepsilon(\lambda)\, l$ can be determined by (1) for a set of initial conditions ($c_0$, $E_0(\lambda)$). One obtains the dependence of concentration vs. extinction:

$$c = c_0 \frac{E(\lambda)}{E_0(\lambda)} \tag{2}$$

The differential equation of reaction rate, considering BLB law is given by:

$$\frac{dE}{dt} = kE^n \tag{3}$$

where k is the global constant of reaction rate and n is the order of reaction.

By integrating relation (3) one can obtain the dependence E=E(t) in the following form:

$$kt = \begin{cases} \ln\left(\dfrac{E_0}{E}\right); & if \quad n = 1 \\ \dfrac{1}{n-1}\left(E^{1-n} - E_0^{1-n}\right); & if \quad n \neq 1 \end{cases} \tag{4}$$

The relation (4) can be expressed in a liniar form by:

$$\begin{cases} \ln\left(\dfrac{E_0}{E}\right) = kt; & if \quad n = 1 \\ \dfrac{E^{1-n}}{n-1} = \dfrac{E_0^{1-n}}{n-1} + kt; & if \quad n \neq 1 \end{cases} \tag{5}$$

Let be G(t,n) defined by:

$$G(t,n) = \begin{cases} \ln\left(\dfrac{E_0}{E}\right); & if \quad n = 1 \\ \dfrac{E^{1-n}}{n-1}; & if \quad n \neq 1 \end{cases} \tag{6}$$

For a given supposed order of reaction one represents graphically G(t,n) vs. time. If the supposed order is correctly chosen, then the points are in the vecinity of a line.

## RESULTS AND DISCUSSIONS

The spectral recordings, were performed, at equal periods of time, in two ways. Between the recordings, in the first case, the samples were subjected to a continuous lighting at 21,000 $cm^{-1}$ (corresponding to ICT band maximum of ylid, Fig.1 for benzene and Fig. 2 for ethanol solvent), while in the second one, the samples were not irradiated (Fig.3 for benzene).

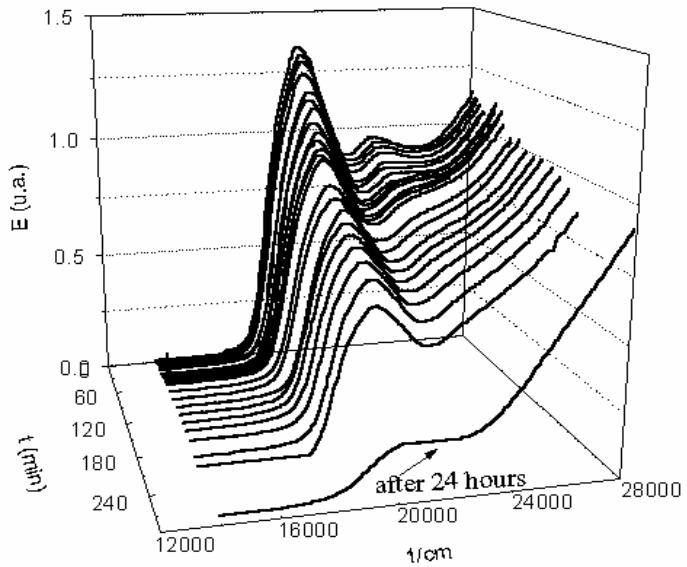


**Fig. 1.** The time dependence of the (30,000÷14,000) $cm^{-1}$ absorption spectrum for the continuous lighting at 21,000 $cm^{-1}$ in benzene solvent.

In order to obtain more information about reaction mechanism, the influence of the solvent on the system was studied, using two different type of solvent: polar solvent (ethanol) and non-polar solvent (benzene). The obtained results concerning the reaction order are presented in Fig. 4 for ethanol and in Fig. 5 for benzene.

The results suggest that the solvent influences the reaction mechanism. From the Figs. 4 and 5 it results that the reaction order is n=1 for ethanol and n=0.5 for benzene. The results can be explained taking into account the interactions between solvent and reaction intermediates. In ethanol (polar solvent) these interactions are stronger than in benzene (non-polar solvent).

For a non-polar solvent, in which the interactions are weak, the reaction ways are not affected, because there is no possibility to block the reaction intermediates by this kind of interactions. In the case of benzene solutions the reaction order n=0.5 indicates a complex kinetic of the process.

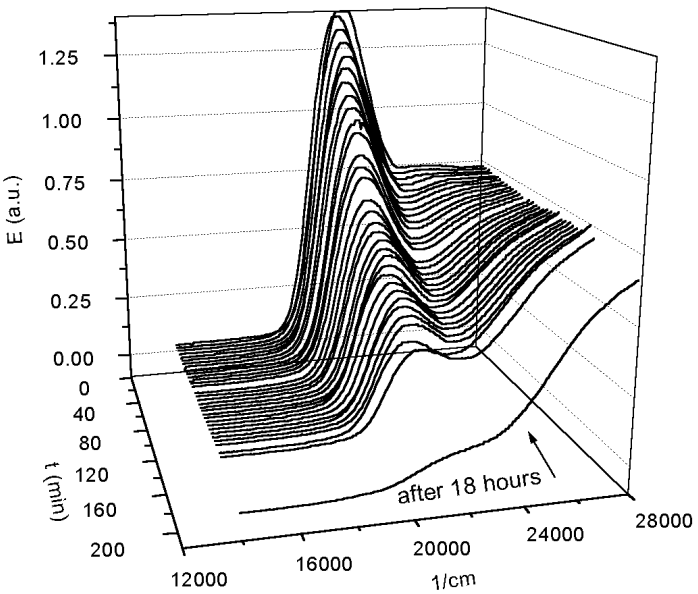


**Fig. 2.** The time dependence of the (30,000÷14,000) $cm^{-1}$ absorption spectrum for the continuous lighting at 21,000 $cm^{-1}$ in ethanol solvent.

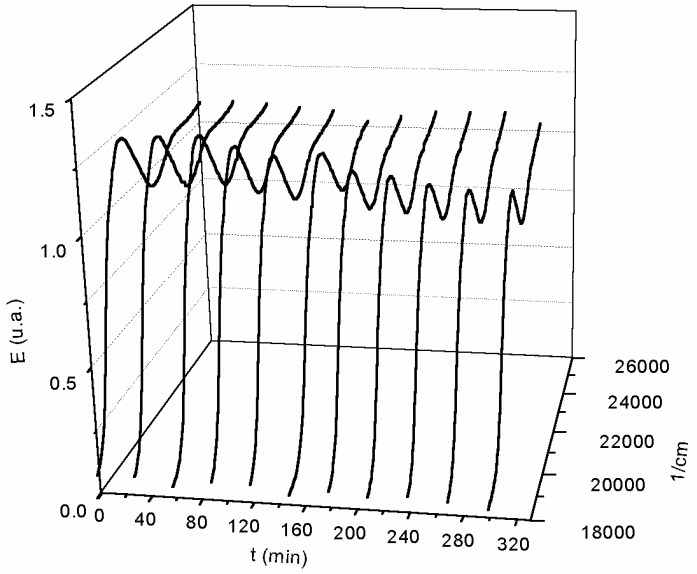


**Fig. 3.** The time dependence of the (30,000÷14,000) $cm^{-1}$ absorption spectrum in absence of light in benzene solvent.

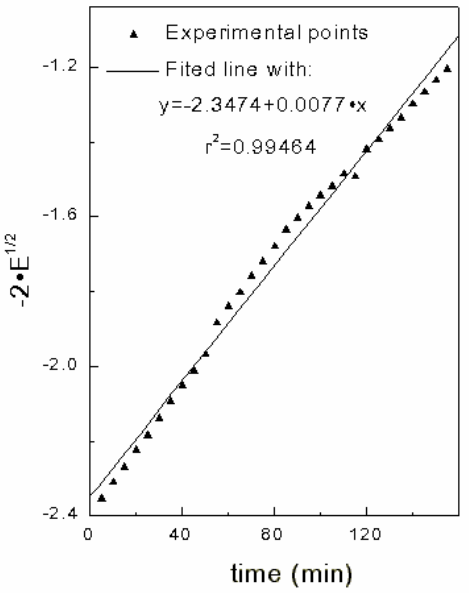


(a)

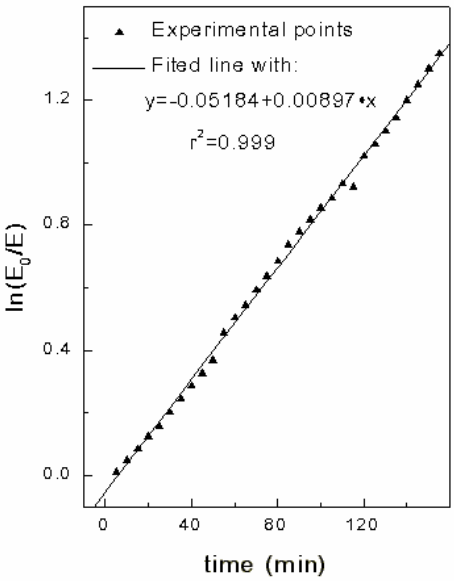


(b)

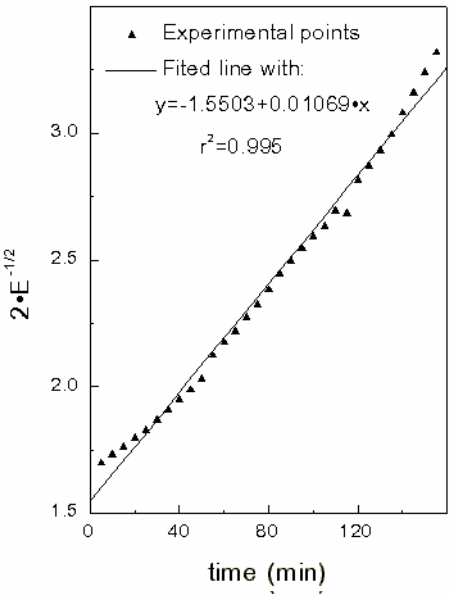


(c)

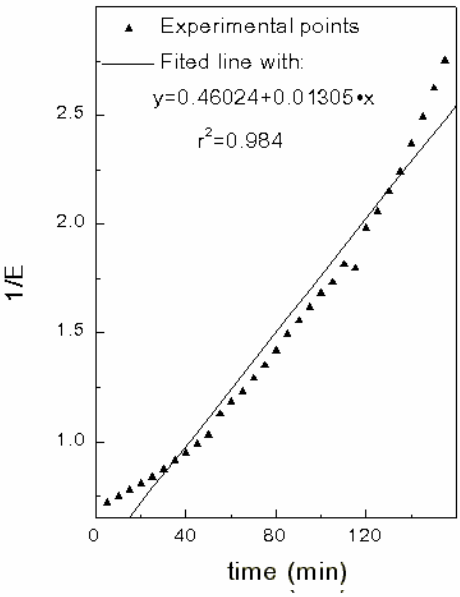


(d)

Fig. 4. Experimental and linear points for the supposed reaction order: (a) n=0.5; (b) n=1; (c) n=1.5, (d) n=2 with case of ethanol solvent.
$r^{20}$ represents the regression cofficient normated to unit.

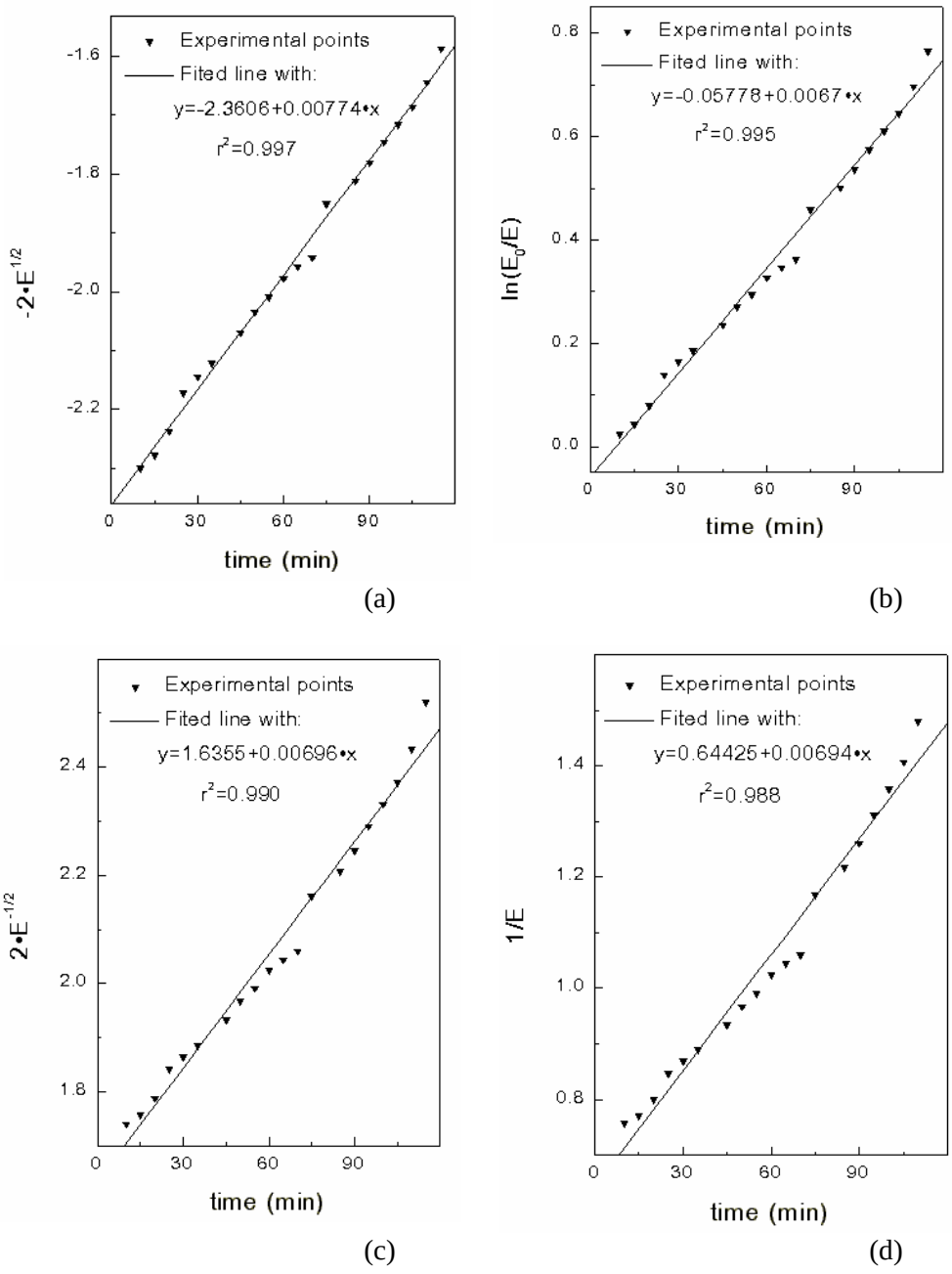


**Fig. 5.** Experimental and linear points for the supposed reaction order:
(a) n=0.5 (b) n=1; (c) n=1.5, (d) n=2 with case of benzene solvent.

Taking into account the perturbation of the process during spectral recording, we propose a loop kinetic mechanism for 3+3 dipolar thermal dimerization of BPPBM (Fig. 6).

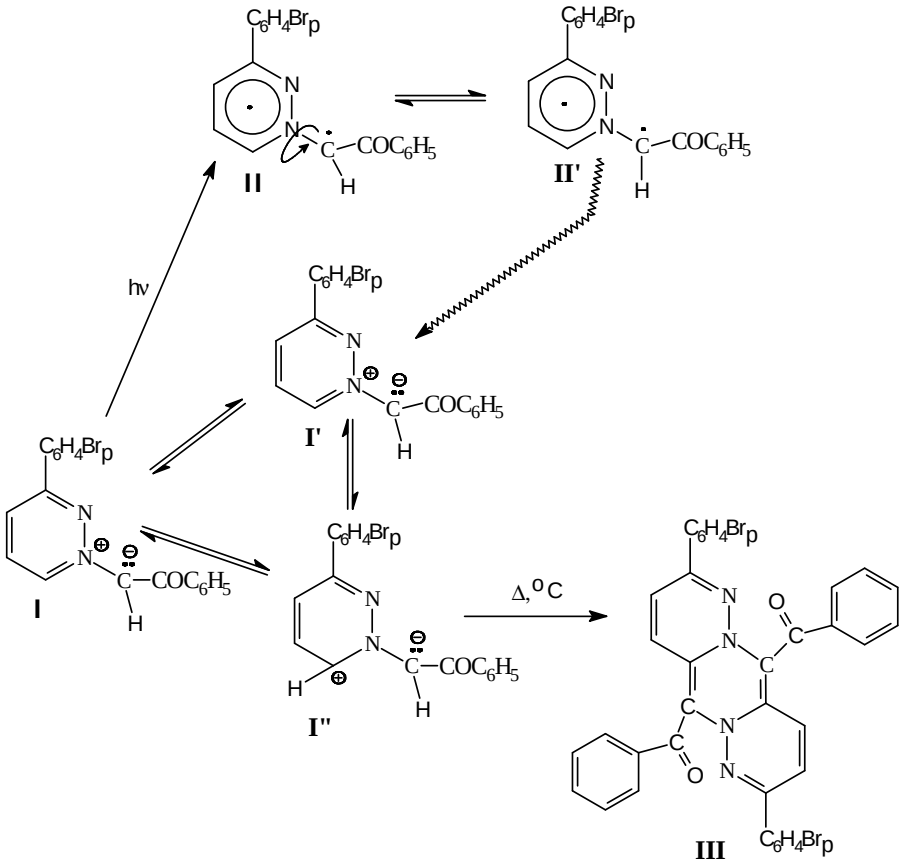


**Fig. 6.** The 3 + 3 dipolar dimerization mechanism of BPPBM.

Figure 7 shows the potential energy for a given electronic state as a function of the representative $N^+$ - $C^-$ internal coordinate of the studied molecules and the vibrational energy levels, as well as the energy states reached in the absorption and relaxation processes of pyridazinium ylid. Comparatively with the electronic configurations of diatomic molecules, the poliatomic molecules present electronic configurations whose potential energy curves have crossing points [11]. It is well known that, excepting $v = 0$, the vibrational probability functions $|\Psi|^2$ is higher in the neighbourhood of the potential barrier and growths with the quantic vibrational number increasing.

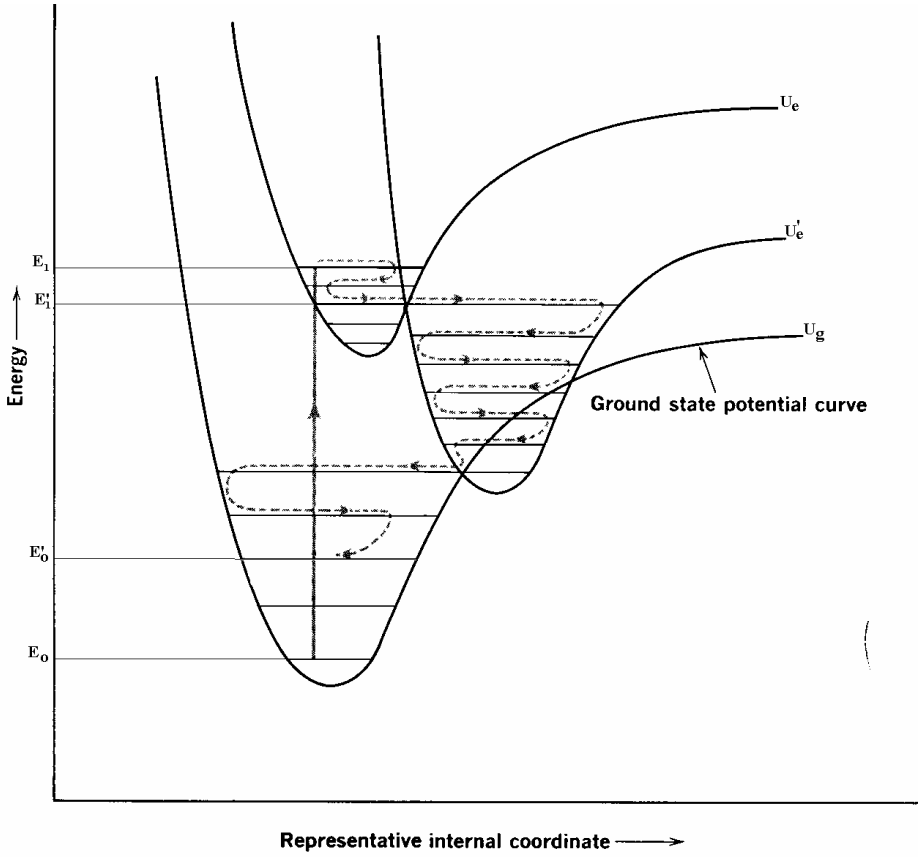


**Fig. 7.** The energy states reached in the absorption and relaxation processes of pyridazinium ylid.

Due the maximum of probability value at potential barrier, the crossing of the potential curves is facilitated. At the crossover point, the potential energies of the two electronic states are equal, and the vibrational kinetic energy of the molecule in either state would be zero.

At room temperature, the molecules are found in the fundamental state $E_0$ ($U_g$ potential profile), corresponding to (I) conformation of pyridazinium ylid (Fig. 6). In ICT process (Fig. 7) due to $hc\bar{\nu}_{ICT}$ radiation absorption, the molecules reach the excited state $E_1$ ($U_e$ potential profile), corresponding to (II) molecular conformation (Fig. 6).

In the fundamental state of the ylid, the hybridization of its carbanion is between $sp^2$ and $sp^3$ [1]. Thus, the $N^+$ - $C^-$ bond presents a partial double bond nature. This determines a relative rigidity of the carbanion substituent configuration. In the pyridazinium ylid excited state $E_1$ the carbanion from (II) molecular conformation passes in a $sp^3$ hybridization. The changes both in the charge distribution and in the

bond character make $E_1$ become instable. The carbanion substituents become relaxed by a complex vibration - related to the $N^+$ - $C^-$ bond. The complex vibration mode (which can be regarded both as a normal vibration along the $N^+$ - $C^-$ bond and as internal rotation arround this bond) makes the potential profile $U_e$ become $U'_e$, with the energy $E'_1$ ($E'_1 < E_1$, Fig. 6). The passings from $E_1$ to $E'_1$ and from $E'_1$ to $E'_0$ are nonradiative, because as we have already mentioned, in the internal conversion processes the two electronic states have equal energies at the crossing point. In this case the vibrational kinetic energy of the molecules is zero. The (I′) configuration is the same with (I), the difference being noticed in the energy values $E'_0 > E_0$. From the (I) or (I′) conformation the pyridazinium ylid molecule undergoes inactivation process for the 3 + 3 dipolar dimerization thermally permitted. The mechanisms presented above can explain the difference between the two decreasing velocities of the ylid concentrations in the two ways of recordings.

In the case of continuously lighting the preponderant 3 + 3 dipolar dimerization way is (I′) → (I″) → (III). In the second case the (I) → (I″) → (III) way is realised only in the inevitable spectrum recording action. Thus, in this case the preponderant dimerization way is (I) → (I″) → (III).

## CONCLUSION

- The spectral analyses reveals the catalytic effect of light on 3 + 3 dipolar dimerization processes of carbanion monosubstituted 3 - (p - bromo - phenyl) - pyridazinium benzoyl methylid. The reaction mechanism is considerably affected by the type of the solvent used.
- It is proposed a loop kinetic mechanism of 3 + 3 dipolar thermal dimerization for the studied ylid.
- The extinction decreasing in the case of monosubstituted pyridazinium ylid in an aprotic solvent can be explained by dimerization of the ylid molecules in which the lone electron pair of the carbanion participates in covalent bond with the proton of - CH groups located near the nitrogen - atom from heterocycle.
- This mechanism is based on ICT transition and nonradiative relaxation process.

## REFERENCES

1. I. Zugrăvescu and M. Petrovanu, N-Ylid Chemistry, Academic Press, Mc.Graw Hill, London, (1976)
2. G. Surpățeanu, Alain Lablache Combier, *Heterocycles*, **22**, 2079, (1984)
3. D. Dorohoi and V. Holban, *J.Mol.Struct.*, **129**, 1-3, 133-136, (1993)

4. D. Dorohoi, H. Partenie, C. Anton and L. Chiran, *J. Chim. Phys*., **91**, 419-431, (1994)
5. D. Dorohoi and H. Partenie, *J. Mol.Struct*., 129, 1-3, 129- 132, (1993)
6. V. Pop, D. Dorohoi and V. Holban, *Spectrochimica Acta*, 50A, nr.14, 2281-2289, (1994)
7. C. Mihul, D. Dorohoi, L. Sitaru and G. Surpățeanu, *An. St. Univ*. Iaşi, s.Ib, Fizică, **20**, 174, (1974)
8. M. Petrovanu, D. Dorohoi and Mai Van Tri, *An. St.Univ*. Iaşi, s.Ib, Fizică, **22**, 41, (1976).
9. Mangalagiu, I. Druță, M. Caproşu, M. Petrovanu, *An. St.Univ*. Iaşi, s1c, Chimie, **1**, 51, (1993).
10. J.D. Ingle Jr., Stanley R. Crouch, Spectrochemical Analyses, Prentice - Hall International Editions, 1998, pp. 35.
11. Barrow, Introduction to Molecular Spectroscopy, McGraw - Hill Book Company, Inc., 1962, pp. 304.

STUDIA UNIVERSITATIS BABEŞ-BOLYAI, PHYSICA, SPECIAL ISSUE, 2000

# DIPOLE MOMENTS AND POLARIZABILITIES IN THE EXCITED STATES OF SOME CARBANION DISUBSITUTED PYRIDINIUM YLIDS

**DANA DOROHOI[1], MAGDALENA POSTOLACHE[1], DANIELA IONESCU[2], D.DUMITRIU[1] AND M.POSTOLACHE[2]**

*1.Al.I.Cuza University, Faculty of Physics, Iaşi, Bd. Copou, nr.11, 6600 Iasi, Romania, E-mail ddorohoi@uaic.ro*
*2.G.Asachi Technical University, Iaşi, Bd. Copou, nr.11, 6600 Iasi, Romania*

**ABSTRACT.** The dipole moments and the polarizabilities in the excited states of some pyridinium ylides were estimated using the results of the statistic cell model proposed by Takehiro Abe.

**Keywords:** dipole moment and polarizabilities, cycloimmonium ylids

## INTRODUCTION

Pyridinium ylids [1] are dipolar molecules in the ground electronic state. They have a visible electronic absorption band that appear by an intramolecular charge transfer (ICT) from the carbanion to the heterocycle. This band is very sensitive at the solvent nature. A study about the solvent influence on the ICT visible band offers information on the ylid electric parameters modifications by passing from the ground state to its excited state.

## THEORETICAL ASPECTS

Takehiro Abe statistic cell model of a pure liquid [2] permits to express the spectral shifts in function of the microscopic parameters both of the solvent and of the spectrally active molecule. In this model a spectrally active molecule is surrounded by concentric solvatation spheres containing identic, spherical solvent molecules. The spheres containing solvent molecules have their centers on the solvatation sphere surface (Fig.1).

The p-th solvatation sphere radius can be expressed as function of the radius of the spheres that represent solvent and solute molecules, $r_u$ and $r_v$ respectively:

$$R_{uv(p)} = r_u + (2p+1)r_v \tag{1}$$

The system of the spheres is considered in two electronic states:

- ground state (g) in which all the molecules are in their ground electronic state
- excited state (e) corresponding to the ground state of the solvent molecules and to the excited electronic state of the central, spectrally active molecule.

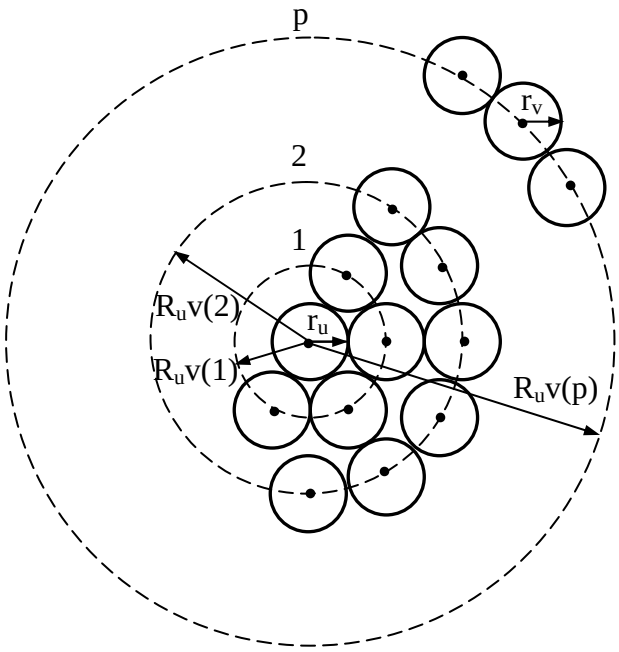


**Fig. 1.** The arrangement of the molecules in Abe model.

The chosen states correspond to the experimental check of the model, by spectral means. The used liquids for spectral recordings may be transparent in the absorption range of the spectrally active molecule. Durring spectra recordings, the solvent molecules do not change their electronic state.

In liquid state, the molecules interact. The solvatation energies in the states participating to the electronic charge transitions are:

$$\begin{aligned} W_g &= W_g^0 + W_g(u) + W_g(v) \\ W_e &= W_e^0 + W_e(u) + W_g(v) \end{aligned} \tag{2}$$

where $W_{g,e}^0$ represent the energies in the ground and excited states of the system, for its gaseous state; $W_{g,e}(u)$ - interaction energies between the central molecule (in the two states of the transition) and the solvent molecules surrounding it; $W_g(v)$ -the interaction energy between the solvent molecules. The energies in the gaseous state of the system can be express by the following terms:

$$\begin{aligned} W_g^0 &= W_g(u) + W_g(v) \\ W_e^0 &= W_e(u) + W_g(v) \end{aligned} \tag{3}$$

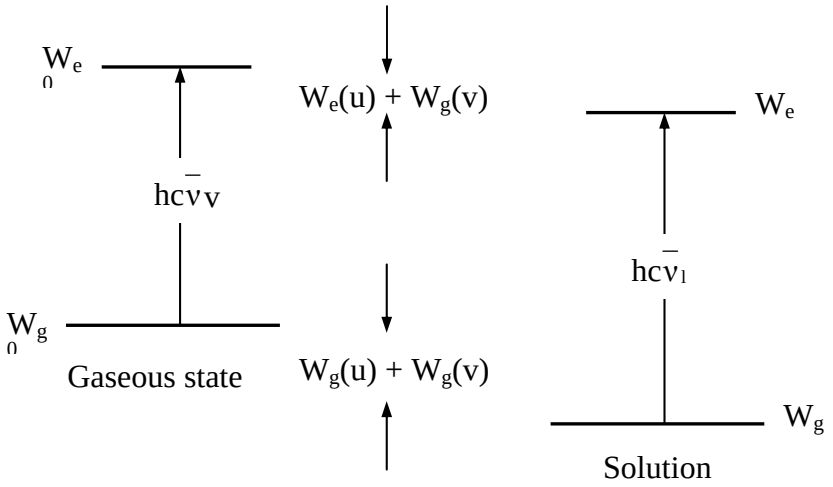


**Fig. 2.** The electronic shifts by passing from gaseous to liquid solution.

From Fig.2 and the relations (2) and (3), it results that spectral shift by passing from gaseous state to the binary solutions is proportional with the difference between the solvatation energies of the spectrally active molecule in the two electronic states of the transition.

$$hc(\bar{\nu}_l - \bar{\nu}_v) = W_e(u) - W_g(u) \tag{4}$$

Taking into account Van der Waals interactions, Abe expressed the spectral shift by the relation (5):

$$hc(\bar{\nu}_l - \bar{\nu}_v) = -\sum_p R_{uv(p)}^{-6}\left\{\frac{2}{3kT}\mu_g^2(v)\left[\mu_e^2(u) - \mu_g^2(u)\right] + \alpha_g(v)\left[\mu_e^2(u) - \mu_g^2(u)\right] + \mu_g^2(v)\left[\alpha_e(u) - \alpha_g 9u)\right]\right\} -$$
$$-\sum_p R_{uv(p)}^{-6}\left\{\frac{3}{2}I_g(v)\alpha_g(v)\frac{I_g(u) - hc\bar{\nu}_l}{I_g(v) + I_g(u) - hc\bar{\nu}_l}\alpha_e(u) - \frac{3}{2}I_g(v)\alpha_g(v)\frac{I_g(u)}{I_g(v) + I_g(u)_l}\alpha_e(u)\right\} \tag{5}$$

Relation (5) has been obtained in the hypothesis of the additivity of the orientation, induction and dispersion energies of the pairs of molecules. In this relation the index "u" reffers to the spectrally active molecules and "v"- to the solvent ones; g and e describe the ground and the excited states of the molecules and ν is the wave number in the maximum of the pyridinium ylids electronic absorption band, measured in liquid solution (l) and in vaporous state (0); μ represents the dipole moment and α - the polarizability. C is a constant dependent on the molecular weights and on the densities of the molecules [2]:

$$hcC = -\sum_{p} R_{uv(p)}^{-6} = n(1)R_{uv(1)}^{-6} + n(2)R_{uv(p)}^{-6} + ... + n(p)R_{uv(p)}^{-6} =$$
$$= -\frac{16\pi^3 N_A^2}{9}\left(\frac{\rho_v}{M_v}\right)^2 \left\{\left[\left(\frac{M_u}{\rho_u}\right)^{1/3} + \left(\frac{M_v}{\rho_v}\right)^{1/3}\right]^{-4} + \left[\left(\frac{M_u}{\rho_u}\right)^{1/3} + 3\left(\frac{M_v}{\rho_v}\right)^{1/3}\right]^{-4} + ...\right\} \quad (6)$$

The radius of a solvent and solute molecule was express in (6) as function on molar mass and density of the corresponding substance.

In order to estimate the dipole moments and polarizabilities in the excited state of pyridinium ylids, a formula resulting from (5) and (6) has been used:

$$\left[\mu_e^2(u) - \mu_g^2(u)\right] + T_1(v,u)\alpha_e(u) - T_2(v,u)\alpha_g(u) + \frac{\nu_l - \nu_v}{C} = 0 \quad (7)$$

where:

$$T_1(v,u) = \frac{\mu_g^2(v) + \frac{3}{2}\frac{I_g(v)\left[I_g(u) - hc\overline{\nu}_l\right]}{I_g(v) + I_g(u) - hc\overline{\nu}_l}\alpha_g(v)}{\frac{2}{3kT}\mu_g^2(v) + \alpha_g(v)} \quad (8)$$

$$T_2(v,u) = \frac{\mu_g^2(v) + \frac{3}{2}\frac{I_g(v)I_g(u)}{I_g(v) + I_g(u)}\alpha_g(v)}{\frac{2}{3kT}\mu_g^2(v) + \alpha_g(v)} \quad 9)$$

and

$$T_3(v,u) = \frac{\nu_l - \nu_v}{C} \quad (10)$$

The terms $T_i(v,u)$, i=1,2,3 can be computed using the microscopic parameters both of the ylid and solvent and the wavenumbers of the ICT band. So, relation (7) permits to estimate, by regressional method, the dipole moments and the polarizabilities of the pyridinium ylids.

## RESULTS AND DISCUSSIONS

The studied ylids were: pyridinium acetyl benzoyl methylid ($Y_1$); pyridinium anilido benzoyl methylid ($Y_2$); pyridinium dicarbetoxy methylid ($Y_3$).The ionization potential and the value of the dipole moment in the ground state of pyridinium ylid was estimated by PM3.

The visible electronic absorption band of the studied pyridinium ylids was recorded in aprotic solvents with known parameters mentioned above.

**Table 1**

The solvent parameters and the wavenumbers in the ICT visible band

| Nr | Solvent | μ(D) | $10^{25}\alpha$ | I(eV) | ρ (g/cm$^3$) | M (g/mol) | ν(cm$^{-1}$) | | |
|---|---|---|---|---|---|---|---|---|---|
| | | | | | | | $Y_1$ | $Y_2$ | $Y_3$ |
| 1 | n-Heptan | 0 | 136.1 | 10.35 | 0.68 | 100.2 | 22600 | 22150 | 22080 |
| 2 | Cyclohexane | 0 | 108.5 | 11.00 | 0.78 | 84.2 | 22550 | 20970 | 21910 |
| 3 | $CCl_4$ | 0 | 105 | 9.72 | 1.59 | 153.8 | 22610 | 20970 | 21900 |
| 4 | Dioxan | 0 | 94.4 | 9.52 | 1.42 | 88.1 | 23830 | 22350 | 22950 |
| 5 | Mesitilen | 0 | 161.2 | 8.76 | 0.86 | 120.2 | 23100 | 21730 | 22410 |
| 6 | Chloroform | 1.05 | 82.3 | 11.50 | 1.49 | 76.1 | 24630 | 22470 | 23280 |
| 7 | Methanol | 1.62 | 32.6 | 10.97 | 0.70 | 32.0 | 24500 | 24400 | 25230 |
| 8 | Methyl acetate | 1.67 | 69.9 | 10.51 | 0.97 | 74.1 | 24330 | 23030 | 23400 |
| 9 | Ethanol | 1.69 | 50.6 | 10.70 | 0.79 | 46.1 | 26760 | 24400 | 24970 |
| 10 | Aceton | 2.80 | 63.9 | 9.89.9.77 | 0.79 | 58.1 | 24480 | 23240 | 23450 |
| 11 | Acetophenon | 3.94 | 143.7 | 12.39 | 1.03 | 120.1 | 24720 | 22990 | 23370 |
| 12 | Acetonitrile | 4.25 | 44.0 | | 0.79 | 41.1 | 24600 | 23560 | 23750 |

**Table 2**

The parameters $\mu_g$, ρ, M and I of the studied ylids

| Nr | Ylid | $\mu_g$ (D) | ρ (g/cm$^3$) | M (g/mol) | $I_g$ (eV) |
|---|---|---|---|---|---|
| 1 | $Y_1$ | 5.6 | 1.41 | 239 | 8.96 |
| 2 | $Y_2$ | 5.9 | 1.76 | 253 | 8.72 |
| 3 | $Y_3$ | 4.1 | 1.53 | 293 | 8.93 |

The terms $T_i(v,u)$, i=1,2,3 was estimated using the microscopic parameters both of the ylid and solvent and the wavenumbers of the ICT band from Tables 1 and 2.

Using a Multireg BASIC program [5], both the dipole moments in the excited state and the polarizabilities in the ground and the excited states of pyridinium ylids were estimated.

**Table 3**

Dipole moments $\mu_e$ (u) and polarizabilities $\alpha_g(u)$ $\alpha_e(u)$ of the studied ylids

| Nr | Ylid | $\mu_e^2(u) - \mu_g^2(u)$ | $\alpha_g(u)\,10^{25}$ | $\alpha_e(u)\,10^{25}$ | $\mu_e(u)$ (D) |
|---|---|---|---|---|---|
| 1 | $Y_1$ | -36.76 | 48.4 | 40.0 | 2.32 |
| 2 | $Y_2$ | -22.61 | 66.4 | 41.4 | 3.49 |
| 3 | $Y_3$ | -22.35 | 34.1 | 13.1 | 1.91 |

The obtained data (Table 3) reflect that, in the intramolecular charge transfer process, the dipole moment of pyridinium ylids decreases and changes its sens, concomitantly with an decrease of the molecular polarizability. The values for the dipole moments of pyridinium ylids are in good agreement with the values obtained in [4] for some pyridazinium ylids.

## REFERENCES

1. I. Zugravescu and M. Petrovanu, N Ylid Chemistry, Acad.Press, London, 1976.
2. Takehiro Abe, Bull.Chem.Soc.Japan, 38,1314, 1965; 39, 936, 1966.
3. G. Henrion, A. Henrion and R. Henrion, Beispiele Zur Datenanalyse mit BASIC Programmen, Berlin, 264-282, 1988.
4. D. Dorohoi, G. Surpateanu and L. Gheorghies, Balkan Phys.Letters, 6(3), 198, 1998.

STUDIA UNIVERSITATIS BABEŞ-BOLYAI, PHYSICA, SPECIAL ISSUE, 2000

# PROTON NMR RELAXIVITY OF BLOOD SAMPLES IN THE PRESENCE OF SOME GADOLINIUM AND DYSPROSIUM COMPOUNDS

**I. COROIU[1], AL. DARABONT[2] and M. BOGDAN[3]**

*[1] Technical University, 3400 Cluj-Napoca, Romania*
*[2] Babes-Bolyai University, 3400 Cluj-Napoca, Romania*
*[3] National Institute for Isotopic and Molecular Technology, P.O. Box 700, 3400 Cluj-Napoca, Romania*

**ABSTRACT.** The longitudinal and transverse relaxation rates of some gadolinium and dysprosium compounds have been measured on $^1H$ in aqueous solutions and in blood as a function of molar concentrations. The different relaxation characteristics were analysed and certain explanations concerning the molecular sources of these variations were advanced. The evidenced properties of the compounds studied by us are promising for novel and interesting applications in medicine.

## INTRODUCTION

The MRI tissue and blood characterisation, based on relaxation times measurement cannot be properly used until the molecular sources of variation are understood. Tissues and blood are complex molecular systems with complex NMR properties. A better comprehension of the molecular basis of relaxation offers the possibility to predict the changes expected for a given pathology. The purpose of this contribution is to evidence the different relaxation characteristics of some gadolinium and dysprosium compounds in the presence and absence of the blood and to give a possible explanation about the molecular processes that cause the change's occurrence.

## METHODS

Some gadolinium and dysprosium compounds such as: Gd-CIT (gadolinium citrate), Dy-CIT (dysprosium citrate), Dy-DTPA (DTPA - diethylenetriamine pentaacetic acid), iron oxide - gadolinium oxide - dextran and iron oxide - dysprosium oxide - dextran complexes were prepared. Citrates of gadolinium and dysprosium were prepared [1] starting from respective metal (99.9% purity, purchased from Chemical Corp, Sun Valley) firstly transformed in chlorides and then in citrates. The silver nitrate was added to establish the purity level, for the control of complete elimination of chlorine ion. Furthermore, the products were purified by recrystallization. The Dy-DTPA complex was obtained from respective citrate and afterwards purified by recristallization.

The preparation of the compounds ($5Fe_2O_3$+$3Gd_2O_3$)-dextran [2], and ($5Fe_2O_3$+$3Dy_2O_3$)-dextran were made using microemulsion method in the water/ toluene system. The starting materials $FeCl_3$ / $GdCl_3$ or $FeCl_3$ / $DyCl_3$ in molar ratio of 5:3, 420 ml of water, 120 ml of toluene and 1 gram of dextran, were poured into a beaker. These solutions were stirred and then kept on a water bath about 10-12 hours. The molecular weight of dextran was 40000.

The longitudinal $T_1^{-1}$ and transverse $T_2^{-1}$ relaxation rates' measurements have been carried out as a function of molar concentrations. All measurements have been made at room temperature (about 25°C) and the proton Larmor frequency $\nu_o$=90MHz. The pulsed NMR spectrometer utilised was a commercial Bruker SXP 4/100 spectrometer. Transverse relaxation rates measurements have been made using the Carr-Purcell method, while longitudinal relaxation rates measurements using the inversion recovery pulse sequence, 180°-τ-90°. The accuracy was about 2-3% for the longitudinal relaxation rates and about 5-7% for the transverse relaxation rates. $R_1$ and $R_2$ relaxivities, in $mM^{-1}s^{-1}$ were determined from the least-squares determination of the slopes of plots $1/T_{1,2}$ versus molar concentration of compound, using at least five independent measurements at several concentrations among 0 and 2mM.

## RESULTS AND DISCUSSIONS

The measured $R_1$ and $R_2$ relaxivities of studied compounds in the presence and absence of the blood is shown in Table 1. The proton relaxation rates (Figs. 1a, 1b, 1c and 2a, 2b 2c) are linearly dependent on the concentration of the compounds. This certifies the absence of the solute-solute interaction [3].

**Table 1.**

The $R_1$ and $R_2$ relaxivities for the studied compounds

| **Compounds** | **$R_1$ $mM^{-1}s^{-1}$** | **$R_2$ $mM^{-1}s^{-1}$** |
|---|---|---|
| Gd-CIT | 15 | 30.54 |
| Gd-CIT and blood | 3.624 | 32.635 |
| Dy-CIT | 0.452 | 1.023 |
| Dy-CIT and blood | Coagulation of the blood | Coagulation of the blood |
| ($5Fe_2O_3$+$3Gd_2O_3$)-dextran | 61.78 | 201.39 |
| ($5Fe_2O_3$+$3Gd_2O_3$)-dextran and blood | 11.86 | 188.725 |
| ($5Fe_2O_3$+$3Dy_2O_3$)-dextran | 24.52 | 82.48 |
| ($5Fe_2O_3$+$3Dy_2O_3$)-dextran and blood | 0.241 | 38.67 |
| Dy-DTPA | 0.79 | 1.61 |
| Dy-DTPA and blood | 0.42 | 93.72 |

It is obvious that the relaxivities of gadolinium citrate (Gd-CIT), and of the compounds ($5Fe_2O_3$+$3Gd_2O_3$)-dextran and ($5Fe_2O_3$+$3Dy_2O_3$)-dextran are rather high, but the mechanisms involved in that are quite different. In the case of paramagnetic

complexes, positive susceptibility is necessary, but not sufficient for effective relaxation enhancement. The magnitude of relaxation enhancement depends also on proximity of nuclear and electronic spins and on the correlation times.

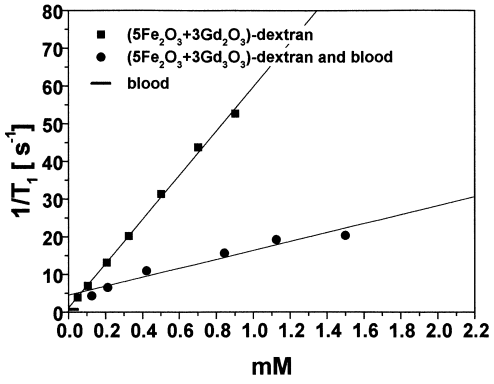


**(1a).**

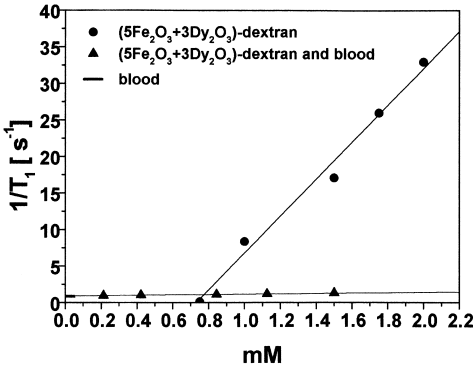


**(1b).**

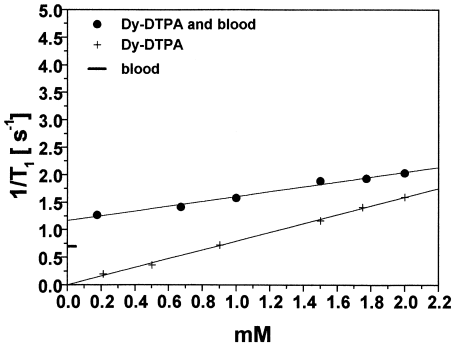


**(1c).**

**Fig. 1a, 1b and 1c.**

Proton longitudinal relaxation rates at 2.11T and 25°C, as a function of compounds' concentration in the presence and the absence of the blood.

The differences in the $R_1$ and $R_2$ relaxivities of dysprosium and gadolinium citrates should be justified in the first approximation through different electron spin relaxation times ($T_{1e}$) about $10^{-8}$ -$10^{-9}$ s for gadolinium and $10^{-12}$ -$10^{-13}$ s for dysprosium. For metal ion with relatively long $T_{1e}$ 's the magnitude of the outer-sphere relaxivities scales roughly with the square of the effective magnetic moment (or S(S+1) (value) of the metal ion ($S_{Gd}$=7/2, $S_{Dy}$=5/2).

The $1/r^6$ dependence in dipolar interactions presents the opportunity to increase relaxivity by chemically inducting an orientation of bound water molecules such that the protons are closer to the metal centre or unpaired spin density. The dipole-dipole term, affected critically by $r^{-6}$ can be offset by unpaired electron spin density at the nucleus, a scalar (or "contact") effect. That is, quantum mechanics predict a probability that the electron and nucleus coincide in space, dominating relaxation. In situations where such an effect is significant [4], $T_2$ relaxation enhancement can exceed $T_1$ enhancement.

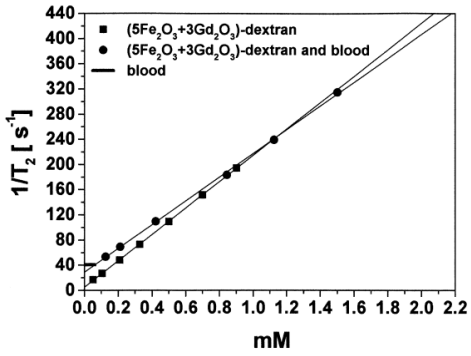


**(2a).**

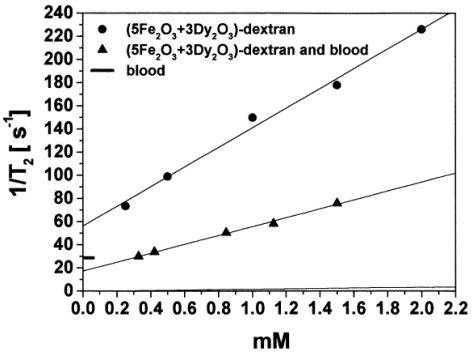


**(2b).**

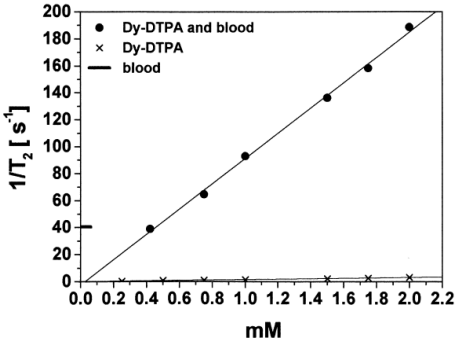


**(2c).**

**Fig. 2a, 2b and 2c.**

Proton transverse relaxation rates at 2.11T and 25°C, as a function of compounds' concentration in the presence and the absence of the blood.

Solvent relaxation in the presence of superparamagnetic particles like the compounds ($5Fe_2O_3$+$3Gd_2O_3$)-dextran and ($5Fe_2O_3$+$3Dy_2O_3$)-dextran, chiefly differs from that in the presence of paramagnetic solutes due to much greater weighting of the magnetic moment contribution. Compared with paramagnetic solutes, superparamagnetic particulates have increased effective magnetic moment, decreased freedom of molecular motion, and decreased water $^1H$ exchange. The much greater effective magnetic moment dominates all the possible factors discussed previously, by creating greater field heterogeneity characteristically manifest at $T_2$ shortening much greater for a given $T_1$ effect than occurs in the presence of paramagnetic solutes. Of course, the role of diffusion cannot be neglected that usually modulated these phenomena [5, 6]. The stabilisation in dextran of ($5Fe_2O_3$+$3Gd_2O_3$) and ($5Fe_2O_3$+$3Dy_2O_3$) nanoparticles increases their size and mass causing anisotropic motion and becoming an additional factor of importance in relaxation.

These facts should apply in many other situations. For example, although Dy-DTPA relaxes strongly through dipole-dipole interactions with water within hydration sphere of each ion, it can also introduce susceptibility effects that may account for its greater efficacy on blood relaxation than can be accounted for by considering only

exchange-mediated dipolar processes [7]. The magnetic anisotropy of Dy-DTPA, as well as the high magnetic moment of the Dy (III) ion (10 Bohr magnetons) should produce susceptibility effects.

Increasing in $R_2$ relaxivity observed for Dy-DTPA in the presence of the blood should be moreover explained by PRE effect [8]. The PRE effect is operative when metal ion or intact compound is covalently or noncovalently attached to a macromolecule (for example to protein amino acid residues). The largest gain in $R_2$ relaxivity seems to imply a noncovalent binding to proteins (possible β-globulins) and an anisotropic motion. The protein-compound binding energies are likely determined by a number of relatively small contributions such as: electrostatic, hydrogen-bonding, Van der Waals and hydrophobic forces, from different groups on complex. These interactions may result in less internal flexibility and higher relaxivity when the compound is attached to a single residue on the protein surface. The greater part of the relaxivity probably stems from hydrogen-bounded water molecules in the second co-ordination sphere.

The opposite case of gadolinium compounds $R_1$ relaxivity decreasing in the presence of the blood implies probably a covalent binding to proteins, high degree of internal flexibility and a low number of bounded water molecules.

A plausible explanation of the coagulation of the blood in the presence of the dysprosium citrate should be that the dysprosium ions activate *in vitro* the Hageman factor [9] of coagulation. A similar evolution occurs *in vitro* in the presence of the dysprosium phosphate. Another explanation, more probable, could be based on first experimental investigations on the relations between electron transfer processes and thrombogenesis by Sawyer et al. [10] and on theory describing the contact activation of fibrinogen in terms of exchange currents proposed by Brauerschmidt [11]. According to this model, an electron transfer between the semiconducting protein and a solid induces fibrin formation. The dysprosium compounds represent the solid in our case. Thus the degree of antithrombogenicity of a given material is dependent on its electronic structure. The dramatic decrease of the $R_1$ and $R_2$ for $(5Fe_2O_3+3Dy_2O_3)$-dextran compound in the presence of the blood should be elucidate on this theory.

## CONCLUSIONS

Several gadolinium and dysprosium compounds were prepared and their $R_1$ and $R_2$ relaxivities were measured in the presence and absence of the blood. The increase or decrease of $R_1$ and $R_2$ relaxivities in the presence of the blood depends on the number of factors as compound mass, size and composition and is the combined result of more than one type of relaxation processes.

The possible applications of the dysprosium compounds include implementation of new laboratory tests for haematological pathology. Using of $(5Fe_2O_3+3Gd_2O_3)$-dextran compound for cancer targeting and for cancer treatment with the new method [12]: *magnetic fluid hyperthermia* (MHF) is the next challenge for the future.

## REFERENCES

1. I. Coroiu, Al. Darabont, M. Bogdan, D.E. Demco, Rom. J. Biophys., 7, 103 (1997).
2. I. Coroiu, Al. Darabont, M. Bogdan, D.E. Demco, Rom. J. Biophys., 7, 95 (1997).
3. K. Marcus, in: Ion solvation, Chapter 5, Wiley, Chichester, U.K., 1985.
4. C.F. Geraldes, A.D. Sherry, R.D. Brown III, S.H. Koenig, Magn. Reson. Med., 3, 242 (1986).
5. Y. Rozenman, X.M. Zou, H.L. Kantor, Magn. Reson. Med., 14, 31 (1990).
6. Y. Rozenman, X.M. Zou, H.L. Kantor, Radiology, 175, 655 (1990).
7. A.Villringer, B.R. Rosen, J.W. Belliveau, J.L. Ackerman, R.B. Lauffer, R.B. Buxton, Y.S. Chao, V.J. Wedeen, T.J. Brady, Magn. Reson. Med., 6, 164 (1988).
8. R.B. Lauffer, T.J. Brady, R.D. Brown, S.H. Koenig, Magn. Reson. Med., 3, 541 (1986).
9. A.J. Erslev, Th.G. Gabuzda, in: *Pathophysiology of Haematological Disorders*, Saunders Comp., Philadelphia-Londra-Toronto, 1979.
10. P. Sawyer, W. Brattain, P. Boddy, in: *Electrochemical criteria in the choice of materials used in vascular hemostasis and intravascular thrombosis*, Appleton-Century-Crofts, New York, 1965.
11. P. Bauerschmidt, M. Schaldach, J. Bioeng., 1, 261 (1977).
12. D.C.F. Chan, D.B. Kirpotin, P.A. Bunn, JMMM, 122, 374 (1993).

STUDIA UNIVERSITATIS BABEŞ-BOLYAI, PHYSICA, SPECIAL ISSUE, 2000

# RAMAN MICROSPECTROSCOPIC STUDY ON THE INFLUENCE OF SALTS ON LOW pH-INDUCED DNA STRUCTURAL CHANGES: LOW CONCENTRATIONS OF DIVALENT IONS

**C.M. MUNTEAN*, G.J. PUPPELS**, J. GREVE and G.M.J. SEGERS-NOLTEN**

** National Institute for Research and Development of Isotopic and Molecular Technologies, R-3400 Cluj-Napoca, P.O. 5, Box 700, Romania*
*** Rotterdam University Hospital "Dijkzigt", General Surgery 10M, 3015 GD Rotterdam, The Netherlands*
*Department of Applied Physics, University of Twente, P.O. Box 217, 7500 AE Enschede, The Netherlands*

**ABSTRACT**. In this work, a confocal Raman microspectrometer was used to investigate the influence of low concentrations of divalent ions on low pH-induced DNA structural changes. Based on the observation that the midpoint of transition of Watson-Crick GC-basepairs to protonated GC-basepairs lies around pH 3 (analyzing the 681 $cm^{-1}$ line) (Puppels, *et al*, 1994), measurements were carried out on calf-thymus DNA at neutral pH and at pH 3. Spectra are presented in the wavenumber region describing base electronic structures and base pairing (1150-1680 $cm^{-1}$). Effects of low concentrations of divalent cations upon protonation mechanism of opening AT- and changing the protonation of GC basepairs in DNA are considered.

## Introduction

The predominant DNA conformation in chromosomes and in the nucleus of the eucaryotic cells is the B-form, the canonical right handed double helix. Until the end of the 1970s, it was generally accepted that this biopolymer is very regular and independent on the nucleotide sequence (Palecek, 1991). Today it is a well established fact that the DNA double helix exhibits local polymorphism at the level of the single base pair and of dinucleotide step. DNA structure polymorphy is sequence-dependent and influenced by environmental conditions (pH, ions, superhelical stress, length of particular tracts) (Palecek, 1991). Alternative DNA structures and conformations, such as cruciforms (Furlong, *et al*, 1989), triplex DNA, parallel stranded DNA (Otto, *et al*, 1991), extended stretches of unpaired bases, potential Z-DNA forming stretches of DNA have achieved much interest (Puppels, *et al*, 1994). Biophysical, chemical and enzymatic assays proved that these non-B DNA, unorthodox structures formed under conditions of torsional stress, may play important organizing and/or regulatory roles in vivo (Hanvey, *et al*, 1988).

Canonical B-DNA has no strong protonation sites, and because of this it does not pick up protons with the exception of totally nonphysiological conditions of

extremely low pH. However, protonation is a significant phenomenon for DNA. Unusual DNA structures in which Hoogsteen is a possible base-paired arrangement of protonated dG:$dC^+$ or dA:dT are supposed to be implied in a new mode of recognition.

Binding of $H^+$ to DNA, leads reversibly, to alternative DNA structures, especially to disrupted AT-basepairs and to Hoogsteen syn dG:$dCH^+$ basepairs, which exist under physiological conditions in purified and chromosomal DNA (Puppels, *et al*, 1994). Besides, irreversible changes occur in DNA, when at low pH, upon further protonation, the disruption of not only AT- but also of protonated Hoogsteen GC-basepairs takes place. In a Hoogsteen basepair, protonation of cytosine is accompanied by a conformational change of the guanine from the C2'-*endo*-anti to C2'-*endo*-syn. This enables hydrogen bonding between N(7) of guanine and cytosine N(3). Studies are required to elucidate whether the equilibrium between protonated and non-protonated GC-basepairs can be influenced by chemical parameters.

In this work, a confocal Raman microspectrometer was used to investigate the influence of low concentrations of divalent ions on low pH-induced DNA structural changes. Based on the observation that the midpoint of transition of Watson-Crick GC-basepairs to protonated GC-basepairs lies around pH 3 (analyzing the 681 $cm^{-1}$ line), measurements were carried out on calf-thymus DNA at neutral pH and at pH 3. Effects of low concentrations of divalent cations upon protonation mechanism of opening AT- and changing the protonation of GC-basepairs in DNA are discussed.

## Materials and methods

### *Preparation of MgDNA complexes at neutral pH and low pH*

Calf-thymus DNA (Sigma Type I, D-1501, St. Louis, MO, USA) at a concentration of 15 mg/ml was dialyzed against Tris buffer (10 mM Tris, 10 mM NaCl, 5mM $MgCl_2$ x $6H_2O$) to obtain the MgDNA complexes at neutral pH. Protonated MgDNA complexes (around pH 3) were prepared by dialyzing calf-thymus DNA from the same stock solution against glycine buffer (50 mM glycine, 10 mM NaCl) containing 5 mM $MgCl_2$ x 6 $H_2O$.

### *Experimental*

All Raman spectra experiments with MgDNA complexes were carried out on a confocal Raman microspectrometer developed in the Biophysical Technology group, Department of Aplied Physics, University of Twente, Enschede, the Netherlands, largely identical with a first developed micro Raman set up (Puppels, *et al*, 1994). The microscope was equipped with a 63x Zeiss Plan Neofluar water immersion objective. Laser light of 514.5 nm from an Argon ion laser was used for excitation.

The spectra have been processed by means of the software package RAMPAC (De Mul & Greve, 1993). Each measurement on a DNA sample was followed by a second one (background signal measurement), just next to that of

DNA, in order to determine the signal contributions from buffer, which were then substracted from the resulting DNA sample spectrum.

Each spectrum is the result of more than 12 measurements, which were then averaged. The averaged spectra thus obtained showed only minor variations, not of any consequence for the interpretations given bellow. The wavenumber calibration of the Raman spectra was recorded with the same instrument setting on the basis of an indene. The spectra were corrected for the wavenumber dependent detection efficiency of the confocal Raman microspectrometer (Puppels, *et al*, 1994).

***Difference spectra***

The events occuring in our samples upon lowering the pH are clarified by the difference spectra. An internal intensity calibration was needed to scale the measured spectra, in order to compute difference spectra (Puppels, *et al*, 1994). The spectra were scaled to have equal intensity in the 1094 $cm^{-1}$ line of the DNA backbone $PO_2^-$symmetric stretching vibration. The intensity of this band is not sensitive to DNA protonation down to at least pH 2.35 (O'Connor, *et al*, 1981). Protonation of the DNA backbone phosphate groups occurs around pH 1. Besides, in the conditions employed for the present experiments, the interactions between divalent metal cations and the phosphodioxy anions should be dominated by electrostatics (Duguid, *et al*, 1993).

The events occuring in the MgDNA systems upon lowering the pH, were also monitored by a comparative analysis of the spectra obtained for samples with different stages of DNA protonation.

**Results and conclusions**

Measurements were made on calf-thymus DNA at neutral and low pH (around pH 3), in the presence of low concentrations of $Mg^{2+}$ ions. The choice of the low pH value was based on the observation that the midpoint of transition of Watson-Crick GC-basepairs to protonated GC-basepairs lies around pH 3 (analyzing the 681 $cm^{-1}$ line) (Puppels, *et al*, 1994). Effects of lowering the pH upon protonation mechanism of opening AT- and changing the protonation of GC-basepairs in DNA are discussed.

Spectra are presented in the wavenumber region describing base electronic structures and base pairing (1150-1680 $cm^{-1}$). Main spectra-structure correlations in this range of the Raman spectra of DNA molecules are described in the following.

(a) Various bands in the 1200-1600 $cm^{-1}$ region, assigned to purine and pyrimidine ring vibrations, are sensitive indicators of ring electronic structures and are expected to exhibit perturbations upon metal binding at ring sites or upon DNA denaturation (Thomas, *et al*, 1993) and protonation. Among the most informative of these are the band of guanine at 1488 $cm^{-1}$, which shifts upon binding of electrophilic agents to the N7 acceptor, and bands at 1240 and 1257 $cm^{-1}$. The band

at 1488 $cm^{-1}$ decreases in intensity upon binding of $H^+$ to guanine N7. The band near 1240 $cm^{-1}$ is due predominantly to dT, but has a minor contribution from dC. The band near 1257 $cm^{-1}$ has been assigned to dC. By monitoring these two bands the effect of metal ion binding on dT and dC can be determined independently.

(b) The broad band centered near 1668 $cm^{-1}$ assigned to coupled C=O stretching and N-H deformation modes of dT, dG and dC (Thomas, *et al*, 1993), is sensitive to denaturation, reflecting altered hydrogen bonding states of the exocyclic groups (C=O, NH, $NH_2$).

Our Raman spectra show that low concentrations of divalent cations, protect DNA against protonation of cytosine (line at 1262 $cm^{-1}$). Low salt concentrations do not protect adenine and guanine N(7) against binding of $H^+$ (characteristic lines at 1304 $cm^{-1}$ and at 1488 $cm^{-1}$, respectively). This is consistent with extensive melting of AT-rich regions and limited melting of GC- rich regions.

A possible conformational transition of the guanine from the C2'-*endo*-anti to C2'-*endo*-syn, followed by hydrogen bonding between N(7) of guanine and cytosine N(3) might be considered, after analyzing the corresponding Raman spectra in the wavenumber region 600-1150 $cm^{-1}$.

**Acknowledgements**

This work was supported in part by a CEC grant under contract nr. ERB-CIPA-CT-92-2223. EC financial support and research experience gained at the University of Twente, Enschede, the Netherlands, are greatfully acknowledged by one of us (C.M.M.).

## REFERENCES

1. De Mul, F. F. M., and Greve, J. (1993) RAMPAC: a program for analysis of complicated Raman spectra, *J. Raman Spectrosc.* **24**: 245-250.
2. Duguid, J., Bloomfield, V. A., Benevides, J., and Thomas, G. J., Jr. (1993) Raman spectroscopy of DNA-metal complexes. I. Interactions and conformational effects of the divalent cations: Mg, Ca, Sr, Ba, Mn, Co, Ni, Cu, Pd, and Cd, *Biophys. J.*, **65**: 1916-1928.
3. Furlong, J. C., Sullivan, K. M., Murchie, A. I. H., Gough, G. W., and Lilley, D. M. J. (1989) Localized chemical hyperreactivity in supercoiled DNA: evidence for base unpairing in sequences that induce low-salt cruciform extrusion, *Biochemistry*, **28**: 2009-2017.
4. Hanvey J. C., Klysik, J., and Wells, R. D. (1988) Influence of DNA sequence on the formation of non-B right-handed helices in oligopurine oligopyrimidine inserts in plasmids, *J. Biol. Chem.*, **263**: 7386-7396.
5. Muntean, C. (1994) A Raman microspectroscopic study of the influence of monovalent and divalent cations on low pH-induced DNA structural changes - *European Community Report*, Brussels: pp 40.

6. Muntean, C. M., Puppels, G. J., Greve, J., Segers-Nolten, G. M. J., Otto, O. (1999a) Raman Microspectroscopic Study on Low pH-Induced DNA Structural Transitions: 1. Changes in Base Electronic Structures and Base Pairing, in *"Spectroscopy of Biological Molecules: New Directions"* (8th European Conference on the Spectroscopy of Biological Molecules, 29 August - 2 Septembrie 1999, Enschede, Olanda), J. Greve, G. J. Puppels, C. Otto Eds., Kluwer Academic Publishers, Dordrecht (1999), Olanda, p. 221-222.
7. O'Connor, T., and Scovell, W. M. (1981) pH-Dependent Raman spectra and thermal melting profiles for polycytidylic acid, *Biopolymers*, **20**: 2351-2367.
8. Otto, C., Thomas, G. A., Rippe, K., Jovin, T. M., and Peticolas, W. L. (1991) The hydrogen-bonding structure in parallel-stranded duplex DNA is reverse Watson-Crick, *Biochemistry*, **30**: 3062-3069.
9. Palecek, E. (1991) Local supercoil-stabilized DNA structures, *Crit. Rev. Biochem. Mol. Biol.*, **26**: 151-226.
10. Puppels, G. J., Otto, C., Greve, J., Robert-Nicoud, M., Arndt-Jovin, D. J., and Jovin, T. M. (1994) Raman microspectroscopic study of low pH induced changes in DNA-structure of polytene chromosomes, *Biochemistry*, **33**: 3386-3395.
11. Thomas, G. J., Jr., Benevides, J. M., Duguid, J., and Bloomfield, V. A. (1993) Roles of cations in the structure, stability and condensation of DNA, in T. Theophanides et al. (eds.), *Fifth International Conference on the Spectroscopy of Biological Molecules*, Kluwer Academic Publishers, Dordrecht: 39-45.

STUDIA UNIVERSITATIS BABEŞ-BOLYAI, PHYSICA, SPECIAL ISSUE, 2000

# X-RAY STRUCTURAL DETERMINATION FOR 5'-CMP·$Na_2$ MONONUCLEOTIDE

**GH. MIHAILESCU[1], AL. DARABONT[2], GH. BORODI[1], I. BRATU[1], MIHAELA POP[2]**

[1] *National Institute for Research and Development of Isotopic and Molecular Technologies, P.O. Box 700, R-3400 Cluj-Napoca 5, Romania*
[2] *"Babes-Bolyai" University, Dept. of Physics, Cluj-Napoca, Romania*

ABSTRACT. The paper presents the results obtained in the growing and structure determination by X-ray diffraction of the 5'-CMP.$Na_2$ mononucleotide (5'-cytidine monophosphate disodium salt) single crystal, component of the ARN. The space group, the unit cell parameters and the fractional coordinates were determined.

## Introduction

Cytidine 5'-monophosphate disodium salt (5'-CMP.$Na_2$) is one of the four common ribonucleotides which make up ribonucleic acids (RNA's). The crystal structure of the sodium salt of cytidine 5'-monophosphate 6.5 hydrate provides valuable information on the interaction mechanisms of alkaline metal ions with water and nucleotides. Previous studies have been done on the barium salt of cytidine 5'-monophosphate 8.5 hydrate [1] and some information on the crystal data of disodium cytidine 5'-monophosphate were indicated by these authors. Nevertheless, the molecular structure and conformational parameters are not published yet to our knowledge. Nishimura et al. [2] indicated that the crystal structure of this salt was not solved. Difficulties in growing single crystals of this mononucleotide would be the reason. Despite these difficulties, single crystals have been obtained and the corresponding crystal structure has been determined in this work.

The nucleosides and nucleotides have attracted considerable attention not only because they are building blocks of the nucleic acids, DNA and RNA, which are the center of life processes, but also because they are cofactors and allosteric effectors for many of the fundamental enzymatic reactions. Cytidine 5'-monophosphate disodium salt (5'-CMP.$Na_2$) is one of the four common ribonucleotides which make up ribonucleic acids (RNA's).

## Results and Discussion

The 5'-CMP $Na_2$ compound was crystallized by the slow evaporation method from water-methanol solution using three recrystallization processes. There were obtained transparent single crystals of about 2 x 4 x 1-2 *mm*. From the Laue method we put in evidence the presence of the 2-fold symmetry. By Kulpe method the crystal was oriented along the 2-fold axis and by the oscillation method it was determined the periodicity along this direction, $b$=8.899Å. The spot-layer of superior order proved to be symmetrically disposed relative to the spot layer of zero order indicating again the 2 order symmetry. In the Fig. 1 the oscillation pattern is shown.

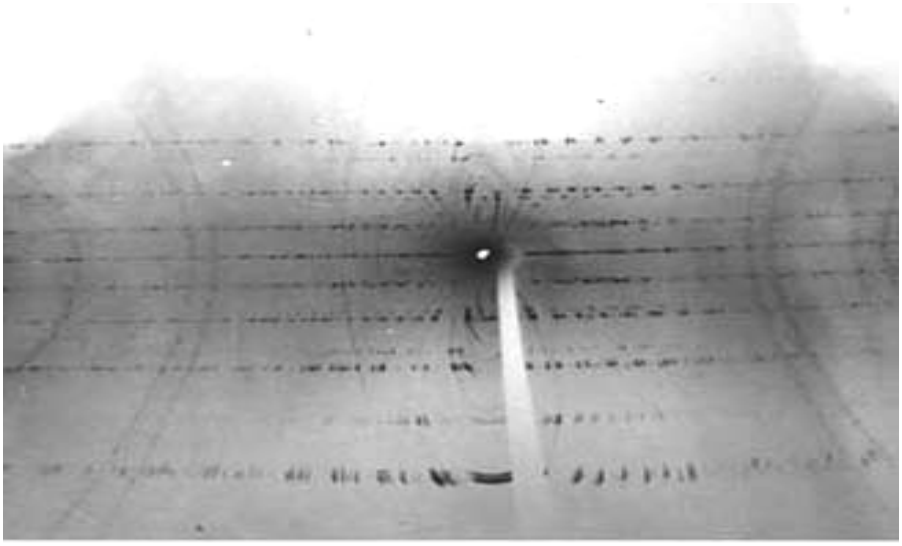

**Fig 1:** The oscillation pattern of the 5'-CMP$Na_2$ . 6.5 $H_2O$ single crystall

From the zero layer Weissenberg pattern [3], Fig. 2, the reciprocal lattice parameters resulted as: $a^*$=0.137, $c^*$=0.122 and $\beta^*$=85.5°. It results $a$=14.08 Å, $c$=15.83 Å and $\beta$=94.5°.

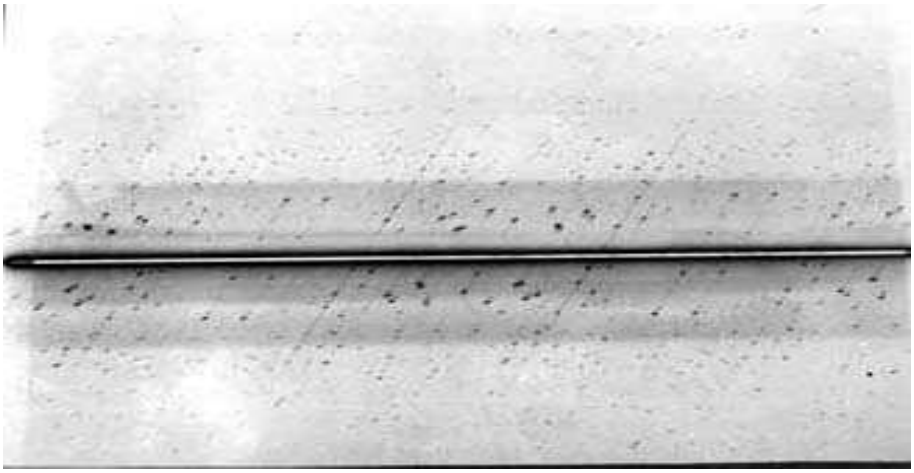

**Fig. 2:** The zero layer Weisenberg pattern for the 5'-CMP$Na_2$ . 6.5 $H_2O$ single crystall

By indexing the powder diffraction pattern the lattice parameters were obtained more precise. The compound density was experimentally determined by the picnometric method, $\rho_{exp}$ = 1.999 $g/cm^3$. From the lattice parameters and the experimental density the molecules number in the unit cell: $Z$ = 4 resulted.

Therefore, the 5'-CMP.$Na_2$ compound crystallizes in the monoclinic system, the space group $P_{21}$ with 4 molecules per unit cell and the lattice parameters are: $a$ = 14.10Å, $b$ = 8.9Å $c$ = 16.05 Å and $\beta$ = 94°.

Intensity data up to $\sin\theta/\lambda=0.594Å^{-1}$ were measured by using a Nonius CAD4 diffractometer with MoK$\alpha$ (0.71069 Å) radiation in the $\omega$-2$\theta$ scan mode from a 0.3 *x* 0.35 *x* 0.35 *mm* single colorless crystal of prismatic shape. A number of 3756 unique reflections ($R_{int}$ = 0.094) were collected out of which 2202 are greater than 2$\sigma$(I). The (-7 0 1) and (-2 1 6) reflections were monitored during data collection to check crystal and instrument stability and no appreciable change in their intensities was detected. The unit cell parameters were refined by least-square refinement of the 2$\theta$ values of 25 strong well centered reflections in the range $13<2\theta<26$.

The refined unit cell dimensions are $a$ = 14.042(5), $b$ = 8.924(5), $c$ = 16.091(5) Å, $\beta$ = 94.410(5) , $Z$ = 4, the cell volume is $V$ = 2010.4 $Å^3$.

The structure was solved by direct methods with SIR97 [4] and SHELX97 [5] software**.**

Almost all the atom positions in the structure were obtained from an E map computed for the best set of phases. Some oxygen atoms from water molecules were subsequently located from difference Fourier maps. The ulterior least-square refinements with anisotropic temperature factors for all the atoms converged with R = 0.065 for the 2202 reflections exceeding 2$\sigma$(I). The H atoms of the nucleotide molecules and three O atoms from water molecules were automatically fixed and isotropically refined. The other ten water molecules in the unit cell were found to be disordered, generating alternative solvent layers between the nucleotide molecules. The final parameters for the non-H atoms and for the O atoms of the water molecules are listed in Tables 1 and 2, respectively.

**Table 1.**

Fractional coordinates (Å) and isotropic equivalent temperature factor ($Å^2$) with s.u. in parentheses

| | **Molecule A** | | | | **Molecule B** | | | |
|---|---|---|---|---|---|---|---|---|
| | **X** | **Y** | **Z** | **$U_{eq}$** | **X** | **Y** | **Z** | **$U_{eq}$** |
| P | 0.16982(19) | -0.0821(4) | -0.06485(17) | 0.0234(7) | 0.3933(19) | 0.1951(3) | 0.63979(17) | 0.0203(7) |
| N(1) | 0.8618(6) | 0.5176(12) | 0.7307(6) | 0.030(2) | 0.7820(6) | 0.0938(11) | 0.6595(5) | 0.026(2) |
| C(2) | 0.8592(8) | 0.5590(15) | 0.6479(7) | 0.026(3) | 0.8767(7) | 0.0448(15) | 0.6698(7) | 0.027(3) |
| O(2) | 0.9275(6) | 0.5240(12) | 0.6059(5) | 0.041(2) | 0.9296(5) | 0.0802(12) | 0.6147(5) | 0.039(2) |
| N(3) | 0.7854(7) | -0.3643(13) | 0.6134(6) | 0.032(2) | 0.9084(7) | -0.0284(12) | 0.7380(6) | 0.030(2) |
| C(4) | 0.7112(7) | -0.3303(13) | 0.6578(7) | 0.025(3) | 0.8471(7) | -0.0594(14) | 0.7956(7) | 0.025(3) |
| N(4) | 0.3614(7) | 0.2385(12) | 0.3806(6) | 0.034(3) | 0.8829(7) | -0.1280(12) | 0.8651(6) | 0.031(2) |
| C(5) | 0.7117(8) | -0.3676(15) | 0.7426(7) | 0.030(3) | 0.7498(8) | -0.0162(15) | 0.7862(7) | 0.029(3) |
| C(6) | 0.7864(8) | -0.4474(15) | 0.7759(7) | 0.031(3) | 0.7199(8) | 0.0563(15) | 0.7172(7) | 0.026(3) |
| C(1') | 0.0604(8) | -0.0741(15) | 0.2310(6) | 0.027(3) | 0.7490(7) | 0.1850(14) | 0.5880(6) | 0.023(2) |
| C(2') | -0.0009(8) | -0.4942(15) | -0.1611(7) | 0.030(3) | 0.6783(8) | 0.1108(14) | 0.5267(7) | 0.024(2) |
| O(2') | 0.0690(6) | -0.4029(10) | -0.1922(5) | 0.036(2) | 0.7239(5) | 0.0247(9) | 0.4687(5) | 0.033(2) |
| C(3') | -0.0377(8) | -0.1289(15) | 0.1098(7) | 0.030(3) | 0.6272(8) | 0.2486(13) | 0.4889(6) | 0.024(2) |
| O(3') | -0.1214(6) | -0.1793(12) | 0.1451(6) | 0.044(2) | 0.6849(6) | 0.3042(11) | 0.4269(5) | 0.039(2) |
| C(4') | 0.0439(8) | -0.2426(15) | 0.1207(7) | 0.029(3) | 0.6269(7) | 0.3577(14) | 0.5593(6) | 0.023(2) |
| O(4') | 0.1006(6) | -0.2012(10) | 0.1960(5) | 0.0319(19) | 0.7020(5) | 0.3088(9) | 0.6203(5) | 0.0288(18) |

| | Molecule A | | | | Molecule B | | | |
|---|---|---|---|---|---|---|---|---|
| | X | Y | Z | $U_{eq}$ | X | Y | Z | $U_{eq}$ |
| C(5') | 0.1082(9) | -0.2512(16) | 0.0504(7) | 0.035(3) | 0.5349(8) | 0.3644(14) | 0.6035(8) | 0.030(3) |
| O(5') | 0.1373(6) | -0.1051(9) | 0.0283(5) | 0.0307(19) | 0.5035(5) | 0.2165(9) | 0.6213(5) | 0.030(2) |
| O(I) | 0.0880(5) | -0.1335(9) | -0.1250(5) | 0.0294(19) | 0.3352(6) | 0.2475(10) | 0.5632(5) | 0.033(2) |
| O(II) | 0.1899(6) | 0.0814(9) | -0.0704(5) | 0.032(2) | 0.3748(6) | 0.2886(10) | 0.7161(5) | 0.032(2) |
| O(III) | 0.2579(5) | -0.1760(10) | -0.0739(5) | 0.0298(19) | 0.3838(5) | 0.0297(9) | 0.6582(5) | 0.0293(19) |
| Na(1) | 0.9163(3) | 0.4168(7) | 0.2672(3) | 0.0427(13) | 0.2778(10) | 0.279(2) | 0.0353(9) | 0.216(9) |
| Na(2) | 0.7664(3) | 0.1465(6) | 0.3426(3) | 0.0404(13) | 0.1729(4) | 0.1898(10) | 0.5252(3) | 0.069(2) |

**Table 2.**

Fractional coordinates (Å) and isotropic equivalent temperature factor ($Å^2$) with s.u. in parentheses for the oxygen atoms of the water molecules.

| | X | Y | Z | $U_{eq}$ |
|---|---|---|---|---|
| O(W1) | 0.7467(5) | 0.3619(11) | 0.2497(5) | 0.040(2) |
| O(W2) | 0.8063(6) | -0.0992(12) | 0.2994(6) | 0.047(2) |
| O(W3) | 0.9229(6) | 0.2336(12) | 0.3739(6) | 0.046(3) |
| O(W4) | 0.6046(8) | 0.0695(12) | 0.2315(7) | 0.065(3) |
| O(W5) | 0.3753(6) | 0.1765(12) | 0.8755(5) | 0.044(2) |
| O(W6) | 0.4992(6) | -0.1763(12) | 0.7343(5) | 0.043(2) |
| O(W7) | 0.2782(9) | -0.4706(13) | -0.0972(7) | 0.066(3) |
| O(W8) | 0.8874(7) | 0.6273(13) | 0.3479(6) | 0.056(3) |
| O(W9) | 0.5325(8) | -0.0234(15) | 0.8900(6) | 0.065(3) |
| O(W10) | 0.4105(8) | -0.2099(17) | 0.0388(8) | 0.081(4) |
| O(W11) | 0.4536(12) | 0.073(2) | 0.0975(9) | 0.115(6) |
| O(W12) | 0.9568(7) | -0.13711(7) | 0.4958(6) | 0.057(3) |
| O(W13) | 0.4228(6) | 0.3294(19) | 0.9945(6) | 0.106(7) |

## Conclusions

The 5'-CMP.$Na_2$ single crystall was grown from a mixture of water-methanol solution and crystallyzes in the monoclinic crystallographic system with four molecules per unit cell and the space group $P_{21}$. The unit cell parameters and the fractional coordiantions were determined.

## REFERENCES

[1] J. Hogle, M. Sundaralingam and J.H.Y. Lin, *Acta Cryst*. 1980, **B36**, 564-570.

[2] Y. Nishimura, M. Tsuboi, T. Sato, and K. Aoki, *J.Mol.Struct.*, 1986, **146**, 123-153.

[3] G.H. Stouth and L.H. Jensen, "X-Ray Structure Determination, a Practical Guide", 2nd Edition, The Macmillan Comp., New York, 1989

[4] A. Altomare, G. Cascarano, C. Giaccovazzo, A. Guagliardi, A.G.G. Moliterni, M.C. Burla, G. Polidori, M. Camalli, R. Spagna, SIR97, *A package for crystal structure solution by direct methods and refinement*, 1997, Univ. of Bari, Italy.

[5] G. M. Sheldrick, SHELX 97, *Program for crystal structure determination*, Univ. of Heidelberg, 1997, Göttingen, Germany.

# CRYSTAL STRUCTURE OF LANTHANUM SULPHATE ENNEAHYDRATE

**AL.DARABONT[1], C.NEAMTU[2], GH.BORODI[2]**

*[1]Faculty of Physics, "Babeş-Bolyai" University, 1 M.Kogalniceanu St., 3400 Cluj-Napoca, ROMANIA (e-mail: daal@physics.ubbcluj.ro)*
*[2]Institute of Isotopic and Molecular Technology, 65-103 Donath St., P.O.Box 700, RO-3400 Cluj-Napoca 5, ROMANIA (e-mail: cneamtu@L30.itim-cj.ro)*

**ABSTRACT.** The structure of lanthanum sulphate enneahydrate ($La_2(SO_4)_3 \cdot 9\ H_2O$) was determined by X-ray diffraction methods. Single crystals of appropriate dimensions ($1 \times 1 \times 0.5\ mm^3$) required for these studies were grown from solution by the slow evaporation of the solvent. The preliminary results show that the orthorhombic unit cell contains four formula units and its parameters are: $a = (9.597 \pm 0.05)$Å, $b = (9.957 \pm 0.05)$Å, $c = (17.483 \pm 0.05)$Å, $\alpha = \beta = \gamma = 90^o$.

## INTRODUCTION

We consider that the crystal structure determination and the study of the physical properties of lanthanum sulphate enneahydrate ($La_2(SO_4)_3 \cdot 9H_2O$) are of interest due to the surprisingly few data available in the literature regarding this compound. As a matter of fact, we found only one reference discussing the crystal structure of $La_2(SO_4)_3 \cdot 9H_2O$ [1].

The main fact that determined us to approach this subject was the big difference between the external shape (habitus) of the single crystals obtained by us (distorted octhaedra-like crystals) and the ones obtained by the authors of the above-mentioned paper (needle-like hexagonal crystals).

Another mentioning in the literature of this material was– in its single crystalline state – as a diamagnetic base for paramagnetic ions studied by EPR [2]. But an accurate interpretation of the EPR spectra of the doped $La_2(SO_4)_3 \cdot 9H_2O$ single crystals also demands an exact determination of the crystal structure.

## EXPERIMENTAL

### a) The preparation of the $La_2(SO_4)_3 \cdot 9H_2O$ single crystals

The first step we performed was the preparation of the polycrystalline $La_2(SO_4)_3 \cdot x\ H_2O$. The starting materials in this process were metallic lanthanum and diluted sulphuric acid. From the chemical reaction of these two components the wanted compound resulted.

The polycrystalline material was purified by repeated recrystallizations from distilled water.

The growth of relatively large and good-quality crystals from aqueous solutions takes place in two stages. First, a crystal nucleus (seed) must be formed, which then grows in a new solution to the desired dimension. Both the formation of the nucleus (seed) and its further growth are based on the relation between solubility and temperature. The nuclei are obtained from unstable solutions, from highly supersaturated solutions. The required supersaturation is, in this case, obtained by the evaporation of the solvent or by a constant increase of the temperature. These methods may be carried out in various ways.

We have produced seed crystals by the slow evaporation of the solvent. The saturated aqueous solution was prepared at room temperature. After several days small single crystals were formed in the solution. From these crystals we selected the ones of good quality and appropriate dimensions ($1 \times 1 \times 0.5$ mm$^3$) for the X-ray measurements.

**b) Crystal structure determination**

The single crystalline quality of the $La_2(SO_4)_3 \cdot 9H_2O$ crystals obtained by us was evidenced by X-ray diffraction methods such as the Laue method, the oscillating crystal method and the Weissenberg method.

The selected small single crystals were fixed on a goniometer head and oriented after one of the crystallographic axes with the help of the photographs obtained in the Kulpe-Schulz convergent camera (using hemicylindrical films) and the Kulpe device for the orientations correction.

The X-ray diffraction measurements were performed on a TUR MX61 apparatus. The crystals were illuminated with a monochromatic beam using the Fe $K_\alpha$ radiation ($\lambda$= 1.9728 Å).

**RESULTS**

Figure 1 shows relatively large $La_2(SO_4)_3 \cdot 9H_2O$ single crystals obtained from solution by the slow evaporation method using seed crystals. For the X-ray diffraction measurements, smaller crystals were used.

The single crystals were at first oriented in a direction of a given symmetry (crystallographic axis) by the Kulpe method.

After the accurate orientation was established, we determined the value of the lattice constant in this direction (for instance *a*) using the rotation pattern. From the as-obtained diffraction pattern we calculated the lattice constant *a*: $a = (9.51 \pm 0.05)$Å.

For the same orientation, using the Weissenberg method, we determined the other two lattice constants: $b = (9.84 \pm 0.05)$Å, $c = (17.40 \pm 0.05)$Å and the angle between them: $\alpha = 90^o$. These values were obtained from the reciprocal lattice constants $b^*$ and $c^*$, the reciprocal lattice being represented on the basis of the Weissenberg pattern.

**Fig. 1.** $La_2(SO_4)_3 \cdot 9H_2O$ single crystals grown from solution by the slow evaporation method.

In order to obtain a consistent set of lattice parameters, measurements were performed also for different orientations of the crystal along the other two crystallographic axes *b* and *c*.

When the crystal was rotated about the *b* axis, from the resulted pattern we obtained $b = (9.96 \pm 0.05)$Å. In this case the Weissenberg pattern gives the following values for *a* and *c* and for the $\beta$ angle between them: $a = (9.60 \pm 0.05)$Å, $c = (17.64 \pm 0.05)$Å, $\beta = 90^o$.

When the crystal was rotated about the *c* axis, the rotating pattern gives a value for c: $c = (17.51 \pm 0.05)$Å. The Weissenberg pattern gives for *b* and *a*: $b = (10.00 \pm 0.05)$Å, $a = (9.64 \pm 0.05)$Å and for the angle between them $\gamma = 90^o$.

From these values and using the experimentally determined value of the density, $\rho = 2.7953$ g/cm$^3$, we deduced that the unit cell contains 4 molecules of $La_2(SO_4)_3 \cdot 9\ H_2O$.

From the above mentioned results we concluded that the unit cell structure contains the following components: 8 $La^{3+}$ ions, 12 $SO_4^{2-}$ ions and 36 $H_2O$ molecules. The possible positions of these ions and molecules in the unit cell of $La_2(SO_4)_3 \cdot 9H_2O$ are presented in Figure 2.

The real space group and the exact position of the structural elements in the unit cell can be determined only if the intensity data are automatically collected using a four-circle diffractometer.

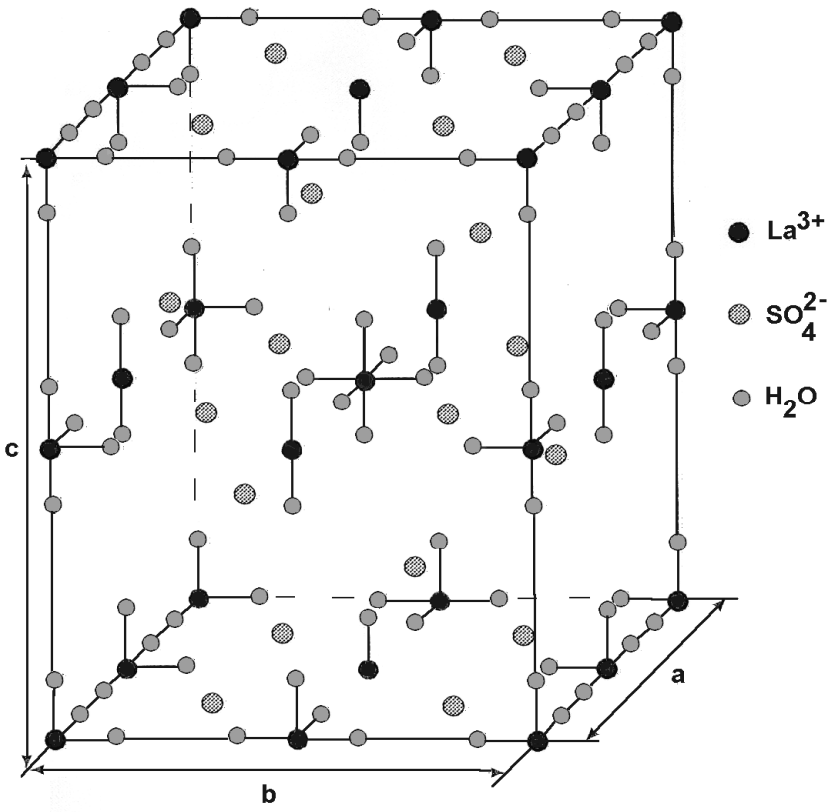


**Fig. 2.** The possible positions of ions and molecules in the unit cell of $La_2(SO_4)_3 \cdot 9\ H_2O$

## CONCLUSIONS

The above mentioned results show that the $La_2(SO_4)_3 \cdot 9\ H_2O$ single crystals prepared by us have indeed a different structure from the one mentioned in [1].

The crystallographic system of our crystals resulted to be orthorhombic, with a *C* type lattice. The Laue symmetry group is *mmm* and a possible space group that can be partially deduced from the systematic absences of the zero layer Weissenberg photographs is *C 2/c 2/c 2/a* .

## REFERENCES

1. E. B. Hunt, R. E. Rundle, A. J. Stosick, Acta Cryst. 7, 106-109 (1954).
2. D.R. Johnston, E.Y.Wong, J. Chem. Phys. **44** (7), 2693-2695 (1966).

STUDIA UNIVERSITATIS BABEŞ-BOLYAI, PHYSICA, SPECIAL ISSUE, 2000

# CONTROL AND DATA ACQUISITION SYSTEM FOR LABORATORY ANALYTICAL INSTRUMENTATION AND EXPERIMENTS

**M. KAUCSAR, H. BENDEA, D. VONICA**

*National Research and Development Institute*
*of Isotopic and Molecular Technologies,*
*P.O. Box 700, 3400 Cluj-Napoca, ROMANIA*

## 1. Introduction

In laboratory instrumentation and also in physical or in chemical experimental process studies the computerised control and data acquisition systems are one of the most important upgrade in our research activity. This allows translating the communication between man and instrument or man and process to a much higher level of human intelligence than before microcomputers were extended. In physics and in chemistry we deal with complex processes where the useful information results after acquiring and processing of a very large set of data. The use of personal computers (PC) is not only recommended but also indispensable.

## 2. Control and data acquisition system topology

Combining the features of the PC's with the one of distributed programmable microsystems in the studying of experimental processes or in the development of new scientific instruments we obtain many advantages. Distributed processing provides us speed and better reliability for the entire system. Depending on system requirements, a compromise between speed and reliability could be accomplished with an adequate hardware and software engineering. The topology of a complete control and data acquisition system is shown in figure 1. Multiple feedback control loops are closed using distributed programmable microsystems. A powerful PC controls the entire distributed microsystem structure. In this complex hardware and software configuration the PC is the master and the microsystems are the slaves. Interfacing an experimental process or a scientific instrument with such a master-slaves computing configuration is one of the most demanding steps in the whole system development. The first task is a logical separation of all functional units in the target controllable system. Depending on the acquired or/and controlled parameter each functional subassembly is equipped with proper sensors, transducers and actuators. Many controlled systems and instruments could be damaged when one or more functional parameter exceeds the maximum rating values. In order to avoid such undesired situations, apart from sensors used in feedback loops, the system is equipped with other transducers. These are intended to watch the maximum or minimum allowed limiting values. Therefore the entire controlled process or instrument will be completed with two very important functional blocks: one is the block of sensors and the another is the block of actuators. These are separated in the logical diagram but in reality they are integrated with the controlled system. All the sensors and actuators must be installed according to the theoretical background and mathematical model of the entire controlled system.

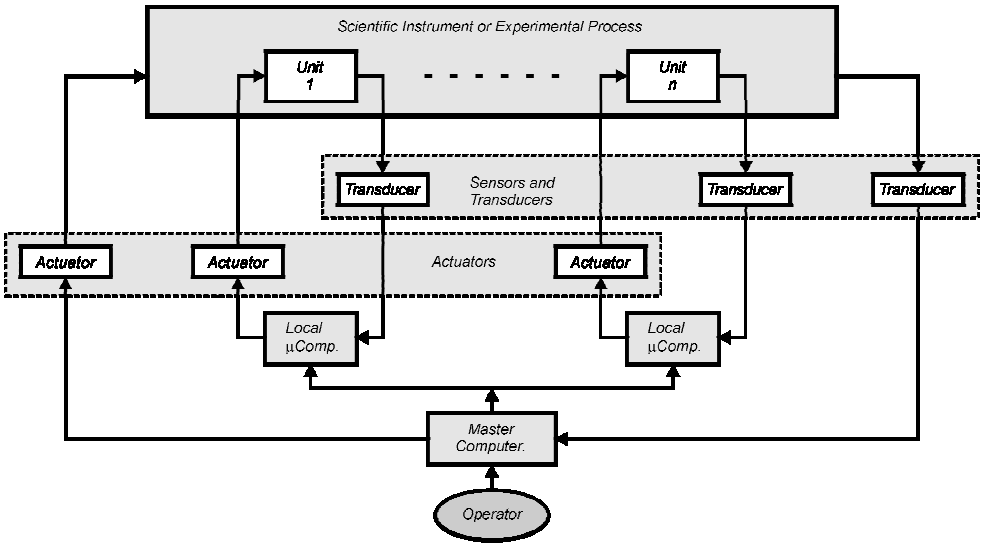


**Fig. 1.** Simplified block diagram of the control and data acquisition system for laboratory analytical instrumentation and experiments

The type of microcomputer was chosen to be appropriate to the task complexity of the correspondent loop and the speed's demands for proper real time functionality. For medium complexity and medium speed is recommended to use microcontrollers, which allow an easy implementation of a local feedback loop with minimum hardware effort. For higher speed and complexity the most suitable are microprocessors (CPU's) from Intel or Zilog. In special situations with very high-speed signals, the choice is DSP (Digital Signal Processor).

The master PC correlates all functional tasks executed individually by the slave microsystems and also implements a friendly interface between the controlled system and the operator. For this purpose is essential to implement a proper communication protocol between the master PC and the distributed slave microsystems. We prefer to use the standard serial communication protocols such as EIA/TIA-232-E, RS-485 or the instrumentation standard communication GPIB-488. It is possible to apply a special bilateral data transmission with the parallel LPT port but only if it has EPP or ECP capability.

## 3. Microcomputer with extended input/output capability – the hardware

The general block diagram of the microsystems and the main computer is represented in figure 2. Every PC is equipped with standard input/output hardware, but in order to use them in complex feedback loops extra input/output hardware must be added. The microsystem with extended analog and digital input/output capability is fitted with dedicated input/output module cards. Depending on the

operating principle of the detectors and actuators the signals involved in the whole system could be analog or digital. The majority of the sensors and transducers provide us analog signals and only a few of them have digital output. The second case is typical for transducers specialised mainly for detecting the level of a parameter. When its output is a logical true level the system works properly. Actuators also need analog or digital control signals, corresponding to their operating principles.

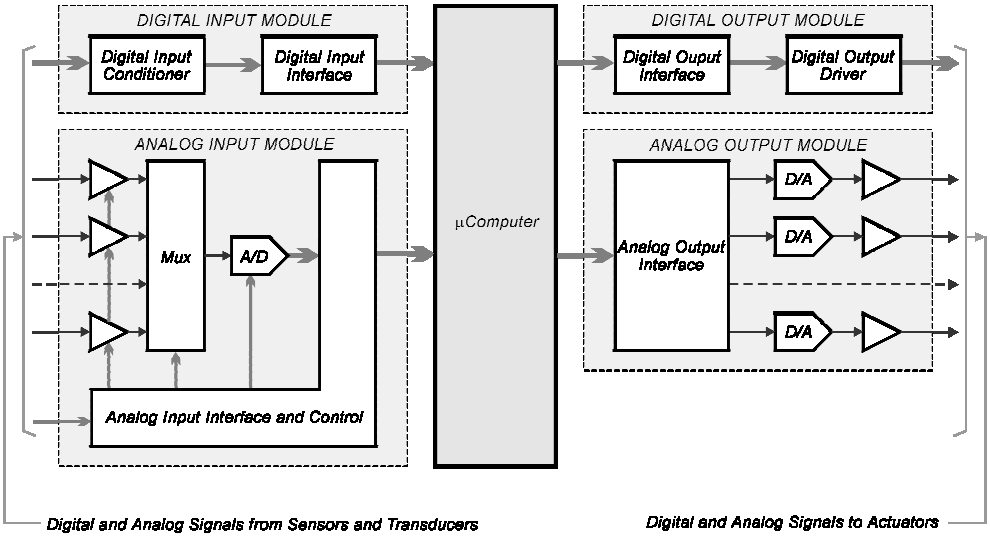


**Fig. 2.** Generalised configuration of the microcomputer with extended input/output capability

### 3.1. Digital input module

Digital signals can be very easy interfaced with any digital microcomputer, therefore the use of digital data is preferred. On the other hand the transmission of digital data is much more reliable than the one of analog transmission, especially in noisy environment. These considerations make us to use transducers with direct digital output where possible. In order to turn to the digital transmission, transducers with analog output placed at long distance from the PC are equipped with local A/D converters. Digital data transmission uses both types of transmission: parallel and serial. With digital parallel data we can accomplish higher bandwidth but at a higher price. Serial formats lead to a lower cost and also offer a more simple way for galvanic separation.

The standard logical signal levels must be applied in every digital transmission. Therefore sender and receiver is equipped with level converters. At receiver the digital noise is eliminated with Schmidt triggers. In special situations, when the sender and the receiver must be galvanically separated, at receiver the input circuits are equipped with optocuplers.

### 3.2. Analog input module

A large number of sensors deliver information carried by analog signals. The main task of this module is to convert the analog input signals to a digital one, making them compatible with further digital processing with computers. If the sensor is not very far from the microcomputer we prefer not to fit every sensor with an expensive A/D (analog to digital) converter. Instead of it we use an A/D card with multiplexed analog inputs and only one converter. In special cases when high acquisition speed and also high accuracy is needed, we apply the expensive solution: each analog input equipped with its own A/D converter and multiplexing in digital signal way. The A/D converter type is chosen according to the speed demands. For higher speed signals we use successive approximation converters and for lower speed dual slope converters. If high accuracy at medium speed is imposed a delta-sigma converter is the best choice.

Analog signals delivered by transducers have various voltage and current levels, depending on their constructive aspects. For optimum accuracy of the A/D conversion we must match these levels with converter input specifications. In order to translate the output range of a transducer to the input range of the A/D converters analog signal conditioners are applied. These circuits accomplish filtering (antialiasing), amplifying and shifting tasks for the given signal. The antialiasing filter is a low-pass filter with cut-off frequency matched with the Nyquist frequency of sampled analog signal. The level of the signal is adjusted to the desired value through software with digitally programmable gain amplifiers.

### 3.3. Digital output module

The digital output module is designated for actuators with digital control inputs. From this category the most widespread are the bipolar on-off regulating elements. Output voltage and current levels, from the basic components of the digital output module, usually don’t match the actuators’ requirements. Therefore we use power drivers. Several drivers were realised: open collector drivers for general purpose, relay output drivers and AC output drivers. The open collector driver is realised also with optocoupler galvanic isolation. The driver for AC lines is also provided with optocoupler separation and with a zero crossing circuit for minimum electromagnetic switching noise.

### 3.4. Analog output module

The analog output module delivers control signals for analog input type actuators. Complex waveforms, needed for testing and characterising the system, can be generated with this module. The basic components of these modules are D/A (digital to analog) converters. In order to assure required voltage and current levels needed by actuators and by signal generators, high precision power amplifiers follow the D/A converters with increased output swing capability.

## 4. The software

Because each feedback loop is closed through a local microcomputer system, proper real time data acquisition and control routines are implemented on each microcomputer system. The master-slave communication needs communication protocol routines. These are implemented on the master PC and on each slave microsystem. On the master PC are implemented the most sophisticated friendly operator interfacing routines.

## REFERENCES

1. Duncan, F.G., Microprocessor Programming and Software Development, Prentice/Hall International Inc., London 1980.
2. Tietze, U., Schenk, Ch., Halbleiter schaltungstechnik, Springer Verlag, Berlin – Heilderberg 1990.
3. Norton, P., Eggebrecht, L.C., Clark, S.H.A., Peter Norton's Inside the PC, Sams Publishing 1996.
4. Schildt, H., C++ The Complete Reference, Osborne Mc-Graw Hill 1995.
5. Oppelt, W., Kleines Handbuch technischer Regelvorgange, Verlag Chemie GMBH, Weinheim/Bergstrasse.

STUDIA UNIVERSITATIS BABEŞ-BOLYAI, PHYSICA, SPECIAL ISSUE, 2000

# IN VITRO ERYTHROCYTE AGEING IN ZERO MAGNETIC FIELD

**D CIORBA*, V.V.MORARIU****

**Clinical Biochemistry Laboratory, Moţilor Street, No 19, Cluj-Napoca, Romania*
*** National Institute for Research & Development of Isotopic and Molecular Technology, P.O. Box 700, R 3400, Cluj-Napoca, Romania, e-mail: vvm@L40.itim-cj.ro*

## Purpose

The natural magnetic field or the geomagnetic field (GMF) is a physical factor of the normal environment. The natural variations of this field can affect the health of man. Consequently we may expect that the lack of GMF or zero magnetic field (ZMF) could influence the living processes as well, possibly even more than the present fluctuations of GMF. At the same time it is possible that ZMF may have qualitatively different effects compared to the geomagnetic storms, or at least we may address this question.

The purpose of our work was to investigate the influence of ZMF on several elementary cell processes after in vitro exposure of human blood to ZMF. We have investigated the alteration of the $Na^+$-$K^+$ ATPase and $Ca^{2+}$ ATPase function by measuring the change of the ion concentrations in the serum as well as the ratio of amino transferase-TGO and alanin amino transferase- TGP activities.

## Methods

Human blood was collected by venipuncture from apparent healthy donors. After coagulation and centrifugation, the following assays were performed in the serum, by using a Beckmann CX5 autoanalyzer: sodium, potassium and calcium concentration as well as the activity of TGO and TGP. The determinations have been performed on samples of blood exposed up to 72 hours at room temperature, at 24 hours time interval.

## Results

Sodium concentration in the serum steadily decreased in the serum while potassium increased as a result of the decreased ion pump activity at room temperature. However in ZMF conditions this process was significantly faster than for controls.

At the same time calcium concentration in the serum decreased as a result of penetration into the blood cells which in turn is possibly due to the lower activity of calcium ATPase induced by ZMF.

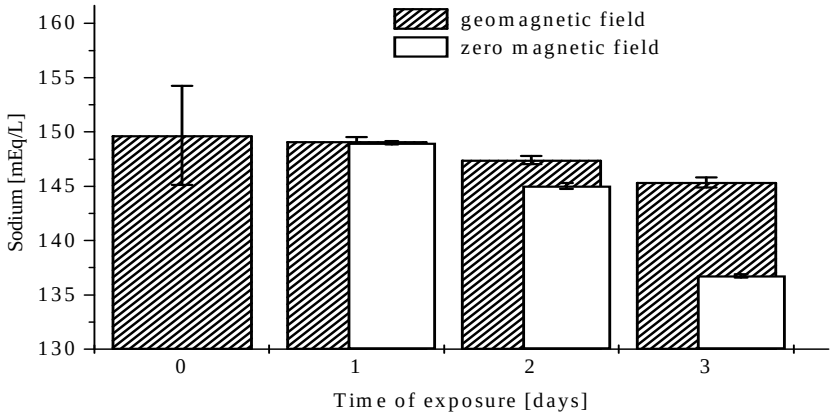


**Fig.1.** Effect o zero magnetic field exposure on the sodium concentration in blood serum

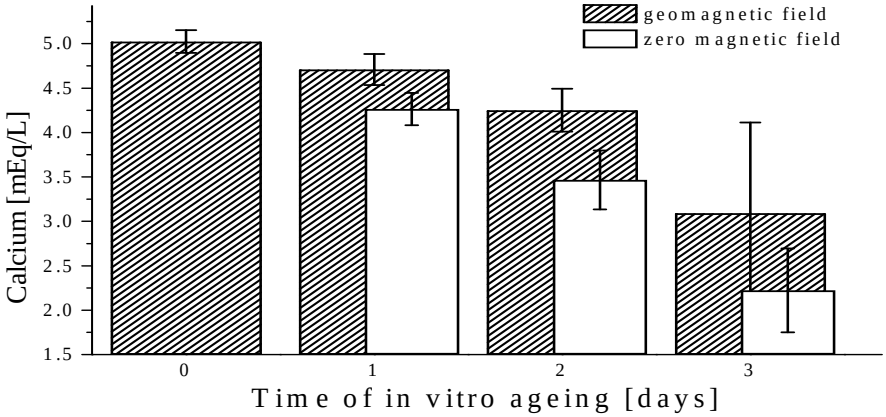


**Fig.2.** Effect of zero magnetic field exposure on the potassium concentration in the blood serum

The effects are summarized in fig.4 which shows that exposure to zero magnetic field has relative important effects. Included are also other observations about Fe and pH, which have not been mentioned in the text. The presence of a relative large quantity of Fe in the serum represent further evidence for an increased hemolysis which is a consequence of the ion disturbed balance in erythrocytes.

It has also been found that the TGO/TGP ratio increase by up to 33% after three days of exposure to ZMF conditions. The faster decrease of TGP activity, suggests that ZMF caused increased cellular death. This result is in agreement with the above findings related to the change of ion concentration in the serum due to disturbed balance between serum and cells.

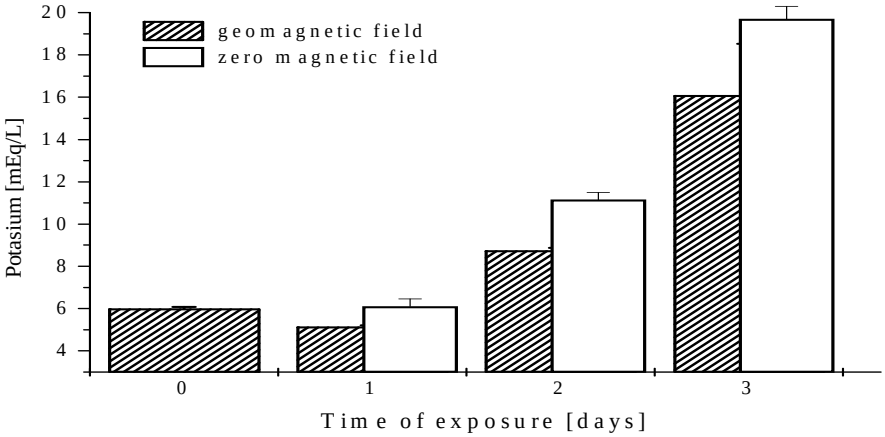


**Fig.3.** Effect of zero magnetic field exposure of blood serum on the calcium concentration

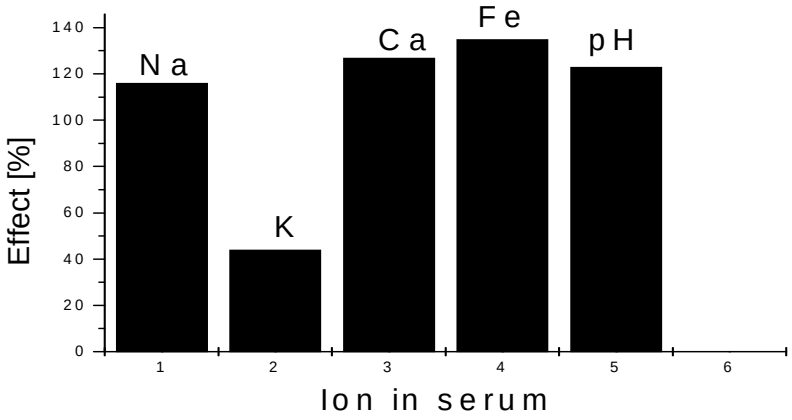


**Fig. 4.** A summary of the effect of zero magnetic field exposure on the rate of change of ion concentration in the blood serum

The whole experiment seem to suggest that the effects represent a result of the alteration of the enzymes activities both in the cell membranes and within the cell. Consequently the ion balance is modified such as to increase the rate of cell aging and final increased hemolysis.

A search of the literature revealed that exposure of enzymes or other proteins to an abnormal magnetic environment, i.e. different to the geomagnetic field, may alter their functional role and therefore our results are on similar line.

## Conclusions

In vitro exposure of human blood to zero magnetic field conditions leads to a significant decrease of the sodium-potassium and calcium ATPase activities as well as of transaminase activities. This implies that in vitro cell ageing and death proceed faster in ZMF compared to natural magnetic conditions. The results may be relevant to in vivo exposure of organisms to ZMF where a similar trend could hold.

STUDIA UNIVERSITATIS BABEŞ-BOLYAI, PHYSICA, SPECIAL ISSUE, 2000

# AN ATTRACTOR CONTROLS THE SPATIAL FLUCTUATIONS OF HUMAN LYSOZYME

**ADRIANA ISVORAN, V. V. MORARIU***

*West University of Timisoara, Faculty of Physics, 1900-Timisoara, Romania, E-mail: adii@galileo.uvt.ro*
**National Institute for R&D of Isotopic and Molecular Technologies, P.O. Box 700, Cluj-Napoca 5, Romania*

## 1. Introduction

The study of the relationship between the structure and the function of proteins is one of the most important tasks of biochemists and biophysicists. Enzymologists have developed methods for studying this relationship that were applicable to study the mechanism of catalysis. However, it has not existed a satisfactory explanation of this phenomenon. A possible explanation could be a special vibrational coupling under the control of an attractor (Havsteen, 1989).

The involvement of deterministic chaos in the function of enzymes have been detected before for chymotrypsin catalysis (Havsteen, 1989, 1991), oxygen-myoglobin binding (Havsteen, 1989) and for human lysozyme when it reacts with tetra-acetylchitotetraose (Isvoran et all. 1998). In the previous study for human lysozyme, the changes in the temperature factors of the amino acids were used as flexibility parameters and it was detected an attractor with the dimension 2.4±0.29 (Isvoran et all, 1998). In this study we have used as flexibility parameters the changes in the spatial coordinates of the lysozyme when it reacted with tetra-acetylchitotetraose. This study had the advantage of a better resolution because the number of data is much greater. The result obtained here has been compared with the previous result.

## 2. Method

The involvement of deterministic chaos in the biological function of human lysozyme was analyzed by using methods of linear and non-linear analysis: the power spectrum, the autocorrelation function, the calculation of the integral correlation function, the Poincaré plot and the Lyapunov exponents (Arghyris, 1994). In these analysis we have used the changes in the spatial coordinates between the free human lysozyme and its complex with tetra-acetylchitotetraose.The values for the spatial coordinates of the atoms for the enzyme and for its complex were obtained from the Protein Data Bank of Brookhaven National Laboratory (code entry 1LZ1, 1LZR).

3. Results

The autocorrelation functions for the changes in the x, y and z coordinates show the damping expected from the control of the attractors (not shown). The Poincaré plots ($x_{i+1}$ versus $x_i$), that are the projections of the attractors in plane, show domains that are preferentially occupied, see Fig.1.

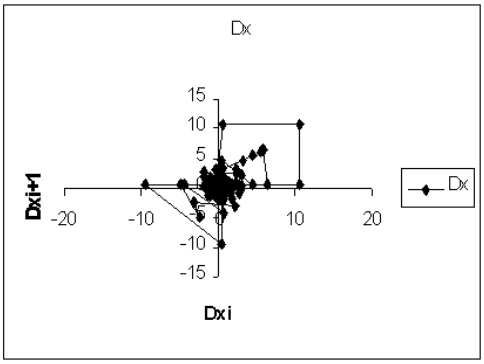


Fig. 1.a

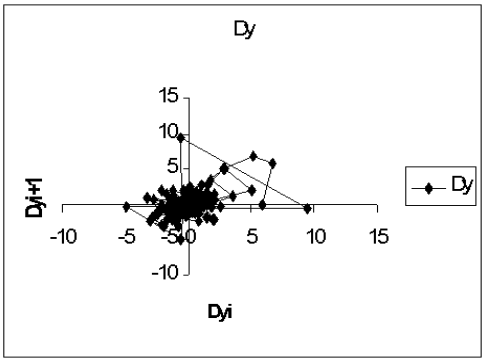


Fig. 1.b

**Fig.1.** The Poincaré plot for the differences in x-coordinates (a), y-coordinates (b)

The strongest indicator of the presence of the attractor is the saturation of the integral correlation coefficient with increasing the number of coordinates in phase space. If we increase the embedding dimension, n, and the gradient of the curves $lnC(r)=d|lnr|$ reach a saturation for relatively small n-values, then an attractor exists for the given series of data points (Arghyris et all., 1994). For the changes in x-coordinates the saturation value is 1.81±0.16 under the control of 5 parameters (fig. 2.a), for the changes in y-coordinates it is 1.88±0.1 under the control of 4 parameters (fig. 2.b) and for the changes in z-coordinates it is 2±0.09 under the control of 5 parameters (fig. 2.c).

The power spectrum is defined as the Fourier transform of the autocorrelation function. Although the autocorrelation function and the power spectrum are equivalent representation of the same process, they reveal quite different characteristics of initial state. The autocorrelation reflects the memory and inner connections of the system whereas the power spectrum informs about basic frequencies. The power spectrum must be broad in order to allow for the existence of an attractor. The reprezentation of the power spectra in log-log scales and the linear fitt of them show broadbands profiles with $1/f^{\alpha}$-like distributions: $1/f^{0.6}$ for the changes in x-coordinates, $1/f^{0.31}$ for the changes in y-coordinates and $1/f^{0.23}$ for the changes in z-coordinates (shown below for the x coordinate only). These distributions are specific for chaotic processes (Goldberger et all., 1986, Ikeguchi and Aihara, 1997).

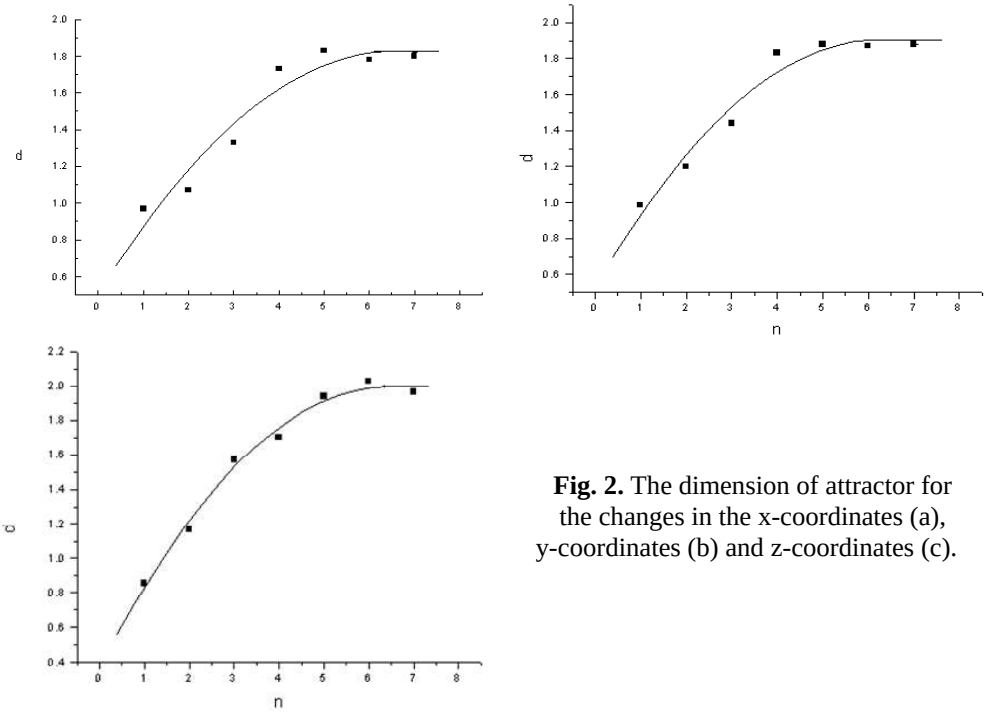


**Fig. 2.** The dimension of attractor for the changes in the x-coordinates (a), y-coordinates (b) and z-coordinates (c).

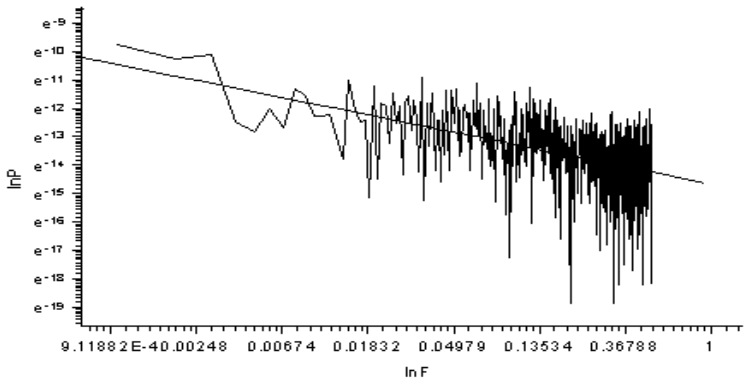


**Fig.3.** Power spectrum of the fluctuations of the x coordinate

The concept of Lyapunov coefficients allow us to make statements regarding the stability of given trajectories. A positive Lyapunov coefficient characterizes the exponential divergence of the trajectories (Arghyris, 1994). The Lyapunov coefficients for the changes in the X coordinates of human lysozyme are shown in the figure 4.

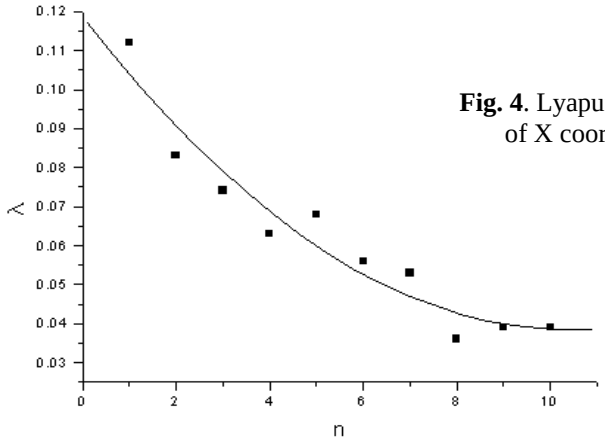


**Fig. 4**. Lyapunov coefficients for the changes of X coordinates of human lysozyme

## 4. Discussion

The results presented here indicate that an attractor controls the spatial fluctuation of human lysozyme when it reacts with TAC. The changes in all the coordinates (x, y and z) are controlled by regular attractors with almost the same dimension: 1.81±0.16 for the changes in x-coordinates, 1.88±0.1 for the changes in y-coordinates and 2±0.09 for the changes in z-coordinates. These dimension are in good agreement with the condition $d \leq 2 \lg N$, were N is the number of data points (Arghyris et all., 1994). The agreement between these dimensions supports the validity of hypothesis of an attractor control. This result comes to confirm the previous result, i. e. an attractor with the dimension 2.4±0.29 that controls the coupling between the molecular vibrations of human lysozyme when it reacts with TAC (Isvoran et all, 1998). It also has the advantage of a better resolution because the number of data used here is much greater.

There are in the literature many other studies in this field. Some of them are the following:

- for chymotrypsin catalysis, a regular attractor with the dimension 1.8±0.2 and a stochastic attractor with the dimension 0.86±0.03 were found (Havsteen, 1989, 1991),
- for the digoxin binding to the specific antibody, an attractor with the dimension 4.0±0.1 in the light chain and one with the dimension 5.7±0.7 in the heavy chain were determined (Havsteen, 1997).

- the vibrational properties of the catalytic H-chain and of a non-catalytic L-chain for an esterolytic antibody are characterized by an attractors with the dimensions 3.0±0.3 for H-chain and 7.5±0.5 for L-chain (Havsteen, 1999),
- for the four Japanese vowels (/a/, /i/, /u/, /e/ ) vocalized by a male subject were determined attractors with dimensions: 2.2-2.4 for the vowel /a/, 2.0 for the vowels /i, /u/ and /e/ (Ikeguchi and Aihara, 1997 a),
- attractors with different dimensions, 2.0 and 1.5 respectively, were obtained for two pulse waves in human finger capillary vessels recorded under two different conditions from the same subject: the subject takes a rest and the subject just finished a physical task (Ikeguchi and Aihara, 1997 a).

In conclusion we take in consideration all these results presented here, we can notice the possible biological role of deterministic chaos.

*Acknowledgements: The authors wish to thank Professor Bent Havsteen for useful discussions and suggestions.*

## BIBLIOGRAPHY

[1] Havsteen B. H., 1989, A new principle of enzyme catalysis: coupled vibrations facilitate conformational changes, J. theor. Biol., **140**, 101-127

[2] Havsteen B. H., 1991, A stochastic attractor participates in chymotrypsin catalysis. A new facet of enzyme catalysis, J. theor. Biol., **151**, 557-571

[3] Havsteen B. H., 1997, Attractor control of the binding to digoxine to a specific antibody, J. theor. Biol., **189**, 367-376

[4] Arghyris J., 1994, An exploration of chaos, North-Holland Ed., 127-182

[5] Goldberger L., West B. J., 1986, Chaos in physiology: health or disease?, NATO ASI Series A: Life sciences, Plenum Press, New York, **138,** 143-156

[6] Ikeguchi T., Aihara K., 1997, Difference correlation can distinguish deterministic chaos from $1/f^{\alpha}$-type colored noise, Phys. Rev. E, **55**, no. 3, 2530-2538

[7] Ikeguchi T., Aihara K., 1997 a, Estimating correlation dimensions on biological time series with a reliable method, J. Intelligent &Fuzzy Systems, **5**, 33-52

[8] Havsteen B.H, 1999, An esterolytic antibody with vibrational properties of a catalytic H chain and a non-catalytic L-chain, J. theor. Biol.,**196**, 337-387

[9] Isvoran Adriana, Morariu V. V., Negreanu-Maior A., 1998, Attractor control of the coupling between the molecular vibration of human lysozyme upon substrate binding, Romanian Conference of Physics, Constanta

# EFFECTS OF RADIATION ON LACTATE DEHYDROGENASE

**A. HATEGAN, D. MARTIN, C. BUTAN, V.V. MORARIU***

*Institute of Atomic Physics, Electron Accelerator Laboratory, P.O.Box MG-36, R-76900, Magurele, Bucharest, ROMANIA, e-mail: ahateg@ifin.nipne.ro*
**National R&D Institute for Isotopic and Molecular Technologies, P.O. Box 700, 3400 Cluj-Napoca, ROMANIA*

**ABSTRACT.** Results on the influence of 6 MeV electron beam and 2.45 GHz 565 W microwaves as well as of the combined treatement, at -3 $^{o}$ C and -196 $^{o}$ C, on lactate dehydrogenase activity are presented. Our data showed a moderate inactivation of the electron irradiated lactate dehydrogenase, in the dose range (0-4.2 kGy). The microwave irradiated samples exhibited a non-linear behaviour (successive activation and inactivation of the enzyme molecules) suggesting the major influence of the nonthermal component of microwave radiation. The combined irradiation lead to similar behaviour of the enzyme as in the case of electron irradiation.

Key-words: lactate-dehydrogenase, electron irradiation, microwaves.

## INTRODUCTION

There is little information on enzyme inactivation with high LET radiations, and electron irradiation was used only in few studies /1,2,3,4/ and still the molecular mechanisms induced are not completely clarified /5,6/. Freezing the samples at low temperatures makes possible the determination of global non-thermal effects (specific effects induced by electromagnetic radiation interaction with the biosystem, distinct from the changes induced by heating that occurs in the irradiated samples/6/) of microwaves/6,7,8/ and the direct effects of electron irradiation (due to direct interaction radiation-biomacromolecule)/5/.

The aim of this paper is to study the direct effects of 6 MeV electron beam and 2.45 GHz microwaves, at -5 $^{o}$ C and -196 $^{o}$ C irradiation temperatures, on lactate dehydrogenase.

## METHODS

Crystallised lactate dehydrogenase in ammonium sulphate solution 3.2 M, pH aprox. 6 was diluted in the ratio 5 µl crystallised enzime/3 ml bidistilled water. 1 ml aliquots of the suspension were placed in thermoresistant plastic trays, for irradiation procedure. The samples were frozen at -3 $^{o}$C using an ethanol-ice bath, and at -196 $^{o}$ C by: a) rapidly immersing the samples in liquid nitrogen, b) freezing the samples at -3 $^{o}$ C (using an ethanol-ice bath) or c) at -10 $^{o}$ C (using a methanol-

ice bath) and afterwards immersing them in a liquid nitrogen bath.They were irradiated in a rectangular cavity designed to permit either electron beam irradiation only, or microwave irradiation only or simultaneous electron beam and microwave irradiation. A microwave generator with the power op to 850 W at 2.45 GHz is coupled to the rectangular cavity sidewalls by means of a floated waveguide system. Scanned electon beam from the ALIN 10 linac of 6 MeV (average intensity of 5-10 μA, frequency of the pulses 100 MHz, time of a pulse 5-10 μs) was introduced perpendicularly by the upper wall end of the thickness of 0.1 mm.y The monitor of the ionising chamber situated under the samples was calibrated in dose units using Fricke dosimetry before irradiation and the dose rate was estimated to be constant during irradiation.

Lactate dehydrogenase catalyses the hydrogen transfer reaction:

piruvate + NADH + $H^+$ <----------> lactate + $NAD^+$

The enzymatic activity of lactate dehydrogenase was determined by measuring the rate of extinction decrease at 340 nm of NADH accompanied by the reduction of pyruvate to lactate, according to the technique of Bergmeyer et al./9/.

## RESULTS AND CONCLUSIONS

Lactate dehydrogenase presents partial unfolding when freezing and thawing /10/, that leads to an irreversible loss of the enzymatic activity. The optimal procedure to prepare the frozen enzyme suspesions for irradiation seemed to be procedure c, which reduces the activity only to 82 %.

It is known that radiation inactivation of enzymes is mainly monoexponential with increasig the dose /1,5,11/. The total inactivation of frozen enzymes, due to direct effects of radiation is obtained for large electron doses as 10-50 kGy /5/. We choosed the electron dose range and irradiation time periods (the same for both radiations) so that the samples to remain in frozen state during microwave irradiation.

High energy electron irradiation of frozen lactate dehydrogenase at -3 $^o$ C and -196 $^o$ C, independent on the procedure of freezing in the dose range 0-350Gy and 0-4.2 kGy leads to a insignificant respectivelly moderate decrease (mainly down to 50% of the frozen enzyme activity) of the enzymatic activity (figures 1-3).

Microwave irradiation leads to variations of the enzymatic activity, presenting zones of activation of the enzyme molecules followed by zones of drastic decrease (figures 1-3), suggesting the major influence of the nonthermal component of microwave radiation. The most semnificative variations are presented by the samples irradiated at -3 $^o$ C (figure 1). The activation of enzyme molecules might be explained by radiation action on the inactive enzyme molecules present in the suspension (obtained inevitably by the standard procedure of enzyme separation from the tissues, and by freezing). Similar repeated results were obtained also for 400 W and 495W microwave powers,but not for 310W microwaves (data not presented here), indicating that the activation of frozen enzyme molecules takes place only at large power levels, the bigger the power level, the increased activation being obtained.

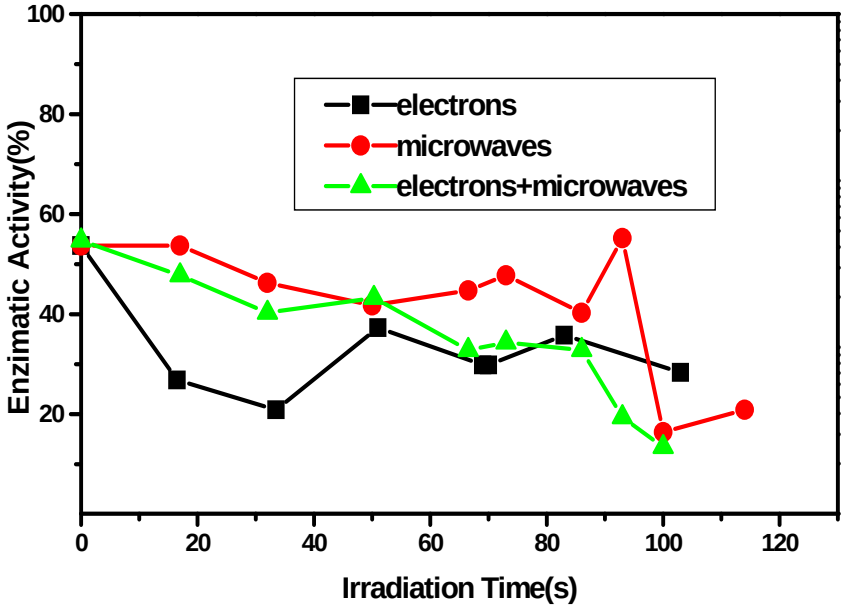


The combined irradiation lead to similar behaviour of the enzyme as in the case of electron irradiation.

Our data inform on electron beam and microwave radiations influence on the enzymatic activity loss during freeze-thawing, when the subsequent growth of the water crystals influences the two and three dimensional structure of the enzyme /10/. The system studied is very complex because of the superposition of freeze-thawing effects on the irradiation effects, both molecular mechanisms being incompletely clarified yet. Further studies are needed to clarify both aspects.

1. Effects of radiation on lactate dehydrogenase activity. The enzyme was frozen at –3$^{o}$ C before irradiation. Electron irradiation was performed at dose rate of 11 Gy/s.

2. Effects of radiation on lactate dehydrogenase activity. The enzyme was frozen at–196$^{o}$ C (two step technique: -3$^{o}$ C, -196$^{o}$ C) before irradiation. Electron irradiation was performed at dose rate of 43 Gy/s.

3. Effects of radiation on lactate dehydrogenase activity. The enzyme was frozen at –196$^{o}$ C (two step technique: -3$^{o}$ C, -196$^{o}$ C) before irradiation. Electron irradiation was performed at 350 Gy/s

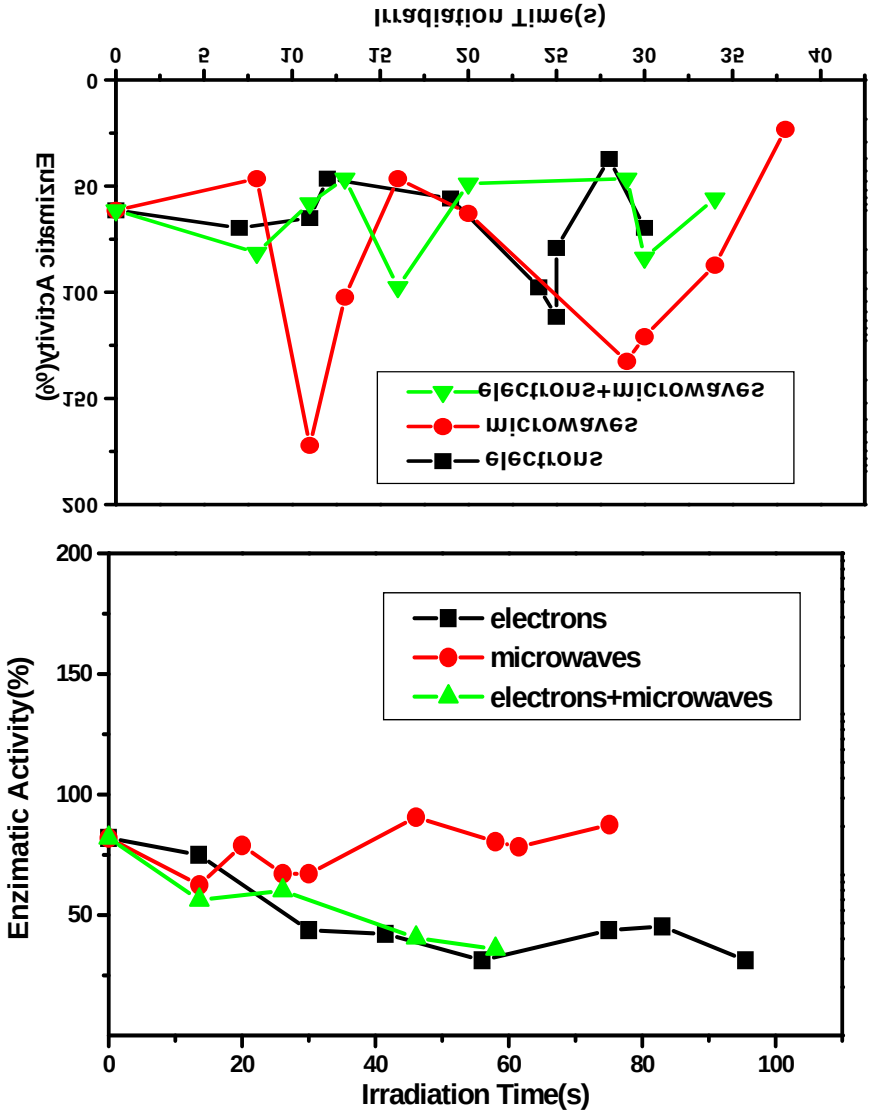


## REFERENCES

1. SAHA, A., P.C. MANDAL, S.N. BHATTCHARYYA, *Radiat. Phys. Chem.*,1995, **46**, No. 1, 123-145.
2. SCHUESSLER, H., A. HERGET, *Int. J. Radiat. Biol.*, 1980, **37**, no.1, 71-80.
3. WINSTEAD, J.A., *Rad. Res.*, **30**, 832-840.

4. WINSTEAD, J.A., T.C. REECE, *Rad.Res.*1970, **41**, 125-134.
5. KEMPNER, E. S., *Quarterly Reviews of Biophysics,*1993, **26**, I , 27-48.
6. G. LENAZ:*Encicl. Appl.Phys.*, E.S. Vera, VCH Publishers, USA (1991) p.13.
7. Y.A. KIM, S.S. FOMENKO, T.F. AGAFONOVA, I.G. AKOEV, *Bioelectromagnetics* **6** (1985) 305.
8. M. MARKOV, *Seminars in Biophysics*, **6** (1990) 159.
9. BERGMEYER, H.U., E. BERNT, B. HESS, Lactat dehidrogenase, in *Methoden der enzymatischen Analyse*, Ed. Bergmeyer, H.U., Verlag Chemie, Weinheim, 1962, 736-740.
10. STRAMBINI, G.B., E. GABELLIERI, *Biophys. J.*, 1996, **70**, 971-976.
11. A.HATEGAN, A.POPESCU, C.BUTAN, C.OPROIU, D. HATEGAN, V.V. MORARIU, *Czech. J. Phys.*, **49** (1999) 535.

STUDIA UNIVERSITATIS BABEŞ-BOLYAI, PHYSICA, SPECIAL ISSUE, 2000

# INFLUENCE OF MICROWAVES AND ELECTRON BEAMS ON RED BLOOD CELLS

**A. HATEGAN[1], D. MARTIN[1], C. BUTAN[1], A. POPESCU[1], C. OPROIU[1], V.V. MORARIU[2]**

*1. Institute of Atomic Physics, Electron Accelerator Laboratory, P.O.Box MG-36, Magurele, Bucharest, Romania*

*2. National R&D Institute for Isotopic and Molecular Technologies, CP 700, 3400 Cluj-Napoca*

**ABSTRACT.** The effects of 6 MeV electron beam ($0^o$ C) and of 2.45 GHz microwave ($-196^o$ C) at 0-850 W, as well as preliminary results of the combined treatment, on the osmotic fragility of human erythrocyte membranes are presented. The changes in the properties of the erythrocyte membranes were estimated by measuring the radiation induced haemoglobin release from the erythrocytes (hemolysis) and the osmotic fragility of the membranes, determined by postirradiation induced osmotic stress. We obtained no hemolysis induced by accelerated electrons in the range 0-400 Gy, whereas the microwave irradiated erythrocytes showed in the ranges (1-2 min) and (400-500 W ) values of very small hemolysis, down to 50% from the control. The osmotic stress experiments indicated a significant increase in osmotic fragility for 200 -400 Gy electron doses, whereas the 100 Gy irradiated sample showed a hemolysis down to 35% from the control. Similarly, the microwave irradiated erythrocytes showed values down to 60% from the control for (1min, 850W). Both radiations induced at definite parameters values of very small hemolysis, suggesting a stabilisation of the membranes and an increase in osmotic resistance. Our preliminary results on simultaneous irradiation of the frozen erythrocytes seem to indicate a significant contribution of microwaves in hemolysis evolution, while the successive irradiation procedure did not allow so far a clear interpretation, further studies being necessary to elucidate the membrane molecular mechanisms induced .

## INTRODUCTION

The actual experimental data provided by the scientific literature concerning the effects of microwave irradiation and combined microwaves with electron irradiation on the biological samples are controversial and the molecular mechanisms involved in the physico-chemical modifications that occur are not completely clarified [1]. Freezing of the samples at liquid nitrogen temperature makes possible the determination of the non-thermal effects of microwaves and the direct effects of electron irradiation on the biomembranes [1,5,6]. The temperature variations in the frozen state of the sample do not affect the erythrocyte membrane properties.

## METHODS

### Sample preparation

Human blood from a healthy donor stored for 3 days in a blood bank was washed three times according to a standard procedure with phosphate buffer solution 150 mM NaCl / 5 mM $K_2HPO_4$ / $KH_2PO4$ at pH 7.4. Packed erythrocytes obtained by this procedure were suspended at a final cytocrit of 16.66%. In the case of microwave irradiation, the packed erythrocytes were suspended at a final cytocryt of 16.66% in a crioprotectant buffer solution consisting of 28 g glicerol/2.8 g sorbitol/ phosphate buffer solution 150 mM NaCl / 5 mM $K_2HPO_4$ / $KH_2PO4$ at pH 7.4.

### Irradiation procedure

**Device:** The samples were irradiated by using: a rectangular cavity (RC) specially designed to permit either electron beam irradiation only, microwave irradiation only, or combined (simultaneous or succesive) electron beam and microwave treatement. Microwave power, up to 850 W at 2.45 GHz is coupled to the RC sidewalls via a slotted waveguide system. Scanned vertical 5 MeV electron beam of a linear accelerator with the following parameters: 5-10 MeV energy of the electron beam, average intensity of 5-10 uA, frequency of the pulses 100 MHz, time of a pulse 5-10 us was introduced perpendicularly by the upper end of 100 um thick.

**Temperature:** The samples were thermostatated at $0^o$ C using a ice-water bath, and at $-196^o$ C using a liquid nitrogen bath .

**Dosimetry:** The dose accumulated by the samples was estimated using Fricke dosimetry in calibrating the monitor of the linear accelerator.The dose rate was estimated to be constant during irradiation (2 kGy/min).

### Hemolysis Measurements

- The irradiation induced hemolysis was determined by measuring the hemoglobin released in the supernatant of the samples because of radiation action. This was achieved by measuring the optical absorbency of the supernatant solution at 540 nm and the results were reported to the total hemoglobin released by the control sample in the presence of distilled water.
- The osmotic fragility of irradiated erythrocytes was determined by measuring spectrophotometrically the hemoglobin loss in the supernatant of the erythrocytes exposed to osmotic shock by suspending them in solutions with different concentrations of NaCl. In the particular case of the microwave irradiated erythrocytes, the cells were washed to eliminate the protector solution, by using a standard procedure which consists of several centrifugations and resuspensions of the cells in buffer solutions of different osmolarities. Finally the cells were suspended in a buffer solution consisting of 150 mM NaCl / 5 mM K2HPO4 /

KH2PO4 pH 7.4, at a hematocrit of 6%, for each sample. The osmotic stress was performed by suspending 300 ul of every 6 % solution in 5 ml of buffer solution containing different NaCl concentrations (final cytocrit of 0.34 %). After 10 minutes necessary for osmotic stress results to be complete, the samples were centrifuged at 500 g for 5 min and the hemoglobin released in the supernatant determined spectrophotometrically. All the results were reported to the value of the maximum hemolysis obtained for the nonirradiated sample.

## RESULTS AND CONCLUSIONS

Our results showed no hemolysis induced by electron irradiation at $0^{o}$ C, in the dose range 0-400 Gy, indicating that the membrane modifications due to radiation interaction do not reach a critical point to cause swelling of the cells and consequent lysis.

The microwave irradiated erythrocytes showed in the ranges (1-2 min) and (400-500 W) values of very small hemolysis, down to 50% from the control (fig.1).

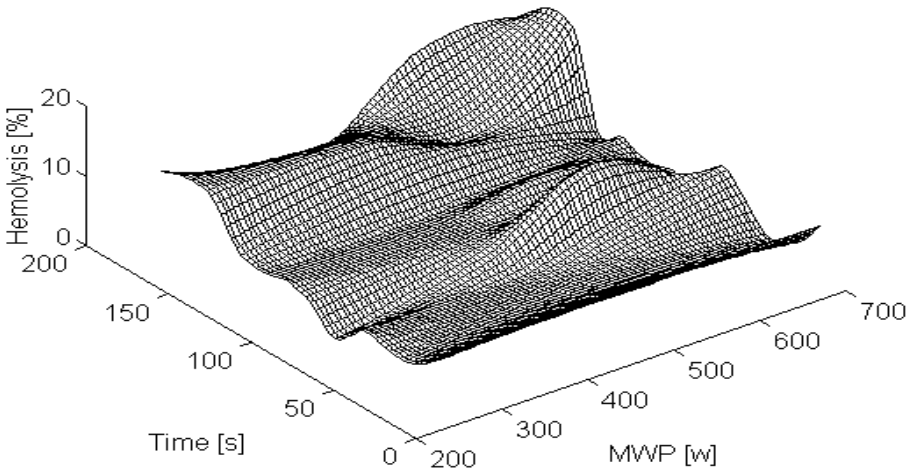


**Figure 1.** Hemoglobin loss from microwave irradiated erythrocytes at different exposure times and different power levels.

The influence of radiation is tested in the osmotic stress experiments performed after irradiation, which give information on the most resistant erythrocyte population in the samples.

The electron irradiated samples showed a drastic behaviour in the osmotic stress experiments (fig.2). They showed a hemolysis induced by the strongest osmotic stress with 75-85 % higher than in the control sample. In the case of a certain electron dose (100 Gy), the hemolysis degree was found much smaller than

for the control sample (35 % from the control, at the strongest osmotic stress). A similar behaviour of the erythrocytes was found in the case of microwave irradiation of the erythrocytes at subzero temperatures.

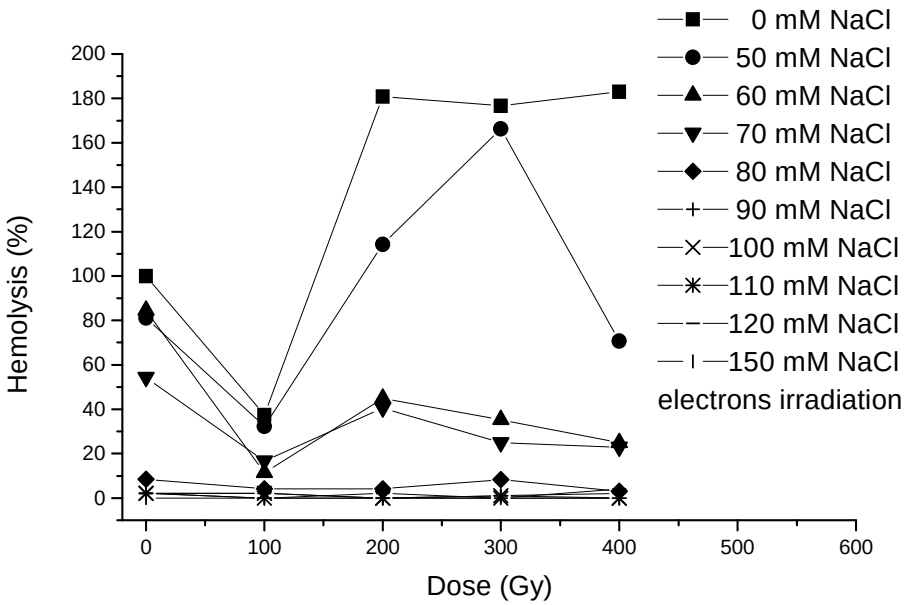


**Figure 2.** Influence of different electron doses on the osmotic fragility of human erythrochyte membranes.

The microwave irradiated erythrocytes at -196$^{o}$ C exhibited a similar behaviour with the electron irradiated red cells (fig.3). The samples irradiated for (1 min, 850W) showed a hemolysis degree of approximativelly 60 % from the control sample. In the case of microwave irradiation it can be assumed that this effect is due to the non-thermal component of electromagnetic radiation. Possible resonances at the molecular level also have to be taken into account for the explanation of the results obtained: the points of very small hemolysis might be seen as resonances at the molecular level, in response to irradiation time. They should be characterised by a "stationary state" of the membranes, that implies an increased resistance of the cells to osmotic stress.

The similarity between the results obtained in the case of electron irradiation at 0$^{o}$ C and microwave irradiation at -196$^{o}$ C, might suggest similar energy absorbtion into the samples,in the two different sets of irradiation conditions (liquid samples at 0$^{o}$ C and frozen samples at -196$^{o}$ C). Much more experimental data is necessary in order to clarify this similar behaviour, obtained for the two different radiations.

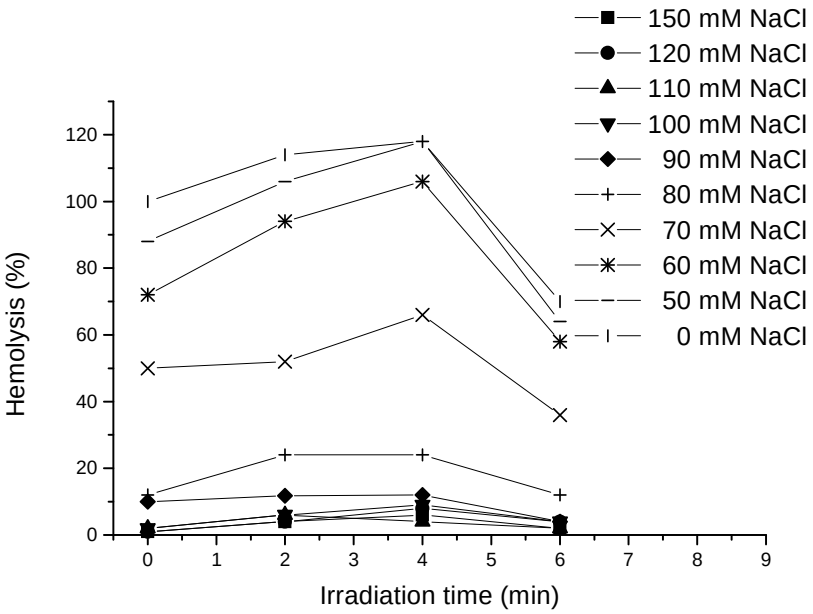


**Figure 3.** Influence of microwave irradiation time on the osmotic fragility of frozen human erythrocyte membranes**.**

Our preliminary results on simultaneous irradiation of the frozen erythrocytes (fig.4 a,b) seem to indicate a significant contribution of microwaves in hemolysis evolution, while the successive irradiation procedure (fig.5) did not allow so far a clear interpretation, further studies being necessary to elucidate the membrane molecular mechanisms induced.

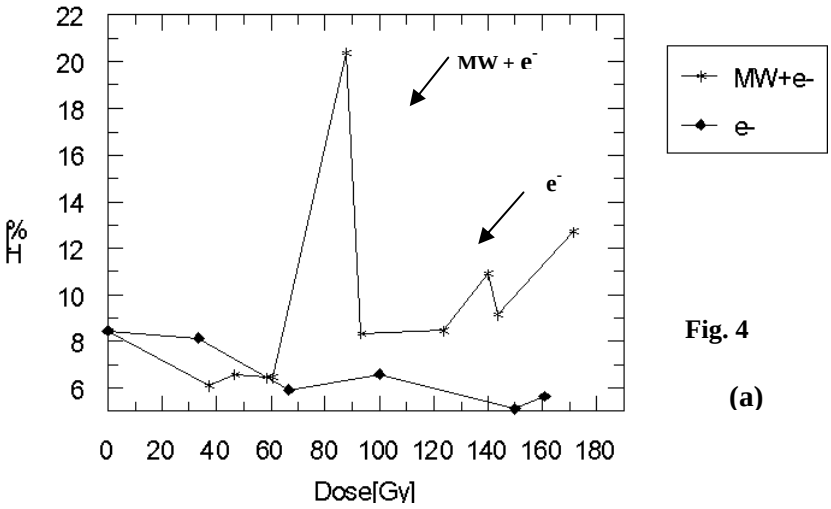


**Fig. 4**

**(a)**

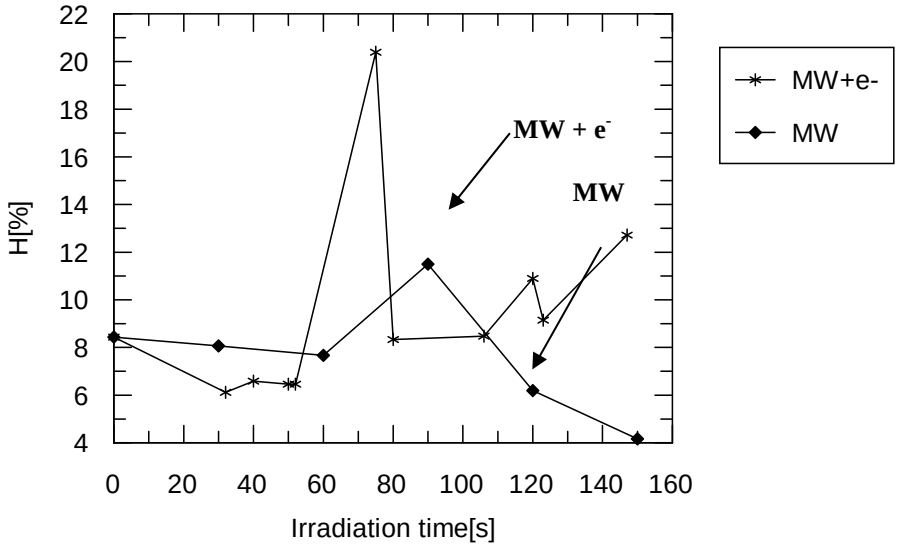


**(b)**

**Figures 4 a,b.** Hemolysis induced by simultaneous microwave and high energy electron irradiation of frozen erythrocyte membranes.

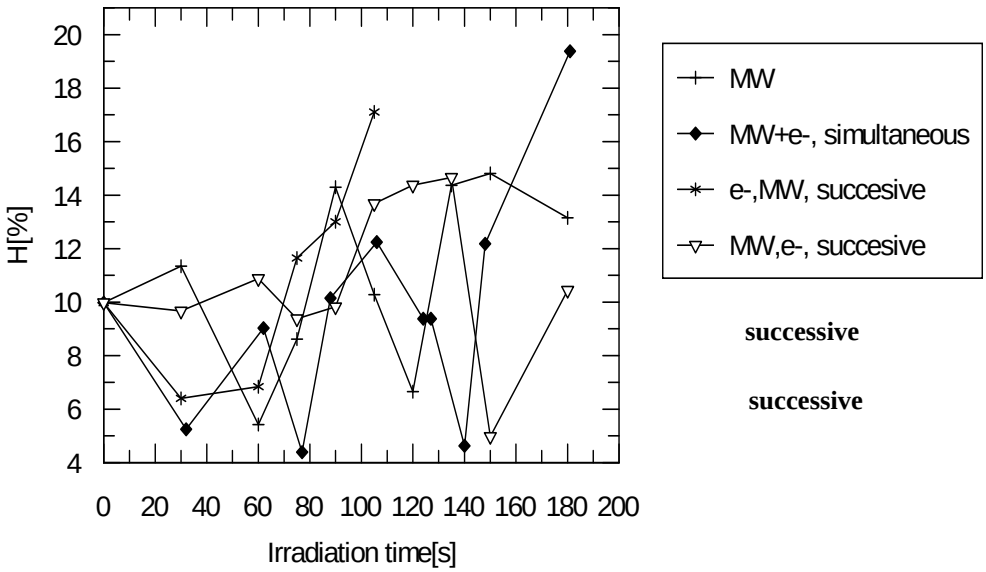


**Figure 5.** Hemolysis induced by simultaneous and successive microwave and high energy electron irradiation of frozen human erythrocyte membranes.

## REFERENCES

1. Kempner E., Quarterly Reviews of Biophysics, **26**, p.27 (1993).
2. Constantinescu A., Frangopol P., Bajenaru L., Niculescu M., Margineanu D., Biomed. Biochim. Acta, **46**, 1, p.67 (1987).
3. Constantinescu A., Bajenaru L., Frangopol P., Margineanu D.,Rev. Roum. Biochim., **23**, 2, p.97 (1986).
4. M. Mohora, R. Olinescu, I.Mihailescu, V. Dinu, Roum. J. Biophys.,Nr. 1, Vol. 3, p. 53 (1993).
5. J.P. Yee and H.C. Mel, Biophys. J., **16**, nr.2, part 2 (1976).
6. G. Kollmann, B. Shapiro and D. Martin, Rad. Res., **37**, p.551 (1969).

# CORRELATION OF THE GEOMAGNETIC ACTIVITY AND THE BETA GLOBULINS IN THE BLOOD SERUM OF HUMAN SUBJECTS

**CRISTINA DRAGU*, V.V.MORARIU**, DANIELA CIORBA*****

*National Institute for Research & Development of Isotopic and Molecular Technologies, Cluj-Napoca

** National Institute for Research & Development of Isotopic and Molecular Technology, R-3400 Cluj-Napoca, P.O.Box 700, vvm@L40.itim-cj.ro, and Faculty of Physics, Babes-Bolyai University, Cluj-Napoca,

***Clinical Biochemistry Laboratory, Moților Street, No 19, Cluj-Napoca

## Scope

The aim of the work is to establish whether solar activity and, implicitly the geomagnetic activity, over a period of one year, can influence the status of the blood serum proteins of human subjects. This investigation is part of a broader research project aiming to two fundamental questions: a) whether the normal healthy subjects are influenced by increased geomagnetic activity and b) to what extend subjects suffering from various diseases are sensitive to the geomagnetic activity. Finally, if the geomagnetic activity were indeed a factor of risk for health it would be desirable to alert people in advance for the increased health risk during the period.

We know by now that many aspects of the health status are influenced by increased geomagnetic activity manifested as magnetic storms. Some examples are: increased risk for heart infarct, depression, cognitive problems to only cite a few (Morariu, 1998; Morariu et al.1999).

## The design of the investigation

One way to approach the problem would be to select a few subjects with a known health status and monitor the serum proteins over a period of time, which would include a magnetic storm. While such an experiment is not impossible, it rises operative difficulties such repeated blood collection from the same patient and also "catching" a major magnetic storm.

An alternative would be an exploratory investigation on all data obtained in a clinical laboratory where five days a week, several tens of patients are received. The disadvantage is that a multitude of cases is involved including various ages, sexes, and pathologies. This information cannot be practically included afterwards in the data analysis. However such an investigation could possibly offer an answer on whether the average clinical data are sensitive to the geomagnetic activity. We have chosen this second alternative for the present work.

Further we know that the geomagnetic activity is increased during the spring and the autumn, therefore we search for effects during these seasons. The solar activity is on the rise of its 23 cycle.

## Materials and Methods

The investigation was carried out on the clinical data obtained at Biochemistry Laboratory of the State Polyclinic of the city of Cluj-Napoca. While the project involves the correlation of a large number of blood characteristics with the geomagnetic activity, the present communication refers only to the beta globulin fraction of the serum proteins. The investigation was carried out for the clinical data recorded in 1998.

Human blood was collected by venipuncture from the incoming ambulatory patients and the serum proteins (albumin, alpha, beta and gamma globulin) have been analysed by electrophoresis. A daily average of each of the serum protein was calculated. It is understood that no data were available for the weekend days as well as for some holidays. These data have been compared to the daily average magnetic activity as measured by the Ap index.

The 1998 geomagnetic activity has been extracted from the data base of US National Geophysical Data Center.The sun spots number, which is a measure of the solar activity has been downloaded from NOAA (US National Oceanic and Atmospheric Administration, data base).

## Results

The data concerning the average beta globulin concentrations and fluctuations and the number of patients with altered values (pathological), are shown in fig.2-4. The next step is to correlate these data with the solar activity and geomagnetic activity respectively.

Although the solar activity modulates the geomagnetic activity there is no perfect correlation between these two parameters. If we examine fig.1, which illustrates the solar activity in 1998 and the geomagnetic activity as measured by Ap index (fig.2-4), apparently there is no much resemblance. However a closer look, reveals that there is a broad similarity in respect to the first half of the year and the second half of the year respectively. The solar activity shows a progressively increasing activity then, despite of fluctuation, the trend seems to level off in the second part of the year. The geomagnetic activity reveals a less active, first part of the year, with a single major magnetic storm, while the second part is filled with minor storms dominated by a major storm. In other words the second part of the year is characterised by a more widespread geomagnetic activity. This is in fact in agreement with the solar activity.

Inspection of fig.2-4 do not reveal any simple or obvious correlation of the beta globulin concentration, its fluctuation or number of patients with altered values and the geomagnetic activity. A most general observation can be made in relation to the solar activity. The beta globulin data show a faster change in the first part of the year whereas during the most part of the year left, this trend disappears. This can be best observed in fig.3 for the fluctuations of the daily average values of

beta globulin concentration. The same figure reveals that the fluctuation is higher during the spring whereas it shows lower values during the rest of the year. This is might suggest that there are more sensitive subjects during the spring which are subjected to greater variations compared to the rest of the year. This is less evident during the rest of the year.

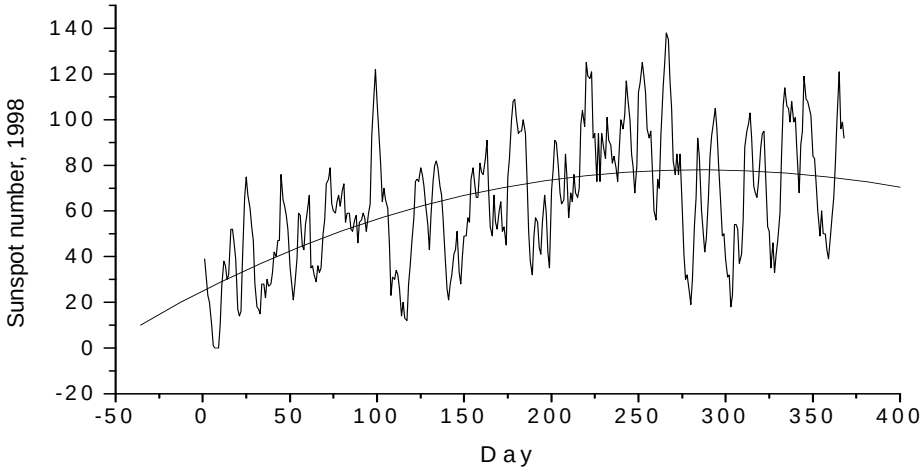


**Fig. 1.** Solar activity in 1998, presented as a plot of the sunspot number versus the day of the year. The plot was fitted with a polynom.

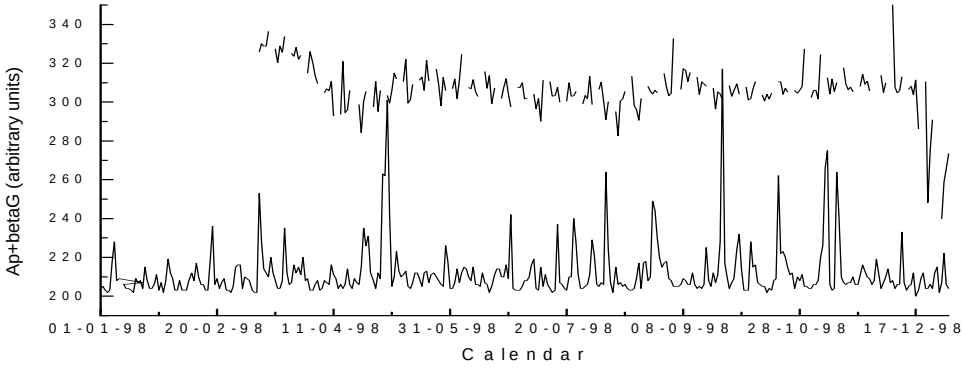


**Fig. 2.** Geomagnetic activity in 1998 (lower curve) and the daily average beta globulin concentration (upper curve) - arbitrary units

Further, figure 5 suggest an interesting feature. It can be noticed the both major storms (spring and autumn, respectively) are followed by a decreased number of patients with normal value in the next several days up to two weeks.

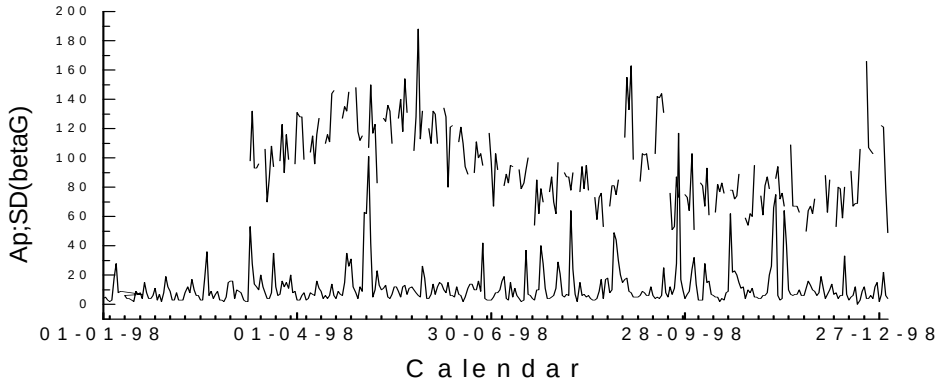


**Fig. 3.** Geomagnetic activity in 1998 (lower curve) and the daily SD of the average daily beta globulin concentration (upper curve) - arbitrary units

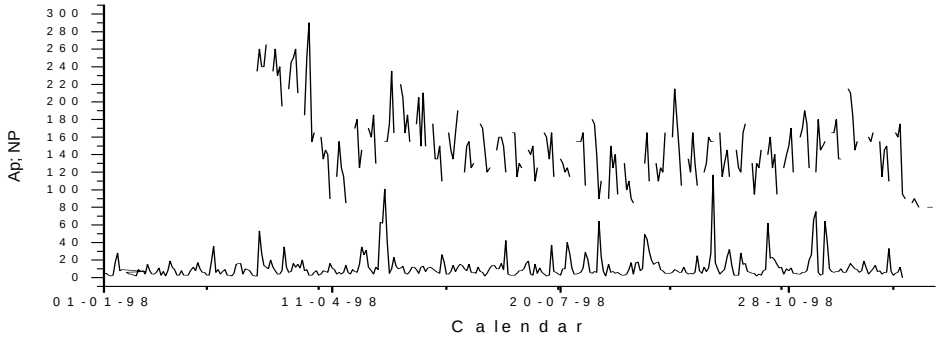


**Fig. 4.** Geomagnetic activity in 1998 (lower curve) and the daily number of patients with pathological values of the beta globulin NP (upper curve) -arbitrary units

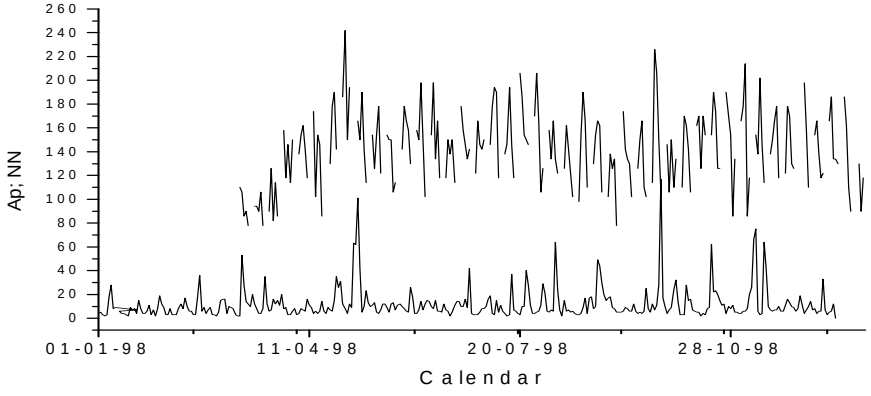


**Fig. 5.** Geomagnetic activity in 1998 - Ap index (lower curve) and the number of daily patients with normal level of beta globulin concentration (upper curve) - arbitrary units

Unfortunately a proper correlation analysis or a spectral analysis of the data cannot be done due to the data gap on the weekends. Consequently only this visual inspection of the plots was possible. In an effort to find a quantitative way to compare the results, we have analysed the distribution of the data. The time series representing the daily average geomagnetic activity in 1998 had somewhat more of an exponential like distribution. The most resembling distribution with the geomagnetic activity appeared to be the values of SD of the daily average beta globulin concentration. In other words the magnitude of the fluctuations of the beta globulin concentration appeared to be somewhat correlated with the geomagnetic activity as already suggested by the visual inspection of fig.3.

## Conclusions

The more geomagnetically active periods during the spring of 1998 appeared to Induce greater changes in the status of the beta globulin of calling patients.

On a short term, it appears that the two major magnetic storms in the spring and in the autumn of 1998 are followed by periods of up to two weeks when the number of patients with normal levels of blood beta globulin decreases.

STUDIA UNIVERSITATIS BABEŞ-BOLYAI, PHYSICA, SPECIAL ISSUE, 2000

# THE ROLE OF THE ELECTRIC FIELD PULSE STRENGTH AND LENGTH IN THE BIOMEMBRANE ELECTROPERMEABILIZATION PROCESSES

**SILVIA NEAMTU, I. TURCU, CRISTINA DRAGU, C. BINDEA**

*National Institute for Research and Development of Isotopic and Molecular Technology, Cluj-Napoca, ROMANIA*

## Introduction

Cell biomembrane acts as a highly impermeable barrier to a free transmembrane exchange of molecules. The application of short, strong electric field pulses make the plasma membrane permeable to the exogenous material. This process called electropermeabilisation or electroporation is reversible in a certain range of electric field and pulse parameters and does not affect the cell viability.

Membrane electropermeabilization is described as a three - step process: i) induction, ii) expansion and iii) resealing of the membrane pores created under the action of electric field pulses[1]. The first step (μs) is thought to be linked to a modulation of the transmembrane potential induced by the external field. If one considers a spherical cell with a radius r, it can be defined as:

$$\Delta U = -3/2\ r\ E \cos\theta$$

where $\Delta U$ - is the induced membrane potential, r is the cell radius, E is the electric field strength and $\cos\theta$ is the angle between the normal vector of the membrane and the electric field. Increasing the electric field intensity, the transmembrane potential reach a threshold value of about 200 - 300mV when the membrane permeability and conductance is strongly enhanced.

The second step is a slow process with a lifetime in ms to minutes range. The membrane-permeated state is controlled by physical and chemical parameters such as pulse strength, number and duration, temperature and pulsing buffer composition [2,3]. While the induction of pores is assumed to be a lipid domain process, the stability of permeable state after poration suggests that in the pores resealing process (the third step), other molecular structures are involved, mainly the membrane proteins and cytoskeleton [4,5,6]. The complete pore closure has a lifetime longer than 10 min [7]

The aim of this study is to find the main contribution of the pulse strength and duration in the membrane electropermeabilization steps. We have investigate four combinations of pulse parameters: amplitudes E = 4 and 5 kV/cm; lengths $\tau$ = 40 and 100 μs.

## Materials and methods

Experiments were performed on human erythrocyte isolated from blood collected on natrium citrate 3.8%. Washed cells were centrifuged 10 min at 3000 g (Ultracentrifuge PJ 180R) and resuspended in pulsing buffer (150 mM NaCl / 5mM Hepes, pH 7.4) at 1% hematocrit. Rectangular pulses with preestablished amplitude and pulse duration are delivered by an electroporation equipment.

Samples, exposed to pulsed electric field in a thermostated chamber at $4^0$C, were incubated for an hour at low temperature (ice bath). The extension of permeabilized area was emphasised by hemoglobin efflux kinetic and manganese ions transport through erythrocyte electropermeabilized membrane. The hemolysis degree was estimated spectrophotometrically (410 nm) from the supernatant of samples taken every ten minutes. The concentration of manganese ions was measured from the electroporated cell suspension by atomic absorption spectrometry technique.

The membrane resealing was tested after 30 and 60 min incubation time at $37^0$C. The used test was the membrane impermeability to manganese ions. Electroporated cells, incubated at $37^0$C, were washed with isotonic salt solution, concentrated at 40% hematocrit and finally incubated for 20 min in a suspending buffer containing 1.4 μg/ml $Mn^{2+}$. The manganese influx has been monitored by the decreasing of ions concentration in the extracellular medium.

## Results

The kinetic of hemoglobin efflux (fig. 1) and extracellular manganese ions concentration (table I) was measured for four combination of pulse parameters:

a) E = 4kV/cm, $\tau$ = 40 μs; c) E = 4kV/cm, $\tau$ = 100 μs;
b) E = 5 kV/cm, $\tau$ = 40 μs; d) E = 5 kV/cm, $\tau$ = 100 μs

The plateau values of hemoglobin efflux are dependent on the four combinations of pulse parameters. These plateau give the permeabilisation efficiency of the investigated electric field pulses and are controlled by the hemoglobin equilibrium balance between intra and extracellular media. At the low hematocrit (1%) we used, at the equilibrium, intracellular hemoglobin concentration decrease at about 3%. Red blood cells partially loaded with hemoglobin are called erythrocytes ghosts.

**Table I**

The manganese ions concentration in cell ghosts and erythrocyte pallets

| | **Amplitude/duration pulse [(KV/cm)/μs]** | **Cell ghost %** | **$Mn^{2+}$ μg/ml cell ghost** | **Erythrocyte %** | **$Mn^{2+}$ μg/ml erythrocyte** |
|---|---|---|---|---|---|
| a | 4 / 40 | 33 | 0.62 | 67 | 0 |
| b | 5 / 40 | 69 | 0.86 | 31 | 0.33 |
| c | 4 / 100 | 68 | 0.87 | 32 | 0.31 |
| d | 5 / 100 | 81 | 0.77 | 19 | 0.71 |

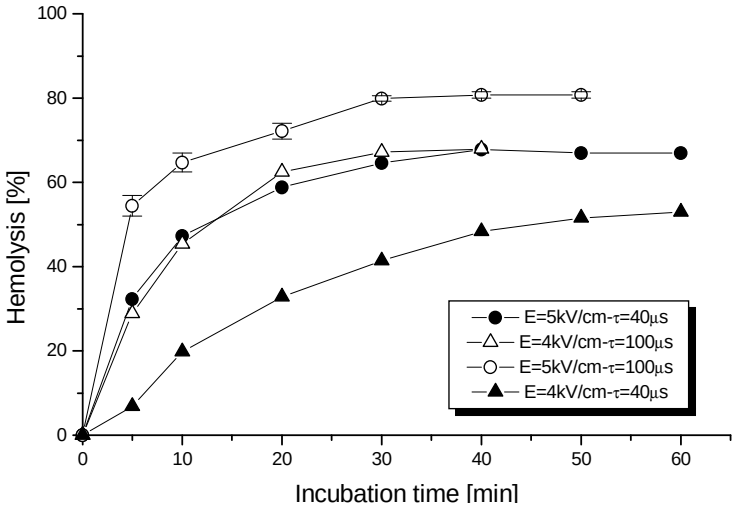


**Fig.1**. The kinetic of hemoglobin efflux through erythrocyte electroporated membrane at different pulse parameters. Incubation temperature - $4^0$C

The kinetics of hemoglobin efflux and ions permeability depends on both amplitude and pulse length. Hemolysis degree and manganese influx increases with the electric pulse amplitude and with the pulse length. A similar hemoglobin and manganese ions membrane permeability is noticed under the action of combination of higher amplitude - lower length (5kV/cm - 40μs) and lower amplitude - higher length (4kV/cm - 100 μs) respectively. For pulses with E=4 kV/cm and τ=40 μs the ghost membrane is permeable to manganese ions while the erythrocytes membrane from pallet is impermeable. At higher values of parameters (5kV/cm - 100 μs), the membrane permeabilisation to manganese ions is similar for ghosts and erythrocyte pallet.

A relevant result obtained from our experiments is related to the fact that different combinations of pulse parameters can induce the same permeabilization.

The pores resealing - process is found to be the step that discriminate between the two cases (b and c) with similar permeabilization efficiency (fig.2).

The electroporated membrane reseals after 30 min incubation at $37^0$ C in the first two cases (a and b). Keeping the pulse amplitude at lower value (4 kV/cm) and increasing the pulse length to 100 μs, the membrane remain highly permeable after 30 min incubation. The impermeability to manganese ions was obtained only after 1 hour incubation at $37^0$ C. These results show that the resealing process depends on pulse length. Exposing the cells to electric pulses with 5 kV/cm amplitude and 100 μs length, the membrane is more drastically affected. In this case, the resealing process requires a careful and a longer incubation treatment.

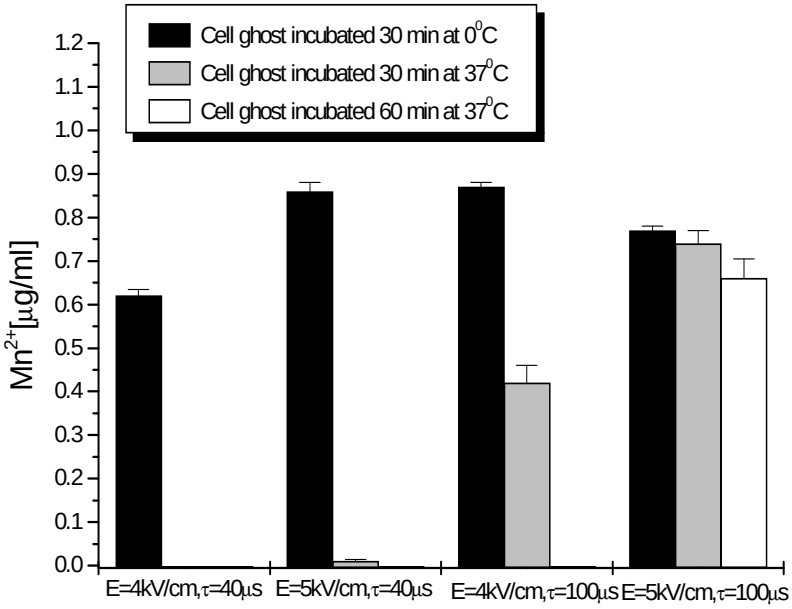


**Fig.2.** Intracellular manganese ions concentration in cell ghosts obtained from erythrocytes exposed to electric pulses with different parameters

## Conclusions

The erythrocyte membrane electropermeabilisation induced by different combination of pulse parameters, was monitored by two different processes: the efflux of hemoglobin (a large molecule - 65 000 Da) and the influx of (relatively small - 55 Da) manganese ion. Results show the dependence of the membrane permeabilisation efficiency on both amplitude and electric pulse length. An interesting result is that the effects are dependent on the molecular weight of the tested molecules. The presence of manganese ions both in cell ghosts and in erythrocyte sediment revealed the size selectivity of membrane permeabilization process. These results emphasise a size dependent distribution of electric pores.

Both hemoglobin efflux and manganese influx revealed the possibility to modulate the membrane permeability using different pulse parameters. The same permeabilisation efficiency has been obtained for two combinations of pulse parameters the discrimination between the two cases being introduced by the resealing step of the electropermeabilization process. Our results show that the pulse length is the determinant parameter that modulates the restoration of impermeability to transmembrane exchange of molecules after electroporation.

## BIBLIOGRAPHY

1. J. Teissié, M.P. Rols, An experimental evaluation of the critical potential difference inducing cell membrane electropermeabilisation, Biophys J. 65 (1993) 409-413.
2. R. Benz, F. Beckers, U. Zimmermann, Reversible electrical breakdown of bilayer membrane: A charge-pulse relaxation study, J.Membrane Biol. 48 (1979) 181.
3. M.P. Rols, J. Teissié, Ionic strength modulation of electrically induced permeabilisation and associated fusion of mammalian cells, Eur.J.Biochem. 179 (1989) 109-115.
4. M.P. Rols, J. Teissié, Experimental evidence for the involvement of the cytoskeleton in mamalian cell electropermeabilisation. Biochem.Biophys.Acta 1111 (1992) 45-50.
5. D.D. Chang, Th.S. Reese, Changes in membrane structure induced by electroporation as revealed by rapid-freezing electron microscopy. Biophys J. 58 (1990) 1-12.
6. Silvia Neamtu, V.V. Morariu, I. Turcu, Alina Hategan-Popescu, Lorelai Cop¾escu, Pore resealing inactivation in electroporated erythrocyte membrane irradiated with electrons, Bioelectrochem. Bioenerg., 48, (1999), 441-445.
7. G. Saulis, M.S. Venslauskas, J. Naktinis, Kinetic of pore resealing in cell membranes after electroporation, Bioelectrochem. Bioenerg, 26 (1991) 1-13.

STUDIA UNIVERSITATIS BABEŞ-BOLYAI, PHYSICA, SPECIAL ISSUE, 2000

# FLUCTUATIONS OF THE HUMAN ERYTHROCYTE

**V.V. MORARIU*, I. GHIRAN****

**Department of Biophysics, National Institute for R&D of Isotopic and Molecular Technologies, P.O. Box 700, R 3400, Cluj-Napoca, ROMANIA, vvm@L40.itim-cj.ro and "Babeş-Bolyai" University, Cluj-Napoca, ROMANIA*

***Harvard Medical School, Boston*

## Purpose

This investigation aimed to analyse the fluctuations of some geometrical parameters of the human erythrocyte: the great diameter D, the small diameter d, and the area. It has been known for a long time that investigation of the erythrocytes by optical microscopy may easily reveal the "flickering" phenomenon, which is due to the membrane undulations. Undulations are sensitive to the membrane elasticity, which in turn is sensitive to many physical, chemical and pathological influences. The main purpose of our work was a methodological one: we attempted to analyse the flickering phenomenon by serial fast recording of a cell image which is subsequently analysed in respect to plan geometrical parameters. This attempt wants to be an alternative at the present method, which is based on the cell thickness measurements, using an elaborate microscopic technique.

## Materials and Methods

Fresh human blood was diluted in the autologous plasma and placed between two glass plates spaced by a 7 microns nylon fibre. Successive images at 0.5 seconds time interval have been taken with a camera attached to a microscope operating in the phase contrast mode. The cell images were subsequently analysed by a using a soft for shape analysis. The time series have been further analysed as such and by performing FFT. Three kinds of samples have been analysed: fresh-floating cells, aged floating cells and trapped cells into the fibrin clot.

## Results

Examination of the time series revealed a multitude of fluctuations having clearly a distribution of frequencies. An example of the fluctuations of the geometrical parameters is shown in fig.1 It appeared that a simple visual examination can make a distinction of the following categories (table 1): a) fast fluctuation possibly associated to the flickering phenomenon, b) slow fluctuations possibly associated to the elongation or shortening of the cells and, c) partial rotation of the cells, i.e. rotation of the cell either around the smaller or the longer diameter. If the data free of the b) and c) fluctuations are subjected to FFT, $1/f^a$ type of spectra results. This

is shown in fig.2. The noise index appeared to be sensitive whether the cell is aged or mechanically trapped into the fibrin clot. The spontaneous elongation of the cell seems to be the first time that has been mentioned. The time series yields the rate of this phenomenon, which obviously is related to the membrane elasticity.

**Table 1**

Types of fluctuation of the geometrical parmeters of erythrocytes

| No. | **Type of fluctuation** | **Origin** | **Time scale [seconds]** |
|---|---|---|---|
| 1 | Fast | Flickering | 0,5 |
| 2 | Slow | cell elongation | 20-30 |
| 3 | Drift | cell rotation | cca 100 |

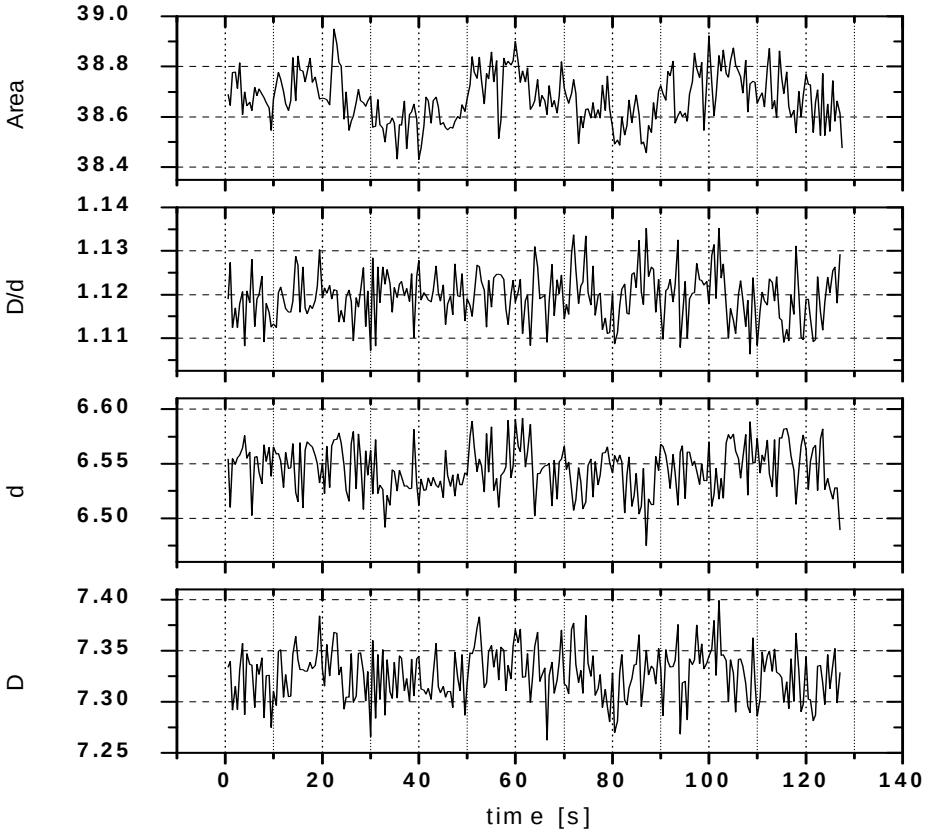


**Fig.1.** The fluctuations of the geometrical parameters (great diameter D, the small diameter d, the cell area A and the ratio D/d for a normal erythrocyte which was immobilised in fibrine

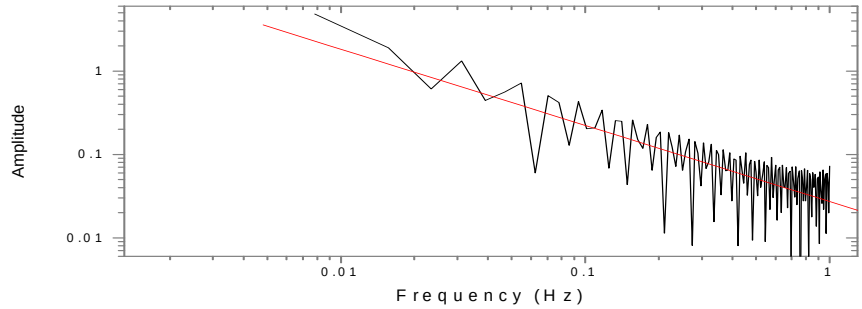


**Fig.2.** The fluctuation spectrum of the area of a normal erythrocyte freely floating in the blood serum. The $1/f^a$ character of the spectrum shoud be noticed.

The change evaluation of the temporal series was based on the following consideration in order to detect the change of shape of the erythrocyte cell or the rotation:

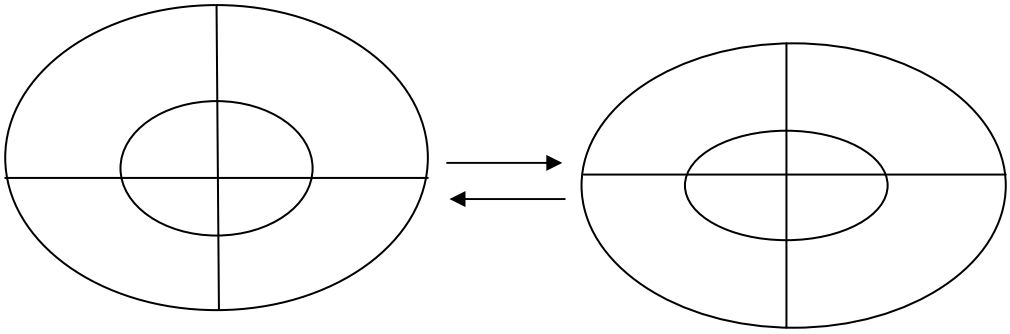


If **D** and **d** are the large and small diameters respectively and the cell changes its shape from **A** to **B** it results that the cell ellongation is accompanied by the following modifications:

**D(A) < D(B)**
**d(A) > d (B)**
**D(A)/d(A) < D(B)/d(B) ≡ ellongation**
**Area (A) = Area (B)**

The examination of the temporal diagrams can reveal changes in either direction:

A → B or A ← B.

The effect of the partial rotation of the erythrocytes on the geometrical parameters is further illustrated:

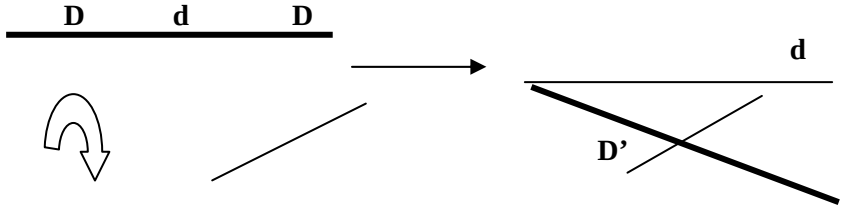


As a result of the rotation arround the small axis, the projection of the large diameter (the effective diameter which is recorded during the microsscope observation) will be;

**D' < D,**
**D'/d** → decreases
While **d = CONSTANT,** the apparent area ( plan projection) will decrease:
**APPARENT AREA (PROJECTION) → DECREASES**

In a similar way we may consider the rotation around the large diameter axis. While this diamter will remain unchanged, the observe projection will change:

**D = CONSTANT**
**d' < d**
**D/d' → decreases**
**Apparent Area → decrease**

The temporal series have been collected for a large number of erythrocytes from normal healthy donors. Not all data proved to be suitable for Fourier transform analysis; this refer to fluctuations superposed on a drift. These data have been excluded from the spectral analysis providing no drift correction was possible due tot the complicated pattern of the drift itself. The actual data are summarized in Table 2.

**Table 2.**

The power law coefficient of the fluctuation spectra of various geometrical parameters of the erythrocyte cell

| No | Sample characteristic | The great Diameter D | The small diameter d | Cell Area A | Other characteristics |
|---|---|---|---|---|---|
| 1 | trapped erythrocyte in the fibrin clot | 0,54 | 0,54 | 0,54 | - |
| 2 | erythrocyte in aged (lysed) fibrin solution | 1,58 | 1,74 | 1,45 | - |
| 3 | aged erythrocyte 24 hours *in vitro*, in plasma | 1,48 | 1,02 | 0,9 | slow oscillations of D and A |
| 4 | crenated erythrocyte | 0,62 | 0,66 | 1,28 | - |
| 5 | fresh erythrocyte (discocit) | 0,84 | 0,9 | 0,9 | slow oscillations |
| 6 | - " - " - " - | 0,86 | 0,58 | 1,24 | - " - " - |
| 7 | - " - " - " - | 0,9 | 0,9 | 0,78 | - " - " - |
| 8 | - " - " - " - | 0,68 | 0,24 | 0,6 | - " - " - |

| No | Sample characteristic | The great Diameter D | The small diameter d | Cell Area A | Other characteristics |
|---|---|---|---|---|---|
| 9 | - " - " - " - | 0,46 | 0,9 | 0,8 | - " - " - |
| 10 | - " - " - " - | 0,94 | 0,82 | 0,8 | - " - " - |
| 11 | - " - " - " - | 0,96 | 0,72 | 0,44 | - " - " - |
| 12 | - " - " - " - | 1,02 | 0,7 | 0,44 | - " - " - |
| | fresh erythrocytes<br>-average<br>-SD | <br>0,82<br>0,097 | <br>0,72<br>0,226 | <br>0,75<br>0,26 | |

## Conclusions

- The fluctuations of the geometrical plan parameters of the human erythrocyte revealed three types of phenomena: a) flickering, b) cell elongation and c) partial cell rotation.

- All data revealed a $1/f^a$ type of spectrum but no pure 1/f spectra have been noticed. The power law coefficient (resulting from the slope of the fitting line of the spectrum on a double logarithmic scale) ranged between 0.13 and 0.87.

- The normal fresh erythrocytes are characterized by power law coefficient around 0.4.

- Trapping of the erythrocytes within the fibrin clot induced a more random character of the fluctuations manifested as a lowering of the power law coefficient.

- In vitro ageing of the erythrocyte increases the coefficient.

These results open the possibility to profitably use the geometrical parameters to investigate cell fluctuations. In addition the present work brings for the first time evidence for the slow spontaneous deformation and motion of the cells.

STUDIA UNIVERSITATIS BABEŞ-BOLYAI, PHYSICA, SPECIAL ISSUE, 2000

# IN VITRO HUMAN BLOOD AGEING IN ZERO MAGNETIC FIELD - THE OLIGOELEMENTS TRANSPORT

**LORELAI I. CIORTEA, V. V. MORARIU**
*The National Institute for Research and Development of Isotopic and Molecular Technologies, P.O.Box 700, R-3400,Cluj-Napoca, ROMANIA*

## Introduction

The effect of the natural magnetic field on living matter, due to the geomagnetic field contribution, has received very little attention compared with the effect of exposure to increased intensities above natural level. However this is a question of interest since: 1) life developed under the influence of the Earth' s geomagnetic field and changes may correspond to a loss of physiological vitality and efficiency in all the functions of the body, and 2) the absence of the natural magnetic environment is relevant for living matter in cosmic conditions (this is the reason the astronauts in space for long periods require artificial magnetic fields to maintain health).

As we know that the GMF fluctuations trigger important effects on living matter, we may expect that the lack of GMF could influence the living processes, as well.

Experimental data on the biological effects of weak static magnetic field, compared to geomagnetic fields are very limited. It is well known that many animals can detect the direction of the geomagnetic field and use it for navigation [1]. These observations suggest that at least some cells or cellular structures are sensitive to weak changes in the static geomagnetic field [2]. Near null magnetic field has been supposed to be an important reference in studies of effects of geomagnetic field on animals and man. On the other hand, earlier results suggested that the natural magnetic field significantly influences health both on the ground and possibly in cosmic conditions. In this sense alterations have been observed in the immune mechanism such as a reduction in the number of T lymphocytes and a significant increase in the peripherial leucocytes count [3].

The role of oligoelements in the immune system is well known: Cu helps strengthen the immune system, Zn helps bolster it and $Mg^{2+}$ deficit has implications in immunity [4]. As we know by now that the immune system is affected by the absence of the normal geomagnetic field we may assume that the balance of these oligoelements is also disturbed.

The aim of our work was to investigate $Mg^{2+}$, Cu and Zn concentrations into the blood serum following *in vitro* exposure to zero magnetic field. It should be pointed out that only the static component of geomagnetic field was compensated, the alternating component remained operative.

## Materials and Methods

The investigations were carried out on human blood collected from apparently healthy donors without any substance to prevent coagulation.

The samples were kept in geomagnetic field conditions, as controls and in near null magnetic field conditions, as probes, at room temperature. The natural magnetic field, mainly the static component of the geomagnetic field was compensated for with a Helmholtz coil, of 1.2 m diameter, mounted on a wooden frame. The coil was oriented in the N-S direction, having an angle of inclination similar to the geomagnetic field. The power supply of the coils was set such as to obtain a magnetic field induction within the coil at the lowest possible average value. The magnetic field was measured with a directional magnetometer having a precision of 1 nT.

Generally, the field induction within the coil volume varied at different positions within a range of 0-500, compared with the natural value of about 47 000 nT. Therefore the reduction factor of the natural magnetic field was ~100. Only the static component of the natural magnetic field was compensated for by this experimental set-up.

We attempted to reduce as much as possible any magnetic perturbations by removing any iron objects or electrical power supply from the close vicinity of the coil and by placing it on the ground floor at a height of about 1.5 m, on a wooden frame. The controls were placed in the same room at a 4 m distance from the magnetic field compensating system.

The determination of ions concentrations ($Mg^{2+}$, Zn and Cu) in blood serum was performed immediately and after 48 hours of blood preservation by atomic absorption spectrophotometry technique.

The significance of differences between mean values in exposed samples and control samples were evaluated by the Student t-test in each experiment.

## Results

The analysis of $Mg^{2+}$ concentration revealed that the ions efflux is inhibated in zero magetic field conditions. The results obtained are plotted in Fig. 1.

The variation of Zn concentration for controls and probes are shown in Fig. 2. One can see that Zn influx is inhibated when the geomagnetic field is lacking.

The evolution of Cu concentration is presented in Fig. 3. The experimental results demonstrate that Cu influx is stimulated in the absence of the geomagnetic field.

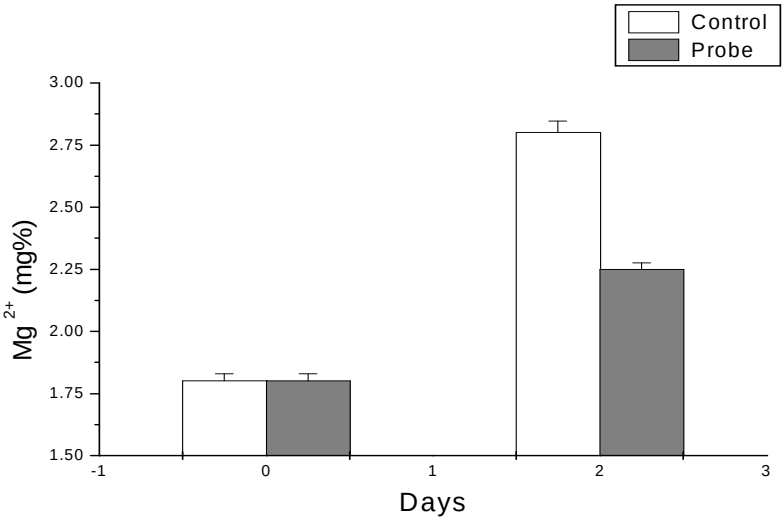


Fig. 1 The variation of $Mg^{2+}$ concentration in blood serum for fresh blood and after 48 hours of blood preservation in geomagnetic field (control) and in zero magnetic field (probe).

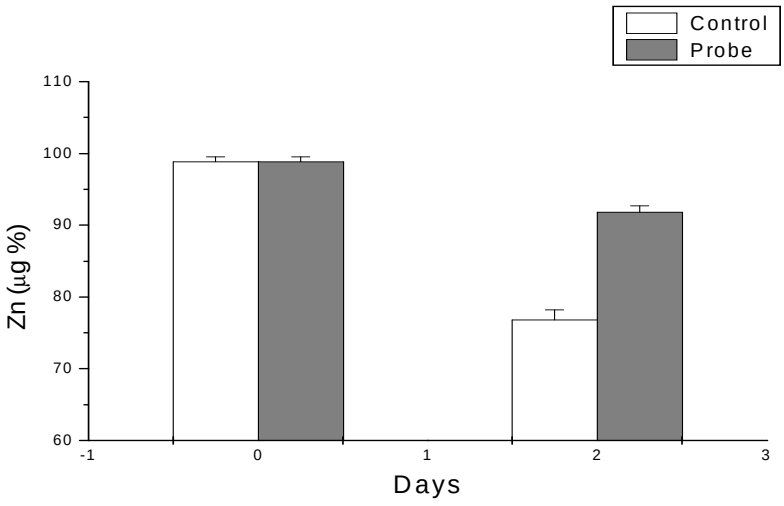


Fig. 2 The variation of Zn concentration in blood serum for fresh blood and after 48 hours of blood preservation in geomagnetic field (control) and in zero magnetic field (probe).

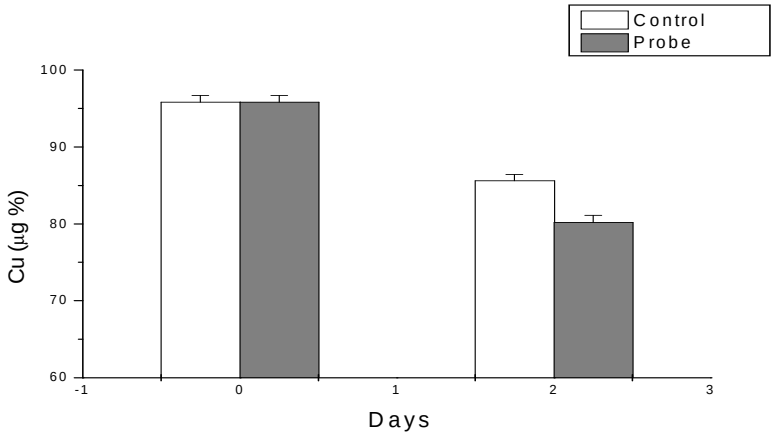


Fig. 3 The variation of Cu concentration in blood serum for fresh blood and after 48 hours of blood preservation in geomagnetic field (control) and in zero magnetic field (probe).

## Discussion

The present results revealed that the lack of natural magnetic field can influence the oligoelements transport.

As one can see from Fig.1, internal red cell $Mg^{2+}$ concentration decreases after 48 hours for controls more than for probes. This fact may be due to the stabilisation character of zero magnetic field on aged erythrocyte membranes with implications at the level of $Mg^{2+}$ passive transport.

Zn might be transported into cells as an amino-acid complex meanly Zn-His complex, using an amino-acid carrier system [5]. The results obtained emphasise that this system may be perturbed in zero magnetic field.

It is well known that normal adults have Cu associated with four components of human plasma: ceruloplasmin, transcuprein, albumin and aminoacids [6,7,8]. On the other hand, inside the erythrocytes Cu exists under two forms: a stable one, undifussional, the ion being bound by a protein- erythrocuprein, and an unstable form, diffusional, non-erythrocuprein. This component is weakly bound by albumin and may have bi-directional movements across the membrane: a rapid intake followed by a rapid uptake, these transports being facilitated by free amino acids, essentially Histidine [8]. This complex may have the trasportor role across membrane, Cu transport being in fact controlled by non-erythrocuprein. All these aspects may suggest that Cu-non-erythrocuprein binding may be perturbed in conditions of zero magnetic field.

All results presented are in agreement with earlier works which revealed that the immune system is affected in conditions of zero magnetic field [3].

## REFERENCES

1. Rosen, A.D., Direct Current Magnetic Fields: Mechanism of Action, in **Biological Effects of Electric and Magnetic Fields**, D.C. Carpenter, S. Ayrapetyan, ed., Academic Press, 165-179, 1984.
2. Semm, P., Schneider T., Vollrath L., Effects of an Earth-strength magnetic field on electrical activity of pineal cells, Nature 288: 607-608, 1980.
3. Dorofteiu M.**,** Morariu V.V., Marina C., Zirbo M., The effects of near null magnetic field upon the leukocyte response in rats, Cytobios, 84: 179-189, 1995.
4. Margineanu O., Miu M., Copper, in **Oligoelements in Biology and Pathology**, Dacia Editure, 20-95, 155-193, 1984.
5. Aiken S.P., Horn N.M., Saunders N.R., Effects of amino acids on zinc transport in rat erythrocytes, J. Physiol. (Lond.), 445:69-80, Jan., 1992.
6. Wirth P.L., Linder M.C., Distribution of cooper among components of human serum, J. Natl. Cancer Inst., 75(2): 277-284, 1985.
7. Weiss K.C., Linder M.C., Copper transport in rats involving a new plasma protein, Am. J. Physiol., 249(1 Pt 1): E77-88, 1985.
8. Margineanu O., Miu M., Copper, in **Oligoelements in Biology and Pathology**, Dacia Editure, 68-101, 1984.

# SPECTROSCOPIC STUDY OF SOME SUPRAMOLECULAR AGGREGATES PORPHYRINS-PHTHALOCYANINES AND THEIR IMPLICATIONS IN PHOTOMEDICINE

**R.M. ION[*], M. GRIGORESCU[*], F. SCARLAT[**], V. NICULESCU[**], K. GUNAYDIN[***]**

[*] *ZECASIN S.A., Photochemistry Dept., Splaiul Independentei 202, Bucharest-79611; E-mail:rmion@pcnet.pcnet.ro*
[**] *Institute of Radiation Physics, Pasma and Lasers, Bucharest*
[***] *Mustafa-Kemal Univ., Chemistry Dept., Antakya-Hatay, Turkey*

**ABSTRACT.** The aggregates of porphyrins and phtalocyanines can provide promising properties in the search of new molecular materials for medicine, and could be readily monitored spectroscopically, since it causes strong perturbations of their absorption spectra. The formation of water-soluble heteroaggregates from Ni, Co, Pd, Rh complexes of 5,10,15,20-tetra-methyl-pyrydil porphyrin (Me-TMPyP) and Zn complex of 2,9,16,23-tetra-carboxylate-phthalocyanine (ZnTCPc) has been investigated in this paper by using UV-Vis and IR spectra. The formation of such adducts involves intensive interactions between two differently charged macrocycles, this interaction being strong influenced by the nature of the metal from inside the macrocycle. The singlet oxygen generation is also stimulated by this heteroaggregation. Some data about the application of such heteroaggregates in photodynamic therapy of cancer were evaluated.

**Key words**: porphyrins, phthalocyanine, heteroaggregates, photodynamic therapy.

## 1. Introduction

The photodynamic therapy of tumour is an innovative method for cancer diagnosis and treatment of various types of tumours by the combined action by oxygen, light and sensitizer [1,2].

PDT is an indirect treatment; firstly the photosensitizer dyes are applied to the sample. Following illumination these usually produce singlet oxygen that acts efficiently on the cells.The uptake and the retention time of the dyes should be different for the normal and cancer tissue /3/.

The sensitizer should have some special conditions:

-be incorporated into malignant cells at a much great efficiency than its incorporation into normal cells ;

-be efficiently fluorescent and produce the singlet oxygen, or the other species which can destroy malignant cells;

-be non toxic for the healthly cells and,if possible, it should be quickly expelled from the organisms.

Porphyrins and phtalocyanines are promising candidates for sensitizing PDT action, because:

-are typical NIR dyes with red absorption band located in a region of low absorption of tissues;

-are non-toxic for different healtly cells;

-are much better incorporated into different kind of human cells than other dyes;

-are much soluble in different polar or aprotic solvents;

-due to their aggregation capacity, they could penetrate much better the membrane cells, after this being recovered into their monomeric forms;

The molecular mechanisms involved in photodynamic therapy are:

-radicalic sensitized photooxidation (type I reaction);

-singlet oxygen sensitized photooxidation (type II reaction);

-photosensitized reactions without oxygen(type III reaction).

In spite of the contribution of each such mechanisms, the main active specie causing damage of cancer cells is singlet oxygen [4,5].

The generation of $^1O_2$ molecules occurs through the following mechanism:

$$P(S_o) + h\nu \text{ -------> } P(S_1) \xrightarrow{\text{ISC}} P(T_1)$$

$$P(T_1) + {}^3O_2 \text{ ------> } P(S_o) + {}^1O_2$$

In spite of their good properties, the porphyrins easily support a photodegradation reaction (called "photobleaching") which occur under irradiation in oxygen atmosphere, leadind in a short time to some toxic products and lower efficiency [6,7].

Porphyrins and phthalocyanines are the most used compounds in the photodynamic therapy of cancer, due to their NIR absorbing wavelenghts, non-toxicity and high singlet efficiency generation [8-10].

Phthalocyanines, which are structurally related to the porphyrins, are more stable than porphyrins and with adequate properties for photodynamic therapy (absorb visible light at a substantially longer wavelenghts than porphyrins).

By coupling porphyrins with phthalocyanines, could be obtained heterocomplexes useful for photodynamic applications. Surprisingly, in the last decade the association of the two compounds has not received much attention in the literature [11-15]. Their association is based on "electrostatic" mixed dimers by pairing porphyrin and phtalocyanine bearing oppositelly charge substituents, and have higher efficiency and stability [16].

In this paper, the existence of such porphyrin-phtalocyanine heteroaggregates will be demonstrated using UV-Vis absorption spectroscopy. Also, the singlet oxygen generation capacity for all the studied compounds are evaluated by means of 1,3-diphenylisobenzophuran test [17].

## 2. Experimental part

### 2.1. Materials

Ni(II)TMPyP, Rh(III)TMPyP,Pd(II)TMPyP and Co(II)TMPyP were synthesized following the procedures in the references [18]. The metal complexes of TMPyP have been converted into their chloride salts by passing them through the VIONIT AS-14 ion-exchange column in the chloride form. First of all, the phthalocyanine was transformed into its sodium salt. A 0.088 g sample of ZnTCPc was dissolved on a stoichiometric amount (1:4) of NaOH (3.9 ml, 0.1 M). The solution was filtrated and the filtrate was dried under a stream of air overnight.

A 0.05 g amount of this product was dissolved in 30 ml of water. In another beaker, an equimolar amount of Me-TMPyP (0.05 g) was dissolved in the same amount of water and the two solutions were mixed. The final solutions were left for three weeks to ensure complete precipitation and then filtered by gravity**.**

In order to evaluate the photochemical efficiency was used a special trap for singlet oxygen test -1,3-diphenylisobenzofuran(DPBF) prepared and purrified in the laboratory after the literature data [6].

### 2.2. Apparatus

UV-Vis spectra (for freshly solutions) were recorded on a SPECORD M400, Carl Zeiss Jena spectrophotometer with a microprocessor.

IR spectra (for KBr pellets) were run on a SPECORD M80 Carl Zeiss Jena spectrometer with a computer command.

### 2.3. Singlet oxygen test

Measurements were carried out in a quartz cell (1cm x 1cm) at $20^{o}$C. A DMSO solution (2.3 ml) containing sensitizer ($4.8 \times 10^{-5}$ M) and DPBF ($2.7 \times 10^{-5}$ M) was irradiated with light beam from a UV-Vis spectrophotometer. Solutions of sensitizers were freshly prepared and kept in the dark before measurements. The decreasing of the DPBF concentration was followed by a special programm ruled on a computer at the absorbance from 415 nm (the molar coefficient of absorption for DPBF is 23300 $M^{-1}cm^{-1}$) as function of the irradiation time (irradiation cycles 50 x 25 s). The reaction showed a zero order-kinetics in the first 100 s. The incident photon flow was $4.65 \times 10^{-9}$ $M.s^{-1}$. Using the absorption spectra of the photosensitizer, the absorbed photon flow ($I_{abs}$) was evaluated. The quantum yield of the photooxidation of DPBF was calculated from the eq.l

$$\Phi_{DPBF} = ([DPBF]/I_{abs}.V);\ V= 3\ cm^3 \quad (1)$$

The quantum yield for singlet oxygen generation was calculated from eq.2.

$$1/\Phi_{DPBF} = 1/\Phi\ ^1O_2 + (1/\Phi\ ^1O_2\ K_d/K_a)\ (1/[DPBF]) \quad (2)$$

From the intercept of the Stern-Volmer plots,we obtained the quantum yield for singlet oxygen generation.

### 2.4.The Job method

The control of the complex formation and determination of their stoichiometry were carried out according to Job's method [19]. This method is based on the spectrophotometric analysis of mixtures of equimolar solutions of all the reagents from the studied system. It was made for example, by adding the measured volume of TSPP $10^{-4}$ M concentration to the solution of the phthalocyanine (Pc56) $10^{-5}$ M. Were obtained the absorbance changes of the series of solutions in which the ratio of the three differently charged compounds varied in increments from 10:0 up to 0:10.

By coupling porphyrins with phthalocyanines, it could be obtained heterocomplexes usefull for photodynamic applications. Their association is based on pairing porphyrin and phthalocyanine bearing oppsotelly charge substituents, the obtained heterodimers having higher efficiency and stability.

In this study we report about the synthesis, spectral characterization and application in photodynamic applications of some water-soluble heterodimers MP/MPc by pairing MTMPyP with ZnTCPc.

It was observed that by using ionizing radiation (electron or photons beam) was possible to short the synthesis time and to increase the synthesis yield .

### 2.5. Photodynamic test on Saccharomices Cerevisiae

In all the experiments described in this paper, subcultures of the diploid SC-6 starin of the yeast SC were grown on malt agar slants at 30 C for 48 H to 72 h. Immediatelly prior to irradiation or other experimental procedures, these resting cells were harvested, washed, and resuspended in double glass distilled water, to a final concentration of $10^6$ cells/ml.

The survival fraction of irrdiated cells was determined by measuring the coloni-forming ability of the cells.

The cells were inoculated in 25 $cm^3$ plastic flasks and incubated for 5 hours for proper attachement to the substratum. The cells were then exposed to 10 mM of each sensitizer for 18 h and subsequently to light from 650 nm monochromatic light provided from a medium-pressure Hg lamp. After light exposure the cells were incubated in a sensitizer free medium for 6 days at 37 C and then the colonies counted.

### 2.6. PDT-induced tumour regression

Was used a brain tumor provided from mice (50 mm3). It was then treated with a PDT protocol that has been described previously [20].

In brief, the tumour were exposed to 650 nm wavelenght light emitted from an argon-pumped dye laser 24 h after innoculation with 2 ml from the solution of the best singlet oxygen generator Rh(III)TMPyP/ZnTCPc - 0.93).

The fluence was 135 W/cm$^2$ and was delivered at a fluence rate of 0.084 W/cm$^2$. The treatment was 1 cm in diameter, which included at least 1 mm margin of the non-neoplastic tissue.

## 3. Results and discussion

The porphyrins and phthalocyanines represent two classes of very chemically versatile compounds. Depending of the nature of the central metals and the peripheral substituents, a wide range of photophysical, photochemical properties and also interesting applications can be obtained, the photodynamic therapy being the most important between them .

Phtalocyanines are azaporphyrins consisting of four benzoindole nuclei connected by nitrogen bridges in a 16-membered ring of alternating carbon and nitrogen atoms arround a central metal atoms which form stable chelates with metal cations (dia or paramagnetic ion), figure 1.

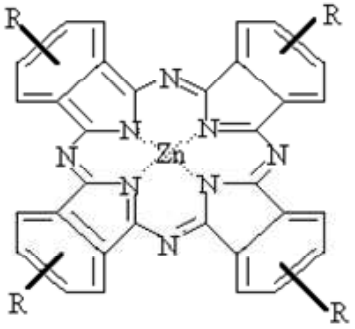


Fig.1. The structure of the phthalocyanine molecule

R=COO $^-$ Na$^+$

Porphyrins are tetrapyrrolic pigments based on porphine, Figure 2, which made up of four pyrrole subunits joined together by four methine bridges to give a cyclic molecule.

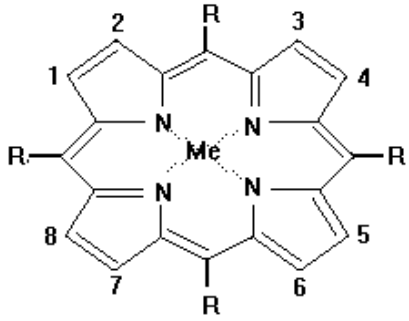


Fig. 2.The structure of the porphyrin molecule

R = $C_5H_4$-$N^+CH_3Cl^-$

Me=Rh,Pd,Co,Ni

The hetero-aggregates of porphyrins and phthalocyanines grafted with ionic substituents of opposite charges have been subjected to extensive investigations in the last two decades,because such assemblies can provide promising properties in the search for new molecular materials for electronics or photodynamic therapy [21,22].

The hetero-aggregation will occur only between $N^+$ substituents from the porphyrin and the sulfonated ones in the 4,4',4',4''' positions of the phthalocyanine ring.

The electronic spectra of porphyrins differ drastically from those of the phthalocyanines. The porphyrins display an intense Soret band and four Q bands in the 500-700 nm spectral region [15].

During the contact between the porphyrin and the phthalocyenine a hypsochromism and a broadening of the Soret band of the porphyrin were observed (fifure 3) this observation being as an evidence for the aggregation between both components (table 1).

**Table 1.**

UV-Vis wavelengths of the heterodimers Me-P/Me-Pc

| Compound | Soret band(nm) | | Q band (nm) | |
|---|---|---|---|---|
| NiTMPyP | 420 | 440 | 553 | 600 |
| ZnTCPc | 435 | | 635 | 686 |
| NiTMPyP/ZnTCPc | 415 | 470 | 535 | 560 |
| CoTMPyP | 430 | | 455 | 545 |
| CoTMPyP/ZnTCPc | 431 | 546 | 626 | 696 |
| RhTMPyP | 430 | 500 | 550 | 590 |
| RhTMPyP/ZnTCPc | 428 | 556 | 596 | 648 |
| PdTMPyP | 438 | | 520 | 565 |
| RhTMPyP/ZnTCPc | 431 | | 545 | 646 |

Knowing that at a constant wavelength, when two equimolar solutions are mixed in equal volumes, the absorbance of the mixture should be equal with the sum of the absorbances os the individual solutions (if there has been no interaction between the two solutions), in the studied case were observed relevant differences between the expected and found absorbances, Table 2.

This observation reprezent another proof for the heterodimerization between MeTMPyP and ZnTCPc.

The IR spectra recorded for the studied systems, showed some strong differences between the heteroaggregates and the monomeric forms, especially for the band around 1500 $cm^{-1}$. For ZnTCPc upon dimerization, the band from 1390 $cm^{-1}$ (attributed to symmetric strech of carboxylate ion) shifts to 1372 $cm^{-1}$ and the band from 1585 $cm^{-1}$ (attributed to asimmetric frecquency of the same carvboxylate ion) shifts to higher frequency, Table 3.

**Table 2.**

UV-Vis absorption intensities (A) for the hetetodimers MeP/MePc

| Compound | Soret band (nm) | A found | A calculated |
|---|---|---|---|
| NiTMPyP/ZnTCPc | 415 | 2.02 | 2.67 |
| CoTMPyP/ZnTCPc | 431 | 1.23 | 1.67 |
| RhTMPyP/ZnTCPc | 428 | 1.94 | 2.07 |
| PdTMPyP/ZnTCPc | 431 | 1.67 | 2.03 |

$A_{calculated} = A_{MeP} + A_{MePc}$

**Table 3.**

IR data for carboxylated stretch in $cm^{-1}$

| Compound | Sym. stretch ($cm^{-1}$) | Asym.strech ($cm^{-1}$) |
|---|---|---|
| NiTMPyP/ZnTCPc | 1377 | 1590 |
| CoTMPyP/ZnTCPc | 1375 | 1588 |
| RhTMPyP/ZnTCPc | 1374 | 1590 |
| PdTMPyP/ZnTCPc | 1379 | 1589 |
| NiTMPyP | 1382 | 1582 |
| CoTMPyP | 1390 | 1586 |
| RhTMPyP | 1392 | 1585 |
| PdTMPyP | 1389 | 1584 |
| ZnTCPc | 1390 | 1583 |

The observed data could argue the symetry distorsion of phthalocyanine upon dimerization.

Before testing these photosensitizer systems into some photodynamic applications, was necessary to evaluate their capacity for singlet oxygen generation.

All the studuied systems are ghood sensitizers for photo-oxidation of DPBF with high quantum yields (table 4).

**Table 4.**

Singlet oxygen generation by the studied compounds

| Compounds | Φ(1O2) |
|---|---|
| NiTMPyP/ZnTCPc | 0.7 |
| CoTMPyP/ZnTCPc | 0.801 |
| RhTMPyP/ZnTCPc | 0.85 |
| PdTMPyP/ZnTCPc | 0.93 |

| Compounds | Φ(1O2) |
|---|---|
| NiTMPyP | 0.07 |
| CoTMPyP | 0.13 |
| RhTMPyP | 0.23 |
| PdTMPyP | 0.3 |
| ZnTCPc | 0.7 |

From this table could be observed that the best photosensitizer is the system RhTMPy/ZnTCPc with a very high value for the quantum yield of singlet oxygen-0.93.

After exposure of the yest Saccharomices Cerevisiae to certain agents (light and porphyrinis drug) a great decrease in viability is observed if the treated cells are incubated in the dark for 6 hours or more in distilled water at 30 C. It seems reasonable to assume that the light inactivation of Saccharomices Cerevisiae is due to the enzymatic destruction of DNA [23], Fig.5.

Different applications of PDT have been, in the last 4-5 years, effectively developed. The selective degradation of cancerous cells is obtained, for example, by the intravenous injection of photosensitizer followed by illumination of the pacient with red light. Such procedure has already been applied on more than 10,000 occasions. It is primarily applied in clinical treatment, because only one photosensitizer (Photofrin II) has been approved for wider applications in hospitals. In clinics and, of course, in model investigations, various group of dyes are being investigated to find the most effective photosensitizers for a given type of therapy having the highest selectivity of incorporation into malignant and healthy cells. Up to now, several dyes, e.g., merocyanines, phthalocyanines, and several types of porphyrins have been most widely investigated [24].

The effect of PDT on the microvasculature of the brain tumour cells in the first few hours after treatment was studied by electron microscopy. The red light led to a rapid necrosis of tumour which was not the result of the direct killing of tumour cells, but destruction of tumour microvasculature. It has been shown that the vascular damage expressed by a decreased blood flow stasis are immediate and major consequences of the photodynamic treatment with photodynamic systems introduced in these experiments.

The first observable sign of the destruction occur in the collagen fibers and other connective tissue elements located in the subendothelial zone of the tumour capillary wall. The altered permeability and transport through the endotellial cell layer resulting from erithrocyte swelling and increased intraluminal pressure may be another keys feature in the photodynamic destruction.

From the micrograms recorded (Figure 6) before and after the PDT treatment of the brain culture tissue, could be observed the dissapearance of the tumoral zone from the studied cellular mass [24].

All these experiments are in work and they should be improved in future.

## 4. Conclusion

The heterodimerization based on pairing porphyrins and phthalocyanines bearing appositelly charge substituents, yields to the final heterodimers having higher efficiency and stability.

The hetero-aggregation will occur only between Cl- substituents of the porphyrin and the sodium ion from the carboxilated substituents of the phthalocyanine ring.

The heterodimerization was investigated by spectral methods (UV-Vis,IR spectroscopy) and the final heterodimer was tested as photosensitizer by DPBF test, the best being the system RhTMPyP/ZnTCPc .

All these systems were also tested into PDT clinical application on the brain tumorla cells provided from mice (in vitro), the PDT protocol yielding to the dissapearance of the tumour.

## REFERENCES

1. R.M.Ion, Progr.Catal., 6, 1, 55(1997);
2. R.M.Ion, A.Planner, D.Frackowiak, K.Wiktorowicz, Acta Biochimica Polonica, **45**, 3, 833(1998);
3. I.Rosenthal, Photochem.Photobiol., 53, 859(1991);
4. R.M.Ion, G.A.Petre, Rev.Chim., Bucharest, 47(2), 113(1996);
5. P.Gregory, "High Technology Applications of Organic Dyes", Plenum Press, N.Y., 1991;
6. R.M.Ion, Ph.D.Thesis, Bucharest, 1994;
7. J.Goc, D.Wrobel, R.M.Ion, J.Mol.Structure, 450, 239(1998);
8. D.Frackowiak, A.Planner, R.M.Ion, K.Wiktorowicz, The First INTERNET Conf. Photochem.Photobiol., 1997; R.M.Ion, Rom.J.Biophys., 2, 62(1998);
9. R.F.Pasternack, L.Francesconi, R.Raff, Inorg.Chem., 12, 2606(1973);
10. M.Ochsner, Photochem.Photobiol., B:Biol., 32, 3(1996);
11. T.H.Tran-Thi, S.Gaspard, Chem.Phys.Lett., 148, 327(1988);
12. T.H.Tran-Thi, S.Palacin, Chem.Phys.Lett., 157, 92 (1989);
13. T.H.Tran-Thi, J.-F.Lipskier, J.-F Simoes, S.Palacin, Thin Solid Films, 210, 150(1992);
14. J.-F.Lipskier, T.H.Tran-Thi, Inorg.Chem., 32, 722(1993);
15. T.H.Tran-Thi, J.-F.Lipskier, D.Houde, C.Pepin, E.Keszei, J.P.Jay-Gerin, J.Chem.Soc., Faraday Trans., 88(15)2129 (1992);
16. T.H.Tran-Thi, Coord.Chem.Rev., 160, 53(1997);

17. R.M.Ion, M.Grigorescu, F.Scarlat, V.Niculescu, J.Balkan Union Oncology, submitted 1999;
18. A.D.Adler, J.Org.Chem., 32, 467(1967);
19. P.Job, Ann.Chem., 9, 113(1928);
20. Pascu, R.M.Ion, L.Danaila, L.Tugulea, Int.Symp.Lasaers.Bucharest, 1998;
21. Radzki, C.Giannotti, Inorg.Chim.Acta, 138, 139(1987);
22. Radzki, S.Gaspard, C.Giannotti, J.Chem.Res., M, 3101(1986);
23. K.Gunaydin, R.M.Ion, The Int.Conf.Electron Microscopy, Bursa, sept.1999;
24. Frackowiak, A.Planner, R.M.Ion, K.Wiktorowicz, in Near IR dyes for high technology applications, S.Daechne (Ed.), 1998, Kluwewr Acad. Publ., N.Y., pp.87-114;

STUDIA UNIVERSITATIS BABEŞ-BOLYAI, PHYSICA, SPECIAL ISSUE, 2000

# STUDY OF INTENSITY AND IONIZING RADIATION TYPE INFLUENCE ON SOME PORPHYRINS WITH APPLICATIONS IN CANCER THERAPY

**R.M. ION[*a], M. GRIGORESCU[*], F. SCARLAT[**], V NICULESCU[**], K. GUNAYDIN[***]**

[*] *ZECASIN S.A., Photochemistry Dept., Splaiul Independentei 202, Bucharest-79611, Romania; e-mail: rmion@pcnet.pcnet.ro*

[**] *National Institute of Physics for Lasers, Plasma and Radiation, Bucurest-Magurele, P.O.Box MG-36, Romania;*

[***] *Mustafa Kemal University, Faculty of Science and Letters, Chemistry Department, Antakya-Hatay,Turkey*

**ABSTRACT.** This paper deals with the experimental results about the modifying effects of ionizing radiation (electron and photon beam) at different intensities (200-30,000 R) and/or light on tetra-kis-p-sulfonato-phenyl-porphyrin (TSPP) in water solution as new and efficient sensitizer used in photodynamic applications.

The spectral changes upon ionizing radiation of TSPP show the formation of phlorin -type species. When these irradiated porphyrin solutions were exposed to light, J-and H-aggregated species were generated. The small intensity of ionizing radiation stimulate H-aggregation. Different proportions (experimentally determined) of singlet and triplet excited states are formed initially by ionizing irradiation as compared with light irradiation. By irradition of TSPP firstly with ionizing radiation, the subsequently light irradiation of this porphyrin yields to the generation of triplet states, the proportions being being much less than when TSPP was firstly excited with light and after that was treated with ionizing radiation. In the former case, the singlet excited state of TSPP was be the major specie generated in the studied system, but with a reduced yield than using only ionizing radiation .

The singlet oxygen generation (the photochemical efficiency) is enhanced is face-to-face configurations (H-aggregated forms) are formed. The porphyrin is efficiently incorporated in a monomeric form in granulocytes and leukocytes and in a J-aggregated fluorescent forms in granulocytes. The implications of such aggregated forms of TSPP in photodynamic applications were evaluated.

Key words: porphyrins, photodynamic therapy, aggregates;

[a] the correspondence author

## 1. Introduction

Porphyrins, free bases or metallo-complexes have an important role in many electron and energy-transfer processes [1].

The knowledge about their reactivity and synthesis, oriented their applications for medical area and photodynamic therapy of cancer, especially [2,3]. The interpretation of mechanistic studies of porphyrins requires the study of their aggregation [4], and ionization processes [5,6].

Although the dimer structure remains unclear, in the literature existing a lot of reports about this aspect [7-12], must be noted that several pulse radiolysis studies have been devoted to the reduction of porphyrins in aqueous solution [13-17] in order to establish the reduction mechanism of porphyrins. In aqueous solutions, the porphyrins undergo several one-electron reduction steps to form π-radical anions, dianions and more highly reduced species generally stable in aprotic solvents, while in aqueous solutions supporting disproportionation and/or protonation. The products of these processes are phlorins generated by protonation at a meso-position and phlorin anions, where one proton is added at the meso-position which could be oxidized rapidly by oxygen to the original porphyrin.

This paper is deals with the experimental results about the modifying effects of ionizing radiation (electron and photon beam with different intensities) and/or light on tetrakis-4-sulfonato-phenyl porphyrin (TSPP) in water as solvent.

## 2. Experimental part

### Materials

The porphyrin TSPP was synthesized and purrified in tha laboratory as was reported elsewhere [26].

The cells incubation was achieved on heparinized blood samples, as was reported elsewhere [28]. Whole heparanized blood samples remaining after routine analysis were incubated with porphyrins by means of a lysing reagent (Ortho Diagnostic USA).

The quantum yield for singlet oxygen generation is determined by 1,3-diphenylisobenzofuran test [6].

### Methods

The electron and photon radiation beams were supplied by the 7.0 Mv Linear Accelerator of the National Instituted for Laser, Plasma and Radiation Physics, Romania.

All the irradiation processes with light were achieved with a medium-pressure 250-W mercury lamp (Romlux-Romania).

The visible absorption spectra were recorded on a SPECORD M400 Carl Zeiss Jena spectrophotometer. All spectroscopic studies were performed in the porphyrin concentration range of $8 \times 10^{-5}$ to $1 \times 10^{-8}$ M.

The 3-fluorescence flow cytometer (Cytron Absolute, Ortho) equipped with an argon ion laser was used. The dependence of forward light scattering versus right angle light scattering enables to distinguish various types of cells. The fluorescence excited at 488 nm, was measured through the orange band pass filter (563-607 nm) and through red filter ($\lambda > 620$ nm) in the direction perpendicular to that of the exciting light and the cells stream. The intensity of emission of a given population of the cells was obtained from a specialised program using the gate

analysis method [18,19]. Was appreciated the number of stained cells (lymphocytes and granulocytes), incubated with porphyrins either in their monomeric forms or in their aggregated forms.

## 3. Results and discussion

The radiolytical oxidation and reductions of porphyrins by using photon or electron beam are very important method [18] for studying such compounds; the main advantage of this method is due to the well-defined nature of the reducing or oxidizing species. Radiolysis of water is known to produce the primary radicals $e^-_{aq}$, H and OH. with respective yields of 2.7, 0.5 and 2.7 eV. In addition, protons and hydroxyl ions are formed with yields of 3.4 and 0.7 eV. Hydrated electrons reduce either the ligand or the metal, while H and OH are likely to add to the ligand.

Tetrakis-4-sulfonato-phenyl-porphyrin (TSPP) is an anionic porphyrin, a very large disk-shape molecule which possess four negative charges the sulfonate groups from the four corners (Fig.1).

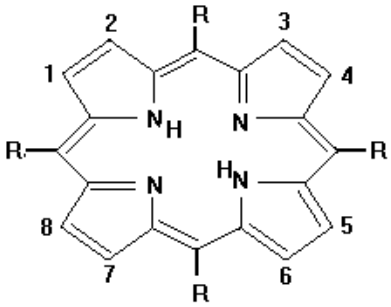


Fig.1 The structure of the porphyrin molecule

$R = SO_3^-$

In aqueous solutions, at neutral pH, the electronic absorption spectrum of TSPP is typical of free base porphyrins ($D_{2h}$ symmetry) and is characterized by an intense Soret band at arround 420 nm and four Q bands in the 500-700 nm range (the aetio-type spectrum).

In acidic medium, new absorption bands (from 490, 707 nm) become dominant when the concentration of TSPP exceeds $10^{-5}$ M and they were attributed to the aggregated forms of dications species ($C>10^{-4}$ M). The band from 490 nm arises from the J-aggregate (edge-to-edge interaction) of porphyrin molecules [20]. TSPP is perhaps unique because J-aggregation is the most facile and very low concentration of the dye is required for J-aggregation,Fig.2. One another band from 422 nm arises from the H-aggregate of porphyrin molecules [6,21] (face-to-face interaction) and appear at $c> 2.5 \times 10^{-3}$ M.

First, TSPP is a very large disk-shape molecule with charges at the four corners and at the geometric center. Could be a zwitterion between the central diacid group and one of the sulfonic groups, which could be more responsible for J-aggregation. Because of static Coulombic repulsion, the two central N-H + fragments are probably distorted out of the aromatic plane, as was reported

elsewhere [22,1]. The electrostatic interaction between the zwitterionic no doubt facilities these aggregations.After some authors [23], TSPP without the capability of zwitterion formation do not aggregate. Zwitterion form contain a double charge in the macrocycle and four other negative charges on the sulfonic groups from the molecule.

**Table 1.**

The specific absorption bands of different TSPP forms

| Porphyrinic forms | B band $\lambda/\varepsilon \times 10^{3}$ (nm/$M^{-1}.cm^{-1}$) | Q bands |
|---|---|---|
| $H_2TSPP^{-4}$ | 412/355 | 515/130<br>551/4.5<br>579/1.9<br>633/1.01 |
| $H_4^{+2}TSPP$ | 433/357 | 550/140<br>594/3<br>644/14 |
| $H_4^{2+}TSPP^{4-}$ first aggregate(J) | 422 490 | 707 |
| $H_4^{2+}TSPP^{4-}$ second aggregate(H) | 401 | 517<br>552<br>593<br>650 |

J-aggregates are formed with the monomeric molecules arranged in one dimension such that the transition moment of the monomers are parallel and the angle between the transition moment and the line joining the molecular centers is zero [23].

H-aggregates are again a one-dimensional arrangement of strongly coupled monomers, but the transition moments of strongly coupled monomers are perpendicular to the line of centers [23]. A H-aggregate is more favourable formed because the macrocycle is neutral and because of the spacing and shielding provided by the complex.

Until 800 R, the UV-Vis absorption spectrum of the J-aggregate obtained by ionizing irradiation of TSPP is characterized by relatively sharp red-shifted peaks at 492 and 706 nm. The H-aggregate could be obtained slowly in time from J-aggregate, this new form being characterized by a blue-shifted Soret absorption peak at 400 nm; the Q-band region consists of four bands (Fig. 2).

At higher intensities (800-6000 R for photon beam and 800-30000 R for electron beam) the obtained $\pi$-radical anions exhibit a broad absorption in the region 600-800 nm which is dependent of pH, changing with pH due to protonation at a pyrrolic nitrogen (Fig.3).

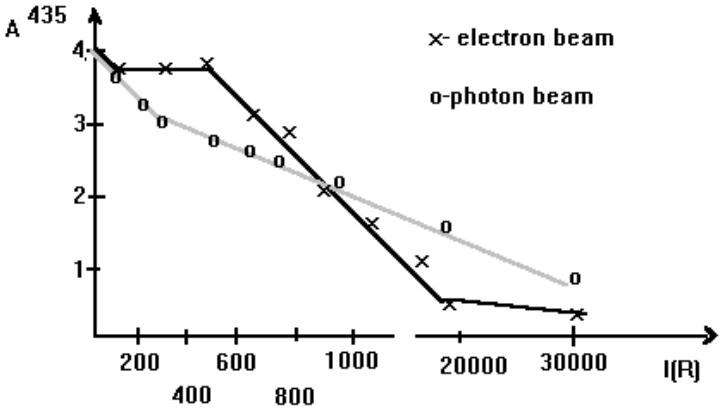


**Figure 3.** The variation of the absorbance from 435 nm of TSPP vs. the intensity of electron or photon-beam.

The J-aggregate is formed initially as a transparent colloidal solution which is then precipitated from the aqueous solution with time by exposure to light (after ionizing tratment of TSPP the light had a strong aggregation effect . The precipitated is insoluble in water wherein the aggregate dissociates into monomeric porphyrin.

If TSPP was firstly light-irradiated and then photon-or electron irradiated, were not obtained important changes in the spectrum of the porphyrin. Only a small decrease of the 700 nm absorption band was observed, probably due to the heating and slow evaporation of the solvent from cuvette.

Both the variation of the radiation intensity and the radiation type are decisive for such radiolytic processes. The photons stimulate the aggregation, the H-aggregates being generated only with photons at 800 R intensity. Also, at low intensities of the radiation no effect was observed, but at higher intensities the same $\pi$-radical anion being obtained. With an electron beam, the reverse situation was observed: only low intensities stimulated the aggregation (100-200 R) the higher intensities having the same effect on the porphyrinic solution. A specific photodegradation process could be obtained during a long light irradiation of TSPP in water-solution [25-29].

Which are the implications of all these experiments in the photodynamic therapy of cancer?

First of all, as we already know end-to-end configurations (as it is in our case the J-aggregate) exhibit weak emission properties comparable with those of monomer [23,22] or the H-aggregates.

The singlet oxygen formation, so the photochemical efficiency is enhanced if face-to-face configurations (H-aggregates) are formed [21,23]. Or, in all our previous experiments was observed a high singlet efficiency at the incorporation of some different cells [30,27],Table 2.

**Table 2.**

The quantum yields for singlet oxygen generation by TSPP in different conditions

| Condition | $\Phi(^1O_2)$ |
|---|---|
| TSPP | 0.78 |
| TSPP+electrons | 0.83 |
| TSPP+photons | 0.56 |
| TSPP+electrons+hν | 0.90 |
| TSPP+photons+hν | 0.63 |
| h ν+TSPP+electrons | 0.62 |
| h ν+TSPP+photons | 0.12 |

Also, because the protonation of the inner nitrogen atoms drastically prevents the incorporations into blood cells [30], and our porphyrins had good incorporation properties, we could presume that this porphyrins exists firstly as H-aggregates, beacuse they are neutral (not at all charged) and stable in solution. This rule could be an logical explanation for the fast application of such porphyrin in biological application, in order to delay the J-aggregates formation as precipitate . Meantime, we could presume that H-aggregates exist concomitently with the J-aggregates, because some literature sources presume that the J-aggregates are formed initially as a transparent colloidal solution which is then precipitated from the aqueous solution with time, or by light irradiation or by heating [28]. The precipitate is insoluble in water, but soluble in DMSO, wherein the aggregate dissociates into monomeric porphyrin .

By flow cytometry (the dependence of foreward light scattering vs. the right angle scattering) the investigated cells were analysed only the regions which include gathered lymphocytes and granulocytes [31]. Number of stained cells of given type was obtained from the percent of gated cells exhibiting the observed fluorescence, Table 3.

**Table 3.**

Incorporation of TSPP into cells

| Dye | Cells | % stained cells | Mean intensity | State of dye fluorescence |
|---|---|---|---|---|
| $TS_4PP$ | L | 44 | 89.7 | M |
| $TS_4PP$ | G | 67 | 121 | M |
| $TS_4PP$ | L | 0 | 91 | A |
| $TS_4PP$ | G | 0.1 | 77 | A |

M=monomer; A=aggregates.
L=lymphocytes; G=granulocytes.

The fluorescence of lymphocytes and granulocytes was analysed separately. The different ratio of "mean fluorescence intensities" of the same cells stained can suggest that the aggregation of the dye is different or perhaps, the interaction of these dye with the cell membrane are different [32]. From these hystograms, it can be assumed that aggregated forms are better penetrating membranes (from the higher values of the mean intensity fluorescence parameter) but once in the membranes, the dye is deaggregated by interaction with lipids, therefore exhibiting similar efficiency of fluorescence as the incorporated monomeric form. In both cases penetration into granulocytes is more efficient than into lymphocytes. Structural constraints caused by an over-crowding of this porphyrin molecule in a small space show us that this porphyrin could interacts with very polar regions in close contact with the solvent. It suggests that in both solvents the both forms of TSPP penetrate the cell membrane. The percent of stained fluorescent in aqueous DMSO is much higher in DMSO because in in aqueous DMSO the porphyrin is in high degree aggregated forms. In both cases, penetration to granulocytes is more efficient than into lymphocytes.

## 4. Conclusions

The spectral changes upon photons or electrons irradiation of the porphyrin TSPP show the formation of phlorin-type species with a strong absorption near 700 nm. When the ionizing irradiated TSPP solution was exposed to light H- and J-aggregated species were generated. The photons (only 800 R) stimulate the H-aggregation and electron beam (100-200 R) stimulate the J-aggregation. The higher intensities will yield to $\pi$-radical anion inactive in photochemical processes.

Porphyrins have potential applications in the photodynamic therapy of tumours (PDT); they produce the necrosis of different incipient forms of cancers due to their singlet oxygen capacity. This capacity is enhanced if face-to-face configurations (H-aggregates) are formed. The porphyrin TSPP as J-aggregate fluorescent form, has an increased penetration capacity into the components of human blood cells, higher for the granulocytes than for the lymphocytes.

The aggregated forms of TSPP are better penetrating membranes of blood cells, but in membrane TSPP is deaggregated by the interaction with lipids and subsequently exhibit similar efficiencies as in monomeric forms. TSPP is efficiently incorporated into lymphocytes and granulocytes but only in monomeric form.

## REFERENCES

1. Levy, J.C., M.Obochi, New applications in photodynamic therapy, *Photochem. Photobiol., 1996, 64, 737-739;*
2. Ion, R.M., The photodynamic therapy of cancer - a photosensitisation or a photocatalytic process?, *Progr.Catal., 1997, 1, 55;*

3. Ochsner, M., Photophysical and photobiological processes in the photodynamic therapy of tumours, *J. Photochem. Photobiol., B:Biol., 1997, 39, 1-18;*
4. Pasternack, R.F., P.R.Huber, P.Boyd, G.Engasser, L.Francesconi, E.Gibbs, P.Fassella, G.Cerio Ventura, L.De Hinds, On the aggregation of meso-substituted water-soluble porphyrins, *J.Amer.Chem. Soc., 1972, 94, 13, 4511 -4517;*
5. Pottier, R., J.C.Kennedy, The possible role of ionic species in selective biodistribution of photochemotherapeutic agents toward neoplastic tissue, *J.Photochem.Photobiol., B:Biol., 1990, 8, 1-16;*
6. Ion, R.M., G.A.Petre, Spectral study of some porphyrins used in the photodynamic therapy of cancer. The ionization processes., *St.Cerc.Biotehnol., 1997, 29-30, 216-222;*
7. Abraham, R.J., p-p Aggregation in metalloporphyrins causative factors, *J.Chem.Soc., Chem.Comm., 1978, 699-700;*
8. Ion, R.M., The spectral study of the porphyrins used in PDT. The aggregation processes, *St.Cerc. Biotehnol., 1997, 29-30, 205-212;*
9. Chikira, M., ESR Evidence for dimer formation in high spin iron (III) EOP., *J.Chem.Soc., Chem. Comm., 1978, 906-907;*
10. Krishnamurthy, M, J.R.Sutter, P.Hambright, Monomer-dimer equilibration of water soluble porphyrins as a function of the coordinated metal ion, *J.Chem. Soc. Chem. Comm., 1975, 13-15;*
11. Das, R.R., R.F.Pasternack, R.A.Plane, Fast reaction kinetics of porphyrin dimerization in aqueous solution, *J.Amer. Chem.Soc., 1970, 92, 11, 3312-3316;*
12. Brown, S.B., M.Shillcock, P.Jones, Equilibrium and kinetic studies of the aggregation of porphyrins in aqueous solutions, *Biochem.J., 1976, 153, 279-285;*
13. Mosserri, S., J.C.Vialocq, B.Perly, Porphyrins-cyclodextrins. III-breaking of cofacial dimers and multi-electron reduction of free base porphyrin within and outside of cyclodextrin cavities, *Rad.Phys.Chem., 1992, 39, 2, 223-233;*
14. Mosseri, S., J.C.Mialocq, B.Perly, P.Hambright, Porphyrin-cyclodextrin. I.Photooxidation of ZnTSPP in cyclodextrin cavities. The characterization of ZnTSPP dication: photolysis, radiolysis and NMR studies, *J.Phys.Chem., 1991, 95, 2196-2203;*
15. Kier, W.F., E.J.Land, A.H.MacLennan, D.J.McGarvey, T.G.Truscott, Pulsed radiation studies of photodynamic sensitizers the nature of DHE, *Photochem.Photobiol., 1987, 587-589;*
16. Kumar, M., P.Neta, T.P.G.Sutter, P.Hambright, One-electron reduction and demetallation of copper porphyrins, *J.Phys.Chem., 1992, 96, 23, 9571-9575;*
17. Ballard, D., C.Mauzerall, Photochemical ionogenesis in solutions of ZnOEP, *J.Chem. Phys., 1980, 72(2), 933-947;*
18. Planner, A., R.M.Ion, K.Wictorowicz, D.Frackowiak, The incorporation of porphyrins in human leucocytes measured by flow cytometry absorption and emission spectroscopy, *"First Internet Conference on Photochem. Photobiol.", http://www.netsci-journal. com/97v3/intro.htm.*
19. Carter, R., E.W.Meyer, Introduction to principles of flow cytometry, in *"Flow cytometry. A practical approach", M.G.Ed.Oxford Univ.Press, Oxford-New York-Tokio, 1990, p.1-28;*
20. Bagdonas, S., R.Rotomskis, Investigations of spectroscopic properties of TSPP in aqueous solutions at different acidity, *Lith.J.Phys., 1998, 38, 75-80;*
21. Harel, Y., D.Meyerstein, On the mechanism of reduction of porphyrins . A Pulse radiolytic study, *J.Amer.Chem.Soc., 1974, 96, 2720-2727;*

22. Pasternack, R.F., K.F.Scaefer, P.Hambright, Resonance light-scattering studies of porphyrin diacid aggregates, *Inorg.Chem., 1994, 33, 2062-2065;*
23. Ribo, J.M., J.Crusats, J.-A.Farrera, M.L.Valero, Aggregation in water solutions of tetrasodium diprotonated meso-tetrakis (4-sulfonatophenyl) porphyrin, *J.Chem. Soc., Chem. Comm., 1974, 681-682;*
24. Chou, I.Y., A.J.Hallock, Absorption study of an aggregated porphyrin under high pressure, *J.Chem.Phys., 1995, 107(22), 9297-9301;*
25. Ohno, O., Y.Kaizu, H.Kobayashi, J-Aggregate formation of a water-soluble porphyrin in acidic media, *J.Chem.Phys., 1993, 99(5), 4128-4132;*
26. Maiti, N.C., S.Mazumdar, N.Periasamy, J-and H-aggregates of porphyrins with surfactants, stopped-flow and electron microscopy studies, *J.Porphyrin Phtalocyanines, 1998, 2, 369;*
27. Sutter, T.P.G., R.Rahini, P.Hambright, J.C.Bommer, M.Kumar, P.Neta, Steric and inductive effects on the basicity of porphyrins and on the site of protonation of porphyrin dianions, *J.Chem.Soc., Faraday Trans., 1993, 89(3), 495-500;*
28. Ion, R.M., C.Mandravel., The photodegradation reaction of some porphyrins, *South.Braz.J.Chem.Soc., 1997, 2, 62-71;*
29. Rotomskis, R., S.Bagdonas, G.Streckyte, Spectroscopic studies of photobleaching and photoproduct formation of porphyrins used in tumour therapy, *J.Photochem. Photobiol., B:Biol., 1996, 33, 61;*
30. Ion, R.M., Spectral studies of TSPP and TSNP used in PDT.I.Monomer- dimer equilibrium, *Rom. J. Biophys., 1996, 6(3-4), 213-218;*
31. Ion, R.M., A.Planner, K.Wiktorowicz, D.Frackowiak, Incorporation of various porphyrins into human blood cells measured using the flow-cytometry, the absorption and emission spectroscopy, *Acta Biochimica Polonica, 1998, 45(30), 833-845;*
32. Frackowiak, D., A.Planner, R.M.Ion, K.Wiktorowicz, Incorporation of dyes in resting and stimulated leukocytes, in *"Near-infrared dyes in high technology fields", Ed.S.Daehne, Kluwer Acad.Publ., NATO ASI Series, 1998, 87-114;*